Title
On the Fluctuations that Order and Frustrate Liquid Water

Author
Limmer, David

Publication Date
2013

Peer reviewed|Thesis/dissertation

On the Fluctuations that Order and Frustrate Liquid Water

By

David Tyler Limmer

A dissertation submitted in partial satisfaction of the

requirements for the degree of

Doctor of Philosophy

in

Chemistry

in the

Graduate Division

of the

University of California, Berkeley

Committee in charge:

Professor David Chandler, Chair
Professor Phillip L. Geissler
Associate Professor Burkhard Militzer

Spring 2013

On the Fluctuations that Order and Frustrate Liquid Water

Abstract

On the Fluctuations that Order and Frustrate Liquid Water

by

David Tyler Limmer

Doctor of Philosophy in Chemistry

University of California, Berkeley

Professor David Chandler, Chair

At ambient conditions, water sits close to phase coexistence with its crystal. More so than in many other materials, this fact is manifested in the fluctuations that maintain a large degree of local order in the liquid. These fluctuations and how they result in long-ranged order, or its absence, are emergent features of many interacting molecules. Their study therefore requires using the tools of statistical mechanics for their their systematic understanding. In this dissertation we develop such an understanding. In particular, we focus on collective behavior that emerges in liquid and solid water. At room temperatures, the thermophysical properties of water are quantified and rationalized with simple molecular models. A key feature of these models is the correct characterization of the competition between entropic forces of packing and the energetic preference for tetrahedral order. At cold temperatures, the properties of ice surfaces are studied with statistical field theory. The theory we develop for the long wavelength features of ice interfaces allows us to explain the existence of a premelting layer on the surface of ice and the stability of ice in confinement. In between these extremes, the dynamics of supercooled water are considered. A detailed theory for the early stages of coarsening is developed and used to explain the peculiar observation of a transient second liquid state of water. When coarsening dynamics are arrested, the result is the formation of a glassy states of water. We show that out-of-equilibrium the phase diagram for supercooled water exhibits a rich amount of structure, including a triple point between two glass phases of water and the liquid. At the end, we explore possible technological implications for the interplay between ordering and frustration in studies of water at metal interfaces.

To Jenna

Contents

Acknowledgments

I owe an enormous debt of gratitude to everyone in my life who has helped shape the person and researcher I am today. It is both an honor and a pleasure to be able to thank them here.

First and foremost, I would like to thank my family for their love and support. From my earliest days in Clovis, New Mexico my parents instilled in me a deep love of learning, a passion for reading and a sincere skepticism. I am not sure if they knew then that these gifts would be essential to the scientist that I would become, but they are. I am also truly grateful to them for their patience with me and their unconditional love. I am thankful to my sister Sarah and brother Michael, who I am happy have become two of my best friends. We have been through a lot together and I am excited to see where we each go from here. To the rest of my family in New Mexico, Reba, Lecile and Tim and elsewhere, Lecia, Pearl, and especially Danny and Debbie, thank you for reminding me where I have come from. Finally, my role model and the person who taught me what was important in life, Lou Limmer. He was my hero and I wish he could still be here with us.

Intellectually, I am forever indebted to my advisor, David Chandler. He has been a tireless source of guidance, enthusiasm and support. Over the last five years, I have learned a great deal from him about how to do science and communicate it effectively, and also how to be a good mentor and run a world-class research group. His dedication to science is a constant source of inspiration. It is a tremendous privilege to count myself as a member of the extraordinary group of people that he has trained through his lifetime. More than just professionally, David has been a generous source for advise and friendship and it has been a great pleasure getting to known him and his wife Elaine over the last few years.

While I am proud to be from the Chandlerian school of statistical mechanics, many of the tools I learned to use during my time at Berkeley were initially provided to me by Phill Geissler. It was in his graduate stat mech class that I was first exposed to the microscopic world behind thermodynamics, it was in his simulations course that I learned to approximate complex problems, and it was in his volunteered summer lectures that I was first taught the wonders of gaussian field theory. Phill has been a great source of advice, both scientifically and professionally, and I am very thankful to have been able to interact with him and his group.

I would not have made it this far without the help and guidance of many other people throughout my education. During my time at New Mexico Tech, I was fortunate enough to

interact with a number of terrific teachers and researchers. I owe my initial excitement for the challenges of physical chemistry to Larry Werbelow, my first foray into simulation and the theory of liquids to John McCoy and my teaching philosophy to the time I spent in the ARC with Elaine DeBrine-Howell. I likely would not be at a first class research institute like Berkeley if it were not for Don Weinkauf and his organizing a year long internship for me at Los Alamos National Laboratory where I was exposed to independent research for the first time. During my time at Los Alamos, under the direction of Mike Smith and Steve Rutherford, I fell in love with applying the rules learned in the classroom to messy, real world questions. I am forever grateful to the both of them for taking me in and nurturing my initial scientific development. Those early years spent learning the predictive power of modeling set me on a path that I find myself now, as a student of statistical mechanics.

I have also been privileged to have interacted with a number of senor scientists through the years whose encouragement and excitement has been important to maturation as a scientist. In particular, I have benefited from visits with Eran Rabani, Valeria Molinero and Austen Angell, who always have interesting insight. I am thankful to Rich Saykally and Shakar Garde for their professional encouragement. Gabor Somorjai turned David and I on the phenomenology of the ice interfaces. Jurg Hutter allowed me to visit his lab in Zurich for a few wonderful weeks in the summer of 2011 and learn to do some basic calculations with CP2k. Mikhail Sprik taught me what little I know about theoretical electrochemistry. Conversations with Steve Harris have provided excitement and a fresh perspective in my last semester. All of my work on water at metal interfaces is an offspring of the groundbreaking work of Paul Madden and has proceeded in a collaboration with him. Visits from Benjamin Rottenberg have been very stimulating and new directions in the study of electrified interfaces that I am pursuing now are an exciting collaboration with him. I am thankful to Burkhard Militzer for a critical reading of this dissertation and discussions on different ice phases of water.

During the initial work on the putative second critical in supercooled water, I benefited from interactions with a number of researchers. I am thankful to Phill and Berend Smit who provided a critical assessment of the initial. During the writing of the manuscripts, I also had discussions with a number of people including Mikhail Anisimov, Chris Bertrand, Roberto Car, Pablo Debenedetti, Athanassios Panagiotopoulos, Peter Poole, Alan Soper, John Weeks, Ben Widom, Michael Widom and Yang Zhang I must thank H. Eugene Stanley for inviting me to speak to his group in the summer for 2011, where I first presented these ideas. Sow-Hen Chen and Anders Nilsson have in subsequent years provided similar venues for this ongoing discussion.

As for my fellow students and post-docs I owe sincere amount of gratitude to a number of individuals who along the way have served as unofficial mentors and sounding boards. Adam Willard played a big role in my joining the Chandler group and served as an important example of success. As my scientific "big brother," he taught me how to conduct myself in the group and how to make myself understood. After he left, I was fortunate to be able to work with him on the metal interfaces studies, presented in the last chapter of this dissertation. This collaboration has been incredible fruitful and it has been a pleasure to continue working

with Adam. Early on, I benefited from the wisdom and knowledge of Thomas Speck. His kindness in fielding my naive questions during late night sessions in the Pitzer center was an important part of my initial training. Patrick Varilly is an amazing scientist and person and it was my pleasure to share an office with him my first three years. His careful and methodical approach to science is something I aspire to. In my last few years, it has been a pleasure to work and learn from Aaron Keys. Apart from being an invaluable resource on a broad array of topics, he offered a valuable friendship during the last few years.

Other older members whose company and discussion was appreciated include, Yael Elmatad, Lester Hedges, Ulf Pedersen and Kafui Tay. In the last few years, it has been my pleasure to work with new members in the group including Alex Hudson, Kelsey Schuster and Dayton Thorpe. I am thankful to Dayton in particular for proof reading the chapter on ice interfaces. In the greater Pitzer center community, I have benefited from interacting with a number of other people including Anna Schneider, Chris Ryan, Katie Klymko, Julian Azar, Paul Horn, David Stuck, John Parkhill, Tom Baker, David Sivak. Michael Grünwald, Suriyanarayanan Vaikuntanathan, Todd Gingrich, Ayelet Benjamini, Eric Sundstrom and Pat Shaffer in particular have been good friends as well as important colleagues.

A number of other people outside the Pitzer center have had a positive impact on my time at Berkeley. At various times I have enjoyed friendships with Billy Martin, Nicole Travis, Doran Bennet, Yuval Benjamini, Craig Settles, Erica Shultz and David Laponite. These people have helped me remember that there is life outside of science. I am also thankful to the staff of the chemistry department, and administrators that have helped make my time here easier. Specifically, assistants in the Pitzer center, Cheryl Higley, Lisa Littlejohn, Cheryn Gliebe and Sonia Waters have been wonderful. I am thankful to Jon Forrest, William Chen and Kelly McDonald for keeping the computers running. I am thankful to Kathy Durkin for the 10s of posters she has printed for me over the last few years.

Finally, I am supremely thankful to Jenna Jeffrey. She has been my best friend throughout graduate school. In the five years that we have known each other, she has been a constant source of happiness in my life. Whether it was our first year where time was limited yet we still stole away almost weekly to the Down Low for salsa dancing. Or during our qualifying exams, where we still made time for brunches at La Mediterranee and dinners over the cribbage board. Or in our last semester, where we spent hours on end together in libraries, coffee shops, and at our dining room table writing our dissertations. Jenna has been my closest advisor and my pillar of support. Her dedication to her work inspires me to worked harder. Her excitement for life keeps me active and engaged. Her English skills keep my papers intelligible. While the past five years have been some of the best of my life, because of her, I am excited for the next five years as we continue traveling forward together. But for now, we are done!

Chapter 1

Introduction

Water is the most abundant molecule on Earth: it fills the oceans and clouds the sky. It is one of the few substances that exists in liquid, solid and gaseous forms over the range of naturally occurring conditions. It is a testament to this ubiquity that the physics and chemistry of water has fascinated scientists for centuries[10].

The water molecule itself is almost unremarkable. Two hydrogens reduce a single oxygen producing a stable chemical compound, H_2O. However the resultant electronic structure affords forces between water molecules that are striking. Unlike many other small molecules, the energetics of water are not determined by isotropic steric constraints, but rather by strong, directional electrostatic interactions termed hydrogen bonds. Broadly, relating microscopic forces to observable physical properties is the subject of statistical mechanics, and applying the tools of statistical mechanics to relating the forces of hydrogen bonds to the properties of liquid and solid water is the subject of this dissertation.

Of the many peculiar properties of water, the fact that it expands upon freezing is perhaps the most readily associated with these strong, directional forces[49]. At low pressures, most substances contract when cooled in an attempt to maximize a given molecule's interactions with its surroundings. Consequently, when such substances solidify the resultant structure is determined by how these molecules pack together. This is not the case with water. When water freezes at low pressures, its open structure maximizes hydrogen bonding creating an ordered solid that is locally tetrahedral and less dense than the liquid from which it transforms. In fact, this tetrahedral structure is conserved in the liquid where water forms four hydrogen bonds on average, though fluctuations away from this local order are common and no long-ranged order is present[49]. The unique thermodynamic properties of liquid water manifest how the strength of these hydrogen bonds are modulated by pressure and temperature. As will be discussed later, no single theoretical interpretation exists that satisfactorily connects these properties to the microscopic interactions of water. This dissertation takes an important step in this direction.

When hydrogen bonds are broken or otherwise disrupted at an interface, water is forced to adopt configurations that are not as energetically favorable as those in the bulk. At the

surface of ice, this results in the top layers of water being disordered.[1] Such disorder makes it possible for the water at the surface to flow, accounting for why ice is slippery[191]. At a liquid surface, where the molecules are already disordered, this interface engenders water with an ability to sustain large density fluctuations. These density fluctuations make it easier for water to solvate large nonpolar molecules producing the hydrophobic effect. In both cases, resolving how the fluctuations of water are modified in the presence of such topological constraints provides a great deal of insight into the collective behavior of water. Because these fluctuations occur on length scales larger than the individual molecules, general coarse-grained arguments can be formulated to quantitatively describe this behavior, as will be shown in the following chapters.

Reorganizing the hydrogen bond network of water into configurations with long-range order such as ice can take a significant amount of time because doing so requires the co-operation of many molecules. Since these times can be large, it is possible over shorter times to observe liquid water below its freezing point, where it can exist in a supercooled metastable state. While generic to most supercooled liquids, one of the most interesting observations made under this condition of metastability is the dramatic slowing down of the liquid as the temperature is lowered. At low enough temperatures, provided crystallization can be avoided, the supercooled liquid can become kinetically trapped where dynamics are constrained and reorganization is imperceptible on laboratory timescales. Kinetically arrested materials made from water are called amorphous ices[146]. Unlike most liquids, though, the aqueous materials formed from this out-of-equilibrium process exhibit a wide variety of structural diversity. In fact, it has been proposed that certain states accessed in this way can be interconverted through something analogous to a phase transition between amorphous ices[157]. This phenomena is called polyamorphism, and has evaded systematic study because the formalism for describing materials generically far from equilibrium did not exist. Near the end of this dissertation, a formulation of phase transition theory for non-equilibrium materials is used to place polyamorphism on rigorous ground and conclude that is indeed an example of a first-order nonequilibrium transition.

The rest of the dissertation is organized as follows. First in Chapter 2, some facts about the water molecule, the thermodynamics of its liquid state, and what is currently known regarding its phase diagram are reviewed. These facts serve to motivate simple, effective interactions between molecules that form the basis of the statistical mechanical description that is elaborated on throughout the text. This chapter also serves to review previous interpretations of existing data. Next in Chapter 3 numerical techniques for simulating the behavior of water-like models and testing hypotheses related to their behavior at low temperatures are detailed. This largely methodological chapter accomplishes two important goals– 1) in calculating the low temperature phase diagram for a variety of models it elucidates a common set of energy and timescales for water-like models and 2) it overturns a widely held view that water-like fluids support two different liquid phases. Chapter 4 presents a simple statistical field theory for ice interfaces based on broken orientational symmetry. This

[1] The existence of a premelting layer on the surface of ice was first proposed by Michael Faraday in 1842 and eventually verified from X-ray scattering in 1987[131].

theory, based on assumptions justified with molecular dynamics simulations, is capable of quantitatively explaining the existence and thickness of the premelting layer on the surface of ice and the dependence of the melting temperature under confinement. Chapter 5 examines the dynamics of liquid water at low temperatures. The behaviors detailed are used to clarify how water becomes kinetically arrested at its glass transition and how water crystallizes in a homogeneous solution. Understanding the equilibrium dynamics of supercooled water clarifies what happens when water is driven out of equilibrium. Specifically using large deviation function formalism and statistical mechanics of trajectories, the phase behavior of glassy water is elucidated. The phase diagram arrived at in this way includes first order transitions between liquid water and glass as well as a line of first order transitions between two distinct glasses. Finally, Chapter 6 illustrates how the emergent behavior detailed in the previous chapters is modulated in the presence of ordered interfaces with different degrees of compatibility with preferred water structures. In particular, the resultant behavior of water on metal surfaces and its consequences for technologically relevant interfaces are explored.

Chapter 2

Structure and thermodynamics of water

Thus one is led still more nearly inevitably to
conclude that water is not a simple substance at all
- Lavoisier[129]

This chapter begins by addressing some preliminaries about the water molecule, in particular its geometry and electronic structure.[1] The intermolecular potential that results is discussed briefly and its implications for the condensed phases of water are shown. These facts are used to motivate simple, effective interaction potentials that are tractable to the molecular simulation techniques used in later chapters. Next, the equilibrium phase diagram for water is discussed along with a formulation of metastability. The thermodynamics and equation of state of liquid water are reviewed, including those properties measured in supercooled, metastable equilibrium where the properties of water are particularly striking. Finally, the prevailing microscopic interpretations for the properties of liquid water are presented.

2.1 The water molecule

The water molecule is formed from two hydrogens covalently bonding to a single oxygen. The resulting equilibrium geometry of the isolated molecule is known experimentally to remarkable accuracy from the moments of inertia deduced by vibro-rotational spectroscopy. Figure 2.1a depicts the results of such studies. Most notably, water adopts a bent structure with an HOH angle, $\theta_{\mathrm{HOH}} = 104.5^{\mathrm{o}}$ and OH bond lengths, $r_{\mathrm{OH}} = 1\text{Å}$, on average[49]. This geometry can be rationalized from molecular orbital arguments in which the molecule is sp^3 hybridized, with the two hydrogens and the four paired electrons pointing at the opposite ends of a tetrahedron resulting in C_{2v} point group symmetry. While this qualitative description is faithful to the molecular geometry of water, the actual molecular orbital structure is

[1] The discussion borrows largely from much more comprehensive texts such as Eisenberg and Kauzmann's classic treatise, *The structure and properties of water*[49].

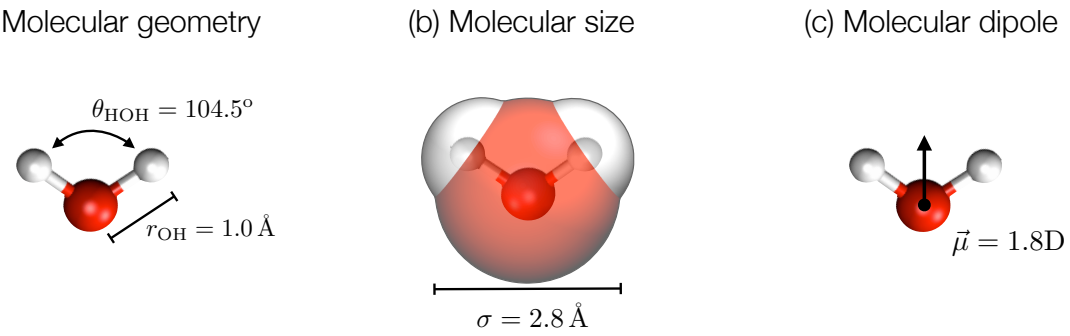

Figure 2.1: Geometry of an isolated water molecule.

more subtle.[2]

The large disparity in electronegativities between oxygen and hydrogen results in the majority of the electron density for this closed-shell, neutral molecule to be localized on the oxygen atom. This localization leads to the molecule being roughly spherical, as shown in Fig. 2.1b, with a van der Waals radius determined from the crystal structure of ice of 2.8 Å, which is identical to isoelectronic particles, methane and neon. The different electronegativities of oxygen and hydrogen coupled with the molecular symmetry, endows water with a large dipole moment. In a dilute vapor the molecular dipole can be measured with microwave spectroscopy and for water this yields a value of 1.85 D. In liquid and in ice Ih, water is further polarized by its surroundings leading to static dipole moments of 2.95 D and 3.0 D[49].

The nature of the interactions between water molecules has been the subject of decades of research. At large distances, the net neutrality and symmetry of the molecule dictates that the leading order electrostatic interactions will be dipole-dipole interactions. These interactions decay characteristically as $1/r^3$, where r is the distance between two point dipoles. At very close distances the closed shell electronic structure ensures that the interactions between molecules is sharply repulsive. In between these two limits however, the potential is complicated and varies rapidly with the relative orientation of the two molecules. This is due largely to classical electrostatics, but also to the partial covalent nature of a hydrogen bond that results in some charge transfer.

Theory is required in order to understand the interactions between molecules at a molecular level of detail. Figure 2.2 shows the results of a full configuration interaction, electronic structure calculation for a water dimer[152]. As shown in Fig. 2.2, the hydrogen bond is strongest for separations, $r_{OO} \approx 3.0$ Å, and relative angles, $\theta_{HB} < 20^o$. In this optimal, linear geometry, the hydrogen-bond has an adhesive strength of about 6 kcal/mol. This

[2]An isolated water molecule does not have two localized lone pairs of electrons, as typically illustrated in basic chemistry textbooks, but rather forms delocalized p-like orbitals perpendicular to the plane of the molecule in the highest occupied level[9, 46].

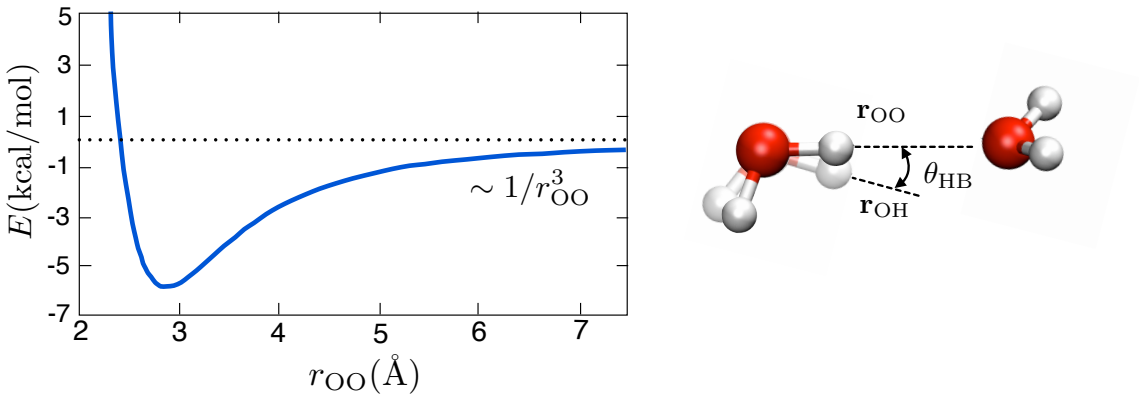

Figure 2.2: Potential energy for a linear water dimer computed from full configuration interaction electronic structure calculations, adapted from Ref. [152].

value can be anticipated from the heat of sublimation of ice Ih, $\Delta H_{\text{sub}} \approx 6$ kcal per mol of hydrogen at 273 K. Here, per mol hydrogen, acts as a proxy for the number of hydrogen bonds, as each hydrogen makes only one hydrogen bond in ice. Relative to typical thermal energies, 0.6 kcal/mol at 298 K, this attraction is large, however it is only this large over a small range of relative positions and orientations. Most of the hydrogen-bond strength decays for $r_{\text{OO}} > 4.0$ Å and $\theta_{\text{HB}} > 30^{\text{o}}$[152].

The interactions between water molecules are in stark contrast to other small molecules such as methane, CH_4, ammonia, NH_3, and neon, Ne. While all of these molecules are similar in size and molecular weight to water, none of them attract nearly as strongly. As a consequence, all of these molecules all have boiling points that are more than 100 K less than that of water[132]. Methane molecules, for example, interact with an isotropic dispersion potential with a maximum binding energy of around 0.6 kcal/mol[100]. While ammonia molecules have permanent dipoles and can hydrogen bond, their geometries make it difficult to form linear bonds like those made in water resulting in interactions with lower maximum strength of 2.7kcal/mol[81]. Thus, it would seem that it is the distinct chemical make-up and resultant geometry of water that conspire to endow it with such strong interactions.

2.2 Structure in condensed phases

The forces discussed above have a profound impact on the molecular structure of the condensed phases of water. In particular, the subtle interplay between strong intermolecular interactions and geometry results in the structure and properties of water being very different from other molecules that interact with isotropic dispersion forces.

In ice, the molecular structure of water is a nearly perfect tetrahedral network that is coherently ordered over macroscopic distances. This structure is known experimentally from

X-ray crystallography studies dating back to the 1930's[49]. At low pressures, individual molecules hydrogen-bond to four other waters producing an open structure. A typical configuration of low pressure, ordinary, ice Ih is shown in Fig. 2.3a. Hydrogen bonds based on a geometric criteria consistent with the optimal geometry discussed previously are drawn with dashed lines. One locally tetrahedral molecule with its four closest neighbors is highlighted in blue. At ambient temperatures, the positions of the oxygens are ordered but their orientations and the positions of the hydrogens are not. As first discussed by Pauling, every oxygen is bonded to the total of four hydrogens, two of these bonds are covalent and two of them are hydrogen bonds[175]. This proton disorder is found for many different ices, as elaborate below, and it responsible for the significant residual entropy of ice Ih observable near 0K[175].

At elevated pressures, the open structure of ordinary ice becomes unstable. For pressures, $p \gtrsim 2$ kbar denser crystalline phases of water are formed spontaneously[49]. One example of a denser phase of ice, ice VII, is shown in Fig. 2.3b. Notice in this figure that the hydrogen bonding network is conserved, even though the structure is no longer as open as in ice Ih. In fact, molecules are still linearly hydrogen bonded randomly to four other molecules as highlighted in blue, even though the molecules are closed-packed (the positions of the oxygens in ice VII form a body-centered cubic lattice typical of isotropically interacting molecules). This is because hydrogen bond energies are large even compared to pressures of $p > 1$ kbar. In terms of molecular and thermal units, one kbar is 4×10^{-2} kcal/mol Å^3, which for typical molecular volumes $v \sim 30$Å^3 is still an order of magnitude less than a hydrogen bond energy. Many ices accommodate this hydrogen bonding preference at high densities by organizing into interpenetrating networks of hydrogen bonds. In some cases, denser structures are formed by distorting hydrogen bonds but usually not more than a few degrees.[3]

At high temperatures when ice melts, only a small amount of energy is released, $\Delta H_{\rm fus} =$ 1.4 kcal/mol, which is about 10 percent of the heat of sublimation[49]. Given this, it is not surprising that even in the liquid much of the hydrogen bond network of ice is maintained. Figure 2.3b shows a typical configuration of liquid water, where hydrogen bonds are drawn with dashed lines and again a representative tetrahedral molecule, with its neighbors, is highlighted in blue. Whereas in ice the hydrogen bonding network is static over long timescales, in the liquid hydrogen bonds are constantly breaking and reforming. While on average a water molecule will have four hydrogen-bonding partners, this number fluctuates and at any point in time a given molecule might be bonded to anywhere between two to five other waters, depending on the exact definition.

Because of the disorder inherent to the liquid state, the exact structure of a liquid is not as well defined as the singular structure that characterizes a crystal. One experimentally accessible measure of structure in a liquid is a pair distribution function, $g(r)$, which records the probability that two atoms are a given distance, r, apart and can be determined from

[3]This is not true for very high pressures. Hydrogens in ice X, which is stable for $p > 600$ kbar, are located in symmetric, covalently bonded positions around oxygen atoms[179].

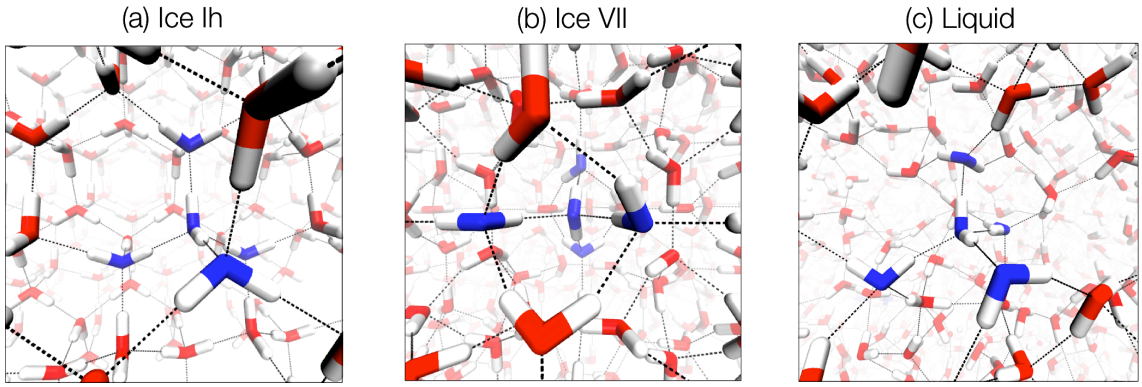

Figure 2.3: Typical configurations of liquid and solid water taken from molecular simulations. Hydrogen bonds are drawn in black and a representative tetrahedrally coordinated molecule and its neighbors are highlighted in blue.

scattering experiments[28]. More precisely,

$$\rho g(r) = V \left\langle \sum_{i>1} \delta(\mathbf{r}_1)\delta(\mathbf{r}_i - \mathbf{r}) \right\rangle \tag{2.1}$$

where ρ is the molar density of water, V is the volume of the system, $\mathbf{r}_i$ is the position of the ith molecule, $\langle \dots \rangle$ denotes a thermal average, and δ is Dirac's delta function, which has unit volume and is nonzero only where its argument is zero. In a liquid, which is isotropic on average, the pair distribution function depends only on the magnitude of $\mathbf{r}$, $r = |\mathbf{r}|$. While the sum in Eq. 2.1 is, in principle, over all atoms in the system including both hydrogens and oxygens, depending on the type of scattering experiment the relative contributions of both atom types need not be the same. In fact, X-ray scattering experiments report the oxygen-oxygen pair distribution function between to a remarkable degree. This is because X-rays scatter off of electrons and the majority of the electrons in water are spherically symmetric and localized on the oxygen[26]. Neutron scattering experiments can be used to obtain information on the relative positions of the hydrogen atoms, though these experiments typically require isotope substitutions and significant modeling to accurately deduce the structure.

Figure 2.4 shows pair distribution functions for the oxygen atoms in liquid water at room temperature, 298 K, and elevated temperature, 330K, taken from an X-ray scattering experiment[168]. The first peak in the $g(r)$ corresponds to the effective van der Waals diameter of nearly 3 Å. The second peak in the ambient temperature curve corresponds to water molecules that share a common hydrogen-bonding partner with local tetrahedral order, as is indicated by the schematic in the right panel. By integrating the pair distribution function up to the first minimum over the appropriate radial volume element, the average number of nearest neighbors can be determined. In water at ambient conditions this is very

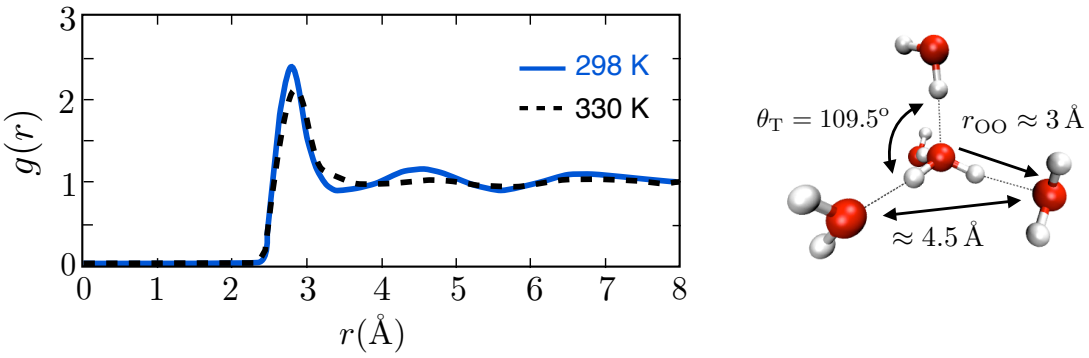

Figure 2.4: Oxygen-oxygen radial distribution function for liquid water, obtained from the X-ray scattering data at two different temperatures. This plot is adapted from Ref. [168]. Data has been smoothed for clarity.

nearly 4. Thus, this distribution function is consistent with and supportive of a picture in which liquid water is organized with a preference for local tetrahedral ordering.

For liquids with isotropic dispersion forces, the attractive interactions are well described by a mean field that imposes a uniform adhesion[79]. While this adhesion in part determines the equilibrium number density of the liquid, to a remarkable degree it does not determine the liquid structure. As elaborated and quantified by Weeks, Chandler and Andersen, the structure of such a liquid is determined by the repulsive part of the potential and subsequently reflects entropic packing constraints[227]. This is why the structure of many liquids is relatively athermal. The structure of water is largely due to direction energetic constraints, and small changes in temperature can result in large structural changes. This is evident in Fig. 2.4 where the tetrahedral structure prevalent at room temperature is diminished when the temperature is elevated to 330 K and as a consequence, the $g(r)$ is relatively featureless beyond the first peak.

This microscopic picture of liquid water is well captured by simple potential energy functions amenable to molecular simulation[209]. As will be discussed in detail later, molecular simulation is critical in understanding experimental probes of water structure and dynamics. Briefly, interactions between water molecules are typically modeled by assigning an isotropic pair potential to the center of mass that is repulsive at short distances and attractive at long distances. These forces are standard and recover simple liquid behavior where interactions are isotropic and packing constraints largely determine structure. The preference for hydrogen bonding is incorporated through the addition of point charges or three body interactions that are constructed to bias towards local tetrahedral structures. These forces, which attempt to recover the local ordering associated with the formation of hydrogen bonds, are far from standard. As a result, many different water models exist with slight variations in the parameterizations for these forces. More will be said about individual water mod-

els later as it is necessary, but it suffices for now that these simple functions can be tuned to recover a remarkable degree of agreement with experimental measures of structure and thermodynamics of water. The later topic is the focus of the next section.

2.3 Thermodynamics of liquid and solid water

As with all other substances, the phase diagram of water and its thermophysical properties are dictated by the interplay of energy and entropy and how this balance is modulated with temperature and pressure. At low temperatures, energy dominates and water is a solid, at high temperatures entropy dominates and water is a gas and in between these two extremes, energy and entropy are subtly balanced and water is a liquid. This delicate balance in liquid water gives rise to physical properties that are strongly dependent on the conditions.

2.3.1 Equilibrium phase diagram

At low temperatures water freezes into an ordered solid phase. At different pressures, however, the characteristics of this solid phase are widely different. For example, water forms 15 different polymorphs, or unique crystalline phases, at various temperatures and pressures[132]. Some of these phases are summarized in the phase diagram in Fig. 2.5, where a limited range of conditions is presented. The structures of different ice phases have been determined from X-ray diffraction studies and differ notably in point group symmetry, density and dielectric constant[49]. In all phases for $p < 10^3$ kbar, neutron scattering and vibrational spectroscopy indicate that water molecules are intact and have a geometry not very different than that of an isolated molecule.[4] In each ice, molecules are hydrogen bonded to four neighbors and are locally tetrahedral. At elevated pressures, the water adopts denser crystal structures that contain either slightly bent hydrogen bonds (ice II, III, V and VI) or interpenetrating networks of linear hydrogen bonds (ice VII and VIII). At very low temperatures, some ices undergo a proton ordering transition. In particular, ices Ih, V, and XII have proton ordered analogues, ices XI, XIII, and XIV, respectively. The phase boundaries between different ices can be rationalized from the Clausius-Clapeyron relation[28]

$$\left(\frac{dp}{dT}\right)_{\alpha,\beta} = \frac{\Delta s}{\Delta v} \tag{2.2}$$

which relates the slope of the boundary, $(dp/dT)_{\alpha,\beta}$, between phases α and β to the change in molar volume, $\Delta v = v_\alpha - v_\beta$, and the change in molar entropy, $\Delta s = s_\alpha - s_\beta$, on transitioning. While the volume change between different ices can be large, the entropy changes are often very small resulting in horizontal phase boundaries. Figure 2.5 depicts boundaries between ices II and VIII that are noticeably not horizontal, indicating a non-negligible entropy change. This entropy change can be accounted for mostly by the proton ordering of these ices.

[4] There is recent speculation that at very high pressures, water ionizes and forms a metal[156]

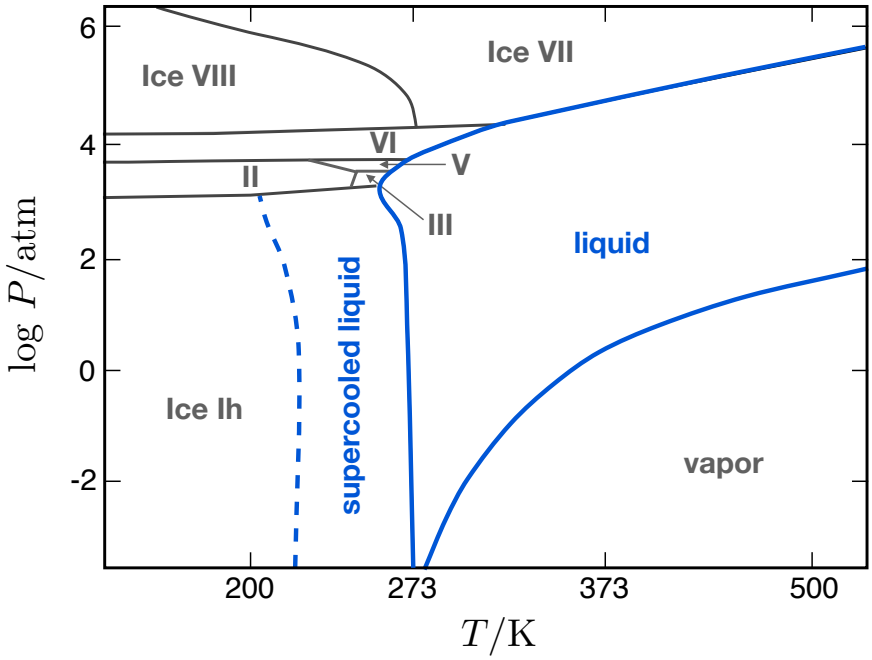

Figure 2.5: A portion of the phase diagram of water, adapted from Ref. [132].

As can be seen in Fig. 2.5, liquid water shares a phase boundary with 5 different ices[225]. At low pressures, $p \lesssim 2$ kbar, this boundary is between water and ordinary hexagonal ice, ice Ih. As before, the negative slope in the T, p plane can be easily rationalized form the Clausius-Clapeyron relation. While freezing is always accompanied by a loss of entropy, $\Delta s < 0$, only at low pressures is it also accompanied by an increase in volume, $\Delta v > 0$, resulting in the negative slope. At high pressures, $p \gtrsim 2$ kbar, water freezes into more compact structures, an example of which was shown in Fig. 2.3b. The pressure at which higher density ices become stable is indicative of a change in the balance between the isotropic forces of repulsion and the directional forces of hydrogen bonds. The latter result in open structures that are disfavored entropically but are manifestly dominant at low pressures whereas the former are favored entropically and due to their smaller molar volumes, dominant at elevated pressures. As will be shown shortly, the pressure range where this balance begins to shift, corresponds to where the properties of liquid water become less strongly temperature dependent.

Bounding the other side of the liquid state is the line of liquid-vapor transitions. Like melting, boiling always corresponds to a gain in entropy. Unlike melting, when a liquid changes into a vapor there is no spontaneous ordering that occurs and thus no symmetry change in the underlying molecular configurations. This fundamental difference results in the boundary between the liquid and the vapor ending in a critical point, which for water is at 647 K and 0.22 kbar[132]. At ambient conditions, water is far away from this critical point and the liquid is homogeneous, with only short ranged correlations. However, the ambient

liquid is close to the triple point, $T = 273$ K and $p = 6 \times 10^{-3}$ bar, between liquid, solid and vapor coexistence[132]. This proximity to the triple point is not unique to water, as most liquids at ambient conditions are close to their triple points by virtue of the smallness of ambient pressure compared to thermal energies. However, as will be discussed at length, the implications for water being close to coexistence with both its vapor and its crystal, are that small changes to the boundary conditions to can result in large changes in the properties of water. Different interfaces can thus induce large correlations not present in the uniform liquid.

At present, a number of hypotheses relating to other phases of water have not gained wide acceptance[43]. Most of these relate to alternative amorphous materials, distinct from the equilibrium liquid. An important class of such materials are called amorphous ices. Amorphous ices are disordered, kinetically arrested structures created through irreversible experimental protocols[6]. These different disordered structures have been generally partitioned into at least two general categories known as either low-density amorphous ice (LDA) or high-density amorphous ice (HDA) due to the change in density relative to liquid water on their preparation. While the amorphous ices exhibit a wide and interesting array of structural diversity, they are glasses whose properties depend delicately on the particular protocol by which they are prepared. As such, amorphous ices are not equilibrium structures and it is generally accepted that they do not warrant placement on a phase diagram for water. Some researchers postulate that amorphous ices are nonequilibrium manifestations of distinct liquid phases that reside in an area of the phase diagram that has not yet been probed directly by experiments[185]. This specific correspondence and its consequences for the interpretation of the behavior of water will be reviewed at the end of this chapter.

2.3.2 Metastability and supercooled liquids

Like most materials, liquid water can be cooled below its freezing point and its properties observed for some time before it undergoes an irreversible, crystallization transition. Water in such a state is said to be in metastable equilibrium and is referred to as supercooled water. Figure 2.5 illustrates where supercooled water can be observed with a dashed blue line. This boundary is not thermodynamically meaningful as its location implies an observation timescale. In what follows, the concept of metastability is made more concrete.

Hamiltonian dynamics and chaos ensure that, if left unperturbed for a sufficient amount of time, complex systems will evolve to a time-independent equilibrium state[242]. Thermodynamics identifies this equilibrium with a minimum of a free energy, whose details depend on the constraints on the system. These constraints enumerate the globally conserved quantities like energy, mass, ect. The resultant definition of the free energy, F, under, for example, constant temperature, T, pressure, p, and number of molecules, N, is in the differential

$$dF = -SdT + Vdp + \mu dN \tag{2.3}$$

where S, V and μ are the entropy, volume and chemical potential, respectively. The condition for stability of an equilibrium state is that small fluctuations away from equilibrium are zero

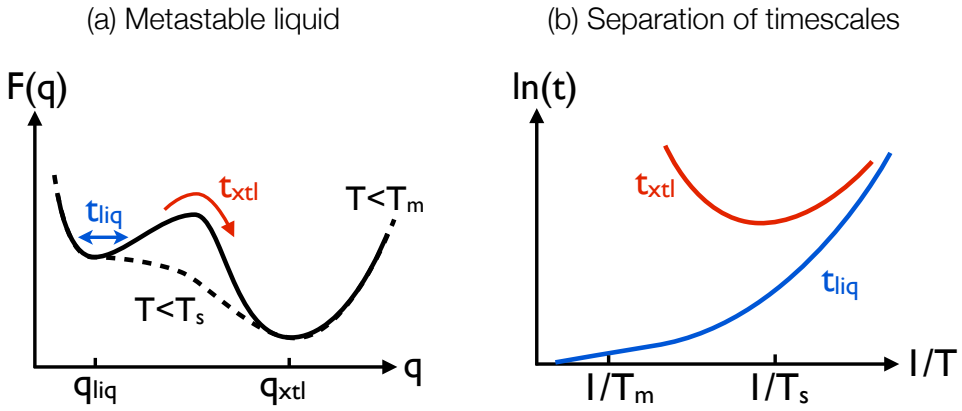

Figure 2.6: Illustration of thermodynamic metastability and its resultant separation of timescales for a supercooled liquid. Within the metastable liquid, t_{liq} defines the mean structural reorganization time, or the timescale to decorrelate local density fluctuations. The average timescale for fluctuations that result in significant crystallization, t_{xtl}, is defined by the build up of long range order. While t_{liq} is a monotonically increasing function of $1/T$, t_{xtl} is non-monotonic as it involves both nucleation and growth of the crystal. Here T_{m} defined the melting temperature, and T_{s} the limit of liquid stability.

on average, $(\delta F) = 0$, and the mean-squared fluctuations act to return small perturbations back to equilibrium, $(\delta F^2) > 0$. Graphically, this implies that a local equilibrium sits at the bottom of a basin in the free energy landscape, around which small fluctuations can occur. These small fluctuations experience restoring forces that bring the system back towards the local minima of free energy.

As shown in Fig. 2.6a for the free energy projected along an arbitrary extensive variable, q, a local minimum similarly supports small fluctuations around a mean value of q. This locally stable minimum, that is not the global minimum, is known as a thermodynamically metastable state. Supercooled liquids are such states, as they are observable and have well-defined properties even below their melting temperature, $T < T_{\text{m}}$. For very low temperatures, however, the free energy response as a function of the control parameters can change, and in particular for temperatures far below the melting temperatures, $T \approx T_{\text{s}} \ll T_{\text{m}}$ the free energy will no long support two regions of local positive curvature.

A consequence of this behavior of the free energy is a separation of timescales for relaxing within a metastable basin, t_{liq}, and transitioning from that basin into the global minimum, t_{xtl}. The typical temperature dependence of these timescales for a supercooled liquid are shown in Fig. 2.6b[42]. In this case, t_{liq} corresponds to the timescale to decorrelate microscopic configurations. At high temperatures, this time corresponds to the fundamental diffusive motion of molecules, which occurs on picoseconds, 10^{-12} s. Below some temperature, typically within the supercooled regime, t_{liq} increases rapidly with decreasing temperature.

For most liquids including water, this increase occurs with a scaling greater than would be expected for crossing a single, temperature independent barrier[7]. Theories for quantitative predictions of this behavior will be discussed in Chap. 4, but for now the qualitative description depicted in panel (b) suffices. The timescale, $t_{\rm xtl}$ corresponds to the timescale to nucleate and grow the stable phase, which in this case is the crystal. This time is characteristically nonmonotonic in temperature, since it relates to both the induction time to form a stable cluster of crystalline material, which decreases with supercooling, and growth time to add material to that cluster, which grows as $t_{\rm liq}$ and increases with supercooling[42].

The shape of these curves for a particular molecule dictate the observation times and preparation protocols available for a given metastable state.[5] In particular, cooling protocols to access supercooled liquid state must be slower than the internal relaxation time of the liquid in order for the properties to maintain an equilibrium. If cooling rates are too fast, $\mathrm{d}\ln T/\mathrm{d}t > 1/t_{\rm liq}$, the system can be driven out of equilibrium. If cooling rates are too slow, $\mathrm{d}\ln T/\mathrm{d}t < 1/t_{\rm xtl}$, then on average the system will have crystallized before a measurement has been made. In between these extremes a supercooled liquid can be prepared and observed. Typically, a supercooled liquid just below its melting temperature is easily observed on laboratory timescales and only at large supercooling does this separation of timescales break down. Below these temperatures, $T < T_{\rm s}$, the only way to access amorphous configurations is to cool the liquid fast enough to form an amorphous solid. The specific region where this separation of timescales holds for water is illustrated in Fig. 2.5. In the region denoted supercooled water, the cold liquid water is easily equilibrated and its properties measured over laboratory timescales, i.e. seconds or minutes. Below the dashed line, nucleation of ice occurs on millisecond timescales, fast for most experiments. Liquid water prepared below that line, which is identified as the crossover temperature, $T_{\rm s}$, is thermodynamically unstable. While amorphous ice can still be prepared and exist for minutes or hours at temperatures, $T \ll T_{\rm s}$, these materials do not equilibrate and are therefore no longer representative of liquid water.

2.3.3 Thermodynamics of supercooled water

Water exhibits anomalous thermodynamic properties at low temperatures, properties that are non-singular but nonetheless unusual[43]. The most notable of these properties are the nonmonotonic change in density and the increase in the compressibility and constant pressure heat capacity upon cooling. While the density maximum has been known for a very long time,[6] the increase in heat capacity and compressibility were only discovered in 1973 by Rasmussen et. al. [188] and in 1976 by Speedy and Angell[206], respectively, opening a door to a significant discussion regarding their origins.

[5]This discussion of metastability assumes that the liquid is completely free of impurities and neglects surface effects. Both of these features can act to decrease barriers to crystallization through heterogeneous nucleation processes and result in dramatically decreasing $t_{\rm xtl}$.

[6]The first reported measurements of the density of supercooled water date back to 1837 when Despretz performed accurate density studies to -9^oC[44].

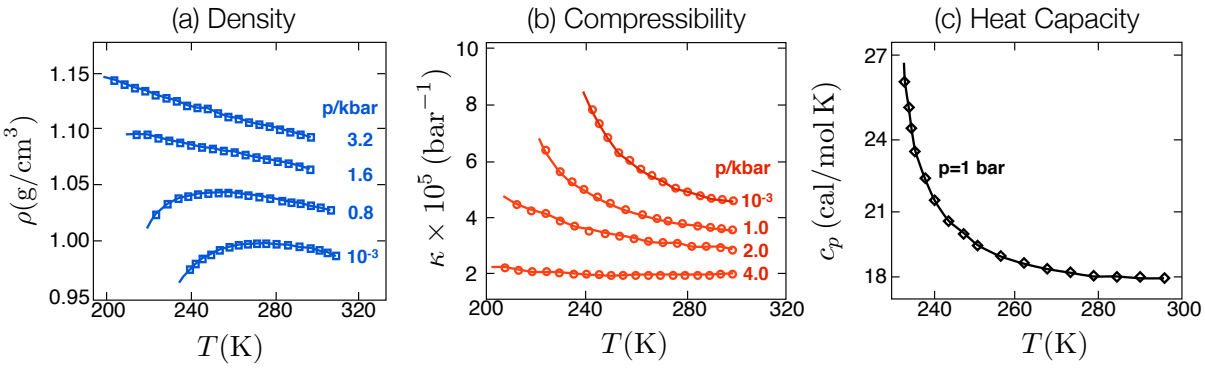

Figure 2.7: The anomalous thermodynamics of stable and supercooled water[43].

Figure 2.7 shows the thermophysical properties of stable and supercooled water taken from a recent review [43]. In panel a, the density as a function of temperature, for pressures up to 3 kbar, is plotted. At ambient pressure, liquid water contracts on cooling until 277 K, below which it begins to expand. This density maximum reflects the competition between isotropic dispersion and orientational hydrogen bonding forces, which are balanced at $T = 277$ K and $p = 1$ bar. At increased pressures, $p < 2$ kbar, dispersion interactions are favored and the density maximum moves to lower temperatures. For higher pressures, $p > 2$ kbar, the density maximum is no longer evident and rather the density changes monotonically.

Panel b shows the compressibility, κ, as a function of T for different p. The isothermal compressibility measures the response of the density to applied pressure at constant temperature and through the fluctuation-dissipation relation is a measure of volume fluctuations[28]. Specifically,

$$\kappa = -\left(\frac{\partial \ln V}{\partial p}\right)_{\mathrm{T}} = \frac{1}{k_{\mathrm{B}} T \langle V \rangle} \langle (\delta V)^2 \rangle \tag{2.4}$$

where k_{B} is Boltzmann's constant and $\delta V = V - \langle V \rangle$, is the instantaneous deviation of the volume from its average. At ambient pressure, the compressibility has a minimum at 319 K and increases by a factor of 1.5 upon supercooling. From equation Eq. 2.4 this implies that fluctuations in volume are becoming larger. Qualitatively, this can be rationalized by appealing to an increase in the local ordering of the liquid as it becomes more difficult for thermal energies to distort the hydrogen bonding network. This local ordering is accompanied by a decrease in local density. Like the density anomaly, at elevated pressures the peculiar behavior of the compressibility shifts to lower temperatures and ceases for pressures larger than about 2 kbar.

Panel c shows the isobaric heat capacity, c_{p}. The heat capacity measures the response of the enthalpy to changes in temperature at constant pressure and through the fluctuation-

dissipation relation is a measure of enthalpy fluctuations. Specifically,

$$c_{\mathrm{p}} = \left(\frac{\partial H}{\partial T}\right)_{\mathrm{p}} = \frac{1}{N k_{\mathrm{B}} T^2} \langle (\delta H)^2 \rangle \tag{2.5}$$

where H is the enthalpy, and $\delta H = H - \langle H \rangle$. Data for the heat capacity is only available for $p = 1$ bar. As with the compressibility, there is a notable rise in the heat capacity starting at around 308 K and peaking with a value about 1.5 times its ambient temperature value. While this temperature dependence is interesting, it is worth noting that the absolute value of the heat capacity of water itself is noteworthy, even at high temperatures. Most nonpolar liquids have heat capacities that range from 8 to 12, short of the 18 cal/mol K of water[132]. The excess energy fluctuations for water come from the distortion of hydrogen bonds in the liquid, which as described, can store a significant amount of energy.

The low-temperature end of each of these graphs locate the point where the liquid becomes unstable, and crystallization occurs on the timescale of the observation time required for the experiment. The temperature where this occurs in experiment is known as the homogeneous nucleation temperature as it indicates where the timescale for homogeneous nucleation is fast enough to compete with heterogeneous nucleation[43]. This temperature was alluded to in the previous section as T_{s} and approximates a crossover region in which the separation of timescales required for metastable equilibrium ceases to exist. The crossover line, T_{s}, is marked in Fig. 2.5 with the dashed blue line. It begins at about 220 K at ambient pressure and follows the slope of the melting line at elevated pressures, ending at about 200 at $p = 3$ kbar.

Down to T_{s}, the growths of κ and c_p are notable but modest in size and far from the sort of divergent behavior one would ordinarily associate with a critical point or phase boundary. Nevertheless, researchers beginning with the very first reports of these data have attempted to associate singularities to these functions[206]. The locations for such singularities are determined by fitting the data to power law of the form, $A(T) = A_{\mathrm{o}}(T - T_{\mathrm{x}})^{\alpha}$, where T_{x} is the location of the singularity. A consensus for this singular behavior has eluded the scientific community, however the next section reviews some of the prevailing interpretations.

Ever since the pioneering work of Speedy and Angell[206], a number of theoretical interpretations have been given to explain the anomalous thermodynamic properties of supercooled water. While numerous, these interpretations fall into two basic classes: those that presume an otherwise undetected singularity, such as a second critical point deep within the supercooled region of water's phase diagram and conclude that the increases in response functions diverge at lower temperatures and those that do not posit a singularity; and attempt to explain the behavior from other perspectives, but that conclude that the response functions do not diverge at any temperature[42].

The most widely accepted scenario for supercooled water that invokes a singular response was originally formulated by H. Eugene Stanley and collaborators in 1992[185]. The liquid-liquid critical point interpretation, as it is known, attempts to unify the anomalies of supercooled water with observations of nonequilibrium behavior in glassy water. According to this view, water at ambient conditions is a supercritical mixture of two liquid phases, one with

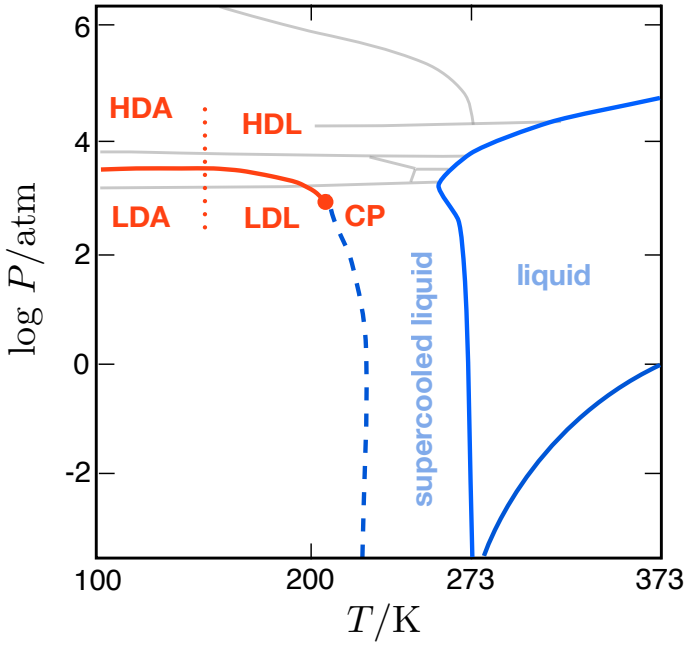

Figure 2.8: Phase diagram assuming the existence of a liquid-liquid critical point in supercooled water[185]. Though a prevailing theory in the 2000's, work in this dissertation summarizes a growing body of evidence contradicting this interpretation.

a lower density than the other. At elevated pressures this mixture encounters a metastable critical point where macroscopic fluctuations between mixed and demixed regions of these two forms of water, result in divergent energy and volume fluctuations. The increases in heat capacity and compressibility are rationalized as the repercussions of approaching, though not actually encountering, this critical point. At higher pressures and low enough temperatures this mixture is suggested to undergo a first-order liquid-liquid phase separation between a low-density liquid (LDL) and a high-density liquid (HDL). These phases are conjectured as being the equilibrium, ergodic analogues of low density and high density amorphous ices, LDA and HDA respectively. Away from the first order line and critical point, within the single phase regions, the equation of water is predicted to be like that of a normal fluid (i.e with monotonically decreasing density with increasing temperature, and no anomolously increasing heat capacity).

2.4 Interpretations for the anomalies of water

Equations of state based on theories for two component mixtures have been shown to be thermodynamically consistent with the available experimental data. However, there are at least two reasons to be cautious regarding such results. First, these theories all place

the second critical point near but below the experimentally accessible region of the phase diagram. Thus the location of the critical point is always purported by extrapolation and, consequently, predictions for the location of the second critical point vary widely. One such prediction for the critical point and accompanying first-order transition line is shown in Fig. 2.8, and locates the critical point at 227 K and 0.13 kbar[87]. Second, such empirical constructions require numerous adjustable parameters. The study locating the critical point in Fig. 2.8 requires 18 parameters to fit the equation of state. To refine the accuracy of such ideas requires either a derivation from microscopic principles or obtaining experimental data deeper in the supercooled regime. With rare exception, microscopic probes of two state behavior that relate experimental observables with molecular simulation have been inconsistent with this behavior, making a microscopic derivation untenable, (See Ref. [59] and Ref. [35] for examples). Developing experiments that probe further into the supercooled regime are an active area of research. Such efforts face an exponentially increasing nucleation rate upon linear changes in temperature, rendering these experiments difficult as well.

Efforts to suppress the freezing transition through artificial means have increasingly become an experimental way to address this problem[16]. For instance, by confining water to substrates with small characteristic dimensions, the properties of water far below T_s can be probed. For pore sizes on the order of a nanometer, calorimetry experiments suggest that water can remain amorphous to arbitrarily low temperature. Two interesting observations made in such strong confinement are the existence of a density minimum at $T = 210$ K[141] and a dynamic crossover in the single-particle dynamics at $T = 225$ K[57]. These experiments are difficult to interpret because the water under such strong confinement is largely perturbed, so theory is needed in order to relate the observations to the properties of bulk water. Most of these observations have been largely motivated by the liquid–liquid critical point hypothesis, subsequently most interpretations have been through that lens. Chapter 4 will review some of these interpretations in detail, as well as offer an alternative, quantitative theory relating the observations to the freezing transition rather than a second critical point.

More than anything else, the liquid-liquid phase transition hypothesis has been motivated by molecular simulations. In fact, the original hypothesis by Stanley et al. stemmed from a series of calculations of a point charge model of water that exhibits qualitatively similar anomalous thermodynamic behavior to that of supercooled water[185]. In their molecular dynamics simulations, Stanley et al observed that the average pressure as a function of density for low temperatures exhibited an inflection point at high density. They asserted that the shape and temperature dependence of the inflection region were similar to what would be expected if a critical point were approached, as an inflection is a sign of a thermodynamic instability. While no standard methods for determining phase behavior were employed[65, 127] this work and the hypothesis put forward in it nevertheless spurred a large number of publications that used similar equation of state extrapolations to attempt to locate a second critical point (Refs. [2, 23, 37, 80, 117, 164, 184, 235, 238] are representative, but by no means comprehensive). As has been the case for experimental data, the extrapolative procedures used have made it difficult to confirm the existence, or locate the precise position, of a second critical point, and up to 2009, 17 years after its proposal, no straightforward

study using robust free energy calculations or finite size scaling analysis had yet been done to probe the underlying assumption of a second critical point for model systems. The next chapter in this dissertation addresses this hole in the literature in great detail and concludes that when robust techniques are applied to model systems, the results are incompatible with a second critical point.

Theories that attempt to explain the thermodynamics of liquid water without invoking a singular response, typically referred to as singularity-free scenarios, have had some success in explaining particular observations of supercooled and solid water. For instance, straightforward thermodynamic consistency arguments can be made to rationalize the increase in the compressibility provided the existence of a line of density maxima and its negative slope in the T, p plane[43]. However, clear connections to microscopic behavior and quantifiable explanations are largely lacking in these and similar ideas. Further a single coherent set of assumptions does not exist to unify the broad scope of observations that the liquid-liquid critical point hypothesis attempts to organize. What will follow from this chapter is the beginnings of such an alternative. In particular, Chapters 3 and 4 examine experimental observations thought to be consistent with the idea of two liquids. The major conclusion of these chapters is that understanding the fluctuations that result in long-ranged tetrahedral order is essential to explain the behavior of supercooled and solid water. At equilibrium, these fluctuations can be enhanced through low temperatures which drive water to freeze or they can be modulated by surfaces and leave water amorphous. However, when water is perturbed in a time dependent manner, the dynamics of order fluctuations that evolve water to its crystal can become frustrated. This frustration can result not only in interesting changes to well understood phenomena like nucleation and coarsening but also to novel nonequilibrium phenomena such as polyamorphism.

Chapter 3

Low temperature phase diagram

Whenever a theory appears to you as the only possible one,
take this as a sign that you have neither understood the theory
nor the problem which it was intended to solve.
-Karl Popper [187]

In this chapter, the tools for studying phase behavior on a computer are reviewed. These techniques are then employed to compute the low temperature and low pressure portion of the phase diagram for models of water. This chapter borrows largely from previous work, *J. Chem. Phys.* 135, 134503 (2011), and *J. Chem. Phys.*, in press (2013). Two principle results are presented. First, models of water that have locally tetrahedral liquids, generically support freezing transitions like that of water and ice, but not a low temperature critical point as has been conjectured. Second, at low enough temperatures, these liquids are unstable and spontaneously crystallize with coarsening dynamics that are well described by a theory based on a separation of timescales for density and long ranged order fluctuations. This liquid instability and the dynamics that arise from it are used to explain previous observations of short-lived, low density liquid states and transient polyamorphism found in computer simulations.

3.1 Introduction

This chapter reports the results of numerical studies aimed at elucidating the phase transition behavior of models of water at low temperatures. Particular attention is paid to evaluating the existence of the purported liquid-liquid phase transition and critical point in supercooled liquid water[158, 185]. The results indicate that this imagined polyamorphism does not exist in atomistic models of water. While not contradicting the existence of irreversible polyamorphism of the sort observed in non-equilibrium disordered solids of water, [7, 77, 99, 147, 183] and not excluding the possibilities of liquid-liquid transitions in liquid mixtures [197] or some theoretical models,[96, 186, 212, 231] the results do suggest that a reversible transition and its putative second critical point are untenable for one-component

liquids, like water, that exhibit local tetrahedral order and freeze into crystals with similar but extended order. What others have viewed as a second liquid phase, these results indicate is actually the unstable liquid in its nascent stages of forming ice.

The terminology "transition" is used here to refer to distinct phases, where coexistence implies the formation of interfaces that would spatially separate the coexisting phases or to response functions that diverge in the thermodynamic limit[28]. The structural changes for a transition between two liquids or between a liquid and a crystal are distinct from continuous pressure-induced changes in normal liquid water[204]. These changes associated with a phase transition are global and therefore are also distinct from bi-continuous behaviors that do not persist beyond small length scales[230].

Reversibility is particularly important to the issues addressed here. Distinct reversible phases can be interconverted, with properties that are independent of the paths by which they are prepared. Reversible liquid phases are thus not the same as amorphous solids or glasses. The former are reversible and ergodic, so their measured stationary behaviors are independent of history. The latter, like high-density or low-density amorphous ices, are not ergodic, so their behaviors depend much on history (i.e., preparation protocols). Observed transitions between HDA and LDA phases,[157] therefore, are necessarily different than reversible liquid-liquid transitions. Melting amorphous ice to produce a non-equilibrium liquid that then crystalizes is also different[118].

Figure 3.1 shows the relevant part of water's phase diagram and corresponding free energy surfaces. The liquid is the stable equilibrium phase for temperatures above the melting temperature, i.e., $T > T_{\rm m}$, and it is unstable for $T < T_{\rm s}$. In between, the liquid is metastable with respect to crystal ice. Throughout much of that intermediate region, structural reorganization of water is slow, and it becomes slower in a super-Arrhenius fashion as temperature is lowered[6]. This sluggishness can present problems for straightforward molecular simulation, as noted below, but it is not so sluggish to prevent certain crystallization of water when the liquid is cooled close to or below $T_{\rm s}$. Coarsening of water in that regime occurs on the time scale of microseconds – fast for experiment, but slow for simulation[121]. All speculations on the existence of a liquid-liquid phase transition in water locate that transition near or below $T_{\rm s}$, the so-called "no-man's land" for liquid water. As such, it is difficult for experiments to prove or disprove the liquid-liquid hypothesis. It is left to simulation, which can reversibly control crystallization, to see if such an idea could be correct within the purview of statistical mechanics for plausible models of water or water-like systems.

Specifically, sufficiently realistic models can be studied computationally while controlling order parameters that distinguish liquid from crystal. It is in this way that we examine the reversible behavior of models of water. Along with establishing coexistence between liquid and crystal, we are able to study the dynamics of the transition between these phases. We also locate and explore the free energy surface for the region of the pressure-temperature phase diagram known as "no man's land"[158]. This is the region where amorphous behavior would be unstable in the absence of control. Our results indicate that some observations attributed by others as manifestations of a liquid-liquid transition are in fact observations of the temperature-pressure boundary separating the region of amorphous instability from

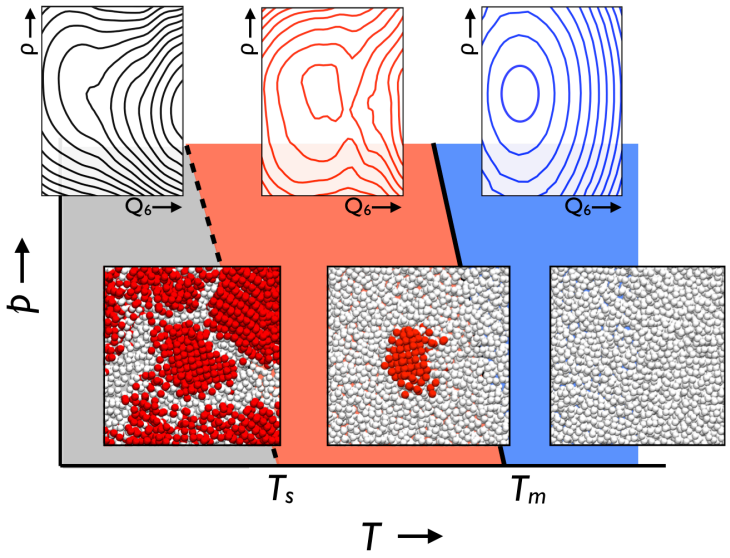

Figure 3.1: Phase diagram, free energy surfaces and typical configurations of cold water. Typical of all systems considered in this thesis, the specific pictures render results from molecular simulations of one particular model. Quantitative scales of temperature, pressure and free energy depend upon simulation model, and these scales are omitted here because this figure serves a qualitative purpose only. For experimental water, the phase diagram covers pressures p ranging from 1 bar to 3 kbar, and temperatures T ranging from 150 K to 300 K. T_{m} and T_{s} stand for temperatures at the melting and liquid-stability lines, respectively. Blue region in the p-T plane is where liquid is stable, red region is where liquid is metastable with respect to ice I, and grey region is where liquid is unstable (i.e., it is the liquid's "no-man's land"). Corresponding free energy surfaces are shown above as functions of density ρ and crystal-order variable Q_6. Corresponding molecular configurations shown below are cuts through a simulation box at the ends of trajectories that are initiated in a liquid configuration and that run for times shorter than required to crystalize the entire sample. Molecules located in crystal-like regions are colored red. Figure taken from Ref. [136].

that of a single phase of amorphous metastability.

Calculations of free energy functions of relevant order parameters are required when using simulation to establish phase behavior [65]. As noted, such calculations can be difficult, especially for supercooled water because fluctuations in this regime are collective and slow. To address this difficulty and sort out the phase behavior of supercooled water, we have found it convenient to consider two order parameters. One is molecular density, ρ, that distinguishes different amorphous phases. The other must distinguish an amorphous phase from a crystalline phase and reflect the broken symmetry accompanying a freezing transition. One particularly useful order parameter, the Steinhardt-Nelson-Ronchetti Q_6 parameter, is used largely in this chapter and equations for its computation are in Section 3.2.2. The two variables, ρ and Q_6, fluctuate on significantly different time scales. For example, the liquid structural relaxation time (i.e., the equilibration time for ρ) around $T \approx T_s$ is of order 10^{-8} s or shorter, whereas the relevant equilibration time for Q_6, or similar long-range order parameter, in this regime is the time to form a crystal, 10^{-6} s or longer. This wide separation of time scales is typical of systems undergoing crystallization transitions[42]. In the case of water, we will see that it is a principal source of confusion in simulation studies that claim evidence for a liquid-liquid phase transition.

Section 3.4 of the current chapter provides a quantitative theoretical analysis of this behavior. It shows specifically how the polyamorphism is an irreversible effect reflecting the time-scale separation between fluctuations in ρ and fluctuations in Q_6. During the time of coarsening, the faster order parameter, ρ, fluctuates between typical crystal and liquid values. References [109, 144] report this type of behavior, which they call "phase flipping." On the time scale of the flipping, the drift in mean value of Q_6 can be almost imperceptible, but it does drift. The authors of Refs. [109, 144] describe the flipping as evidence of a second metastable liquid. The analysis of Section 3.4 shows that this flipping is not a consequence of such metastability, but rather the coarsening of the crystal from the unstable or nearly unstable liquid, occurring steadily and irreversibly on a time scale long compared to those considered in Refs. [109, 144].

Before that, we first detail how pertinent free energies can be computed and phase behavior evaluated for atomistic models. The techniques employed are standard methods of importance sampling with a statistically efficient sampling algorithm known as hybrid Monte Carlo. These methods rely on the use of reasonable order parameters to enhance the sampling of rare fluctuations that take configurations between phases. A discussion and definition of bond order parameters that quantify orientational symmetry-breaking accompanies this method section. To illustrate this procedure and the finite-size scaling analysis that accompanies its careful extrapolation into the thermodynamic limit, we study the freezing transition of a particular model of water.

3.2 General methodology

We proceed with a methodology based on Monte Carlo simulations[65]. Briefly, a Monte Carlo procedure is a way to estimate expectation values of high dimensional probability distributions where straightforward computation is intractable. These methods are based on constructing a Markov chain that has a desired distribution as its steady-state. The distribution of states in the chain after a large enough number of steps is then used as an expectation of the equilibrium distribution.

One straightforward way to construct a Markov chain that will converge to the correct equilibrium distribution is to impose a balance condition on the transition probabilities. Specifically, if P_i is the equilibrium probability of observing a microstate i, and ω_{ij} is the probability for transitioning between states i and j, then the equality,

$$P_i \omega_{ij} = P_j \omega_{ji} \tag{3.1}$$

imposes the physical constraint of detailed balance [65]. By rearranging Eq. 3.1 it follows that the ratio of transition probabilities, ω_{ji}/ω_{ij}, must be equal to the ratio P_j/P_i. As first proposed by Metropolis, Rosenbluth and Teller,[154] this constraint can be satisfied by factorizing ω_{ij} into a probability to attempt a transition, $\alpha(i \to j)$, and a probability to accept that attempt, $\mathrm{acc}(i \to j)$. Then, a new trial move for the Markov chain may be accepted with the probability,

$$\mathrm{acc}(i \to j) = \min\left(1, \frac{P_j\ \alpha(j \to i)}{P_i\ \alpha(i \to j)}\right). \tag{3.2}$$

In practice, pseudo random numbers are drawn to propagate a random walk consistent with the statistics of this rule.

If moves are attempted in a symmetric fashion, then the ratio of generation probabilities, $\alpha(j \to i)/\alpha(i \to j)$ is unity and the resultant acceptance probability reduces to a ratio of microstate probabilities or the ratio of Boltzmann factors. The details of the transitions that are attempted and the desired equilibrium distribution that they are accepted with depend on the system. Methods for applying this technique for calculating the phase behavior of supercooled water are elaborated below.

3.2.1 Hybrid Monte Carlo calculations.

We choose to use a Monte Carlo method with constant number of molecules, N, pressure, p, and temperature, T. This ensemble is appropriate for determining conditions of phase coexistence and is well suited for sampling dense liquid and crystalline states. This ensemble also accommodates large fluctuations in energy and density needed for nucleation and phase separation processes. Density, $\rho = N/V$, fluctuates with p and N fixed because volume, V, fluctuates. The probability for observing a given microstate in this ensemble is given by

$$P(\mathbf{r}^{3N}, V) = \frac{e^{-\beta U(\mathbf{r}^{3N}) - \beta p V}}{\Xi}, \tag{3.3}$$

where $U(\mathbf{r}^{3N})$ is the potential energy function and

$$\Xi = \int \mathrm{d}\mathbf{r}^{3N} \int \mathrm{d}V e^{-\beta U(\mathbf{r}^{3N}) - \beta p V} \tag{3.4}$$

is the isothermal-isobaric partition function. The integrals above span the space of all possible positions of the particles and all possible values of the volume. In practice, finite systems are used with periodic boundary conditions to approximate the inifinite system limit of this partition function. This probability depends both on the positions of all N molecules as well as the volume. Accurate estimates of this distribution are obtained only if both configuration space and volume are sampled.

The move set we employ to sample this distribution is chosen to mitigate long correlation times expected for supercooled liquids and coarsening crystals. Specifically, to allow for collective reorganizations, we use a hybrid Monte Carlo algorithm[45] that propagates an initial configuration with Boltzmann distributed velocities under symplectic, norm preserving, molecular dynamics.

Because hybrid Monte Carlo is not very widely used, we provide a short derivation for the move's acceptance criterion. For an initial condition $\mathbf{r}_{\mathrm{o}}^{3N}$, a trial configuration is generated by drawing a set of momenta from a Maxwell-Boltzmann distribution with temperature T,

$$P_{\mathrm{MB}}(\mathbf{p}_{\mathrm{o}}^{3N}) \propto \exp\left(-\sum_{i}^{N} \mathbf{p_i}^2/2mk_{\mathrm{B}}T\right) \tag{3.5}$$

and integrating the set of positions, $\mathbf{r}_{\mathrm{o}}^{3N}$ and momenta, $\mathbf{p}_{\mathrm{o}}^{3N}$, with a deterministic equation of motion and fixed volume. This integration can be written as the action of a propagator, $\mathcal{L}$, on the complete phase space point $\left(\mathbf{r}_{\mathrm{o}}^{3N}, \mathbf{p}_{\mathrm{o}}^{3N}\right)$. The form of the propagator depends on details of the integration such as the discrete time-step, δt, and the number of integrations steps, n. Nevertheless, its action is to specify a unique map from the initial phase space point to a new point, $\left(\mathbf{r}_{\mathrm{n}}^{3N}, \mathbf{p}_{\mathrm{n}}^{3N}\right)$,

$$\mathcal{L}^{n\delta t}\left(\mathbf{r}_{\mathrm{o}}^{3N}, \mathbf{p}_{\mathrm{o}}^{3N}\right) = \left(\mathbf{r}_{\mathrm{n}}^{3N}, \mathbf{p}_{\mathrm{n}}^{3N}\right) \ . \tag{3.6}$$

The uniqueness of this map means that the generation probability is just given by the probability to draw momenta that determine the beginning point in phase space,

$$\mathrm{gen}(\mathbf{r}_{\mathrm{o}}^{3N} \to \mathbf{r}_{\mathrm{n}}^{3N}) = P_{\mathrm{MB}}(\mathbf{p}_{\mathrm{o}}^{3N}) \tag{3.7}$$

and consequently from Eq.3.2,

$$\alpha(\mathbf{r}_{\mathrm{o}}^{3N} \to \mathbf{r}_{\mathrm{n}}^{3N}) = \min\left(1, \frac{P(\mathbf{r}_{\mathrm{n}}^{3N})\, P_{\mathrm{MB}}(\mathbf{p}_{\mathrm{n}}^{3N})}{P(\mathbf{r}_{\mathrm{o}}^{3N})\ P_{\mathrm{MB}}(\mathbf{p}_{\mathrm{o}}^{3N})}\right) \tag{3.8}$$

$$= \min\left(1, e^{-\beta\delta H}\right) \tag{3.9}$$

where $\delta\mathcal{H} = \mathcal{H}(\mathbf{r}_{\rm n}^{3N}, \mathbf{p}_{\rm n}^{3N}) - \mathcal{H}(\mathbf{r}_{\rm o}^{3N}, \mathbf{p}_{\rm o}^{3N})$ is the change in the total energy, which is in general nonzero due to the discretization of the equations of motion. If the propagator is time reversal symmetric,

$$\mathcal{L}^{n\delta t}\mathcal{L}^{-n\delta t} = \mathbf{1} \tag{3.10}$$

and preserves the volume of phase space,

$$\det \frac{\partial \mathcal{L}^{n\delta t}\left(\mathbf{r}_{\rm o}^{3N}, \mathbf{p}_{\rm o}^{3N}\right)}{\partial\left(\mathbf{r}_{\rm o}^{3N}, \mathbf{p}_{\rm o}^{3N}\right)} = 1 \tag{3.11}$$

then detailed balance follows as,

$$\begin{aligned}
P(\mathbf{r}_{\rm o}^{3N})\omega(\mathbf{r}_{\rm o}^{3N} \to \mathbf{r}_{\rm n}^{3N})\mathrm{d}\mathbf{r}_{\rm o}^{3N}\mathrm{d}\mathbf{p}_{\rm o}^{3N} &= P(\mathbf{r}_{\rm o}^{3N})P_{\rm MB}(\mathbf{p}_{\rm o}^{3N})\alpha(\mathbf{r}_{\rm o}^{3N} \to \mathcal{L}^{n\delta t}\mathbf{r}_{\rm o}^{3N})\mathrm{d}\mathbf{r}_{\rm o}^{3N}\mathrm{d}\mathbf{p}_{\rm o}^{3N} \\
&= P(\mathbf{r}_{\rm n}^{3N})P_{\rm MB}(\mathbf{p}_{\rm n}^{3N})\alpha(\mathcal{L}^{n\delta t}\mathbf{r}_{\rm o}^{3N} \to \mathbf{r}_{\rm o}^{3N})\mathrm{d}\mathbf{r}_{\rm o}^{3N}\mathrm{d}\mathbf{p}_{\rm o}^{3N} \\
&= P(\mathbf{r}_{\rm n}^{3N})P_{\rm MB}(\mathbf{p}_{\rm n}^{3N})\alpha(\mathbf{r}_{\rm n}^{3N} \to \mathcal{L}^{-n\delta t}\mathbf{r}_{\rm n}^{3N})\mathrm{d}\mathbf{r}_{\rm o}^{3N}\mathrm{d}\mathbf{p}_{\rm o}^{3N} \\
&= P(\mathbf{r}_{\rm n}^{3N})P_{\rm MB}(\mathbf{p}_{\rm n}^{3N})\alpha(\mathbf{r}_{\rm n}^{3N} \to \mathcal{L}^{-n\delta t}\mathbf{r}_{\rm n}^{3N})\mathrm{d}\mathbf{r}_{\rm n}^{3N}\mathrm{d}\mathbf{p}_{\rm n}^{3N} \\
&= P(\mathbf{r}_{\rm n}^{3N})\omega(\mathbf{r}_{\rm n}^{3N} \to \mathbf{r}_{\rm o}^{3N})\mathrm{d}\mathbf{r}_{\rm n}^{3N}\mathrm{d}\mathbf{p}_{\rm n}^{3N}
\end{aligned}$$

Standard molecular dynamics integrators conserve energy to second order in the timestep, δt^2. This conservation implies a scaling for the acceptance probability that is proportional to $\exp\left(-\delta t^2 \delta\mathcal{H}^2\right)$. Physical systems with finite ranged correlations have mean squared fluctuations that scale as the system size, so the efficiency of the hybrid Monte Carlo approach is highest for small systems where propagation with large timesteps can be accepted.

For the models with internal degrees of freedom we use the SETTLE integrator [160] while for single-site models we use a velocity Verlet integrator[65]. Because each move is accepted with the Metropolis criterion, energy need not be conserved and consequently δt need not be small. In practice, we generally take $\delta t \approx 5 - 30$ fs and the number of steps in a trial trajectory, n, to vary between 1-20 depending of the steepness of the free energy landscape. The choices are made systematically to minimize correlation times. Trial volume changes, drawn from a logarithmic distribution, are used at a ratio of 2 hybrid Monte Carlo moves to 1 trial volume displacement. The relatively large value of δt serves to swiftly propagate dynamics over long time scales.

We have found that at supercooled conditions for $N \approx 200$, this calculation significantly reduces correlation times for structural relaxation relative to energy conserving dynamics. For instance, in the case of the ST2 model[210] discussed in detail below, the characteristic structural relaxation times under these moves are between 10^2 to 10^3 Monte Carlo steps, depending on the specific value of density and temperature. In contrast, single particle Monte Carlo moves reported previously[144, 145, 181, 196] yield structural relaxation times that

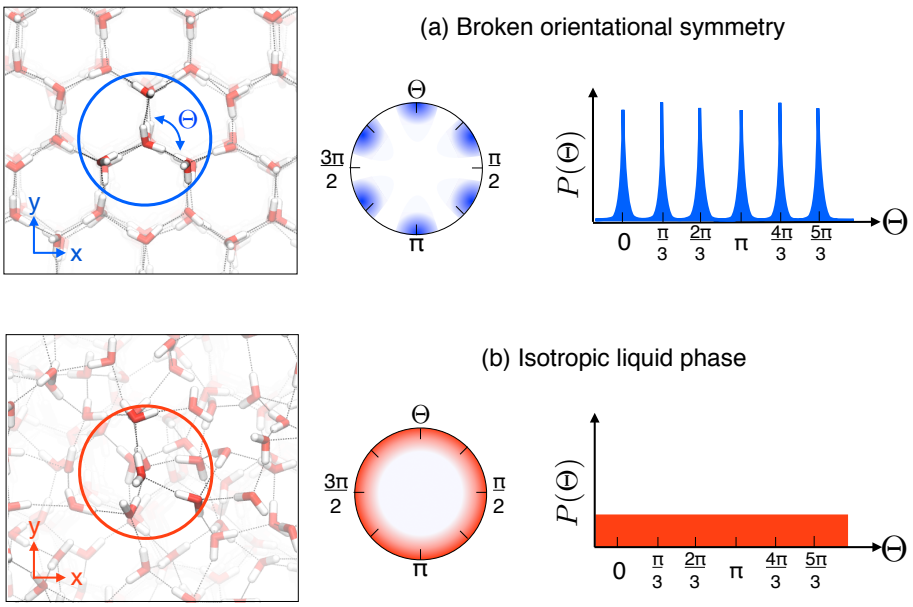

Figure 3.2: Illustration of broken orientational symmetry accompanying crystallization, with bond-order parameters that are able to distinguish these phases. (a) Distribution of angles projected into two dimensions relative to a fixed coordinate system for ice 1h. (b) Distribution of angles projected into two dimensions for a liquid.

are between 10^5 to 10^7 Monte Carlo steps, and molecular dynamics[109] yields structural relaxation times that are between 10^6 to 10^8 integration steps. Accounting for the factor $n = \mathcal{O}(10)$, these correlation functions demonstrate that our choice of hybrid Monte Carlo moves is computationally more efficient by 1-3 orders of magnitude over single particle moves and by 2 orders of magnitude over molecular dynamics. This remarkable speed up must in part reflect the highly non-linear and correlated nature of dynamics at supercooled conditions.

3.2.2 Order parameters

Order parameters are used throughout statistical physics to distinguish distinct phases[26]. They function as a reduced representation of state of the system at a level between the energy and the total configuration. As a reduced representation, order parameters are global quantities containing sums over all particles. When they are chosen carefully, their symmetries determine possible phase transitions and their spatial patterns reflect the energy scales for collective excitations[128].

For cold water, we use two types of order parameters. One is bulk density, the other quantifies orientational order. For the latter, we use Steinhardt, Nelson and Ronchetti's Q_6

and ψ_6[207]. For a finite system analyzed with computer simulation, these variables prove more convenient than Fourier components of the density. They also prove more useful than dynamic measures, such as the mean-squared displacement, which cannot distinguish liquid from crystal at supercooled conditions, where diffusion is slow in the liquid due to glassy dynamics and nonzero in the crystal due to defect motion.

Figure 3.2 illustrates how these order parameters work in a $2d$ system. Shown are typical snapshots of both a symmetry-broken crystal phase and an isotropic liquid phase. In the crystal, "bonds" drawn between nearest neighbors occur at specific angles, Θ, relative to an arbitrary coordinate system. In the liquid, these bonds are uniformly distributed. Cylindrical, or spherical, harmonics are akin to a Fourier transform on the unit circle, or sphere. As such, an order parameter based on these functions can be constructed that is invariant to rotations and independent of coordinate system. In the example in Fig. 3.2, the periodicity is sixfold, and dimensionality is 2, so a cylindrical harmonic with multipole number, $\ell = 6$, would yield a large value in the crystal and a vanishing value in the liquid.

Both Q_6 and ψ_6 are functions of a projection of the density field into averaged spherical harmonic components in a $3d$ analogue to the $2d$ picture in Fig. 3.2. To evaluate Q_ℓ, for each water molecule i, we calculate the set of quantities

$$q^i_{\ell,m} = \frac{1}{4}\sum_{j\in n_i}^{4} Y^m_\ell(\phi_{ij},\theta_{ij})\,, \quad -\ell \leqslant m \leqslant \ell\,, \tag{3.12}$$

where the sum is over those nearest 4 neighbors. $Y^m_\ell(\phi_{ij},\theta_{ij})$ is the ℓ, m spherical harmonic function associated with the angular coordinates of the vector $\mathbf{r}_i - \mathbf{r}_j$ joining molecules i and j, measured with respect to an arbitrary external frame. Since $q^i_{\ell,m}$ is defined in terms of spherical harmonics, it transforms simply under rotations of the system or the arbitrary external frame. These quantities are then summed over all particles to obtain a global metric

$$Q_{\ell,m} = \sum_{i=1}^{N} q^i_{\ell,m}\,, \tag{3.13}$$

and then contracted along the m axis to produce a parameter that is invariant with respect to the orientation of the arbitrary external frame,

$$Q_\ell = \frac{1}{N}\left(\sum_{m=-\ell}^{\ell} Q_{\ell,m}Q^*_{\ell,m}\right)^{1/2}. \tag{3.14}$$

The other orientation order parameter we consider, ψ_ℓ, is evaluated by first defining bond variables through local contractions of the $q_{\ell,m}$, which are reference frame independent,

$$b_{ij} = \frac{\sum_{m=-\ell}^{\ell} q^i_{\ell,m}q^{j*}_{\ell,m}}{\left(\sum_{m=-\ell}^{\ell} q^i_{\ell,m}q^{i*}_{\ell,m}\right)^{1/2}\left(\sum_{m=-\ell}^{\ell} q^j_{\ell,m}q^{j*}_{\ell,m}\right)^{1/2}}, \tag{3.15}$$

and then summing over all of the bonds made between molecule i and its nearest 4 neighbors,

$$\psi_\ell^i = \frac{1}{4}\sum_{j\in n_i}^{4} b_{ij} \tag{3.16}$$

Finally, the global parameter is obtained by summing over all molecules,

$$\psi_\ell = \frac{1}{N}\sum_{i=1}^{N} \psi_\ell^i \tag{3.17}$$

The mean or most probable value of Q_ℓ for an amorphous phase approaches zero in the thermodynamic limit, while it is finite for a crystalline phase. As such, Q_ℓ is a distinguishing order parameter for amorphous and crystalline phases. In contrast, because its contractions occur locally and not over the entire system, ψ_ℓ is non-vanishing in the thermodynamic limit for both disordered and ordered states. Nevertheless it is a useful measure of orientational order because the distributions of ψ_ℓ^i for the low temperature liquid are sensitive to the amount of crystallization in the system, and their mean values at low temperatures differ significantly between liquid and crystal. Further, as ψ_ℓ retains local information, it is useful in determining the existence of grain boundaries and defects. We have taken the $\ell = 6$ multipole because we have found empirically that it is particularly sensitive to distinguishing liquid water and ice.

3.2.3 Enhanced sampling methods

Fluctuations that result in phase transformations are exponentially rare at conditions of coexistence or modest supercooling. Standard methods of umbrella sampling get around the rare-event problem by adding biasing potentials, $W(\mathbf{r}^{3N})$, to the Hamiltonian in order to enhance occurrences of otherwise improbable fluctuations[65]. Re-weighting configurations can correct for the biasing. The form of an added energy function can be chosen for convenience, but in order to guarantee the system will reach a stationary state it must be time-independent.

Free energy methods that do not strictly adhere to this condition, such as metadynamics [125] and Wang-Landau sampling,[126] converge only conditionally in the limit that the biasing degree of freedom is the slowest mode or when the change in the biasing term asymptotes to zero. This issue is particularly relevant for supercooled water because pathways beyond the early stages of coarsening generally involve several slow variables in addition to the global crystal order parameter, Q_6. An incorrect free energy estimate will be obtained if one or more of those slow variables is not controlled in meta-dynamics or Wang-Landau algorithms.

The order parameters, ρ and Q_6, are chosen to distinguish phases of broken symmetries expected to result in water-like models at low temperatures. We will show later that Q_6 is a sufficiently sensitive order parameter to distinguish globally ordered from disordered states accompanying a freezing transition[133]. This virtue noted, it must also be appreciated that

Q_6 deviates from its disordered value only after a substantial amount of orientational order has developed in the system.

The umbrella biasing potentials we employ are of the form

$$W(\mathbf{r}^{3N}) = k\left[\rho(\mathbf{r}^{3N}) - \rho^*\right]^2 + \kappa\left[Q_6(\mathbf{r}^{3N}) - Q_6^*\right]^2, \tag{3.18}$$

where $\rho(\mathbf{r}^{3N})$ and $Q_6(\mathbf{r}^{3N})$ are the order parameters discussed previously, evaluated for configuration $\mathbf{r}^{3N}$. The biasing potential, with force constants κ and k, keep these order parameters close to their target values ρ^* and Q_6^*. Each pair of target values defines a specific sub-ensemble or so-called "window" in configuration space. After collecting statistics in one window, the window is moved by changing the pair of target values, ρ^* and Q_6^*, whereupon statistics in the new window are collected. The procedure is carried out throughout the ρ-Q_6 plane, making sure that passage from one region to another is fully reversible, and that adjacent regions have sufficient overlap of statistics to enable further analysis. For this purpose, for systems of $N \lesssim 1000$, we find that κ in the range of 500 to 10,000 $k_\mathrm{B}T$ and k in the range of 1,000 to 2,000 $k_\mathrm{B}T$ cm^{6}g^{-2} is satisfactory.

Statistics gathered in these biased ensembles are related to averages in the ensemble defined in Eq. 3.3 by

$$\langle A \rangle = \frac{\langle A e^{\beta W} \rangle_\mathrm{W}}{\langle e^{\beta W} \rangle_\mathrm{W}} \tag{3.19}$$

where A is an arbitrary observable and $\langle \ldots \rangle_\mathrm{W}$ denotes averages in the biased ensemble. The term in the denominator can be recognized as ratio of the partition functions for the different ensembles. For computing expectation values over many independent ensembles, multiple ratios of partition functions, or identically multiple free energy differences, must be computed self-consistently. To do this we use the MBAR algorithm [198], which is a minimal variance estimator. For the specfic observable, $A = \delta(\rho(\mathbf{r}^{3N}) - \rho)\delta(Q_6(\mathbf{r}^{3N}) - Q_6)$, this procedure yields an estimate of the joint probability of ρ and Q_6, due to the identity

$$P(\rho, Q_6) = \langle \delta(\rho(\mathbf{r}^{3N}) - \rho)\delta(Q_6(\mathbf{r}^{3N}) - Q_6) \rangle \,. \tag{3.20}$$

Stitching together data from different sub-ensembles yields the joint probability and thus free energy $\beta F(\rho, Q_6; p, T) = -\ln P(\rho, Q_6)$, up to an additive constant, for very rare fluctuations. Here p and T, respectively, denote the pressure and temperature at which the Monte Carlo trajectory is carried out. Assuming this function is determined accurately over the relevant range of densities, free energies at other relevant pressures are determined from the relationship,

$$F(\rho, Q_6; p + \Delta p, T) = F(\rho, Q_6; p, T) \; + \; \Delta p \, N/\rho \,. \tag{3.21}$$

which is a straightforward re-weighting expected from thermodynamics[28].

In each window, a typical calculation consists of an initial equilibration run for up to 100 structural relaxation times as evaluated for the larger of either the initial liquid density or the equilibrium of bias window density. Then, statistics are gathered over 50 to 1000 structural relaxation times, depending upon the length of time required to obtain reliable

statistics as judged from cumulative averages for Q_6 and potential energy. Here, structural relaxation time refers to the simulation time, t, required for mean square fluctuations in structure factors to decay from their initial to 90% of their relaxed value.

Because deeply supercooled liquids and crystals are nonergodic on the timescales for typical simulations, its important to ensure that estimates of observables are independent of initial conditions. To do this, three different techniques for generating initial conditions were used. Initial seeds were created by cooling an equilibrium liquid initially prepared at $T = 330$ K at a rate of 10 K/ns until it reached the target temperature. Seeds from this procedure were biased into different windows in steps between adjacent windows, by gradually changing parameters of the biasing potential $W(\mathbf{r}^{3N})$, Eq. 3.18, and with re-equilibration runs in between each step. At high Q_6, the crystal that was spontaneously formed using this procedure in all cases was a defected ice Ic. This phase is formed spontaneously for two reasons. For the small systems studied here, it is preferred by the periodic boundary conditions as its lattice fits within the cubic symmetry of the system's volume, unlike ice Ih. For second generation seeds, we assumed that the spontaneously formed crystal was the relevant solid phase, so we prepared a perfect Ice Ic configuration, which was used to sample intermediate and high Q_6 states as well as bias them into low Q_6 regions to sample liquid states. Third generation seeds were obtained by melting an ice Ic configuration and then using states along the melting trajectory to seed intermediate Q_6 windows. These configurations were subsequently biased into the high and low Q_6 regions, again by gradually changing the parameters of $W(\mathbf{r}^{3N})$, and again with new re-equilibration runs.

Reversibility was explicitly checked in our calculations by constructing plots of all two-dimensional histograms and checking for hysteresis. Estimates of errors in free energy differences were made by computing overlaps and gradients of the distributions obtained by various routes. These steps, including bidirectional biasing to and from the crystalline phase and creating many independent realizations of initial conditions, follow standard practices for computing free energies articulated in reviews such as Ref. [178].

3.2.4 Finite size scaling and the freezing transition

Finite-size effects are fundamental to the nature of phase transitions. Establishing the existence of a phase transition on a computer requires studying system-size dependence, for example, by computing changes in free energy barriers with respect to changing N. In this section, we shown how these importance sampling techniques can be applied to determine the existence of a freezing transition in a model of water.

The previous section discussed how to calculated the joint free energy, $F(\rho, Q_6)$. The character of the freezing transition, at conditions far away from any potential triple point, can be analyzed by studying the system-size dependence of the contracted free energy[18]

$$F(Q_6) = -k_{\mathrm{B}}T \ln \left(\int \mathrm{d}\rho \, \exp\left[-\beta F(\rho, Q_6)\right] \right). \tag{3.22}$$

This function is shown in Fig. 3.3 for the mW model of water at one of the pressures and

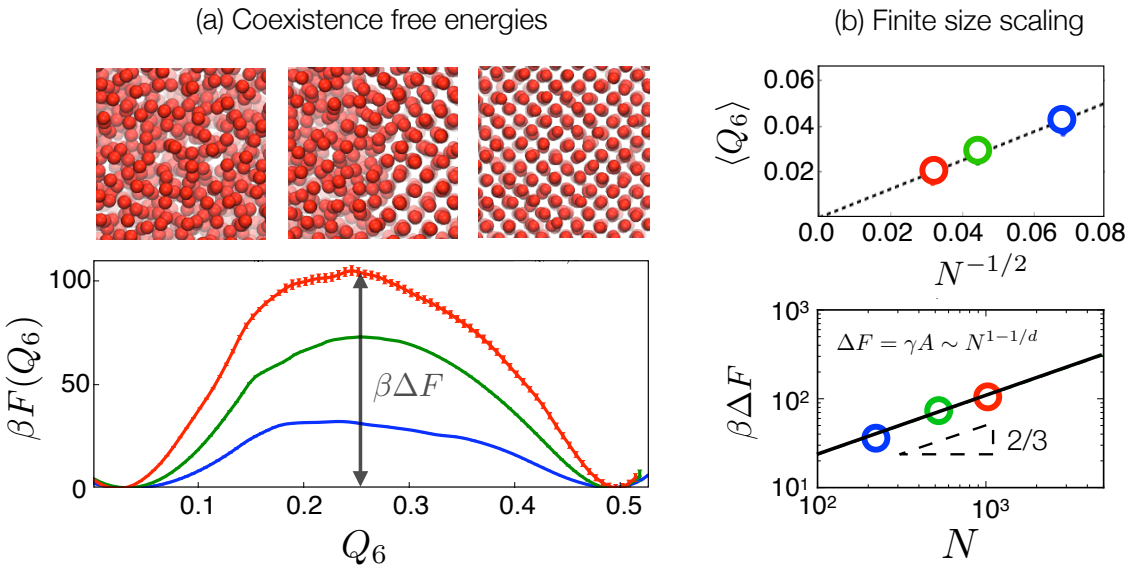

Figure 3.3: Free energies as a function of Q_6 for $N = 216$ (blue), 512 (green), and 1000 (red), calculated at T/T_0=1.09 and p =1 bar and representative snapshots from molecular dynamics simulations. Snapshots above are representative configurations of each, liquid, coexistence and crystal, region. Top right: The mean value of Q_6 for liquid (circles) and crystal (squares) for different system sizes. Bottom Right: Interfacial free energy for different system sizes. For comparison a line of slope 2/3 is also shown. Error estimates are shown in the main figure, but are smaller than the symbols in the panels on the right. This figure is adapted from Ref. [133].

temperatures where an amorphous phase is in coexistence with the crystal. The specifics of the model and its phase diagram are discussed in the next section. The quantity $\Delta F(Q_6) = F(Q_6) - \min[F(Q_6)]$ reaches its maximum value when an interface separating amorphous and crystal phases extends across the entire system. Representative snapshots for these configurations are shown in the top panels. The value of this maximum free energy is the interfacial free energy. Accordingly, for a first-order transition in 3 dimensions, it should be proportional to $N^{2/3}$. This scaling is satisfied to a good approximation for the system sizes considered in Fig. 3.3.

Nonzero values of Q_6 in an amorphous phase are due to fluctuations. As such, the mean value of Q_6 for the amorphous phase should disappear as $1/N^{1/2}$. This scaling is also found for the system sizes studied and is illustrated in Fig. 3.3. In contrast, for a crystal Q_6 will have a nonzero mean that remains finite as $N \to \infty$. This behavior is consistent with our numerical results, as also illustrated in Fig. 3.3. Thus, the transition between liquid and crystal in mW water appears to be a standard freezing transition which is first order and between phases with different orientational symmetry.

3.3 Minimal model of supercooled water

Most of the numerical results we present in this dissertation have been computed with a recently developed model by Molinero, so-called "mW" water[161]. We use this model for three reasons. First, it is a computationally convenient model because it contains no long-ranged forces, relying instead on short-ranged three-body forces to favor microscopic structures consistent with those of water. Second, the behavior of the model is realistic in the sense that in the range of conditions we wish to study, its phase diagram is a reasonable caricature of that for water[95, 165, 166] as we will demonstrate shortly. Third, the results obtained with this model would seem to apply to other systems in addition to water in that the model is a variant of one developed by Stillinger and Weber,[211] which has been used to treat behaviors of Si [13, 194, 222] and SiO_2[61].

Unlike many models of water that generate local tetrahedrally by delicately placed point charge interactions, the mW model balances two and three body interactions to characterize hydrogen bonding interactions. The potential is effectivity generated by integrating out the orientational degrees of freedom associated with the hydrogens in water. The Hamiltonian for the model is a sum over all unique pairs and triples,

$$U(\mathbf{r}^{3N}) = \epsilon \sum_{\mathrm{j>i}} u_2(r_{\mathrm{ij}}) + \epsilon\lambda \sum_{k>j\neq i} u_3(\mathbf{r}_i, \mathbf{r}_j, \mathbf{r}_k) \tag{3.23}$$

where pair potential depends only on the magnitude of its argument,

$$u_2(r) = \left[A \left(\frac{\sigma}{r}\right)^4 - B \right] e^{1/(r/\sigma - a)} \tag{3.24}$$

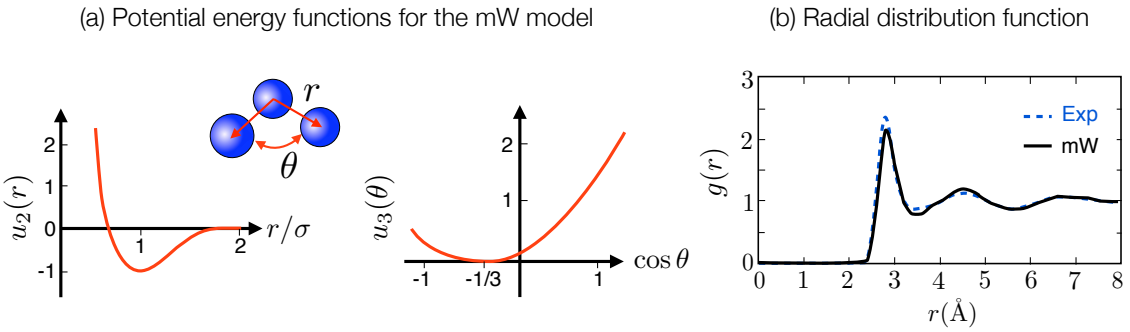

Figure 3.4: Potential energy and resultant liquid structure for the mW model. (a) The two body and three body potential energy functions. The three body potential energy is plotted assuming for each neighboring molecule has $r < \sigma$. (b) Radial distribution function for oxygen atoms, for the mW model[161] and experiment[168] at $p = 1$ bar and $T = 298$ K.

and the three body potential depends on the relative positions of triplets of particles,

$$u_3(\mathbf{r}_i, \mathbf{r}_j, \mathbf{r}_k) = \left(\frac{\mathbf{r}_{ij} \cdot \mathbf{r}_{jk}}{r_{ij} r_{jk}} - \cos\theta_T \right)^2 e^{\gamma/(r_{ij}/\sigma - a)} e^{\gamma/(r_{jk}/\sigma - a)} . \tag{3.25}$$

While it has a number of parameters, $A \approx 7.05$ and $B \approx 4.2$ are chosen so that the pair potential has a depth of 1 at σ, $a = 1.8$ and $\gamma = 1.2$ set the cutoffs for the potential ensuring it is only short-ranged and $\cos\theta_T$ is the cosine of a tetrahedral angle. Therefore, only the basic length-scale, σ, energy-scale, ϵ, and partitioning of two and three body interactions, λ, are adjustable. These three parameters were chosen by Molinero and Moore to determine the melting temperature, density at ambient conditions and heat of vaporization.

Figure 3.4 plots the potential energy functions and compares the resultant $g(r)$ from the model at ambient conditions to the X-ray data shown in the previous chapter. It is evident from these graphs that these simple short-ranged functions are able to recover the basic physics of liquid water, by resolving its tendency to be locally tetrahedral. As will be shown throughout this thesis, this mW water offers a minimal model for studying structural properties of water and ambient temperatures. However, it should be noted that away from liquid conditions, such as in the dense vapor or high pressure crystal, the mW model will likely yield inaccurate results.

The mW model differs from the original Stillinger-Weber inter-particle potential energy function for silicon in two ways. The first is the adoption of different values for the length and energy parameters of the model. This difference is inconsequential because it amounts to a simple rescaling of temperature and density. The second is more substantive but slight. Specifically, to capture some thermodynamic properties of water, the mW model has a partitioning between two- and three-body terms, λ, that differs by 10% from the partitioning for silicon.

3.3.1 Pressure-temperature phase diagram of the mW model

We have studied the phase behavior of the mW model by computing free energy surfaces throughout its condensed phases. Figure 3.5 shows the state points examined. Each circle represents a state point where the free energy has been calculated as a function of the global system density and Q_6 that quantifies broken orientational symmetry. Basins in the free energy surface establish relative stabilities of the phases. As expected from the discussion at the beginning of the chapter, this phase space is partitioned into three regions: where the liquid is stable (blue region), where it is metastable with respect to the crystal (white region), and where it is unstable to the crystal (red region). The boundary separating the stable liquid from the metastable liquid, solid blue line, is readily identified as T_{m} and is determined by the equality of the stability of the liquid and crystal basins. The boundary between the metastable liquid and the unstable liquid, dashed red line, is identified as T_{s} and is determined for the system sizes studied as the conditions where the global barrier to crystallization is on the order of $k_{\mathrm{B}}T$. Notably, throughout this entire region, we do not find any evidence of a second, low temperature critical point.

To put this diagram in context, we highlight state points that others have identified as relevant to a liquid-liquid phase transition in supercooled water. The temperature of maximum density at low pressure sets the scale of the figure. This chosen reference temperature is $T_0 = 250$K for the mW model,[161] and it is $T_0 = 277$K for water[49]. The phase diagram in Fig. 3.5 shows that the density maximum of liquid mW occurs at slightly supercooled conditions while that of experimental water occurs at a temperature slightly higher than the freezing temperature.

The points identified by Liu et al. [142], squares in Fig. 3.5, come from measured relaxation times of water confined in silica nanopores with a 7Å radius. These relaxation times have a temperature dependence that changes from super-Arrhenius to Arrhenius upon cooling below a crossover temperature, $T_{\mathrm{x}}(p)$. This temperature depends upon external pressure p, and points on this line are shown in Fig. 3.5 with unfilled squares, which are attributed in Ref. [142] to crossing a "Widom line". A Widom line refers to a locus of maximum response that ends at a critical point [124]. In cases where a phase transition exists, there are many such lines because different response functions have different lines of extrema. Ambiguity ceases only in the proximity of a critical point. But whether any such lines can be related to $T_{\mathrm{x}}(p)$ is unclear because Widom lines refer to time-independent thermodynamic behavior and $T_{\mathrm{x}}(p)$ refers to time-dependent non-equilibrium behavior.

A different basis for identifying relevant points is made by Zhang et al., diamonds in Fig. 3.5, considering the same system[240]. In this case it is the density of the water that is measured. This observed density exhibits hysteresis upon alternating heating and cooling scans, and the hysteresis grows upon increasing pressure. We have already noted that it is questionable whether the phase behavior of bulk water can be related to that of water confined to narrow pores. Virtually all molecules in those pores are influenced by interfaces. Nevertheless, points of maximum hysteresis, denoted by the filled diamonds in Fig. 3.5, have been attributed to a line of first-order liquid-liquid transitions, and points of less significant

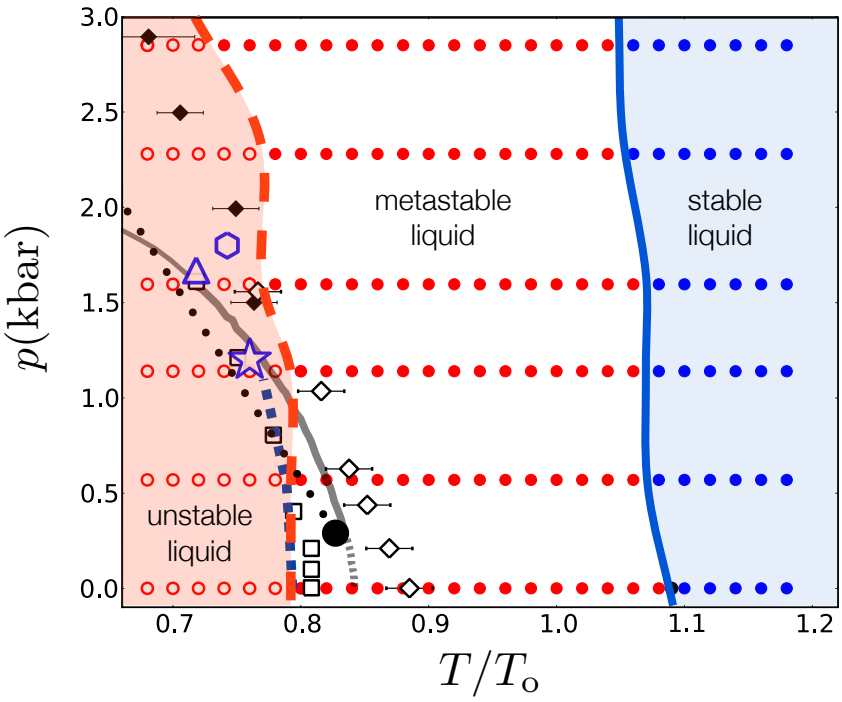

Figure 3.5: Phase space sampled in our calculations for the mW model. Open circles refer to states where the amorphous liquid is found to be unstable, filled red circles refer to states where the amorphous liquid is found to be metastable with respect to the crystal, and filled blue circles refer to states where the liquid is found to be stable with respect to the crystal. Grey and black lines, diamonds and squares locate previous estimates of a liquid-liquid phase transition inferred from experimental results[66, 142, 240], see text for details. A star locates a previous prediction of a liquid-liquid critical point based upon extrapolation of simulation results for the mW model.[164] The purple triangle and hexagon are estimates of low temperature critical point locations obtained from interpreting simulation results for variants of ST2[145, 184]. This figure is adapted from Ref. [133].

hysteresis, marked by open diamonds in the figure, are attributed to a continuation of that transition[240]. In Chapter 4, we will explicitly consider how the phase diagram changes under such confinement.

Another proposed line of liquid-liquid transitions, grey line in Fig. 3.5, is constructed by Fuentevilla and Anisimov[66]. Here, a postulated scaling form is used to extrapolate from experimentally accessible equilibrium thermodynamic data. The resulting prediction and its analytic continuation are drawn as solid and dashed lines in Fig. 3.5. Using a slightly different formulation of this scaling theory, Holten and Anisimov have also proposed the black line and circle for an alternative first order line and critical point[87]. Even if a critical point is present this predicted line is questionable because it is generally impossible to identify critical divergences from a small rise in noncritical background fluctuations of the sort contributing to the heat capacity at standard conditions. This fact is illustrated by Moore and Molinero's predicted critical point for mW water[164]. Its location, the star in Fig. 3.5, is found by extrapolation from a small rise in a response function computed at distant thermodynamic conditions. We find no evidence for a liquid-liquid transition anywhere near this predicted critical point. Rather, it and all other estimates pertaining to a purported liquid-liquid transition lie close to a spinodal associated with crystallization. This finding is not inconsistent with Moore and Molinero's more recent report that the amorphous phase of the mW model seems to be forever changing and impossible to equilibrate at a point in the phase diagram where liquid-liquid transitions have been imagined[165].

Two additional marked points in Fig. 3.5, the blue triangle and hexagon, refer to other estimates of a location for a liquid-liquid critical point. These are estimates obtained from extrapolating simulation results for variants of the ST2 water model,[210] about which we have more to say later.

3.3.2 Anomalous thermodynamics of the mW model

As discussed in Chapter 2, water exhibits anomalous thermodynamic properties at low temperatures. Because these behaviors have been proposed as indicators of a liquid-liquid transition, it is important to show that the mW model exhibits such behaviors. Specifically, we focus on the density maximum as a function of temperature, and the relatively large rate of increases upon lowering temperature of both isothermal compressibility and isobaric heat capacity[43].

We have used constant pressure Monte Carlo simulations to compute,

$$\rho = N/\langle V \rangle \,, \tag{3.26}$$

$$\kappa = \langle (\delta V)^2 \rangle / k_{\mathrm{B}} T \langle V \rangle \,, \tag{3.27}$$

$$C_p = \langle (\delta H)^2 \rangle / k_{\mathrm{B}} T^2 \,, \tag{3.28}$$

for the mW model. Here, N, V and H denote number of molecules, volume and enthalpy, respectively; δV and δH denote deviations from mean values of V and H, respectively; the pointed brackets denote an ensemble average.

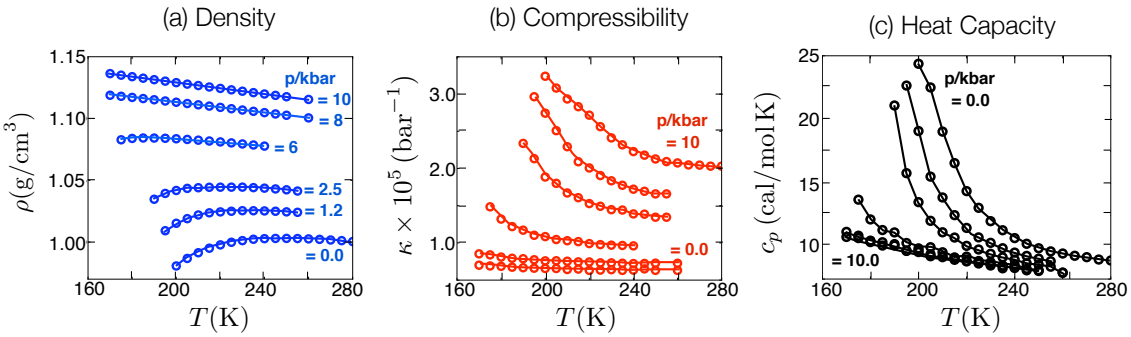

Figure 3.6: Average thermodynamic properties as a function of temperature at different pressures for the mW model of water. Properties have been computed with $N = 8000$ molecules and errorbars are on the order of the size of the markers for most points.

Figure 3.6 shows that the qualitative trends and magnitude of anomalies of mW water agree with those of experimental water shown in Fig. 2.7. As with those experiment results, the low-temperature end of the displayed graphs occurs at the point where the liquid becomes unstable. Down to that temperature, the growths of κ and C_p are notable but modest in size and far from the sort of divergent behavior one would ordinarily associate with a critical point or phase boundary. At all stable and metastable liquid phase states we have studied, see Fig. 3.5, we find similar nonsingular behavior. There are two notable differences between the results for the mW model and those of experiment. First, the fluctuation quantities, C_p and κ are lower for the mW model than for experiment. This is the expected consequence of reducing the number of degrees of freedom by integrating out the orientations. Second, there is a shift in location of the features to lower temperatures and higher pressures. We find that referencing the temperature of maximum density at ambient pressures, the thermal properties of water and the mW model can be reasonably compared. This agreement reflects the nature of the anomalous behavior as resulting from the interplay between entropic packing effects and the local tetrahedral order that oppose it. At the temperature of maximum density, these two effects are nearly balanced, and below it local ordering becomes more extended until the liquid becomes unstable. The small compressibility of the mW model results in a different effective pressure scale for the model relative to experiment. Using a relative scale that reflects the density change on freezing, 3% of the mW model and 10% for experiment, can account for this difference[161].

3.3.3 Free energy surfaces at conditions of metastability

Free energies as a function of density ρ, orientational order parameters Q_6 and ψ_6, and so forth, are related to the probabilities of the order parameters in the usual way. Specifically,

$$F(\rho, Q_6, ...) = -k_\mathrm{B}T \ln P\,(\rho, Q_6, ...) + \text{ const.} \tag{3.29}$$

where the probability $P(\rho, Q_6, ...)$ is proportional to the partition function for microstates with the specified values of the order parameters. The irrelevant additive constant in Eq. 3.29 refers to normalization and standard state conventions.

Figure 3.7 depicts representative free energies for three different state points. Each free energy surface includes the range of densities where liquid and crystal basins are located. With the variable Q_6, we see a significant separation between liquid and crystal basins. For the state points considered in Fig. 3.7, with $N = 216$, the crystal basin is centered around $Q_6 \approx 0.5$, while the liquid basin, when it exists, is centered around $Q_6 \approx 0.05$. As N increases, the former changes little, but the latter tends to zero. This behavior was illustrated explicitly in a previous section.

The state points considered in Fig. 3.7 show how the free energy surfaces evolve as the pressure or temperature are changed. In Fig. 3.7a, a barrier separates the liquid phase from the crystal. Therefore, at that state point the liquid is metastable. Lowering the temperature and increasing the pressure, Fig. 3.7b shows the barrier to crystallization has vanished. At this state point, the liquid is unstable.

Similar behavior is found with the free energy of ρ and ψ_6. This function, $F(\rho, \psi_6)$, is also shown in Fig. 3.7 at two different state points. Figure 3.7c shows this free energy at a temperature and pressure where the liquid is metastable with respect to the crystal. At this state point, the mean value, $\langle \psi_6 \rangle$ is about 0.27, a value that reflects the relatively small amount of local ordering present in the supercooled liquid. In contrast, for the crystal we find $\langle \psi_6 \rangle \approx 0.9$. Fig. 3.7d shows the free energy for a temperature and pressure in the region of the phase diagram where the amorphous phase is unstable, the so-called no man's land. This point is close to a proposed location of a liquid-liquid critical point[164]. We see, however, that it is not a point of criticality, rather an instance of liquid instability. The behavior of ψ_6 is strongly correlated to the potential energy. This fact follows from the functional form of ψ_6 and the three-body potential of the mW model. Thus, the behavior of $F(\rho, \psi_6)$ should be similar to that of $F(\rho, U)$ where U denotes the total potential energy of the mW model.

For all of the state points considered, which includes a broad swath of no-man's land, there is no evidence of a bifurcation of the free energy along the density direction within the liquid region (i.e., where Q_6 and ψ_6 are small). What bifurcation does exist is associated with a transition between an amorphous phase and a crystal. From finite size scaling analysis, we conclude that this bifurcation is associated with a first order freezing transition.

3.4 Theoretical model for initial stages of coarsening

Others have used molecular simulation for models of water [23, 80, 124, 145, 165, 184] and related liquids [13, 68, 194, 222] to examine their possible polyamorphisms.[1] In most cases, previous studies have claimed numerical evidence for a liquid-liquid transition. However, in most cases, the methods employed have been limited in at least one of three ways: time

[1] Those cited here[13, 23, 68, 80, 124, 145, 165, 184, 194, 222] are representative but by no means comprehensive. We exclude from this list models that do not exhibit local tetrahedral order, e.g. Ref. [96]

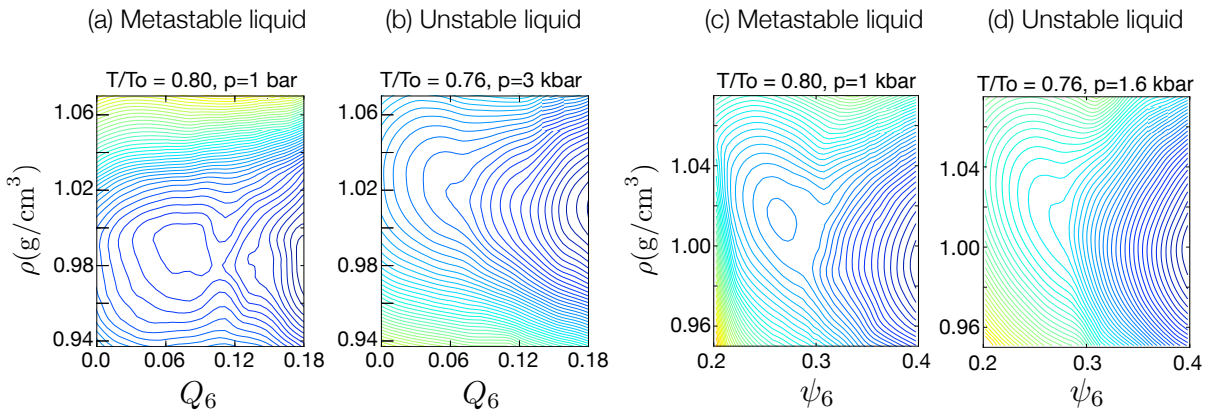

Figure 3.7: Free energy surfaces for mW water as a function of ρ and Q_6 or ψ_6. As shown in (a), the liquid is metastable with respect to the crystal. As the system is cooled, the barrier disappears, as illustrated in (b). Free energy surfaces for mW water as a function of ρ vs ψ_6 at conditions where the liquid is (c) metastable, and (d) unstable. In all calculations, the system is periodically replicated and contains $N = 216$ particles. Adjacent contour lines are spaced by 1 $k_{\rm B}T$, and statistical uncertainties are smaller than that energy. This figure is adapted from Ref. [133].

.

scales that short compared to internal relaxation times, system sizes that are small compared to relevant correlation lengths, and order parameters that fail to discriminate order from disorder or fail to be adequately controlled. By employing multiple order parameters and free-energy sampling methods, we have shown how to overcome these time-scale issues and are able to discriminate between phases of different symmetries. By considering different system sizes and size scaling analysis, we have shown how to overcome uncertainty associated with finite system sizes. Nevertheless, it is instructive to see how the limitations of previous work have resulted in the claims of polyamorphism. To do this, we work out a simple theory for the initial stages of coarsening of liquid water and ice.

Consider the equilibrium joint distribution function for the order parameters, $P(\rho, Q_6)$. It is related to the free energy (or reversible work) surface for these variables as before. Over time scales large compared to those of liquid relaxation but possibly not large compared to those of crystal formation, the joint distribution is in general a non-equilibrium distribution,

$$P_{\rm ne}(\rho, Q_6, t) = P(\rho|Q_6)\, P_{\rm ne}(Q_6, t)\,, \tag{3.30}$$

where $P(\rho|Q_6)$ is the equilibrium distribution for ρ given a specific value for Q_6, and $P_{\rm ne}(Q_6, t)$ is the non-equilibrium distribution for Q_6. The non-equilibrium distribution depends upon the protocol with which the system is prepared, and its time dependence is irreversible. For large enough t, presuming ergodicity, $P_{\rm ne}(Q_6, t)$ approaches the equilibrium $P(Q_6)$. But this limit can require simulation times thousands of times longer than those needed to equilibrate ρ. Not accounting for this behavior can give the illusion of a reversible polyamorphism

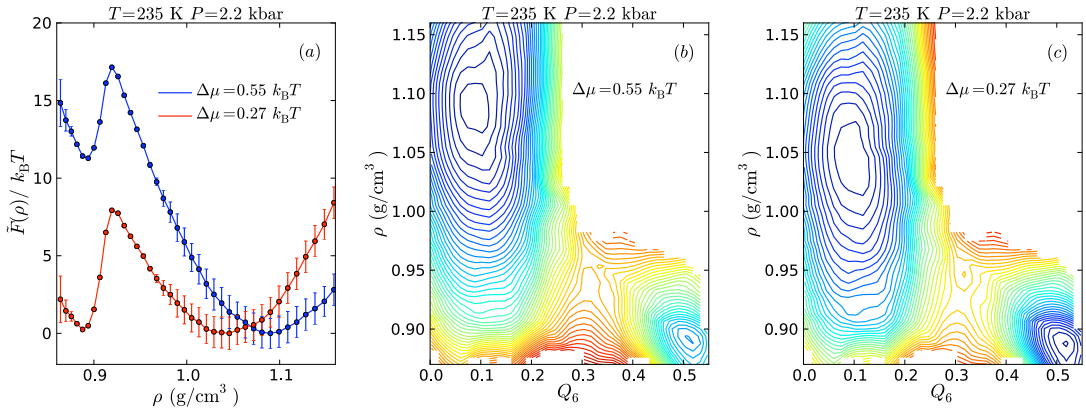

Figure 3.8: Free energies for the mST2 model of water. The system is periodically replicated and contains $N = 216$ molecules. Panel (a) is the contracted $\tilde{F}(\rho)$. Panels (b) and (c) are the surfaces $\tilde{F}(\rho, Q_6)$. Phase coexistence between amorphous and crystal phases occurs at $\Delta\mu = 0.27 k_{\rm B}T$, where $\Delta\mu$ is the chemical potential relative to that of phase space point (T, p)=(235 K,2.2 kbar). Adjacent contour lines in (b) and (c) are spaced by $1\,k_{\rm B}T$ and statistical uncertainties are of the order of, or less than, that energy. Error bars in (a) are one standard deviation. This figure is adapted from Ref. [133].

because the non-equilibrium free energy, $-k_{\rm B}T \ln[P(\rho|Q_6)\, P_{\rm ne}(Q_6, t)]$, can have a low-$Q_6$ basin for times shorter than those required for Q_6 to diffuse towards its equilibrium crystal value at high Q_6.

This possibility, which we refer to as "artificial polyamorphism," can be appreciated by comparing the free energy surfaces shown in Fig. 3.1. In particular, imagine studying the system on time scales where Q_6 can diffuse over no more than the left halves of the pictured free-energy panels. $P_{\rm ne}(Q_6, t)$ would then be peaked at a low value of Q_6, even for cases where a high Q_6 value would be the correct equilibrium value. Thus, if Q_6 is limited in this way to small values, the low-temperature (i.e., left-most) panel would then yield a pseudo free energy, $-k_{\rm B}T \ln P_{\rm ne}(\rho, Q_6, t)$, with an illusory "amorphous basin" at a density lower than that of the metastable liquid. For liquid water at pressures and temperatures in or close to "no man's land," small values of Q_6 will survive while the crystal phase begins to coarsen. The bottom left of Fig. 3.1 shows a configuration of water in that regime.

In order to quantify this idea and make contact with previous work, we will use as input equilibrium surfaces, $F(\rho, Q_6)$, from a model where the most extensive research into potential liquid-liquid coexistence has been done. This model, the ST2 model, and its free energy surfaces near $T_{\rm s}$, are considered below.

3.4.1 Free energy surfaces for ST2

We have considered molecules interacting by a modified form of Stillinger and Rahman's pair potential[210]. This pair potential is a point charge model of water, that includes 5 force centers: 1 central site on the oxygen atom that interacts with a Lennard-Jones potential, 2 positive charge centers located and 2 negative charge centers located at equidistance points of a tetrahedron. The latter charge-charge interactions affect a local tetrahedrally in order to mimic water-like properties. The modification we use here incorporates long-ranged electrostatics rather than the simple spherical truncation of the original model.

In Section 3.5.1, we will consider variants of these long-ranged interactions and it will become convenient to differentiate this specific implementation from others. The model we will consider in this section we refer to as "ST2a," the details of which for the current discussion are unimportant but are detailed later. The ST2a model is more difficult to simulate than the mW model because the former contains long-ranged interactions and the latter does not. As such, our investigation of its behavior is more limited than those we have performed for mW water. Nevertheless, our investigation seems sufficient to challenge previous findings of a liquid-liquid transition at the conditions examined by Liu et al. for a related, "ST2b" model. It also seems sufficient to discount an assortment of less direct simulation studies that also report evidence of a liquid-liquid transition in other ST2 models of water[80, 80, 124, 182, 184].

Figure 3.8 shows free energies we have computed for the ST2a model using $N = 216$ molecules. The procedures we employed are identical to those used for the mW model, except for the technical detail that we modify LAMMPS to handle the specific ST2a potential. We focus on the region of the p-T plane where Liu et al. report bifurcation in the free energy as a function of density. In that region, we too find a bifurcation, but not between two amorphous phases. The grand canonical Monte Carlo simulation method of Ref. [145] is sufficient to detect a phase boundary for the liquid, but it cannot distinguish liquid from crystal because it does not control distinguishing order parameters. In our calculations, where both ρ and Q_6 are controlled, we find that a boundary does in fact exist between liquid and crystal. But at the thermodynamic conditions considered by Liu et al., there is no evidence of a second liquid basin in the free energy $F(\rho, Q_6)$.

The specific free energies shown are found by first computing $F(\rho, Q_6)$ from our simulations at $T = 235$ K and $p = 2.2$ kbar, i.e. we compute $F(\rho, Q_6) = F(\rho, Q_6; p, T)$. The free energy shows that for this point in the phase diagram, the crystal is stable with respect to the liquid. A specific state point considered by Liu et al. is at the same temperature but a different pressure or chemical potential for which the free energy can be reached by a shift in chemical potential

$$\tilde{F}(\rho, Q_6; T, \Delta\mu) = F(\rho, Q_6) - \rho V \Delta\mu, \tag{3.31}$$

with $\Delta\mu \approx 0.55\, k_{\mathrm{B}}T$. Here, $\Delta\mu$ is the chemical potential relative to that at (T, p)=(235 K, 2.2 kbar). A lower value of $\Delta\mu$ brings the system to a point of coexistence between the liquid and the crystal. These free energy surfaces are shown in Panels (b) and (c) of Fig.

3.8. The free energy computed by Liu et al. is the contraction

$$\tilde{F}(\rho) = -k_{\mathrm{B}}T \ln \left(\int \mathrm{d}Q_6 \, \exp\left[-\beta F(\rho, Q_6) - \beta \rho V \Delta\mu\right] \right) \tag{3.32}$$

This function is shown in Panel (a) of Fig. 3.8.

Like Liu et al, we find a bistable free energy. The locations for the minima we find for $\tilde{F}(\rho)$ are in good accord with those found by Liu et al. But our free energy has a large barrier between the two basins, reflecting a finite crystal-liquid surface tension, while that reported by Liu et al exhibits a small barrier. Liu et al. suggest that their result is indicative of a liquid-liquid transition and the proximity of a critical point. However, our free energy surface shows no such phase transition behavior. There is only a crystal-liquid first-order transition. We suggest that the Liu et al. result is a non-equilibrium phenomenon, where a long molecular dynamics run at constant $T - p$ and initiated from their low-density amorphous phase will eventually equilibrate in either the low density crystal or (more likely) in the higher density metastable liquid. The time scale for this equilibration is long, as we discuss in the next section.

Another variant of the ST2 model, the "ST2c" model, considered by Poole et al.,[184] uses a reaction field approximation to estimate the effects of long-ranged forces. Based on an extrapolation from the equation of state computed for ST2c model, Poole et al. predict the presence of a liquid-liquid transition, and the critical point location obtained from that estimate is shown in Fig. 3.5. The density-maximum reference temperature for both ST2a and ST2c is $T_{\mathrm{o}} = 330\,\mathrm{K}$. Poole et al. estimate the critical temperature to be $T_{\mathrm{c}} = 245\,\mathrm{K}$. Our calculations for ST2a, shown in Fig. 3.8, are at the lower temperature, $T = 235\,\mathrm{K}$. Accordingly, at some pressure, we should find bistable liquid behavior if indeed a critical point existed at the higher temperature. But we find that upon adding $\Delta p\, V$ to our computed $F(\rho, Q_6; 2.2\,\mathrm{kbar}, 235\,\mathrm{K})$, where $\Delta p = p - 2.2\,\mathrm{kbar}$, no second liquid basin can be discerned for any reasonable value of p. Therefore, and similar to the behavior found with the mW model, extrapolation from the behavior of a one-phase system as done in Ref. [184] proves to be a poor indicator of a phase transition.

3.4.2 Separation of timescales: density and long range order

This section provides a quantitative theoretical analysis showing the difficulty in obtaining correct reversible free energy surfaces of supercooled water. We do so by examining the effects of time-scale separation for dynamics on a reversible free energy surface. The particular surface we employ is the free energy $F(\rho, Q_6)$ in Fig. 3.8b.

In cases where the crystal is stable but the system is prepared in the liquid, an irreversible drift towards the crystal will occur. To the extent that ρ and Q_6 are the principal slow variables, this coarsening can be described in terms of motion on the $F(\rho, Q_6)$ surface. By using this perspective, and specifically by adopting the free energy surface pictured in Fig. 3.8b, we illustrate here the generic behavior of early-stage coarsening of ice. The behavior is not specific to the particular free energy surface. Rather, it is general consequence of a

Table 3.1: Separation of timescales for fluctuations in density and long-ranged order.

Model	τ_ρ [1]	τ_{Q_6} [2]
mW	10^3 MDS[c]	10^5 MDS[c]
ST2	10^2 MCS[d]	10^4 MCS[d]
ST2	10^6 MCS[e]	10^8 MCS[e]
Experiment	10^3 ps[f]	$> 10^6$ ps[g]

separation of time sales, where the density ρ equilibrates on time scales that are at least two orders of magnitude shorter than the time scales on which Q_6 fluctuates. Such separations of time scales are typical in natural and computer simulated supercooled water. (See Table 3.1)

Due to the separation in time scales, relaxation of $P_{\rm ne}(Q_6,t)$ can be estimated by assuming density ρ is always in equilibrium with the current value of Q_6. An appropriate Fokker-Planck equation[26] is therefore

$$\frac{\partial P_{\rm ne}(Q_6,t)}{\partial t} = D\frac{\partial}{\partial Q_6}\left(\frac{\partial \beta F(Q_6)}{\partial Q_6} + \frac{\partial}{\partial Q_6}\right) P_{\rm ne}(Q_6,t)\,. \tag{3.33}$$

The quantity $F(Q_6)$ is the equilibrium free energy for the crystal-order parameter, $D = \langle(\delta Q_6)^2\rangle/\tau_{Q_6}$ is the diffusion constant projected along the Q_6 direction. The quantity $\langle(\delta Q_6)^2\rangle \approx 0.01$ is the mean-square fluctuation of Q_6 in the liquid basin for the 216-molecule system considered in Fig. 3.9a. The long-time limit is set by the diffusion constant,

$$\lim_{Dt\to\infty} P_{\rm ne}(Q_6,t) \propto \exp[-\beta F(Q_6)]. \tag{3.34}$$

For quantitative treatments of the ultimate equilibration (i.e., of the final stages of crystal coarsening), Eq. 3.33 could be generalized to include Q_6-dependence and memory effects in D. Such generalization could account for the complexity of pathways by which multiple ordered domains reorganize and connect and would be expected to increase the timescales for equilibration. These refinements are unnecessary for the current analysis of early-stage coarsening, where Q_6 does not progress far from its values in the liquid.

We have integrated Eq. 3.33 using a first-order finite difference approach with a small enough discretization of Q_6 and time to ensure numerical stability. [92] Figure 3.9a shows how the distribution evolves in time from an initial Gaussian distribution centered in the liquid region of Q_6. What is notable is that the relaxation to equilibrium takes orders magnitude longer than the basic timescale, τ_{Q_6}.

With this time evolved probability distribution, we have used Eq. 3.30 to estimate a non-equilibrium joint free energy,

$$F_{\rm ne}(\rho,Q_6,t) = -k_{\rm B}T\,\ln\left[P(\rho|Q_6)\,P_{\rm ne}(Q_6,t)\right]. \tag{3.35}$$

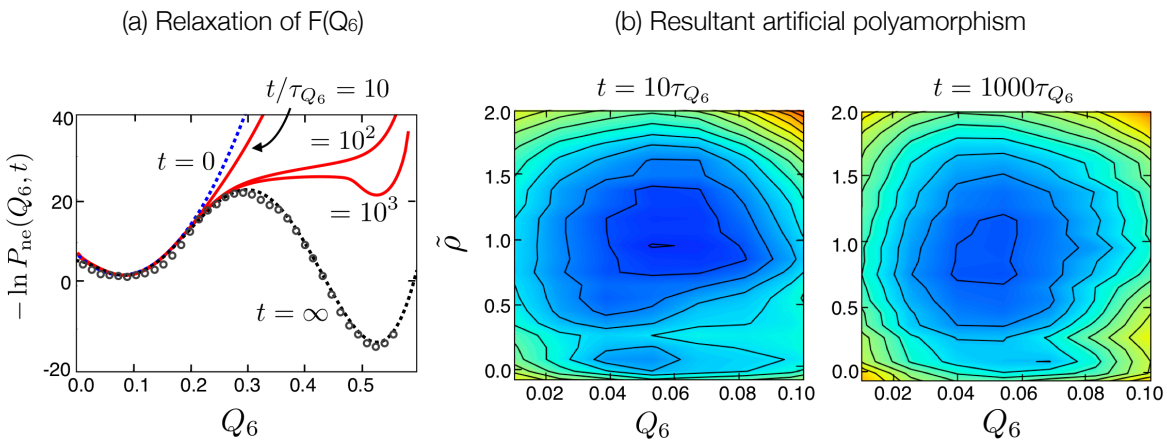

Figure 3.9: Slow relaxation behavior and its consequences for free energy calculations. (a) Negative logarithm of the non-equilibrium distribution for crystal order, Q_6, as it relaxes from the liquid state. It is computed from the Fokker-Planck equation with the free energy surface given in Fig. 3.8 under the assumption that the density, ρ, remains at equilibrium with the instantaneous value of Q_6. (b) Non-equilibrium pseudo free energy surfaces computed from Eq. 3.30 at two intermediate stages of relaxation, $t = 10\,\tau_{Q_6}$ and $t = 1,000\,\tau_{Q_6}$. The unit of time, τ_{Q_6}, is the autocorrelation time for Q_6 fluctuations in the liquid basin (i.e., at small Q_6). The reduced density is $\tilde{\rho} = (\rho - \rho_{\rm xtl})/\Delta\rho$, where $\rho_{\rm xtl}$ is the mean density of the crystal basin (i.e., at large Q_6), and $\Delta\rho$ is the difference between the mean densities of the liquid and crystal basins. Contour lines are separated by 1 $k_{\rm B}T$ and statistical uncertainties are about 1 $k_{\rm B}T$. This figure is adapted from Ref. [136].

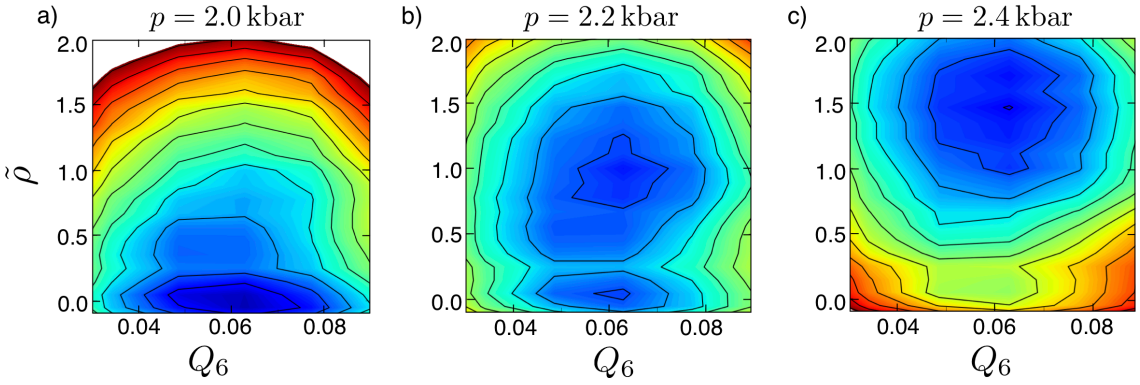

Figure 3.10: Non-equilibrium pseudo free energy surfaces, $F_{\rm ne}(\rho, Q_6, t)$, at three different pressures, illustrating how artificial polyamorphism arises as a finite-time effect. All three surfaces are evaluated by propagating from an initial liquid distribution for a time $t = 10\tau_{Q_6}$. Computed as in Fig. 3.9, with the same notation as used in that figure. Contour lines are separated by 1 $k_{\rm B}T$ and statistical uncertainties are about 1 $k_{\rm B}T$. This figure is taken from Ref. [136].

This pseudo free energy function for two intermediate times is shown in Fig. 3.9b. At the first of these intermediate times, $t = 10\,\tau_{Q_6}$, $F_{\rm ne}(\rho, Q_6, t)$ exhibits two minima at low values of Q_6, and these minima are separated by a small barrier of a few $k_{\rm B}T$. The low density basin is centered at the mean density of the crystal, and the high density basin is centered at the mean density of the liquid. We use the reduced density variable, $\tilde{\rho} = (\rho - \rho_{\rm xtl})/\Delta\rho$, to emphasize these connections to the crystal and liquid basins.

This behavior shown in Fig. 3.9b is precisely the behavior found in Refs. [144, 145, 181, 196] – both the bi-stability and the length of time allowed for equilibration. Those workers find $\tau_{Q_6} \approx 10^8$ Monte Carlo sweeps, and they use 10^9 sweeps to estimate free energies. The low-density liquid minimum eventually disappears, but the time scale for that to occur is orders of magnitude longer than considered in Refs. [144, 145, 181, 196].

To further illustrate the connection between the non-equilibrium calculation shown here with the finite-time sampling results of Ref. [144, 145, 181, 196], Fig. 3.10 shows the effects of pressure variation on the pseudo free energy surfaces. Upon re-weighting to lower pressure, Fig. 3.10a, or to higher pressure, Fig. 3.10c, one of the disordered minima disappears. The specific dependence on re-weighting and the relative locations of the minima are also consistent with the results of Refs. [144, 145, 181, 196]. We have thus reproduced the principal results of those papers by identifying the limited time over which the system was allowed to equilibrate. See for example, Fig. 2 of Ref. [144], as we have purposely used a similar color code in our Fig. 3.10 to emphasize the similarities of our finite-time results with the free energies reported in that paper.

The analysis uses the Fokker-Planck equation in order to elucidate the generality of the phenomena. However, for completeness, these calculations have been also done using another

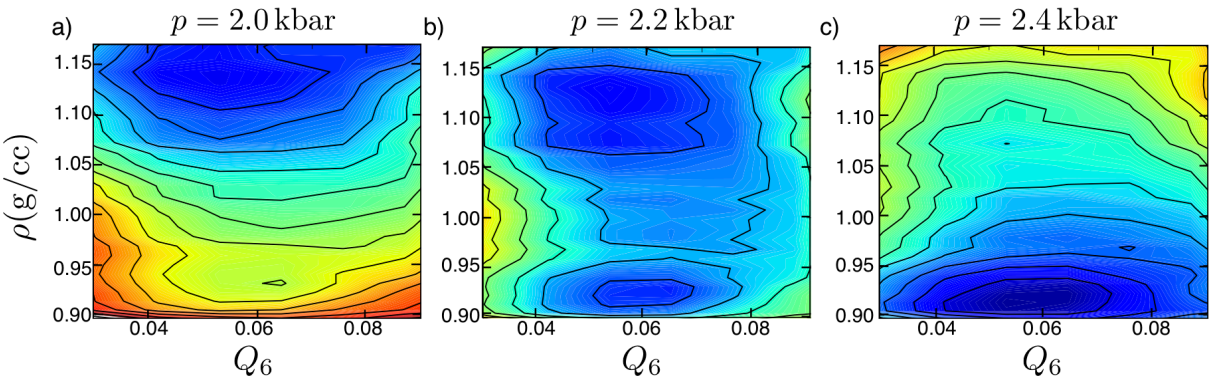

Figure 3.11: Nonequilibrium pseudo free energy surfaces, $F_{\rm ne}(\rho, Q_6, t)$, at three different pressures, illustrating how artificial polyamorphism arises as a finite-time effect. All three surfaces are evaluated by propagating from an initial liquid distribution for a time $t = 10\tau_{Q_6}$. Computed for the ST2b model from the Fokker-Planck analysis with the underlying reversible free energy surface shown in Fig. 3.14b. The appearance of artificial polyamorphism is like that found in Ref. [144] for similar conditions. The time $t = 10\,\tau_{Q_6}$ corresponds to the time used for averaging in Ref. [144]. Contour lines are separated by 1 $k_{\rm B}T$ and statistical uncertainties are less than 1 $k_{\rm B}T$. The correct, reversible free energy surface for $p = 2.2$ kbar is shown in Fig. 3.14b. This figure is adapted from Ref. [136].

variant of the ST2 model, ST2b, at $T = 230$ K with $N = 216$ and pressures ranging from 2 kbar to 2.4 kbar. Section 3.5.1 for a detailed discussion of the differences. These are precisely the conditions and model considered in Ref. [144]. The results are shown in Fig. 3.11. The theoretical results agree with those found in Ref. [144], thus indicating that the free energies reported in that work suffer from finite-time effects.

In addition to the Fokker-Plank analysis, we have computed $P_{\rm ne}(Q_6, t)$ directly from a molecular simulation of the ST2b model, starting from an ensemble of liquid configurations and running for $t_{\rm sim} = 10\tau_{Q_6}$. We have then multiplied that non-equilibrium distribution with the equilibrium $P(\rho|Q_6)$ obtained from the reversible free energy in Fig. 3.14b according to Eq. 3.30. The results are shown in Fig. 3.12. Again, behavior like that reported in Ref. [144] is obtained, thus indicating that the results of that paper suffer from finite-time effects.

3.4.3 Phase flipping

The time-dependent pseudo free energies illustrated above also shed light on previous reports of phase flipping between two seemingly distinct liquids.[109, 144] In those reports, large transient density fluctuations occur intermittently between smaller amplitude motion while the system is globally liquid-like. This behavior is expected for trajectories of ρ when driven by the pseudo free energy surface graphed in Fig. 3.10b. Indeed, Fig. 3.13 shows representative trajectories obtained by running over-damped Langevin dynamics[26] on the free energy surface of Fig. 3.9a with the time-scale separation $\tau_{Q_6} = 100\,\tau_\rho$. The trajectories

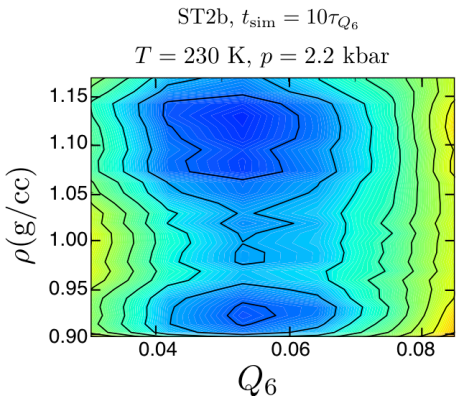

Figure 3.12: Nonequilibrium pseudo free energy surfaces, $F_{\rm ne}(\rho, Q_6, t)$ illustrating how artificial polyamorphism arises as a finite-time effect. The correct reversible surface is shown in Fig. 3.14b. The incorrect surface shown here is computed for the ST2b model from a non equilibrium distribution for Q_6, where the distribution is obtained from simulations initiated in the liquid basin and propagated for a time $10\,\tau_{Q_6}$. The surface shows the appearance of artificial polyamorphism like that found in Ref. [144] for similar conditions. The simulation time $t_{\rm sim} = 10\,\tau_{Q_6}$ corresponds to the time used for averaging in Ref. [144]. Contour lines are separated by 1 $k_{\rm B}T$ and statistical uncertainties are less than 1 $k_{\rm B}T$. This figure is adapted from Ref. [136].

were initiated in the liquid basin at temperature $T = 235$ K. [2] The trajectories look exactly like those presented as phase flipping in Refs. [109, 144]. (The structural relaxation time in those studies is $\tau_\rho \gtrsim 1$ ns.)

Thus, so-called "phase flipping" is not a flipping between distinct liquid phases. It emerges in a single liquid phase because there exists a separation of timescales between density fluctuations and long range order fluctuations. Large density fluctuations occur as the system is attempting to crystallize, accompanied by the formation of sub-critical nuclei formation that shrink and cause further large density fluctuations.

This behavior is transient, as the pseudo free energy is ever-changing with time. An analysis of time series would elucidate this nature of the phenomenon. Specifically, the mean transition time will show a dependence on trajectory length, reflecting the non-stationarity of the system. Consequently, the distribution of transition times will deviate from simple Poisson statistics. Those offering phase flipping as evidence for two distinct liquids have not provided a quantitative analysis supporting such statistics. Rather, studies illustrated in Ref. [108] catalogue many independent trajectories some of which exhibit anomalously long quiescent periods between transitions lasting several times 100 ns $\approx 100\,\tau_\rho$. Data supplied for the ST2 model in Ref. [108] also illustrate that phase flipping occurs at pressures far below

[2] The stochastic steps in the Langevin dynamics for Q_6 use the diffusion constant D and time scale τ_{Q_6} specified for the corresponding Fokker-Planck Eq. 3.33. The stochastic steps for ρ use the diffusion constant $D_\rho = \langle(\delta\rho)^2\rangle/\tau_\rho$, where $\tau_\rho = 10^{-2} \times \tau_{Q_6}$, and $\langle(\delta\rho)^2\rangle \approx 0.05(\text{g/cc})^2$ is the mean-square fluctuation of density in the liquid basin of Fig. 3.9a.

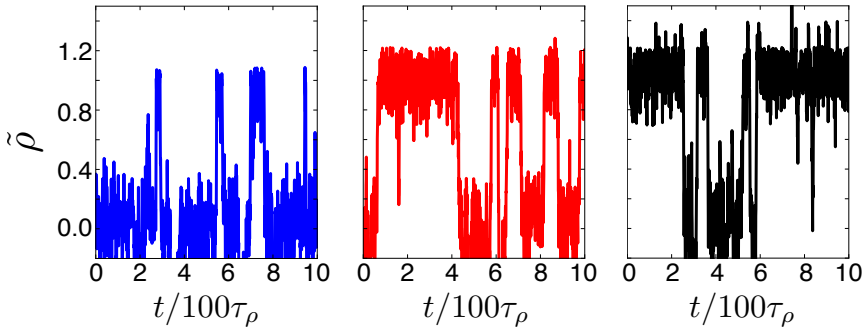

Figure 3.13: Trajectories propagated with over-damped Langevin dynamics on the free energy surface pictured in Fig. 3.9a. The trajectories are initiated in the liquid basin and run for insufficient times to pass to Q_6 values larger than 0.3. The trajectories thus illustrate early stages of coarsening in the ST2a model at $T = 235$ K and $p = 2.2$ kbar. This figure is adapted from Ref. [136].

a proposed critical pressure, in apparent contradiction to the authors' claims that a critical point exists. The model behavior we discuss is a consequence of liquid-crystal coexistence, which by symmetry must not have a critical point and would explain the insensitivity of this behavior to pressure.

The only quantitive analysis provided in studies of phase flipping is the calculation of bi-modal density distributions, which are then fit to a universal Ising form, from which supposed critical parameters are extracted[109, 110]. The barostat used in those simulations is well known to not reproduce correct equilibrium density fluctuations,[89] making such a calculation difficult to interpret.

3.5 Phase behavior in other models

The previous section emphasizes the significance of a time-scale separation and the pitfalls for simulation that result from it. In this section, we use the same robust procedures that can overcome these problems, and we apply these procedures to other models and different phase points than considered previously. In light of recent work,[144, 145, 181, 196] we analyze how these equilibrium surfaces are affected by changes in model parameters and boundary conditions. We also consider a more quantitative model of water, the TIP4P/2005 model, and a model of Silicon, the SW model, to illustrate the generality of these findings.

3.5.1 Results for different variants of the ST2 model

Figure 3.14 shows free energy surfaces we have computed for three different versions of the ST2 model, variants that differ only in the manner by which long-ranged forces are computed. The phase behaviors in each case are similar, with one liquid basin and one crystal basin. Indeed, the *existence* of singularities in a partition fucntion is usually not sensitive

to subtle changes in potential energy function. This is true because the existence of a phase transition is mostly dictated by dimensionality and the general form and symmetry of the potential energy function [73]. In contrast, the *locations* of the singularities (e.g., temperatures and pressures of coexistence) are often sensitive to subtle changes[200]. Recent reports on variants of the ST2 model [144, 181] have hypothesized that differences in electrostatic boundary condition and non-electrostatic cutoff parameters can account for why our previously published results [133] found no liquid-liquid phase transition where others suggest it does exist. The results shown in Fig. 3.14 challenge this hypothesis.

The ST2a model. Panel (a) is for the model we used in Ref. [133], but at a temperature slightly lower than that considered in our earlier work. Our prior reported calculations were for $T = 235$ K, whereas Fig. 3.14a is for $T = 230$ K. The results for $T = 230$ K differ very little from those at $T = 235$ K. The model employs a modification of the original ST2 potential for water[211]. The modification includes forces from the long ranged electrostatics that were neglected in the original model. The inclusion uses an Ewald summation with conducting boundary conditions. The non-electrostatic Lennard-Jones potential is truncated and shifted at 7.5Å. This model was referred to as the mST2 model in Ref. [133]. Here, we identify it as the ST2a model, and distinguish it from a modified ST2 model with insulating boundary conditions.

The ST2b model. Panel (b) shows the free energy we have computed at the same temperature as considered in Panel (a), but now with insulating boundary conditions. In addition, a tail correction has been added to account for the portion of the Lennard-Jones potential neglected in truncation. Panel (b), therefore, shows our results for the equilibrated free energy surface of precisely the variant of the ST2 model used in Refs. [144, 145]. Here, we identify it as the ST2b model. As in Panel (a), the surface exhibits a single crystal basin at large Q_6 and a single liquid basin at small Q_6. The only significant differences between the two surfaces in Panels (a) and (b) are in the location of the liquid basin and the relative stability of the crystal. The density for the liquid basin in Panel (b) is higher than that in Panel (a), and the crystal stability in Panel (b) is reduced from that in Panel (a). Reasons for these differences will be discussed shortly.

The ST2c model. Finally, Panel (c) shows our results for the ST2 model using the variant described in Refs. [181, 196], which we identify as the ST2c model. It uses a reaction-field treatment of electrostatic interactions and a Lennard-Jones tail-correction. This Panel (c), plus Panels (a) and (b) show that small changes in temperature and variation in boundary condition have only marginal effects on the phase behavior of ST2 water.

When effects of changing potential energy or temperature are marginal, the nature of those effects are easily interpreted and computed with the identity[28]

$$\Delta F(\rho, Q_6) = -k_{\rm B} \ln\langle \exp[-\Delta\mathcal{H}/k_{\rm B}T]\rangle_{\rho,Q_6} . \tag{3.36}$$

Here, $\Delta F(\rho, Q_6)$ is the change in free energy surface due to changing the temperature or Hamiltonian by the amount $\Delta\mathcal{H}/k_{\rm B}T$. The angle brackets refer to the ensemble average over configurations with the original temperature and Hamiltonian, and with the order parameters fixed at the values indicated by the subscripts. When $\Delta\mathcal{H}/k_{\rm B}T$ is large, or when its effects

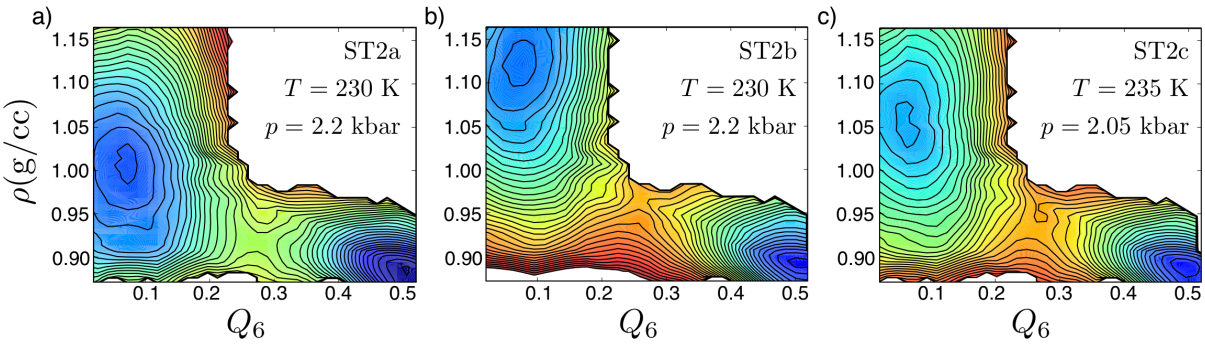

Figure 3.14: Free energy surfaces, $F(\rho, Q_6; p, T)$, for three variants of the ST2 model at temperatures where others report evidence of liquid-liquid coexistence for the ST2 model. Possibilities of two-phase coexistence require changes in convexity, as re-weighting through Eq. 3.21 in that case can produce two basins of equal statistical weight. A coexistence pressure is then the value $p + \Delta p$ at which there is equal statistical weight. For the three variants considered, the only changes in convexity are associated with coexistence between a liquid (low Q_6) and a crystal (high Q_6). a) Free energy for the ST2a variant at $T = 230$ K and $p = 2.2$ kbar, with $N = 216$. b) Free energy for the ST2b variant at $T = 230$ K and $p = 2.2$ kbar with $N = 216$. c) Free energy for the ST2c variant at $T = 235$ K and $p = 2.05$ kbar with $N = 216$. See text for definitions of the different variants. Contour lines are separated by $1.5k_B$ and statistical errors over the surfaces average to less then 1 k_B. Quantitative features will change with system size. For example, as N grows, the mean value of Q_6 in the liquid basin will vanish as $1/N^{1/2}$, while in the crystal basin it will remain finite. This figure is adapted from Ref. [136].

are large, calculations with this formula will yield poor estimates of $\Delta F(\rho, Q_6)$ because exponential averages are slowly converging. [178] On the other hand, if $\Delta\mathcal{H}$ is small, or if its effects are small, averages converge reasonably quickly. In that case, Eq. (4) becomes a computationally convenient estimator. We have checked explicitly that this measure of marginal behavior is satisfied with respect to the above cited variations for the ST2 model at $T \approx 230$ K and $N \approx 200$. For example, the typical size of $\Delta\mathcal{H}/k_{\mathrm{B}}T$ for the comparison between Figs. 3.9a and 3.14b is 30% of the root-mean-square fluctuations in the net energy per $k_{\mathrm{B}}T$.

Explanation for the model differences The conducting boundary condition for Ewald sums, used for Fig. 3.14a, strictly cancels electrostatic surface potentials in the energy function. These surface potentials arise from instantaneous polarization fluctuations and transient dipole moments of the total system. The conducting boundary condition is generally chosen for use with molecular dynamics simulations because the alternative, insulating boundary condition, typically introduces discontinuities in the potential energy whenever a molecule crosses the the periodic boundary. [85] For a dipole disordered system, like liquid water and ice Ih, this boundary condition should be irrelevant as its energy will average to zero.

Assuming the Ewald parameters are chosen such that energy is well converged in both cases, the pressure of the system with insulating boundary conditions is larger than that with conducting boundary conditions by an amount Δp_{surf}. This pressure difference is given by[201]

$$\Delta p_{\mathrm{surf}} = \frac{2\pi\,(2\epsilon - 1)}{3\,(2\epsilon + 1)} \frac{M^2}{V^2}\,. \tag{3.37}$$

Here, ϵ is the dielectric constant of the surrounding medium, M is the total system dipole, and V is the volume. For a disordered system, the average M is zero in the thermodynamic limit, and M^2 fluctuates with values that are extensive in system size. Accordingly, Eq. 5 shows that this strictly positive contribution to the pressure vanishes as $\sim 1/V$. More discussion on subtleties involved in the implementation of the Ewald summation is given in Appendix A.

The non-electrostatic part of the ST2 potential is a 6-12 Lennard-Jones interaction. The simulations yielding Panel (a) truncate and shift this potential to zero beyond the oxygen-oxygen distance $r_{\mathrm{c}} = 7.5$ Å. This truncation produces a net potential energy that is slightly higher than that with no truncation. An accurate correction to the potential energy that accounts for the neglected tail is the mean-field estimate $-16\pi\epsilon_{\mathrm{LJ}}\sigma^6\rho N/3r_{\mathrm{c}}^3$, where the Lennard-Jones energy and length parameters are ϵ_{LJ} and σ, respectively. Differentiation with respect to volume thus gives a tail correction for the pressure,[210]

$$\Delta p_{\mathrm{tail}} = -\frac{16\pi\epsilon_{\mathrm{LJ}}\sigma^6\rho^2}{3r_{\mathrm{c}}^3}\,. \tag{3.38}$$

Thus, while the two simulations yielding Panels (a) and (b) in Fig. 3.9 are both carried out at $p = 2.2$ kbar, the effective pressure of the former differs from the latter by the amount

$\Delta p = \Delta p_{\rm surf} + \Delta p_{\rm tail}$, so that the mean density of the latter will be higher than that of the former by the amount

$$\Delta\rho \approx \Delta p \left[\frac{N}{k_{\rm B}} \frac{\langle(\delta\rho)^2\rangle}{\langle\rho\rangle^2} \right] , \tag{3.39}$$

where the term in square brackets is the compressibility, $(\partial\langle\rho\rangle/\partial p)_T$. Evaluating Δp from the formulas above for the surface and tail corrections, and estimating the mean-square density fluctuations from the widths of the liquid basins in the free energy surfaces, we find $\Delta\rho \approx 0.1$ g/cc, in harmony with the differences seen in Panels (a) and (b) of Fig. 3.14. The system is much less compressible in the crystal basin than in the liquid basin (i.e., the density fluctuations are smaller in the crystal than in the liquid), and as a result, the shift in position of that basin between Panels (a) and (b) is much less than that found for the liquid.

The relative stability of the crystal basin in Panels (b) is notably less than that in Panel (a). This juxtaposition is another manifestation of the fact that with a given external pressure p, the effective pressure of the ST2b model is higher than that of the ST2a model.

In the reaction-field treatment used to compute $F(\rho, Q_6)$ of Fig. 3.14c, Coulomb interactions are summed directly up to a cutoff distance, $R_{\rm c}$, and contributions from larger separations are approximated as those from an ideal polarizable continuum. With this approximation, and assuming the medium has a large dielectric constant, the term

$$\Delta U_{\rm E} = -\frac{1}{2} \sum_{i=1}^{N} \sum_{j=1}^{N} \frac{\mu_i \cdot \mu_j}{R_{\rm c}^3} \left[1 - \Theta\left(r_{ij} - R_{\rm c}\right)\right] , \tag{3.40}$$

must be added to the potential energy evaluated with the truncated direct Coulomb sums. Here, μ_i is the dipole of molecule i, r_{ij} is the distance between molecules i and j, and the Θ-function is unity for positive arguments and zero for negative arguments. This reaction-field approximation is reasonable for a homogeneous system,[208] and the asymptotic large dielectric assumption is isomorphic to the conducting boundary condition used with Ewald sums to construct Panel (a). While, the potential energy computed with a reaction field method is not guaranteed to be the same as that computed by an Ewald summation, judicious choice of cutoff in this instance results in reasonable agreement. Indeed, there is closer correspondence between Figs. 3.14a, c than between Figs. 3.14a,b.

Global order contraction Here, we explicitly demonstrate the importance of Q_6 for analyzing phase behavior of supercooled water by showing the effects of controlling the range of accessible Q_6 fluctuations. In particular, we define a contraction of a constrained free energy,

$$\beta\tilde{F}(\rho; Q_6^{\rm max}) = -\ln\left(\int_0^{Q_6^{\rm max}} {\rm d}Q_6 \, e^{-\beta F(\rho, Q_6)} \right) . \tag{3.41}$$

We compute these functions from our estimates of the unconstrained reversible free energy surface. Functions so obtained are shown in Fig. 3.15a. The unconstrained free energy from which they are derived is $F(\rho, Q_6)$ graphed in Fig. 3.9a and re-weighted to the pressure 2.7

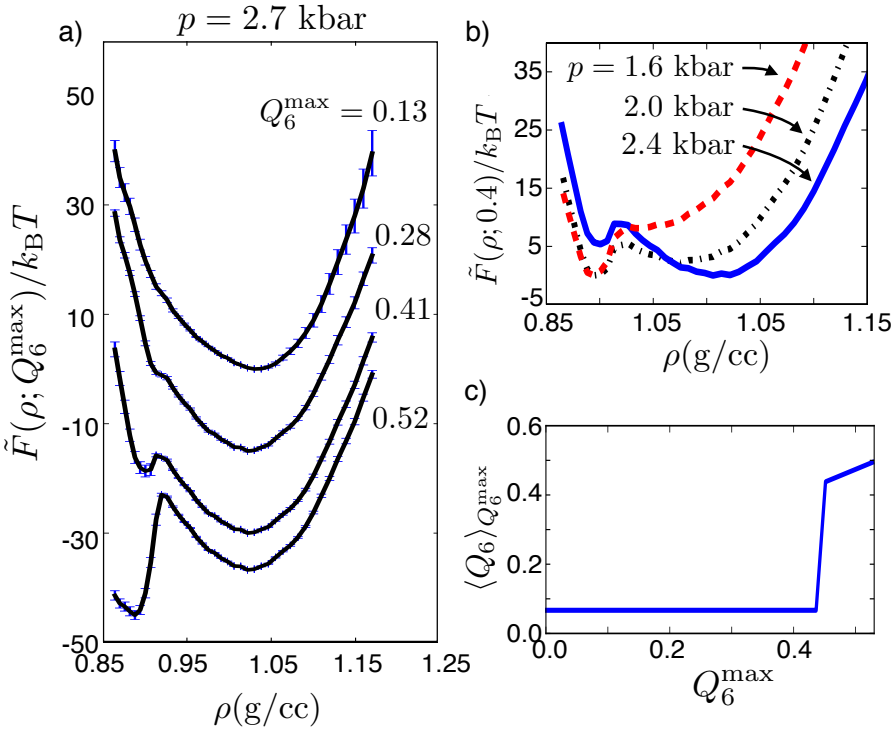

Figure 3.15: Free energy functions and mean order parameters computed for the ST2a model at $T = 235$ K, illustrating artificial polyamorphism arising from incomplete knowledge of Q_6-dependence in $F(\rho, Q_6)$. (a) The restricted contracted free energy function, $\tilde{F}(\rho; Q_6^{\max})$, for $N = 216$ at several indicated choices of $Q_6^{\max}$. The functions are computed from integrating the reversible free energy function in Fig. 3.9a re-weighted to pressure $p = 2.7$ kbar. Error bars indicate one standard deviation. Higher or lower pressures shift the free energy to favor the liquid or crystal, respectively. See Eq. 3.21. (b) Re-weighted contracted free energy function, with $Q_6^{\max} = 0.4$, as if the re-weighting coincided with a Maxwell construction for two coexisting liquid phases. (c) The mean value of Q_6 as a function of the maximum order-parameter value for $T = 235$ K and $p = 2.7$ kbar. This figure is adapted from Ref. [136].

kbar. It is the reversible free energy surface for the ST2a model at temperature $T = 235\,\mathrm{K}$ and at a pressure that puts the system close to coexistence between the liquid and the crystal. At lower pressures, the liquid will be supercooled; at higher pressures, the liquid will be stable with respect to the crystal. The surfaces for those different pressures are obtained from the pictured surface by applying Eq. 3.21.

An upper limit of $Q_6^{\max} = 0.13$ encompasses the liquid basin. The contracted free energy in that case is unimodal, and it does not exhibit statistically meaningful changes in convexity. That is to say, no re-weighting with Eq. 3.21 in that case will produce bi-modality. Thus, there is not a second liquid for all densities (and corresponding pressures) in the range considered.

Notice, however, that this contracted free energy function is skewed in a fashion where fluctuations towards low density are more probable than fluctuations towards higher density. In the limit of large system size, fluctuations within stable or metastable basins are Gaussian. The skewed behavior is therefore a finite system-size effect. Its physical origin can be resolved by increasing $Q_6^{\max}$. For $Q_6^{\max} = 0.25$, a shoulder and change in convexity appears. For larger values of $Q_6^{\max}$, there is systematic growth of the shoulder into a basin. This low density basin is the crystal. The mean value of Q_6 as a function of $Q_6^{\max}$, $\langle Q_6 \rangle_{Q_6^{\max}}$, is shown in Fig. 3.15c. This mean value remains at its liquid state value for $Q_6^{\max} < 0.45$. Thus, by sampling the full surface pictured in Fig. 3.9a, it is possible to identify the low-density basin as the crystal phase.

When limiting the range of Q_6 to $Q_6^{\max} < 0.45$, the features shown in Fig. 3.15 could be easily misinterpreted as indicative of liquid-liquid coexistence. Indeed, by applying an external pressure to re-weight the curves in Fig. 3.15a, with Eq. 3.21 as if $\tilde{F}(\rho, Q_6^{\max})$ was an equilibrium free energy for $0.13 < Q_6^{\max} < 0.43$, a bistable density distribution can be obtained with a low mean value of Q_6. This type of construction is illustrated in Panel (b) of Fig. 3.15. The bi-stability of precisely the sort reported in Refs. [144, 145, 181, 196] is thereby found. But contrary to the interpretation expressed in Ref. [181], the behavior is not reflective of liquid-liquid transition. Rather, the unconstrained free energy shows that the appearance of convexity loss is associated with moving towards and then over the barrier separating liquid and crystal basins.

As the geometry of the total $F(\rho, Q_6)$ changes with system size, N, the re-weighting (i.e., pseudo Maxwell construction) illustrated in Panel (b) and alluded to in Ref. [181] will depend upon system size in ways that are inconsistent with two-phase coexistence. The free energy barrier separating basins of truly coexisting phases scales as $N^{2/3}$. But the low density phase with Q_6 confined to low values cannot equilibrate and thus cannot coexist.

Pressure dependence of $F(\rho, Q_6)$ for variants of the ST2 model References [144] and [181] suggest that the analysis of the ST2a model [133] overlooks a liquid-liquid transition because it examines a pressure that lies outside a hypothesized spinodal region. We examine the validity of this suggestion with Fig. 3.16. This figure shows the free energy surfaces at different pressures for the three variants of the ST2 considered in the main text. The pressure variations are constructed by applying Eq. 3.21 to the surfaces graphed in Fig. 3.14. What is found in each case is that pressures higher than those considered in Fig. 3.14 shift

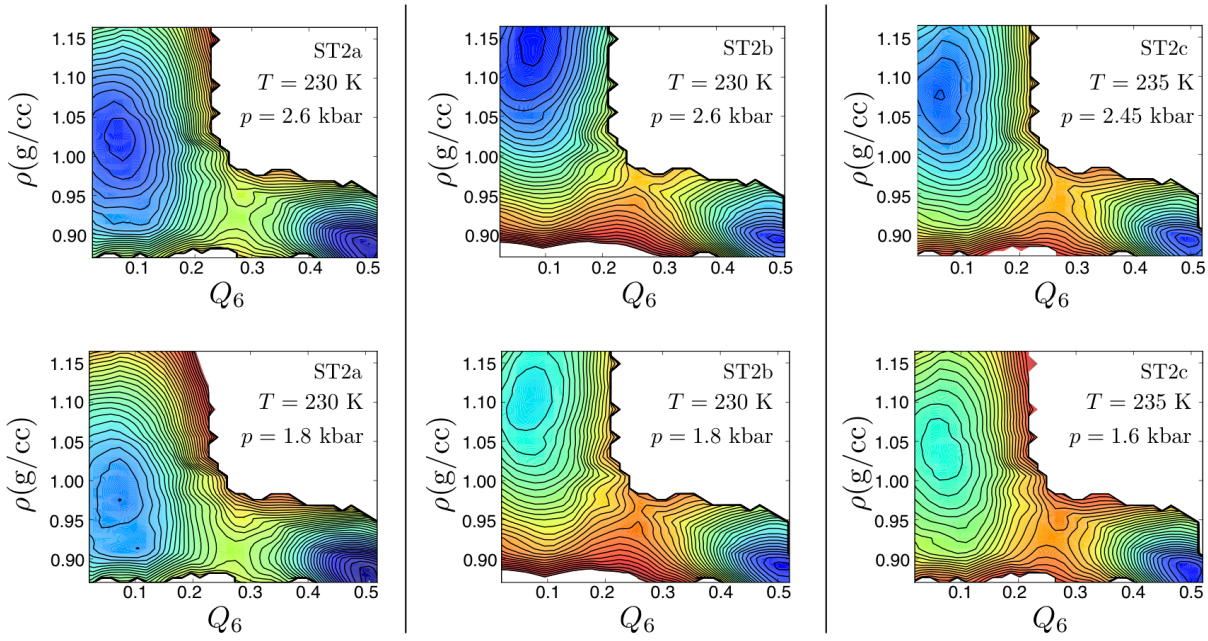

Figure 3.16: Pressure variation of free energy surfaces, $F(\rho, Q_6; p, T)$, for three variants of the ST2 model at temperatures where others report evidence of liquid-liquid coexistence for the ST2 model. Surfaces at intermediate pressures are shown in Fig. 3.14. Contour line spacing and system size are the same as those in Fig. 3.14. This figure is adapted from Ref. [136].

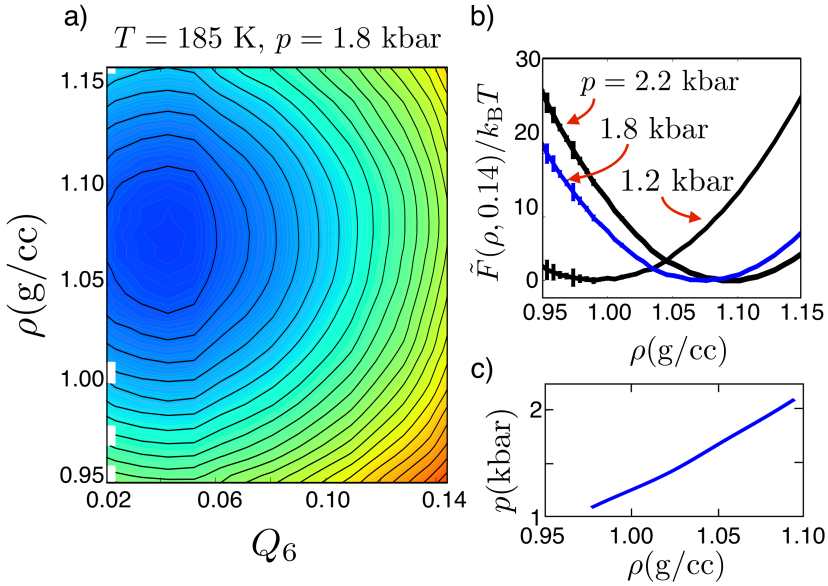

Figure 3.17: Reversible free energies and equation of state for liquid TIP4P/2005 at $T = 185$K and $N = 216$ for pressures between 1 and 3 kbar. a) Free energy, $F(\rho, Q_6)$. Contour lines are separated by 1 k_BT and error estimates are less than 1 k_BT. b) Contracted free energy as a function of density when restricting Q_6 to the liquid basin, i.e., $Q_6 < 0.14$. c) Liquid phase equation of state accessible from the free energy surfaces shown in Panels (a) and (b). This figure is adapted from Ref. [136].

stability towards the liquid and increase density of the liquid, and pressures lower than those considered in Fig. 3.14 shift stability towards the crystal and decrease density of the liquid. Variation of pressure over the ranges considered by Refs. [144] and [181] does not lead to liquid bi-stability in the reversible behavior of the ST2 model. There is one liquid phase, and no liquid-liquid coexistence or spinodal.

3.5.2 Quantitative water model

The recently parameterized TIP4P/2005 water model[1] has had success in quantitatively reproducing many essential properties of water and ice, including the density versus temperature line at $p = 1$ bar. Previous studies have extrapolated equation of state data for this model to estimate the location of a putative liquid-liquid critical point and first order transition line[2]. Using free energy calculations we tested the validity of this extrapolation.

Figure 3.17 shows $F(\rho, Q_6)$ for TIP4P/2005 computed at $T = 185$K and $p = 1.8$ kbar for $N = 216$ molecules. Reference [2] estimates the location of the critical point to be $T = 193$ K and $p = 1.35$ kbar, as shown in Panels (b) and (c) of Fig. 3.17. The free energy in Fig. 3.17 is computed below this purported critical point temperature, yet the distribution is

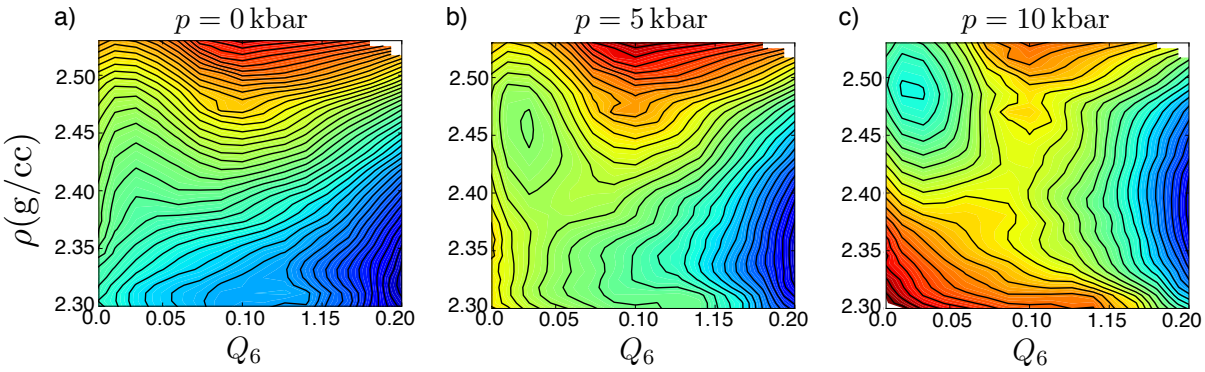

Figure 3.18: Reversible free energy, $F(\rho, Q_6)$, computed for the SW model for $N = 512$, $T = 1050$ K and three pressures. Contour lines are separated by 2 $k_B T$ and error estimates are less than 1 $k_B T$. This figure is adapted from Ref. [136].

clearly monostable at low values of Q_6. High values of Q_6 were sampled, but not shown for clarity. On re-weighting this free energy, Eq. 3.21, bi-stability does not appear throughout the pressure range, 1 kbar $< p <$ 3 kbar. We can conclude, therefore, that for this model of water, a second liquid does not exist at conditions studied. Here too, the putative liquid-liquid transition seems to be an artifact of finite-time sampling, reflecting a liquid-to-ice transition where coarsening is incomplete.

3.5.3 Model of silicon

We have also studied the behavior of the Stillinger-Weber (SW) model of silicon. This model has been the subject of numerous studies[13, 194, 222] that have used equation of state data to propose the existence of a second liquid phase. Using free energy methods, we can test this proposal by examining conditions below the putative liquid-liquid critical temperature.

Figures 3.18a-c shows $F(\rho, Q_6)$ calculation for a system of 512 particles at $T = 1050$ K and a range of pressures, $0 < p <$ 10 kbar. Based on the phase diagram proposed in Ref. [222], also calculated with 512 particles and citing agreement with Ref. [194], this temperature and pressure range should traverse the first-order liquid-liquid phase boundary. Rather than finding two liquid basins upon decreasing pressure, we find the system crosses the line of liquid stability, $T_s(p)$, for pressures lower than $p = 1$ kbar.

Put into context with our discussion in Sec. II, the geometry of the free energy in Fig. 3.18a illustrates how finite-time sampling can produce the illusion of liquid-liquid bistability. Specifically, the facile equilibration in density would result in an abrupt change between the liquid with density at $\rho = 2.45$ g/cc and an amorphous material with $\rho = 2.35$ g/cc, while over short timescales the slow diffusion in Q_6 would keep the value small. In fact this point was noted by the authors of Ref. [222] when they state that out of 10 to 50

trajectories, "Non-crystallizing samples (an average of 5) were run for up to 10 relaxation times when possible."

3.5.4 Summary of calculations on putative liquid-liquid transition

Table 3.2 summarizes all that is now known about the putative liquid-liquid transition in supercooled water and related systems. We see that the low-temperature behaviors of several different models of water-like liquids are similar. The reversible phase behavior in all cases is that of one liquid, a liquid that can coexist with and transform to a lower density ice-like phase. In all cases, the time scales for density fluctuations in the supercooled liquid are several orders of magnitude shorter than those for long-ranged order fluctuations, and both time scales are strongly temperature dependent.

These features lead to a rich non-equilibrium behavior, some of which we have illustrated here in our treatment of the early stages of coarsening, and previously in our treatment of confined supercooled water[134].This non-equilibrium behavior is clearly responsible for the numerous reports of polyamorphism in computer simulations of water, and it is likely important in processes that lead to the formation of glassy phases of water. While the former represent artifacts of finite-time sampling, the behaviors of glasses represent an important class of phenomena worthy of future study. Such far-from equilibrium behavior, is considered in Chapter 5.

Table 3.2: Summary of models and conditions considered in this and in previous studies

Model	AP[a] $(T/\mathrm{K}, p/\mathrm{kbar})$	FE[b] $(T/\mathrm{K}, p/\mathrm{kbar})$
mW	-	(160-300, 0-10.0)
ST2b	(242, 1.8)[c] (240, 1.8)[c] (238, 1.9)[c] (235, 2.0)[c d] (228, 2.2)[d] (224, 2.3)[d]	(230-240, 1.0-3.0)
ST2c	(245, 1.8)[d] (240, 2.0)[d] (235, 2.2)[d] (230, 2.4)[d]	(230-240, 1.0-3.0)
ST2a	-	(230-240, 1.0-3.0)
SW	(1070, 0.)[f] (950, 7.5)[f] (920, 11.3)[f]	(1050, 0-10.0)
TIP4P/2005	(195, 1.45)[g]	(180-190, 1.0-2.6)

[a] Conditions where artificial polyamorphism has been reported.
[b] Conditions where Q_6-equilibrated free energy calculations rule out a liquid-liquid transition.
[c] Short Grand Canonical simulations from Ref. [145], $N \approx 200$.
[d] Q_6-unequilibrated free energy calculations from Ref. [144], $N \approx 200$.
[e] Q_6-unequilibrated free energy calculations from Ref. [181], $N \approx 200$
[f] Short molecular dynamics trajectories from Ref. [222], $N = 512$.
[g] Short molecular dynamics trajectories from Ref. [2], $N = 500$.

The generic nature of what is found in so many models makes it seem unlikely that plausible models of water will exhibit liquid-liquid coexistence and a second low-temperature

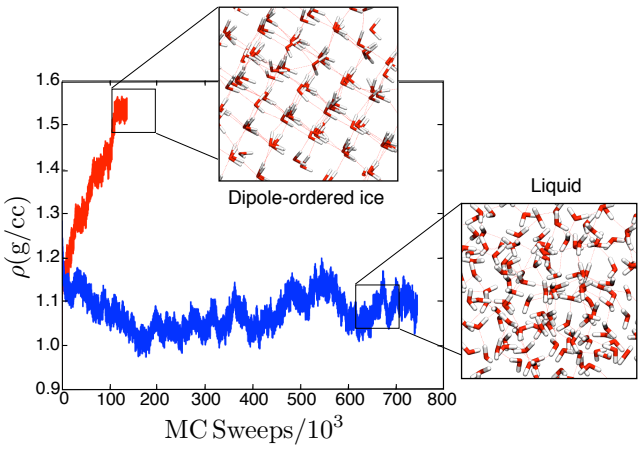

Figure 3.19: Time series illustrating how some choices of parameters for the Ewald sum in the ST2a model, which uses conducting boundary conditions, can lead to the formation of dipole ordered ice, while for other choices the liquid remains stable. See text. This figure is adapted from Ref. [136].

critical point. It also suggests that any model exhibiting a crystal phase with lower density than the liquid phase will also exhibit transient behavior that looks like polyamorphism when viewed on the time scales no longer than those of early-stage coarsening. The reason why this non-equilibrium behavior is not observed in a recent study of the SPC/E model[15] is because that study[71] quenches from temperatures significantly higher than T_s for that model.

The generic nature also implies that simplified models, like mW water, can reliably serve as useful descriptors of water. Hypotheses on the nature of low temperature water could often be studied in that way. Further, computational efforts that struggle with overcoming the separation of time scales inherent in low-temperature water could often be tested with such models. In our own work, it seems clear that errors in prior announcements of liquid-liquid transitions in supercooled water could have been detected by first examining the behavior of mW and SW models.

In documenting the necessity of attending to time scales and relaxation, we have outlined robust methods by which equilibration and reversibility can be achieved. There is clearly need for independent assessment of this growing body of work, which we look forward to seeing in the future.

3.6 Appendix: Common sources of error

3.6.1 Checks on coding and long-ranged force evaluations

While the chapter has postulated reasoned explanations for a discrepancy between the calculations of our pervious work and that of Ref. [144, 145, 181, 196], it does not address

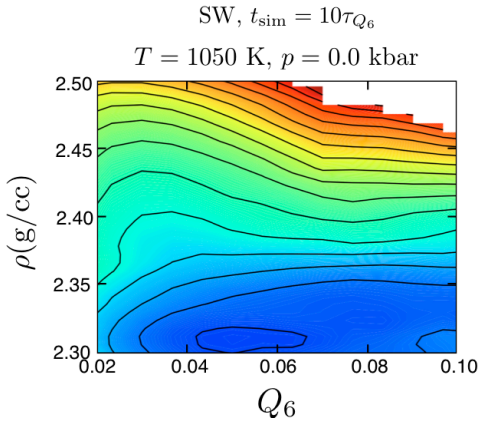

Figure 3.20: Nonequilibrium pseudo free energy surface for the SW model obtained with initial conditions from $T = 1100$ K and short equilibration times. The correct reversible surface is shown in Fig. 3.18a. Contour lines are separated by 3 $k_{\rm B}T$ and statistical uncertainties are about 1 $k_{\rm B}T$. This figure is adapted from Ref. [136].

the possibility of an undetermined error in implementation. To address this we have worked with the authors of Ref. [144] in exchanging data and molecular configurations.[3] The results of these studies were unambiguous: all parties were able to reproduce energy evaluations and standard mean and fluctuation quantities for the ST2b model. Specific statistical properties computed were the average density and compressibility for a system of 200 molecules at two state points, $T = 300$ K, $p = 1$ bar and $T = 235$ K, $p = 2.2$ kbar. Agreement between calculations was found to be within statistical error.[4] Moreover, tests were done swapping configurations of $N = 200$ molecules and obtaining independent evaluation of the energy and Q_6 values. These tests demonstrated that both groups were evaluating the same energy function and the same order parameter. Thus, an implementation error does not seem to be the root cause of this discrepancy.

As reported in Ref. [144], at specific regions of state space, simulations of a stable low temperature liquid are sensitive to details of the Ewald summation. Specifically, the authors of Ref. [144] found that with conducting boundary conditions and $N \approx 200$, liquid configurations spontaneously evolve into a dipole ordered form of ice VII when pressure is elevated and $T < 235$ K. While the authors of that study report they were unable to find Ewald parameters under conducting boundary conditions that did not display this pathological behavior, other studies applying this boundary condition with other electrostatic estimators have not found this same difficulty. For example, Ref. [181] employs a reaction-field treatment of electrostatic interactions with conducting boundary conditions.

By juggling the method of evaluating Ewald sums, we too have been able to reproduce the

[3] We are grateful to Pablo Debenedetti, Yang Liu, Jeremey Palmer, Athanassios Panagiotopoulos for sharing data and results with us.

[4] Y. Liu, Private communication 2012

pathological behavior reported in Ref. [144]. Two of our time series are shown in Fig. 3.19. Using hybrid MC dynamics for 216 molecules and conducting boundary conditions at $T = 228$ K and $p = 2.2$ kbar, we find that changes to the details of the Ewald parameters can result in either stable liquid behavior (blue curve), or spontaneous dipole ordering (red curve). In the stable liquid case, the Ewald parameters are chosen to accurately estimate the energy and forces of the long range part of the potential to 1 part in 10^4 using a standard error estimator and a spherical wave-vector cutoff. [119] In order to maintain this level of accuracy with a changing box size the parameters are updated over the course of the trajectory. In the unstable trajectory a cubic wave-vector cutoff is used, and the parameters are held fixed which reduces the accuracy of the potential estimate. There may be other ways to induce this pathological behavior, and these ways will depend upon the type of dynamics used. The principal point is that it is a finite-size effect that is sensitive to technical but unphysical details in implementing Ewald sums, and the effect can be avoided when sufficient care is applied to the algorithm.

3.6.2 Artifacts of un-equilibrated initial conditions

A somewhat different source of systematic error would be found in simulations that do not completely equilibrate from initial configurations taken from a higher temperature. For example, suppose one has established good equilibrium statistics for a system at temperature $T+\Delta T$, and then wishes to use configuration from that data to seed a free energy calculation at the temperature T. (One can consider parallel tempering[65] as one realization of this idea.) If at $T + \Delta T$ the system exists in a metastable liquid that becomes unstable at the lower temperature T, then configurations from the higher temperature will bias the statistics of the lower-temperature system for time scales short compared to average time for Q_6 to equilibrate (i.e., to leave the liquid region). Therefore, if the runs performed at temperature T are too short, a remnant of the meta-stable liquid basin at temperature $T+\Delta T$ will remain in the estimate of the free energy at temperature T. Figure 3.20 illustrates this problem for the case of the SW model.

The correct reversible free energy surface for the SW model at this condition is shown in Fig. 3.18c. In Fig. 3.20, we show an incorrect surface, which is obtained by using equilibrated data at temperature $T+\Delta T = 1100$ K as initial conditions, and then carrying out trajectories at $T = 1050$ K that run for only $t_{\rm sim} = 10\tau_{Q_6}$. Histograms produced by this procedure yield a pseudo free energy with a low-density liquid minimum at conditions where the actual liquid is thermodynamically unstable. Error estimates performed from the data collected in this way are very small, of the order of 1 $k_{\rm B}T$. These small error estimates reflect the highly correlated nature of the data. Changes of Q_6 are simply too slow to fully develop on the time scales probed.

Chapter 4

Theory for freezing and modulating ice interfaces

The Universe was brought into being in a less than fully formed state,
but was gifted with the capacity to transform itself from unformed matter
into a truly marvelous array of physical structures
- Saint Augustine [8]

In this chapter, we present a theory for the freezing transition and how it is modulated in the presence of different boundary conditions. The techniques employed are statistical field theory and with assumptions checked with molecular simulations. This chapter borrows largely from previously published work, *J. Chem. Phys.* 137, 045509.1-11 (2012). The principle phenomena presented is the generic existence of a premelting layer on the surface of ice. When the surface of ice is exposed to its vapor, the thickness of this disordered layer diverges as the melting temperature is approached. When the surface of ice is surrounded by disordered, hydrophilic confinement, the layer is stabilized creating a surface field that decreases the melting temperature as the characteristic lengthscale of the confinement decreases. Some of the chapter is devoted to the correspondence between molecular configurations and this coarse-grained effective field, other parts explain a number of experimental observations made previously.

4.1 Effective field theory

Our approach for analyzing the freezing transition and how it is modified in the presence of different boundary conditions begins by choosing a general phenomenological Hamiltonian for an order-parameter field parameterized with experimental data[128]. We then perform statistical mechanical calculations for the systems based upon that Hamiltonian, and we test assumptions in our analysis with atomistic simulations.

Specifically, we consider an energy functional or Hamiltonian for an order parameter distinguishing a liquid-like state from a crystal-like state. For bulk water, the two states

can be distinguished with a global order parameter like Steinhardt, Nelson and Ronchetti's Q_6 variable[207] . Complex fields for local order parameters could be used too. Broken symmetry for either Q_6 or a phase of a complex field does not occur for bounded systems like those we consider here. Therefore, we choose to distinguish liquid-like states from more ordered crystal-like states in terms of a local order field that is real. There are many such measures suitable for our purpose. As a specific example, our choice of order parameter could be

$$q(\mathbf{r}) + q_{\rm liq} = \sum_{i=1}^{N} q^{(i)}\, \delta(\mathbf{r} - \mathbf{r}_i)\,, \tag{4.1}$$

where $\mathbf{r}_i$ is the position of the ith oxygen among N water molecules, and

$$q^{(i)} = \frac{1}{4}\left(\sum_{m=-6}^{6} \Big| \sum_{j\in {\rm nn}(i)} q_{6m}^{(j)} \Big|^2 \right)^{1/2}\,, \tag{4.2}$$

with

$$q_{6m}^{(i)} = \frac{1}{4} \sum_{j\in {\rm nn}(i)} Y_{6m}(\phi_{ij}, \theta_{ij})\,. \tag{4.3}$$

Here, the sum over $j \in {\rm nn}(i)$ includes only the 4 nearest neighbor oxygens of the ith oxygen, and $Y_{6m}(\phi_{ij}, \theta_{ij})$ is the $\ell = 6, m$ spherical harmonic function associated with the angular coordinates of the vector $\mathbf{r}_i - \mathbf{r}_j$ joining molecules i and j measured with respect to an arbitrary external frame. This particular order parameter is large in proportion to the concentration of water molecules with neighbors having the same orientations of neighboring bonds as does the molecule itself. The quantity $q_{\rm liq}$ is its non-zero value for the bulk liquid. Past experience has shown that using the $\ell = 6$ spherical harmonics with 4 nearest neighbors is particularly useful for detailing local structure in water[133].

With this or some similar order-parameter field, we choose the energy to have the following form

$$\mathcal{H}[q(\mathbf{r})] = k_{\rm B}T \int_V {\rm d}\mathbf{r}\, \left[f(q(\mathbf{r})) + \frac{m}{2} |\nabla q(\mathbf{r})|^2 \right]\,, \tag{4.4}$$

$$f(q) = \frac{a}{2} q^2 - w q^3 + u q^4\,, \tag{4.5}$$

where $q(\mathbf{r})$ is the deviation of the order parameter field from its uniform value for bulk liquid water, and $a = a_o(T - T_{\rm s})$, with $T_{\rm s}$ being the temperature below which the bulk liquid is unstable. The parameters a_o, w, u, m and $T_{\rm s}$ are positive constants that depend upon pressure but are independent of temperature. They can be determined in terms of the measured properties of bulk water, all as specified below. The zero of energy is that of the disordered amorphous material.

The most significant feature of this phenomenological energy functional are the presence of only one field, specifically one that refers to local order, and that local molecular density is explicitly absent. We adopt this feature for two reasons. First, our prior simulation work

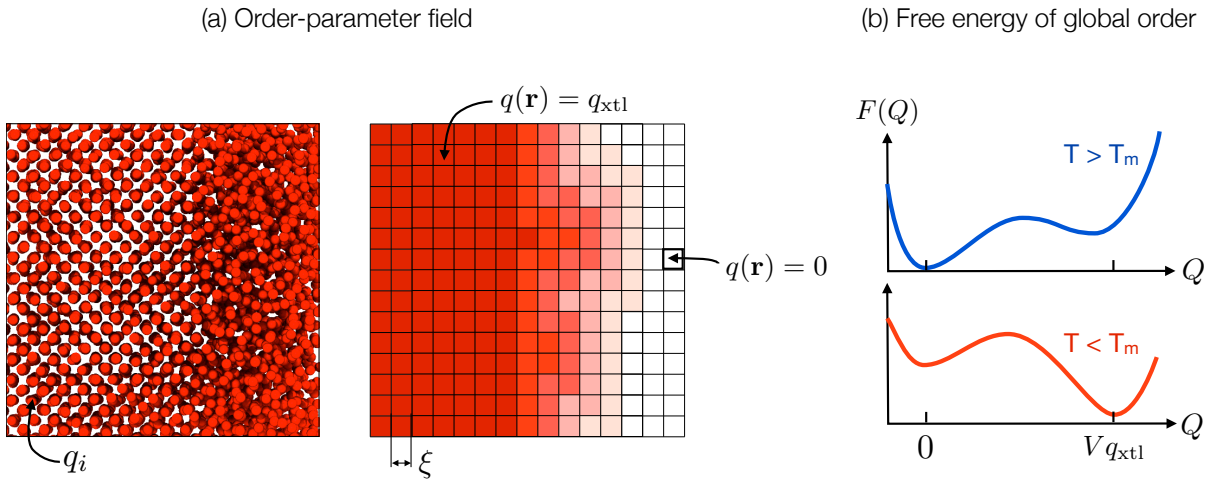

Figure 4.1: Coarse-grained order parameter field and its free energy. (left) A representative configuration of liquid-crystal coexistence taken from molecular dynamics simulations of the mW model of water. Red spheres locate the oxygen positions. (middle) A schematic of a typical coarse-grain continuous order parameter field, projected onto a square lattice. Moving from a representation based on molecular configurations (left panel) to a field (middle panel) involves coarse graining over a lengthscale ξ. The statisitics of this field can exhibit two-phase coexistence in the form of an order-disorder transition.(right) Schematic of the free energy functions for global order above and below the melting temperature. Below $T_{\rm m}$, the globally ordered phase has the lowest free energy and it stable. Above $T_{\rm m}$, the disordered phase is stable.

shown in the last chapter indicates that the reversible free energy function for condensed water has no more than one amorphous-state basin and no more than one crystal-state basin at the conditions we consider[133]. Second, we show below that we do not need to invoke the possibility of two liquid states to explain the experimental data we set out to interpret. In our picture, therefore, molecular density introduces no additional phase-transition-like behavior. To the extent our picture is accurate, integrating out density therefore affects only the values of the parameters already included.

Two other significant features of the energy functional is the truncation at fourth order in the order parameter and the neglect of inhomogeneity beyond the square gradient term. The first feature limits our treatment to no more than two distinct reversible phases, and thus is only accurate to the extent that perturbations do not stabilize phases not present in the equilibrium bulk system. As noted above, we believe this limitation is acceptable for the conditions we consider. The second feature limits our treatment to a long wavelength description of interfaces. It is the simplest description for estimating the role of surface energetics[26]. Typically, such a description of liquid-solid interfacial energetics would be inadequate as it would not distinguish between different crystal facets or allow for high frequency oscillations intrinsic to the discrete nature of a crystal. However, we will show

below that a particular property of ice interfaces, the existence of a premelting layer, allows such a simplistic description to be quantitatively accurate.

Given the energy functional in Eq. 4.4, the partition function, $Z(T,p)$, is determined by the path integral,

$$Z(T,p) = \int \mathcal{D}q(\mathbf{r}) \, \exp\left\{-\mathcal{H}[q(\mathbf{r})]/k_{\mathrm{B}}T\right\} \,, \tag{4.6}$$

where the dependence upon pressure, p, enters through the parameters in the model, as discussed above and detailed further below. This partition function and the field that it derives from is a reduced description of the molecular coordinates. As noted above, only long wavelength inhomogeneities are correctly accounted for within this description. As such, there exists a lower lengthscale beyond which this type of analysis is inaccurate. Figure 4.1 gives an illustration of what this field represents. Specifically, given a density field and Eqs. 4.1–4.3, an order parameter field can be calculated. However, due to the discreteness of atoms and molecules the density field is in general a rapidly oscillating function. One way to create a smooth field that contains only slowly vary components is to average the field over a coarse-graining length, ξ. This can be written as,

$$\bar{q}(\mathbf{r}) = \int_V \mathrm{d}\mathbf{r}' q(\mathbf{r}') \, \phi(\mathbf{r}', \mathbf{r}; \xi) \,, \tag{4.7}$$

where $\phi(\mathbf{r}', \mathbf{r}; \xi)$ is some continuous, bounded function that depends on the lengthscale ξ in a way that in the limit of $\xi \to 0$, $\phi(\mathbf{r}', \mathbf{r}) \to \delta(\mathbf{r}' - \mathbf{r})$. In the next section we will explicitly preform such a coarse-graining.

Given the partition function, which determines the probability of a particular field, we can calculate a free energy as a function of the total amount of crystal-like regions using the standard relation,

$$\beta F(Q) = -\ln \left\langle \delta \left(Q - \int_V \mathrm{d}\mathbf{r} \, q(\mathbf{r}) \right) \right\rangle \tag{4.8}$$

where $\delta(x)$ is Dirac's delta function and V is the volume. As defined, $Q = 0$ for a liquid and $Q = V q_{\mathrm{xtl}}$ for a crystal, where q_{xtl} is the mean value of local order density in a crystal. Examples of $\beta F(Q)$, neglecting fluctuations, are also shown in Fig. 4.1.

The parameters in the energy functional, Eq. 4.4, can be determined through relations with experimental thermodynamic observables derivable at the mean-field level. For instance, by formulating conditions for coexistence, it is straightforward to show that

$$\frac{\partial F_{\mathrm{MF}}}{\partial q} = 0 \,, \tag{4.9}$$

where $F_{\mathrm{MF}}(q)$ is the mean field approximation to the free energy, and

$$F_{\mathrm{MF}}(0) = F_{\mathrm{MF}}(q_{\mathrm{xtl}}) \,, \tag{4.10}$$

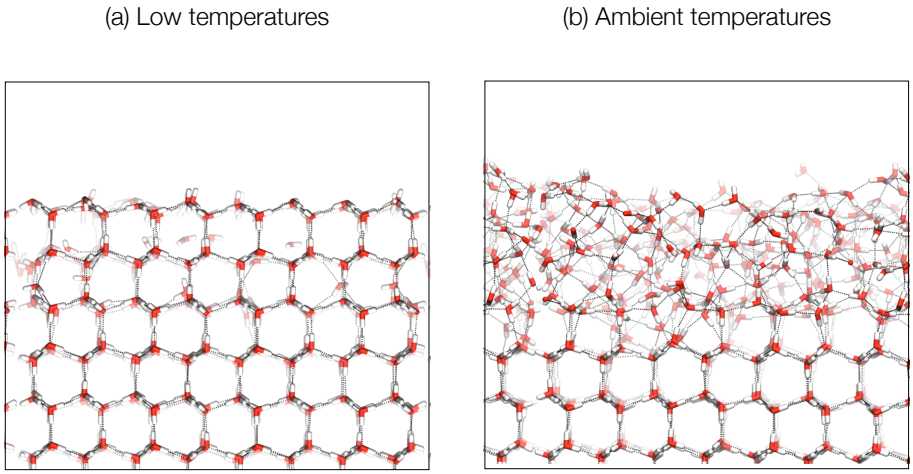

Figure 4.2: Representative snapshots of the surface of ice at conditions (a) far away from the bulk melting temperature and (b) close to the bulk melting temperature taken from molecular dynamics simulations of the TIP4P/2005 model. Far away from coexistence, the surface is ordered and dangling OH groups populate the crystal facet. Close to coexistence, the energetic cost of broken hydrogen bonds is balanced by an entropic disordering or melting.

are sufficient to identify the value of $q_{\rm xtl}$ and determine the mean field melting temperature, $T_{\rm m}$. These equations together with the identities for the entropy change upon freezing,

$$\Delta s = \frac{\Delta h(p)}{T_{\rm m}} = -\frac{1}{V}\left[\frac{\partial F_{\rm MF}(q_{\rm xtl})}{\partial T}\right]_{T=T_{\rm MF}} . \tag{4.11}$$

and corresponding the mean field approximation for surface tension,[192]

$$\gamma = \int_0^{q_{\rm xtl}} \left[2mf(q)\right]^{1/2}\, {\rm d}q\,, \tag{4.12}$$

relate four experimental quantities to the four parameters in Eq. 4.4. After some algebra for a particular pressure, the results are $a_o = 2\Delta h/T_{\rm m}q_{\rm xtl}^2$, $w = 2\Delta h(T_{\rm m}-T_{\rm s})/T_{\rm m}q_{\rm xtl}^3$, $u = \Delta h(T_{\rm m}-T_{\rm s})/T_{\rm m}q_{\rm xtl}^4$, and $m = 18\gamma^2 T_{\rm m}/\Delta h(T_{\rm m}-T_{\rm s})q_{\rm xtl}^2$. Reference [49] gives $\Delta h \approx 3.0\times10^5\,{\rm kJ/m^3}$, and Ref. [75] gives $\gamma \approx 32\,{\rm mJ/m^2}$ for real water.

In the following sections we will use this field theory, parameterized as above from bulk properties, to develop a consistent description of liquid-crystal coexistence and interfaces of ice. Two phenomena that we have studied in depth are the existence of a premelting transition on the surface of ice[131] when it is exposed to its vapor, and the decrease of the melting temperature upon hydrophilic confinement[5]. The results of such studies, both analytic and numerical, are catalogued below.

4.2 Premelting on the surface of ice

The term premelting refers to thermodynamically stable disorder at the interface of an otherwise ordered crystalline solid at temperatures near but below the bulk melting temperature[169]. First proposed by Michael Faraday in 1842 to explain the low friction of the surface of ice[56], definitive experimental proof for surface melting was not observed experimentally until 1987[122]. Since then advances in surface selective experimental techniques have provided powerful tools for direct atomic-resolution observations of this surface phase transition[131]. These experimental studies have been complemented by a number of detailed atomistic simulations that also find a premelting layer on the surface of models of ice[19, 36, 171, 226]. Despite these previous studies, at present no microscopic description exists that both establishes the precise nature of the transition and connects this level of detail with a more coarse grained level necessary to explain experimental observations. Using the field theory described above, complimented with molecular dynamic simulations of the mW model[161], we aimed to address this deficiency.

As reviewed in Chapter 2, most liquids at ambient conditions are close to their triple point. As a consequence, near their melting points the chemical potential differences between the liquid, solid and vapor phase are all very small. Therefore, near $T_{\rm m}$, a thermodynamic criterion for the existence of the premelting layer is given by balancing the different surface terms,

$$\Delta\gamma = \gamma_{s,v} - \gamma_{\ell,s} - \gamma_{\ell,v} \, , \tag{4.13}$$

where $\gamma_{s,v}, \gamma_{\ell,s}$, and $\gamma_{\ell,v}$ are the solid-vapor, liquid-solid, and liquid-vapor surfaces tensions, respectively. When $\Delta\gamma > 0$, there is a thermodynamic driving force for premelting. In the case of water and ice, this driving force can be easily rationalized from a microscopic perspective. Shown in Fig. 4.2 are representative configurations of the surface of ice at conditions far away from, and close to, the melting temperature. At very cold conditions, $T \ll T_{\rm m}$, the surface is ordered and molecules at the surface are forced to break one hydrogen bond on average. This large energetic loss is balanced at higher temperatures, $T \sim T_{\rm m}$ by an entropic melting of the surface. The concomitant enhancement of fluctuations at the interface increase in scale as the melting temperature is approached. Exactly at $T_{\rm m}$, the degeneracy in the free energy dictates that the thickness of the interface may diverge as it is equally likely that the bulk is liquid or crystal.

How the thickness of the premelting layer changes with temperature reflects the interplay between the bulk chemical potential terms that favor order and the boundary condition which excludes it. As reviewed in Ref. [131], experimental estimates of the thickness of the premelting layer at a prescribed temperature, typically $T_{\rm m} - T = 1$ K, vary by over two orders of magnitude depending on the technique and interpretation. Partially, this is because different techniques probe different physical properties that may be more or less correlated with structural disorder. X-ray and proton scattering are typically more sensitive to long ranged order, and other surface selective techniques, such as sum frequency generation spectroscopy[228] and atomic force microscopy[20], have also been used with success. In all cases, however the strong temperature dependence of the thickness enhances problems of

contamination and surface preparation. Further, in all cases it is not straightforward to connect the observations to molecular level details.

Theory and simulation offer a way to clear this ambiguity. Specifically, using sufficiently general statistical mechanical arguments, which relate experimental observable to emergent behavior, and the assumptions of which can be tested with molecular simulation the phenomenology of the premelting layer can be understood and quantified. In what follows, we will show that the field theory laid out above accurately predicts the existence and scaling of the premelting layer as a function of both temperature and system size. This is confirmed by using efficient molecular dynamics simulations of the mW model, which allows us to access length and timescales that would be otherwise unapproachable with simulation techniques.

4.2.1 Order parameter profiles and premelting length

We begin to examine the premelting layer using molecular dynamics simulations of the minimal model of water, the mW model,[161] used in the previous chapter. Calculations are done in the following way. First, a perfectly crystalline ice lattice is created with an equilibrium geometry consistent with zero pressure and low temperatures. This lattice is placed in a simulation box and periodically replicated in the x- and y-direction. The boundary conditions in the z-direction are inhomogeneous. For the surface pointing in the positive z-direction, we have an open boundary condition, where we expose the surface to its vapor. For the surface pointing in the negative z-direction, we attached harmonic restoring forces, with spring constants $k = 20\ k_{\mathrm{B}}T/\text{Å}^2$, to the crystalline lattice positions of the first layer of water molecules to preserve a crystalline boundary condition. The system size is characterized by two lengths, the width of the crystal slab, W, and its length, L. The width is approximately 2 nm and we vary the length between 3 and 13 nm. The temperature is controlled with a Nose-Hoover thermostat, with a time constant of 1 ps. Depending on the proximity to the melting temperature, simulations were run between 10 and 1000 ns in order to obtain converged estimates of the surface properties. The long timescales are required because the size of fluctuations in the interface become as large as the system as T_{m} is approached. Most of the results are performed with the mW model in order to easily access these timescales. Molecular dynamics calculations are performed with LAMMPS[177].

As expected from experiment, the average configuration of the ice slab depends sensitively on temperature. Figure 4.3 shows the mean density (grey lines) and order parameter density (red lines) projected along the direction perpendicular to the plane of the surface. The mean density is calculated by binning the particle positions along the z axis. The density profile is normalized by its mean value in the center of the slab, ρ_{xtl}, as averaged over many unit cells. Near the center of the slab, the density exhibits the expected high frequency oscillations of a crystal. At low temperatures $T_{\mathrm{m}} - T = 10$ K, shown in panel (c), these oscillations persist to the end of the slab. At high temperatures $T_{\mathrm{m}} - T < 1$ K, shown in panels (a,b), these oscillations decay upon approaching the exposed crystal surface. The uniformity of the density in that region, $z > 2.5$ nm, is the first indication that the surface is disordered.

The disorder at the surface can be confirmed by investigating the local order parameter

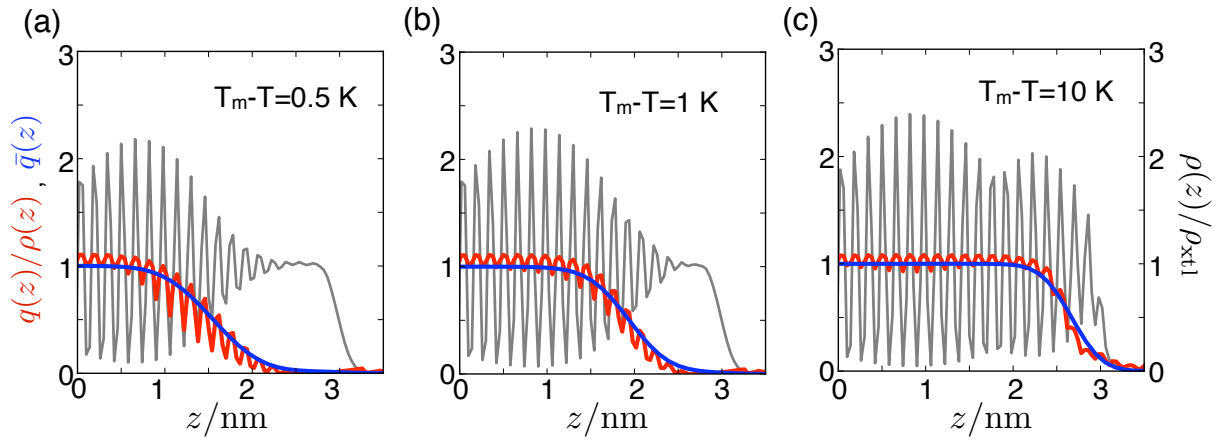

Figure 4.3: Density and order parameter profiles as a function of temperature away from $T_{\rm m}$ computed for the 100 surface of ice Ic for the mW model. Grey lines identify the mean density. Red and blue lines identify the mean order density and its coarse-grained analogue, respectively.

density. The order parameter density is calculated by binning the parameter defined in Eq. 4.1 normalized by its average value in the bulk,

$$q(z) = \langle q(\mathbf{r})\delta(z - \hat{z}\cdot\mathbf{r})\rangle/q_{\rm xtl}\,, \tag{4.14}$$

where $\hat{z}$ is the unit vector in the z-direction. These profiles also oscillate with the periodicity of the lattice, however their amplitudes decay to 0 for z values smaller than the density distributions. For temperatures close to $T_{\rm m}$ the difference in the position of decay of the two profiles is greater than 1 nm apart, while at low temperatures the difference in the position is only on the order of a molecular diameter.

In principle, this gap between the decay of the density and order density distributions provides a way for determining the length of the premelting layer, ℓ. However, any simple definition of the decay of order parameter profile yields a measure of the premelting thickness that is not single valued because of the oscillations in the density and order density. In the next section we show how coarse-graining out these high frequency oscillations yields a smooth profile with a well-defined premelting length.

4.2.2 Coarse-graining local order

To remove the high frequency component of the profiles in Fig. 4.3, and make contact with the long-wavelength description supplied by the field theory discussed at the beginning of the chapter, we must integrate out lengthscales small compared to typical intermolecular distances. Equation 4.7 supplies a way to do this in a computer simulation. Specifically, we

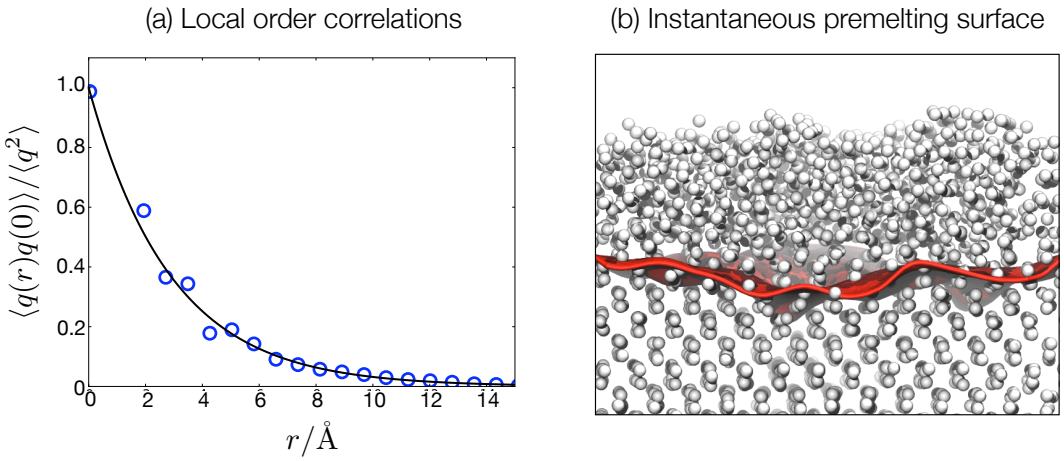

Figure 4.4: Structural correlations in the liquid and the instantaneous local order interface. (left) Order parameter correlation function computed from molecular dynamics simulations of the mW model at $T = 273$ K, $p = 1$ bar. The exponential fit (black line) is of the form $\exp(-r/\xi)/(r/\xi)$ where $\xi = 2.5$Å. (right) A typical configuration of the premelting layer taken from molecular dynamics simulations of the mW model at $T = 272$ K, $p = 1$ bar. The surface, shown in red, located the isodensity 1/2 plane for the local decay of the coarse-grained order parameter field, $\bar{q}(\mathbf{r})$. See text for definition.

can choose as a Gaussian basis function,

$$\phi(\mathbf{r};\xi) = \left(\frac{1}{2\pi\xi^2}\right)^{3/2} e^{-\mathbf{r}^2/2\xi^2} \tag{4.15}$$

parameterized by the lengthscale ξ, and the coarse-grained order parameter field becomes,

$$\bar{q}(\mathbf{r}) = \sum_i^N q_i \phi(\mathbf{r} - \mathbf{r}_i;\xi)\,. \tag{4.16}$$

We want ξ to be on the order of the size of the molecule in order to create a smooth field. In order to determine a reasonable value for ξ, we calculate a correlation length for local order fluctuations by integrating an appropriate correlation function at conditions of coexistence. In particular, we calculate

$$\xi = \int_0^\infty \mathrm{d}r\, \frac{\langle q(r)q(0)\rangle}{\langle q^2\rangle}\,, \tag{4.17}$$

where $\langle q^2\rangle$ are the mean squared fluctuations of the local order, which has mean zero in the liquid where it is evaluated. This integral yield a length of $\xi = 2.5\,$Å. This correlation function is plotted in Fig. 4.4 for a simulation of 8000 mW molecules at $T = 273$ K and $p = 1$ bar. The correlation function is largely exponential in character, as expected for an

isotropic liquid. Also plotted in Fig. 4.4 is a representative configuration of the premelting layer and an iso-density surface locating the instantaneous boundary of the coarse-grained order field. We define this boundary as being where the field is equal to 1/2 of its average bulk value. This procedure for constructing an instantaneous interface is similar to previous calculations used for calculating liquid-vapor interfacial properties[232].

The liquid-crystal surface tension determines the mean squared fluctuations in the height of the interface[169]. The fact that the liquid-crystal surface tension is about half of the liquid-vapor surface tension[49] means that while there is a significant free energetic penalty to forming an interface, the size of fluctuations that result at such an interface are large in amplitude. These fluctuations are larger than what are seen at "soft" liquid-vapor interfaces. The dispersion relation for the size of fluctuations over different lengthscales is the same as found for capillary waves, $\langle |h(k)|^2 \rangle \propto c/k^2$ where $|h(k)|^2$ is the amplitude of the Fourier transform of the height-height correlation function and c is a constants related to the surface tension. The procedure used here recovers this scaling relation.

At the melting temperature, the size of height fluctuations diverge due to the interface becoming delocalized. This can be anticipated by the blue lines in Fig. 4.3 which plot the distribution of the coarse-grain field, calculated in the same way as in Eq. 4.14 but with $\bar{q}(\mathbf{r})$ replacing $q(\mathbf{r})$. As expected, these curves are smooth and lay basically on top of the bare order parameter profile. The width of the interface is proportional to the size of these fluctuations, and as can be seen in Fig. 4.3 grows upon approaching $T_{\rm m}$. To the extent that this coarse-graining procedure provides a map to the statistical field theory presented above, then the sigmoidal character of these curves away from $T_{\rm m}$ can be expected. In particular, in its inclusion of only a squared gradient interfacial term this theory is isomorphic with the van der Waals theory of liquid vapor coexistence, a standard result of which is this density profile[192].

4.2.3 Logarithmic divergence at $T_{\rm m}$

In order to understand the temperature dependence of the premelting layer, we turn to the statistical field theory. We proceed by making a number of simplifications. First, we recognize on average the system is symmetric in the plane parallel to the interface. Therefore we can trivially integrate out those degrees of freedom. Next, we follow seminal work by Lipowsky[138] and enforce the open boundary condition of the free interface by adding a harmonic potential on the order parameter field that acts at the mean location of the end of the slab, z^*.

The resultant one-dimensional Hamiltonian is

$$\mathcal{H}[q(z)] = Ak_{\rm B}T \int_{-\infty}^{\infty} {\rm d}z \left[f(q(z)) + \frac{m}{2} \left| \frac{dq(z)}{dz} \right|^2 + \frac{a_{\rm s}}{2} q(z)^2 \delta(z - z^*) \right] . \tag{4.18}$$

While it is not analytically tractable to solve for the complete partition function prescribed by this Hamiltonian, we can approximate it by neglecting fluctuations and in doing so solve

for the mean interface profile. Specifically as noted before, the mean field free energy is given by

$$F_{\rm MF}(q) = \mathcal{H}(\langle q(z)\rangle)\,, \tag{4.19}$$

where,

$$\frac{\delta\mathcal{H}}{\delta\langle q(z)\rangle} = 0\,, \tag{4.20}$$

and $\langle q(z)\rangle$ is the order parameter profile that minimizes the Hamiltonian. The resultant Euler-Lagrange equation determines the form of the profile,

$$\frac{{\rm d}q}{{\rm d}z} = \sqrt{2/m}\sqrt{f(q) - f(q_{\rm xtl})}\,, \tag{4.21}$$

with the implicit equation,

$$(a_{\rm s}q_{\rm s})^2 = f(q_{\rm s}) - f(q_{\rm xtl})\,, \tag{4.22}$$

for the value of the order parameter at the interface, $q_{\rm s} = q(z^*)$. Given the form of the order parameter profile, we can solve for the equation of the thickness of the premelting layer. As given in Ref. [138], this is a logarithmic function of temperature with a divergence at $T_{\rm m}$,

$$\ell(t) = -\ell_o \ln(t) + \mathcal{O}(1) \quad \text{for} \quad a_{\rm s} \geqslant \sqrt{a_o} \tag{4.23}$$

where $t = (T_{\rm m} - T)/T_{\rm m}$ and $\ell_o = 1/2\sqrt{m/a_o(T_{\rm m} - T_{\rm s})}$. From the parameterization in Section 1, we can determine the bare premelting length in terms of thermodynamic observables, $\ell_o = 3\gamma/2\Delta h$. Such logarithmic divergence is typical of surface transitions and is found in wetting and pinning transitions[169]. In all cases, interface delocalization it due to close coexistence of multiple bulk phases. The criteria in Eq. 4.23 explains why premelting layers do not exist on all solids, for when $a_{\rm s} < \sqrt{a_o}$ the surface changes discontinuously. The parameter, $a_{\rm s}$, is related to the excess surface tension.

Using the coarse-grained profiles in Fig. 4.3, as well as ones at other temperatures, we can calculate the thickness of the premelting layer as a function of temperature for the mW model. Figure 4.5 reports this data. In the semilog plot of Fig. 4.5a, for reduced temperatures, $t < e^{-2}$, there is a significant rise in the premelting thickness that crosses over to logarithmic growth for, $t < e^{-4}$. Also plotted is the predicted scaling from Eq. 4.23 using the parameters calculated for the mW model, which determine $\ell_o = 4.6$Å. As shown, the agreement found is within the error of the calculation, suggesting that additional fluctuation effects are not important for the reduced temperatures approached here. This could be anticipated from previous work, which determined $d = 3$ as the critical dimension for premelting with a thermal field that is unmodified by fluctuations[139].

Also shown in Fig. 4.5 is the scaling of the maximal premelting thickness with the linear dimension of the system, L. Finite-size scaling arguments[140] predict that the maximal premelting length for the system should scale as $\ell \sim \ln L$. This scaling is indeed found for the limited system sizes that we can simulate. Figure 4.5b plots data taken from different sized systems in a semilog plot. The black line is a fit with a correlation constant of that

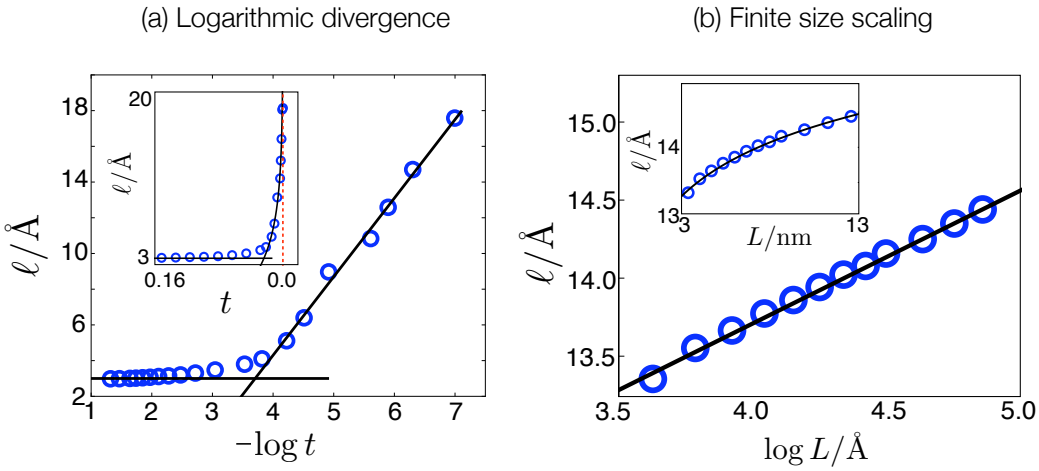

Figure 4.5: Scaling relations for the premelting layer thickness for temperature and system size. Blue data points located simulation results for an mW model ice Ic surface exposed to its vapor. Black lines are predicted forms based on the field theory. Insets reproduce the same data on a linear scale. Errors are the size of the symbols.

is within the uncertainty of the data. This scaling can be rationalized by considering that the coexistence conditions for a finite system change in proportion to the ratio of the surface to volume, which in this case is proportional to $1/L$. The argument in the logarithmic function in Eq. 4.23 for the thickness depends on these coexistence conditions, therefore it is not surprising that this scaling, $-\log 1/L$ exists. This argument for how the freezing temperature changes in a finite system will be made quantitative in a later section.

These results allow us to make a reasonable estimate for the thickness of the premelting layer expected for experiment. In particular, we can use experimental parameters for the heat of fusion and surface tension, to determine $\ell_o = 5.2$, with Eq. 4.23 determines ℓ at 272 K to be 3 nm. This value is in good agreement with near-edge X-ray absorption fine-structure spectra that reports $\ell(272\text{K}) = 2$ nm[12] and reasonable agreement with ellipsometry measurements that reports $\ell(272\text{K}) = 5$ nm[21]. To resolve possible origins for the small disgreements with these measurements, we turn to the dependence of this length on orientation, curvature and the bulk lattice.

4.2.4 Orientation, curvature and bulk lattice

The field theory and its consequences discussed in the previous sections are general. The form for the energy that control the collective excitations, like interface formation and deformation, are dictated entirely by the symmetry of the Hamiltonian. The experimental observable that determine the actual values of these excitations and their likelihood are determined from macroscopic observables. Therefore, to the extent that such obserables do

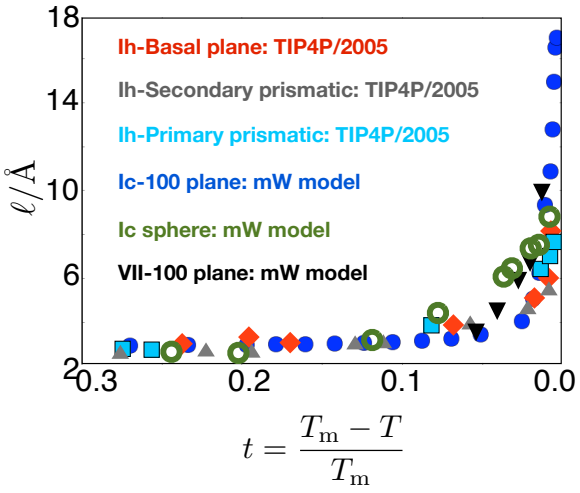

Figure 4.6: Dependence on the premelting layer with model, orientation, bulk lattice and curvature. Spanning a relatively large parameter regime, the basic physics of the premelting layer on the surface of ice is qualitatively insensitive to these details.

not change, it is reasonable to expect that the behavior of the interface will not be sensitive to details such as the crystal orientation or bulk lattice.

Figure 4.6 confirms this expectation. Specifically we plot the premelting layer thickness calculated in the same way as Fig. 4.5 for ice Ih along three different crystal facets, the 100 face of ice VII and a spherical crystal with radius 3 nm. Data from ice Ih has been taken from Ref. [36], which used the TIP4P/2005 model with MD simulations preformed in an analogous way to our results for the mW model. These simulations did not use a coarse-grained order parameter profile to determine the premelting length, however in plotting it here we assume the scaling holds for their calculation up to an additive constant. This constant is $\mathcal{O}(1)$ and depends slightly on the lattice orientation. Data for ice VII are our own results using the TIP4P/2005 model. Data for premelting on the surface of an ice sphere was generated with the mW model. To create this surface, a sphere of radius 3 nm was cut out of a crystalline ice Ic lattice. Prior to simulation, the surface was relaxed by removing molecules coordinated to fewer than 3 neighbors as determined by a radial cutoff of 3.3Å.

In each case presented in Fig. 4.6, a premelting layer exists and grows as the melting temperature is approached. Qualitative details such as the basic form of the temperature dependence and magnitude are conserved, while quantitative details such as the effective, ℓ_o, governing the strength of divergence change with orientation and bulk lattice. For the curved spherical surface, the finite system dictates a small maximal premelting thickness, $\sim \log R$. In all cases, however, the large energetic penalty for breaking hydrogen bonds necessitates an entropic balance found in premelting. It is worthwhile noting that in some instances, for finite systems, it is possible to arrange molecules at the surface in such a way that hydrogen

bond are not broken. These are systems, such as water confined to hydrophobic nanotubes, $R < 20$Å,[116] in which the interface is highly curved. In these instances, a premelting is not expected nor observed, as there is no longer an energetic penalty associated with breaking strong cohesive interactions.

4.2.5 Implications for sublimation kinetics

The physical properties of the surface of ice determine a number of important dynamical processes[38]. In the atmosphere, ice particles are the substrates on which much of atmospheric chemistry occurs. The premelting layer is thought to be especially important in acting as a solvent for acid base reactions. Another simple kinetic process that occurs on the surface of ice is evaporation. Experimentally, it is known that the evaporation of a water molecule from the surface of ice is effectively barrierless between the temperature range of 273 K to 233 K[193]. This is inferred by the activation energy being equal to the thermodynamic heat of sublimation, as determined by measuring the rate of evaporation as a function of temperature with microcalorimetry and mass spectrometry. Recent work on the evaporation from the surface of liquid water that has concluded that this process is similarly barrierless[221]. It would seem that the existence of a disordered interface at the boundary between the condensed phase and the vapor supplies sufficiently facile reorganization around an evaporating molecule that evaporation from either a liquid or a quasi-liquid layer is simply a ballistic process. Only for low temperature, where the premelting layer vanishes, $T \lesssim 230$ K, is evaporation expected to have to overcome a barrier.

4.3 Corrections to freezing for finite systems

Instances of water confined to nanoscopic dimensions are ubiquitous in nature and technology. For example, water confined to silica nanopores coated with catalyst is an efficient system for evolving oxygen, a first step towards artificial photosynthesis[97]. Another example, aquaporin pores in biological membranes confine water to channels in such a way to control water content in cells[4]. Further, silica nanopores are also used to inhibit freezing of water to enable exploration[141, 142, 240] of water's behavior at conditions where the bulk material would spontaneously crystalize. The extent to which behaviors of water confined in this way – to a long hydrophilic nanopore – reflects behaviors of bulk water has been unknown. Here, we address this deficiency by using general theoretical arguments coupled with molecular simulation to construct the phase diagram for water at standard and supercooled conditions as a function of temperature, T, pressure, p, and pore radius.

The class of systems we consider is illustrated in Fig. 6.6, which shows snapshots taken from a molecular simulation of water confined to a silica nanopore, details about which are given later. This confining pore is long and narrow. Its walls are hydrophilic, but with atoms that are in a disordered arrangement, much like a typical arrangement of oxygen atoms in liquid water, except the atoms making up the pore are frozen in place and have a slightly

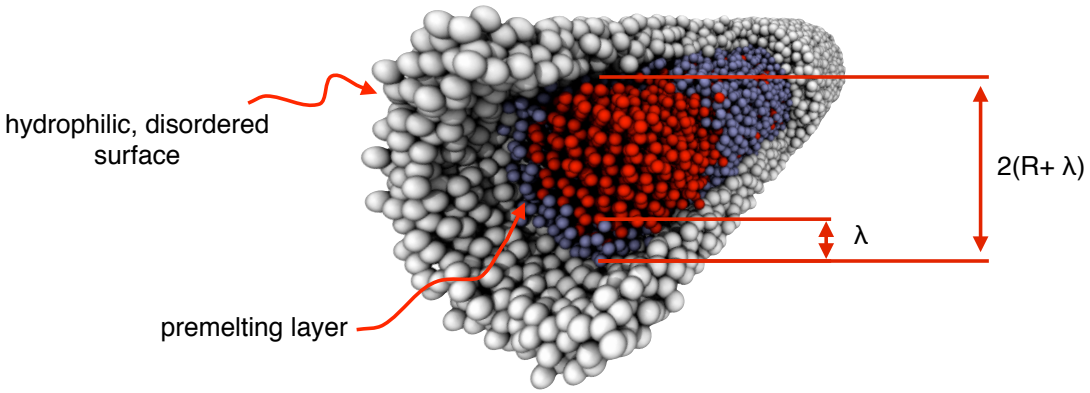

Figure 4.7: Locally crystalline oxygen atoms of water (the red particles) confined in a molecular simulation to a nanopore of length L with a disordered hydrophilic surface chosen to mimic silica in the material named MCM-41.[123] The radius of the pore is $R + \lambda$, where λ is the thickness of an amorphous water mono-layer (the blue particles) adjacent to the pore surface. See text.

larger space filling size than that of water. This static surface disorder inhibits crystal-like structures so that water adjacent to the surface is typically disordered too. We will show that the thickness of that adjacent layer is $\lambda \approx 2.5\,\text{Å}$, about the diameter of one water molecule.

By considering pore radii $R_\text{p} = R + \lambda$ that are twice 2.5 Å or larger, there can remain a significant amount of confined water that is not part of the adjacent mono-layer. This interior water takes on ordered or disordered arrangements, depending upon temperature, pressure and pore radus. For small enough radii, the destabilizing influence of the amorphous layer causes interior ordered water to be unstable, even at temperatures far below standard freezing temperatures. For larger radii, where ordered states are thermodynamically stable, time scales over which an ordered structure might emerge can be very long, so long that the interior water may become glass. These are the features considered in this paper: bulk thermodynamic stability, competing interfacial energetics and time scales to reorganize molecular structures.

4.3.1 Phase diagram for freezing in nanopores

Melting in a bulk macroscopic system coincides with a singularity in a free energy function. In a bounded system, like those we consider here, the transition is smoothed or altogether removed. Two relevant length scales associated with this behavior emerge from the

microscopic theory presented in the previous section. The first,

$$\ell_{\rm m} = 2\gamma/\Delta h \approx 0.21\,{\rm nm}\,, \tag{4.24}$$

reflects competition between bulk energetics favoring order and interfacial energetics opposing order. Here, γ is the surface tension between the ordered crystal and the disordered liquid, and Δh is the heat of fusion per unit volume. The value, $\ell_{\rm m} \approx 0.21\,{\rm nm}$ for water, follows from the values of surface tension and heat of fusion for water-ice coexistence[49, 75]. Both γ and Δh are pressure dependent, but the ratio $\gamma/\Delta h$ is pressure-independent to a good approximation[218]. More is said about this fact later.

When the radius R is significantly larger than $\ell_{\rm m}$, a melting temperature remains finite. This temperature, $T_{\rm m}(p,R)$, is defined as that where the free energy of an ordered structure equals the free energy of a liquid. According to macroscopic thermodynamics, $T_{\rm m}(p,R)$ follows a Gibbs-Thompson equation (like the Kelvin equation in the context of capillary condensation)[55]. Specifically, $T_{\rm m}(p,R) \approx T_{\rm m}(p)(1-\ell_{\rm m}/R)$, where $T_{\rm m}(p)$ is the bulk melting temperature. This approximation describing the reduction in melting temperature with increasing $1/R$ is correct to the extent that $\ell_{\rm m}/R \ll 1$. The melting curve for small $1/R$ shown in Fig. 4.8 follows this equation.

The second relevant length emerging from the theory manifests fluctuations that destabilize order. Specifically, fluctuations renormalize the first length to yield

$$\ell_{\rm s} = \ell_{\rm m}/(1 - T_{\rm s}/T_{\rm m}) \approx 0.91\,{\rm nm}\,, \tag{4.25}$$

where $T_{\rm s}$ stands for the temperature below which a bulk amorphous phase of water is unstable. It is generally pressure dependent, but according to our simulation studies of one water model,[133] the ratio $T_{\rm s}(p)/T_{\rm m}(p)$ is pressure independent. We therefore omit explicit reference to its pressure dependence in Eq. 4.25. Experimentally, it is difficult to measure $T_{\rm s}$, so in order to estimate it for water we rewrite the ratio as $T_{\rm s}/T_{\rm m} = (T_{\rm s}/T_{\rm o})(T_{\rm o}/T_{\rm m})$ where $T_{\rm o}$ is the temperature of maximum density at low pressure. We write these ratios because we have found previously that $T_{\rm o}$ represents the relevant energy scale for supercooled water thermodynamics. Therefore, we expect that for any reasonable model of water $T_{\rm s}/T_{\rm o}$ will be independent of the specific choice of model. As such, it can be extracted from simulation, with which we find it to be $T_{\rm s}/T_{\rm o} = 0.76$[133]. The second term, $T_{\rm o}/T_{\rm m}$, is a model dependent constant, often close to unity and its value for water is known experimentally to be 1.01[49]. We use that value. Therefore, we predict that $T_{\rm s}(1\,{\rm atm}) = 210\,{\rm K}$ for water. This prediction of a lower temperature limit to liquid stability is consistent with experimental observations of rapid spontaneous crystallization of water at 220 K[172]. In addition, it yields the value $\ell_{\rm s} = 0.91\,{\rm nm}$ cited above.

The Gibbs-Thompson correction to the bulk melting line is accurate only when order parameter fluctuations can be neglected. These fluctuations become dominant as R approaches $\ell_{\rm s}$. Specifically, in the next section we derive

$$T_{\rm m}(p,R) \approx T_{\rm m}(p)\left(1 - \frac{\ell_{\rm m}}{R} - \frac{\ell_{\rm s}^2}{8\pi\,(R-\ell_{\rm s})\,R}\right)\,, \tag{4.26}$$

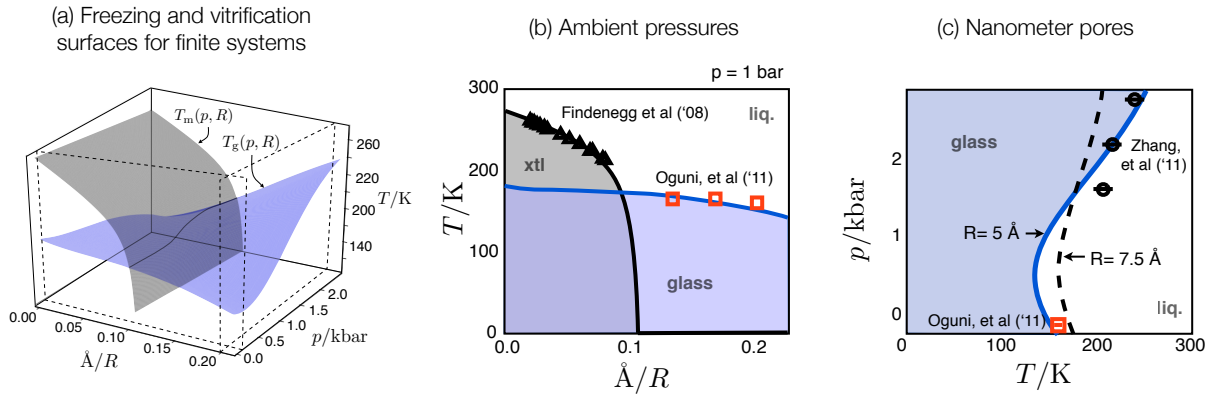

Figure 4.8: Phase diagrams for supercooled confined water. a) Melting and glass transition temperatures, $T_m(p,R)$ and $T_g(p,R)$, respectively, as a functions of pressure p and cylinder radius, R. b) Phase diagram at the constant pressure $p = 1$ bar. Triangular markers indicate melting temperatures measured experimentally.[63] Circles indicate melting temperatures determined through our computer simulation, where errorbars indicate our uncertainty in $T_m(p,R)$. Squares indicate glass transition temperatures measured experimentally with error estimates for R (not shown in figure) of about $\pm$ 4 Å[173]. c) Phase diagram for two different fixed radii $R = 5.0$Å(solid line) and $R = 9.5$Å(dashed line). Circles indicate an onset of thermal hysteresis in experimental density measurements with $R \approx 5.0$Å[240]. Error bars indicate our measure of uncertainty of where hysteresis begins. The square indicates an estimate of the calorimetric glass transition for a pore of approximately the same diameter.[173] The error estimate stated in Ref. [173] is smaller than the size of the symbol. Figure adapted form Ref. [134]

for $R > R_c$, where R_c is the positive root of the right hand side of Eq. 4.26 and is approximately equal to ℓ_s.[1] For $R \leq R_c$, $T_m(p,R) = 0$. This expression is graphed in Fig. 4.8. The fluctuation contribution produces the precipitous end to the melting line near $R \approx 1\,$nm. The comparison of data points and lines in Fig. 4.8 shows that our predicted behavior of $T_m(p,R)$ agrees well with observed calorimetry results for an order-disorder transformation of water in silica pores[63]. Equation 4.26 also agrees well with our molecular simulation results discussed later in this paper.

Also shown in Fig. 4.8 are surfaces for the glass transition temperature as a function of pore size and pressure. This surface will be discussed in the next chapter when we delve into the dynamics of supercooled and glassy water.

[1] $R_c = \ell_s \left[1/2 + \ell_m/2\ell_s + 1/2\left(1 + 1/2\pi - \ell_m^2/\ell_s^2\right)^{1/2}\right]$.

4.3.2 Mean field treatment

Mean field theory identifies the mean value $\langle q(\mathbf{r})\rangle$ as the function $q(\mathbf{r})$ that minimizes $\mathcal{H}[q(\mathbf{r})]$ subject to the boundary conditions imposed by the cylindrical pore. Specifically, as discussed in the premelting section the free energy in this approximation is

$$F_{\mathrm{MF}} = \mathcal{H}[\langle q(\mathbf{r})\rangle]\,, \tag{4.27}$$

where

$$\frac{\delta\mathcal{H}}{\delta\langle q(\mathbf{r})\rangle} = 0\,. \tag{4.28}$$

For boundary conditions applied to solving Eq. 4.28, we assume the effects of the pore are two-fold. First, we assume the pore confines water to a cylinder of radius R_{p}. Second, we assume that disorder of the pore's confining hydrophilic surface induces liquid-like behavior in adjacent water, making

$$\langle q(\mathbf{r})\rangle = 0\,,\ \text{for}\ |\mathbf{r}| \geq R_{\mathrm{p}} - \lambda \equiv R, \tag{4.29}$$

where λ is the thickness of the amorphous boundary layer. Simulation results for various temperatures and pore radii show that crystal-like domains are limited to an inner cylinder of radius $R = R_{\mathrm{p}} - 2.5$Åwhere R_{p} is the mean distance from the center of the pore to the silica wall. Therefore, we take $\lambda \approx 2.5$Åfor all temperatures and pore radii.

In this picture, surface energetics controlling the non-trivial behavior of $\langle q(\mathbf{r})\rangle$ is determined by the interface between liquid water and ice. The silica-water interactions are irrelevant except for producing a layer of disordered water and therefore imposing the boundary condition Eq. 4.29. One important consequence is that the parameter m is determined by the interfacial energy of ice in contact with liquid water.

For an analytical solution to Eq. 4.28, we consider R to be very large. To leading order in $1/R$, the solution to Eq. 4.28 is that of a one dimensional interface that yields a mean field free energy per unit volume

$$\frac{F_{\mathrm{MF}}(q)}{k_{\mathrm{B}}TV} = q^2\left[\frac{a}{2} + \frac{w}{3R}\left(\frac{2m}{u}\right)^{1/2} - wq + uq^2\right]\,, \tag{4.30}$$

where

$$\partial F_{\mathrm{MF}}/\partial q = 0\,, \tag{4.31}$$

with q being the mean-field estimate of $\langle q(\mathbf{r})\rangle$ for $\mathbf{r}$ at the center of the cylinder. With numerical solutions, we have checked that terms beyond linear in $1/R$ would be significant contributors to $F_{\mathrm{MF}}(q)/V$ only for R so small that fluctuation corrections to the mean field approximation are dominant (see below). At that stage, corrections to Eq. 4.30 due to growing curvature are irrelevant.

At a point where a disordered state, $q = 0$, coexists with an ordered state, $q = q_{\rm xtl} > 0$, the mean field condition for coexistence is

$$F_{\rm MF}(0) = F_{\rm MF}(q_{\rm xtl})\,, \tag{4.32}$$

which has a solution at a temperature $T_{\rm MF}(p,R)$, and an entropy difference per unit volume given by

$$\Delta s(p,R) = -\frac{1}{V}\left[\frac{\partial F_{\rm MF}(q_{\rm xtl})}{\partial T}\right]_{T=T_{\rm MF}(p,R)}\,. \tag{4.33}$$

In the limit $R \to \infty$, this coexistence should coincide with bulk freezing transition because it is a first-order phase transition where fluctuation effects are not important. Accordingly, we associate $T_{\rm MF}(p, R \to \infty)$ with the bulk freezing temperature, $T_{\rm m}(p)$, and $\Delta s(p, R \to \infty) \equiv \Delta s(p)$ with the entropy change between water and ice, i.e., $\Delta s(p) = -\Delta h/T_{\rm m}(p)$. These connections to the bulk melting transition together with the corresponding mean field approximation for surface tension,[192] $\gamma = \int_0^{q_{\rm xtl}} [2mf(q)]^{1/2}\,{\rm d}q$, allow us to identify all relevant combinations of parameters in the model in terms of experimentally observed properties of bulk water. Specifically, after some algebra Eqs. 4.24 and 4.31 yield a mean-field expression for the melting surface,

$$T_{\rm MF}(p,R) = T_{\rm m}(p)\,(1 - \ell_{\rm m}/R)\,. \tag{4.34}$$

The mean-field approximation $T_{\rm MF}(p,R) \approx T_{\rm m}(p,R)$ is identical to the macroscopic Gibbs-Thompson estimate noted earlier.

4.3.3 Role of fluctuations

To estimate the effects of fluctuations, we evaluate $\Delta F(q) \equiv F(q) - F_{\rm MF}(q)$ in a Gaussian approximation. That is,

$$\Delta F(q) = -k_{\rm B}T\,\ln \int \mathcal{D}q(r)\,\exp\{-\Delta\mathcal{H}[q(\mathbf{r})]/k_{\rm B}T\}\,, \tag{4.35}$$

with

$$\Delta\mathcal{H}[q(\mathbf{r})] \;\approx\; \frac{k_{\rm B}T}{2}\int_{\mathbf{r}}\left\{\kappa\,[\delta q(\mathbf{r})]^2 + m\left|\nabla\delta q(\mathbf{r})\right|^2\right\}\,, \tag{4.36}$$

where $\kappa = a - 3wq + 6uq^2$. This approximation to $\Delta\mathcal{H}[q(\mathbf{r})]$ comes from expanding $\mathcal{H}[q(\mathbf{r})]$ through quadratic order in $\delta q(\mathbf{r}) \equiv q(\mathbf{r}) - q$.

The geometry of the system plays a role through the Laplacian in Eq. 4.36. For the cylinderical boundary conditions we consider, evaluation of the Gaussian integral prescribed by Eqs. 4.35 and 4.36 can be done by using zeroth order Bessel functions with the limits of integration restricted to allow fluctuations of wavelengths up to $2\pi/R$.

The resulting approximation to the free energy can be used to estimate the temperatures and pressures where the ordered and disordered materials have equal statistical weight, i.e.,

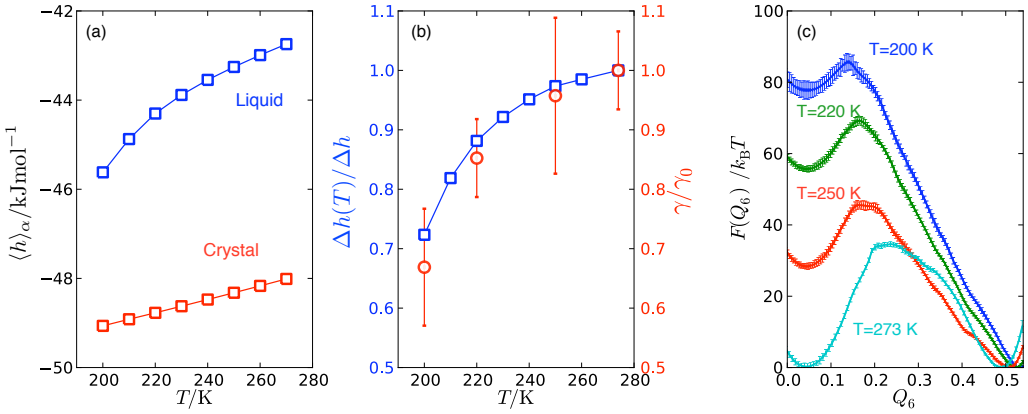

Figure 4.9: Validation of the Turnbull relation, $\gamma/\Delta h \approx$ const. for the mW model. (a) Temperature dependence of the mean enthalpy in the bulk liquid and crystal states. (b) Liquid-crystal surface tension, γ, and the enthalpy of fusion, Δh, divided by their values at coexistence, $T_\mathrm{m} = 274$ K. (c) Free energy computed for a $N = 216$, $p = 1$ atm bulk system illustrating data with which coexistence and surface tension is determined. Figure adapted form Ref. [134]

where Eq. 4.32 is satisfied but with $F_\mathrm{MF}(q)$ replaced with the fluctuation corrected $F(q)$. After some algebra, we find for $R < R_\mathrm{c}$

$$\frac{T_\mathrm{m}(p,R)}{T_\mathrm{m}(p)} = 1 - \frac{\ell_\mathrm{m}}{R} - \frac{\ell_\mathrm{s}^2}{8\pi(R-\ell_\mathrm{s})R}\left[1 + \mathcal{O}\left(\frac{\ell_\mathrm{m}}{R}\right)^2\right], \tag{4.37}$$

where we have noted the order of neglected term. This term, $\mathcal{O}\left(\ell_\mathrm{m}^2/R^2\right)$, refer to a curvature correction that would distinguish slab and cylinder geometries. For water at the conditions we consider, the dominant contribution for small R is due to $\ell_\mathrm{s}/(R-\ell_\mathrm{s})$ being large. As such, Fourier components rather than Bessel functions could have been used to diagonalize the determenent for the Gaussian integral, and equivalently, the partition function we consider is dominated by its largest eigenvalue.

The vanishing of crystal-like stability predicted in this way, where $T_\mathrm{m}(p,R) \to 0$ for $R \to R_\mathrm{c}$, is essentially a Ginzburg criterion[26]. The length ℓ_s is close to but necessarily smaller than this smallest radius, R_c, where crystal-like states can be stable.

4.3.4 Testing the Turnbull relation

The reliability of the temperature dependence of field theory we use relies on the relative temperature independence of the material properties which parameterize the Hamiltonian. In the case of the melting temperature, only ratios of $\gamma/\Delta h$ enter. Therefore to the extent that this ratio is temperature independent, as assumed by Turnbull [218], sources of discrepancy

between our analytic predictions and experimental data are not from neglecting higher order temperature dependences.

To test the applicability of Turnbull's relation $\gamma/\Delta h \approx$ constant, we have calculated the surface tension and enthalpy of fusion as functions of temperature.[218] See Fig. 4.9. Here, $\Delta h(T_{\rm m}) = 5.4$ kJ/mol and $\gamma(T_{\rm m}) = 35.3$ mJ/m^2. To make that figure, we have determined the enthalpy of fusion by calculating the average enthalpy density differences at coexistence, $\langle h\rangle_{\rm liq} - \langle h\rangle_{\rm xtl}$.

Similarly, we have determined the surface tension by calculating the free energy as a function of Q_6, using the umbrella sampling procedure described in the last chapter for $N = 216$ particles at a constant pressure, $p = 1$ atm. See Fig. 4.9. The surface tension is then obtained by taking the difference between the free energy at the top of the barrier and at its stable coexisting basins. Specifically, $\gamma = \Delta F(Q_6)/L^2$ where ΔF is the interfacial free energy calculated by first preforming a Maxwell construction to place the system at coexistence at the different temperatures, and $L = (N/\rho)^{2/3}$[17]. This procedure is exact in the limit of $N \to \infty$. We have checked that we closely approach the limiting value by studying several system sizes up to $N = 1000$ particles. This surface tension is an effective surface tension obtained by integrating over all distinct crystallographic faces and agrees well with that obtained from a recent nucleation study[130].

4.3.5 Disorder width, curvature and premelting layer

Figure 4.10 mean order parameter, $\langle q(r)\rangle$, as defined in Eq. 4.1. These curves are obtained from the mW model by simulation, and from our theory by solving Eq. 4.28 with the parameters appropriate for the mW model. The thermodynamic conditions considered are where the crystal-like state is stable. Several pore diameters were studied, and the illustrated results are typical. In each case, the simulation yields a disordered layer of non-zero particle density and of thickness $\lambda = 2.5$Åadjacent to the pore wall. This thickness of the disorder layer is in good agreement with the value inferred from fitting Eq. 4.34 to experimental data[63].

The simulations also show oscillations in both the density and the order parameter. These oscillations reflect the size of the particles in the simulated model. By construction, the square-gradient theory does not contain these oscillations. Nevertheless, the rise in the mean order parameter from its disordered value at the wall to its crystal-like value in the center of the pore is consistent with those of the simulation when coarse grained over a particle diameter. The general agreement of the profiles calculated with our molecular dynamics simulations with those calculated neglecting curvature corrections indicates those corrections are small.

The amplitude of the oscillations in the mean order parameter obtained from the simulation results are relatively small, typically 10% of the mean, except at the very center of the pore where statistics is unreliable. Away from the center, the oscillations are especially small in comparison to those that would be found in an ordered crystal. The amplitudes are diminished from those of a crystal due to the average over disorder along the length of the

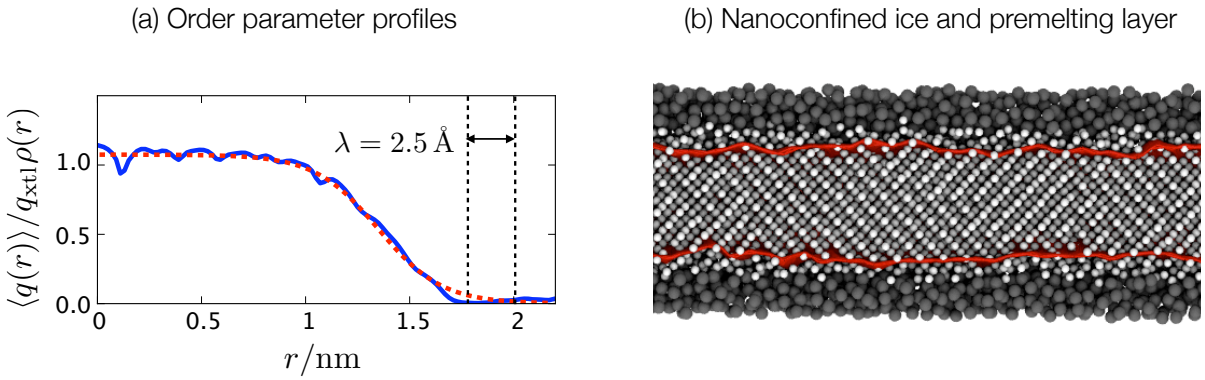

Figure 4.10: Average and instantaneous order profile. (a) Mean orientational order density, $\langle q(r)\rangle$, for water confined to cylindrical pores. r is the radial position of the pore system. The profile is computed with $R_{\rm p} = 20.0$ (blue) computed at $T \approx T_{\rm m}(p, R)$ and $p \approx 0$. The red dashed line is the prediction from the mean field theory, Eq.13, using parameters for $\mathcal{H}[q(\mathbf{r})]$ found with the mW model. Notice that the order remains absent for density within $\lambda = 2.5$Åof the pore wall. Other sized pores fall on this same universal curve (not shown for clarity). (b) A representative snapshot of the instantaneous order parameter surface for a pore with radius, $R_{\rm p} = 20$Å. Figure adapted form Ref. [134].

tube.

The width of the interface exhibits a slight temperature dependence. For larger pores, however, the situation changes. As the radius grows beyond the conditions treated here, the coexistence temperatures will tend towards the bulk melting temperature. A pre-melting layer between the disordered surface and the crystal will then become large and strongly sensitive to temperature[131]. For macroscopic systems, this pre-melting width diverges as T approaches the melting temperature. With the equations we use in our theory, this behavior is isomorphic to a liquid-vapor wetting transition. It is is a general behavior accompanying any first-order transition with appropriate boundary conditions[192].

4.3.6 $T_{\rm m}(p, R)$ for water and the mW model

For our calculations here we assume that the bulk melting line can be accuratly approximated by $T_{\rm m}(p) = T_{\rm m}[1 - pC + \mathcal{O}(p^2)]$. The coefficient C is related to heat of fusion and the change in volume between water and ice determined at ambient pressure, as derived through the Clapeyron equation. For water $C = 0.026\,\text{kbar}^{-1}$ (Ref. [49]) and for the mW model $C = 0.01\,\text{kbar}^{-1}$[161]. This difference in slope between the mW model and real water is due to the mW model over estimating the density of ice Ih[161]. However, by defining a pressure scale in units of C, the equation of state of water and the mW model can be related.

The mW model we calculate $\ell_{\rm m}$ and $\ell_{\rm s}$ to be 2.40 Å and 8.16 Å respectively. These

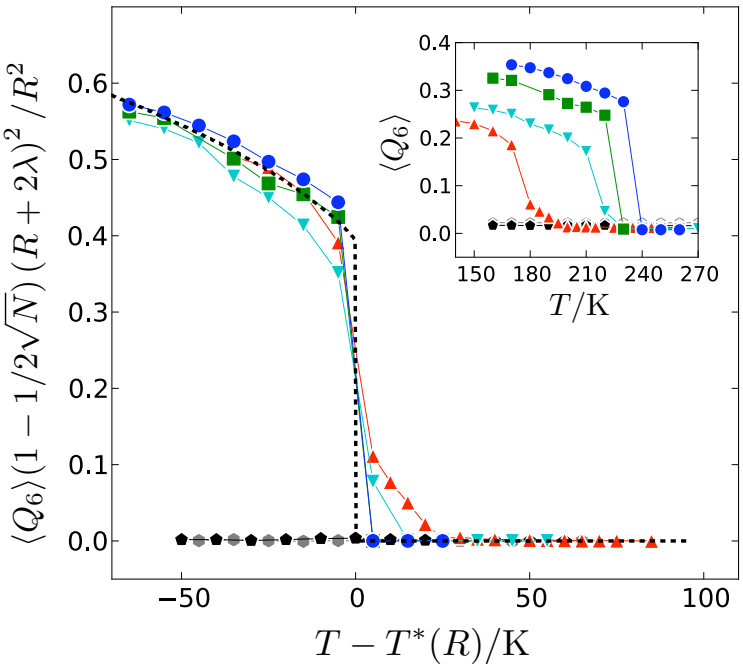

Figure 4.11: Average value of the global orientational order parameter, $\langle Q_6 \rangle$, as a function of temperature for different pore sizes. In the main figure, $\langle Q_6 \rangle$ is rescaled and plotted as a function of $T - T^*(R)$, where T^* is the temperature at which $\mid d\langle Q_6 \rangle / dT \mid$ is maximal. Inset shows the same, but not rescaled. Different markers correspond to different pore size systems, with $R_\mathrm{p} = 2.5\text{Å} + R = 20.0\text{Å}$ (blue ◯), 17.5Å (green □), 15.0Å (cyan △), 12.5 Å (red ▽), 10.0Å (grey ⬠) and 7.5 Å (black ⬡). Figure adapted form Ref. [134].

are slightly different than what we find for real water, and the differences account for the differences between our predicted melting line for real water and the calculated melting temperature of the mW model for $1/R = 0.1\text{Å}^{-1}$. See Fig. 4.8. The melting lengths for both the mW model and experiment agree with previously reported values based on fitting melting data to Eq. 4.34[63, 163].

4.3.7 Determination of $T_\mathrm{m}(R)$ from simulation

In order to determine the low pressure melting temperature in confinement we calculate the temperature dependence of the orientational order parameter Q_6 defined as

$$Q_6 = \frac{1}{N} \left(\sum_{m=-6}^{6} \sum_{i,j}^{N} q_{6m}^{i} q_{6m}^{j*} \right)^{1/2}, \tag{4.38}$$

following Ref. [207]. Rather than a local measure of order, we use this global measure of crystallinity to be sure we are distinguishing crystal from liquid. Figure 4.11 shows the

mean value of orientational order parameter, $\langle Q_6 \rangle$, as a function of temperature for six pore radii, $R_{\rm p}$, ranging between 20.0 Å and 7.5 Å. For the range of temperatures we consider, pores with $R_{\rm p} \leq 12.5$ Å never show pseudo long range order. Pores with $R_{\rm p} \geq 12.5$ Å do show pseudo long range order. The presence of the amorphous interface ensures that $\langle Q_6 \rangle$ converges relatively quickly in comparison to the bulk where large nucleation barriers would separate the ordered and disorder states at coexistence.

Apart from shifting the coexistence temperature, the pore radius changes the maximum value $Q_6(T)$ obtains in the ordered state. This is due to the increased weight that the amorphous boundary layer has on the volume integral for decreasing R and fixed thickness λ. The curves calculated for different R can be collapsed by multiplying Q_6 by a scaling factor. This factor accounts for the total volume available within pore compared to that for crystal-like states, $(R + 2\lambda)^2/R^2$, and subtractes the value for a disordered system of N water molecules.

4.3.8 Molecular simulation model

The molecular dynamics simulations used to test our theoretical approximations and estimate the magnitudes of some differential changes employ the mW model of water[161]. As discussed, this model has proven to yield a good description of water in the liquid phase[41, 164, 237], it reproduces many structural transformations seen in experiment and in other models of water (including freezing into an ice-like structure),[106, 130, 133, 165] and it exhibits the characteristic thermodynamic and dynamic anomalies of water (i.e., density maximum, heat capacity increase, diffusion maximum, and so forth)[133, 161].

To model the hydrophilic pores of MCM-41-S we have followed a procedure similar to that found in Ref. [163]. The pore configurations are obtained by quenching a high temperature liquid configuration of silica. To create the cylindrical geometry, we extract from the simulation box all atoms whose centers lie within a circle of radius $R_{\rm p} = [(x_i - x_c)^2 + (y_i - y_c)^2]^{1/2}$ where (x_c, y_c) is the center of the simulation box and (x_i, y_i) is the coordinate vector for particle i. The remaining atoms are tethered to their initial conditions by a spherically symmetric harmonic potential with a spring constant, 50 kcal/mol Å^2. This procedure yields a mean surface roughness for the pore walls in good agreement with that estimated from experiment on MCM-41-S materials[163]. We have considered pore sizes in the range $R = 5.0$ Å- 17.5 Å. All pores are length $L = 220$ Å to approach a regime where $L > R$. For initializing the combined water, pore system, water molecules are arranged in a hexagonal ice lattice at a density of 0.98 g/cm^3 and placed within the pore with the crystallographic c-axis parallel to the length of the pore.

All of the molecular dynamics trajectories were propagated using the LAMMPS package [177] and a Nose-Hoover thermostat with constant number of particles, N, volume, V, and temperature T. We fill approximately 90% of the length of the pore. Water organizes spontaneously with an interface separating the remaining 10% empty pore from the condensed phase (either liquid or crystal-like). With this procedure, we simulate the condensed material at a low pressure (effectively $p \approx 0$) in coexistence with vapor.

We have adopted an interaction potential for a single site model of silica that is the same form as the mW model, but we have rescaled the interaction strength and particle diameter. Compared to the parameters used in the mW model, these are $\epsilon_{\text{silica}}/\epsilon_{\text{mW}} = 1.15$ and $\sigma_{\text{silica}}/\sigma_{\text{mW}} = 1.05$. The increased interaction strength ensures a hydrophilic surface and the increased particle size frustrates local favored structures.

4.4 Directions for future study

The theory we have employed to describe premelting and freezing in a finite system would also seem applicable to stability and thermodynamics of nano-clusters of ice,[101] and to nucleation of ice on atmospheric aerosols[120]. It might also be generalizable to describe ordering of water in cold micro-emulsions like those recently considered by Tanaka and co-workers[167]. Indications of order-disorder phenomena occurring in the finite water-rich domains of those systems have been interpreted in terms of a doubtful liquid-liquid transition in supercooled water. Based upon what we have derived in this paper, we believe a more natural explanation of Tanaka's observations will be found in terms ice-water equilibrium and the effects of confinement on that phase equilibrium.

Another potentially interesting application of this theory is in the study of antifreeze proteins[40]. These proteins are produced by certain vertebrates, plants, fungi and bacteria that are implicated in their survival a low temperatures. The precise mechanism by which these proteins function is unknown. Research into their inhibition of growth rates on certain planes of ice and the structural correlations induced at these surfaces yield seemingly contradictory interpretations. Whatever the details of the mechanism, it is certainly the case that interfaces of ice are modulated by these proteins. Whether or not this modulation can be understood within the context of the results described herein is an exciting avenue to pursue in the future.

Chapter 5

Supercooled dynamics and nonequilibrium phases

Things that look quiet and still, like a glass of water,...
are active all the time... What looks still to our crude eyes
is a wild and dynamic dance.
- Richard Feynman [62]

In this chapter, we discuss the irreversible fluctuations that relax the liquid, those that transition liquid into the crystal and those that arrest the liquid and form a glass. The techniques employed are varied, including molecular dynamics simulations, simple scaling theory and analysis of experimental data. Parts of this chapter are borrowed from our previously published work, *J. Chem. Phys.* 137, 045509 (2012) and preprint *arXiv:1305.1382*. The principle results presented are an elucidation of the fundamental excitations that reorganize liquid water when it is supercooled and the existence of irreversible dynamic phase transitions between liquid water and its glasses and a between multiple glasses. The former admits the systematic study of the long timescale dynamics probed experimentally in bulk and confined water. The latter offers a well defined statistical mechanical explanation for the existence of polyamorphism in water. These results clarify a number of experimental observations.

5.1 Preliminaries

When water is supercooled, its dynamics slows down dramatically[43]. In this way, water acts like many other ordinary liquids that show an onset to super-Arrhenius temperature dependence when supercooled[7]. While the dynamics of supercooled liquids have been the focus of extensive studies, to date no theoretical consensus exists for its microscopic origin. Some major theoretical approaches that attempt to explain this behavior include

mode-coupling theory and random first order theory, see Refs. [74] and [114] for reviews[1]. An alternative explanation for the slow dynamics has been provided in recent years by dynamical facilitation theory[30]. Rather than emphasizing mean field behavior, it is based on the emergence of fluctuation dominance of the dynamics, which occurs below an onset temperature. While simple liquids above the onset temperature are well described by mean-field theory, temporal correlations at low temperature result in dynamic environments that are transiently different for different particles. In this view, the slow dynamics are controlled by the number of excitations that locate these transient regions of mobility. Our previous work has illustrated the importance of fluctuations on the stability of supercooled water [133, 134, 136]. As dynamical facilitation considers fluctuations directly it provides a natural framework to explore the the dynamic behavior of the liquid. It is within such theoretical structure that we will proceed.

Just as in the study of other condensed phase behavior we have discussed in previous chapters, the notion of an order parameter field is crucial for connecting microscopic configurations to experimental observations. For the dynamics of a supercooled fluid, the relevant field represents the amount of mobility in a specific region of space. Within the context of dynamical facilitation theory the mobility field is coarse-grained both in space and time. A convenient Hamiltonian for this field and its temporal evolution is given by a class of models known as kinetically constrained models (KCMs)[190]. On average the field is noninteracting, but its dynamics are strongly correlated. Specific rules for the evolution of the field vary from model to model, but generically there are kinetic constraints which restrict the volume of space-time phase space trajectories can explore. One important prediction of a particular Hamiltonian known as the East model[94] is a scaling relation for the temperature dependence of the relaxation time. This relation, known as the parabolic law, has a form,

$$\log \tau_{\rm liq}/\tau_{\rm o} = J^2 \ (1/T - 1/T_{\rm o}^*)^2 \tag{5.1}$$

where $\tau_{\rm o}$, J and $T_{\rm o}^*$ are material parameters that reflect the basic timescale, energy scale and onset temperature for relaxation. This form has been used to great success to collapse experimental and simulation data previously [51]. While we will rely heavily on this specific form to extract quantitative parameters for the supercooled dynamics of bulk and confined water, the arguments we will use to understand these parameters are largely independent of the form of the itself and will rather reflect scaling principles for energy and timescales that are conveniently extracted from this equation. Nevertheless, as we show below, in the instances we apply these ideas, the assumptions under which this equation is derived are found to be valid.

Another interesting aspect of kinetically constrained models is the existence of a nonequiliubrium phase transition in ensembles of trajectories[69, 93]. From the dynamic facilitation perspective, this phase transition illustrates the singularity that underlies the nature of the glass transition. Distinct from an equilibrium transition, the phase transition predicted

[1]These approaches are largely based on a mean field approximation for structural correlations that develop in the liquid, and posit singular responses in the equilibrium liquid behavior

in KCMs occurs only in a space of irreversible dynamics that place a liquid and a glass into coexistence. By mapping local molecular configurations to East model-like excitations, we can construct an order parameter for models of water that we find to also display this nonequilibrium singularity[112]. The phase diagrams that we compute in this way exhibit a remarkable amount of structure, with transitions between liquid and glass and between multiple glasses. This irreversible, dynamic phenomena offers a novel interpretation of the existence of polymorphism in water[6].

5.2 Heterogeneous dynamics

On average liquids are isotropic, so reorganization is equally likely to occur in one place as it is another. At high temperatures, liquids do not sustain temporal correlations beyond momenta relaxation, therefore at any given time diffusive motion occurs spatially throughout the system[79]. At low temperatures, while the liquid is structurally homogeneous on average, long temporal correlations exist that can result in transient regions of space where relaxation occurs preferentially[47]. Only over times much longer than the average structural relaxation time, do the dynamics appear uniform. This phenomena is known as dynamic heterogeneity, which is distinct from static heterogeneity that is absent in liquid matter. It is the existence of dynamic heterogeneity that is the central focus of the dynamic facilitation theory of the glass transition.

Microscopically, the onset of dynamic heterogeneity is a hallmark of the dynamics of supercooled liquids. Observations that supercooled liquids exhibit pronounced dynamic heterogeneity were first made in the 1990's in both experiment[34, 195], and computer simulation[115, 159]. Figure 5.1a provides an illustration of dynamic heterogeneity from a computer simulation of water. In particular, we render the field,

$$c(\mathbf{r}) = \sum_i^N c_i \delta(\mathbf{r} - \mathbf{r}_i) \,, \tag{5.2}$$

where c_i is an order parameter that distinguishes instantaneous regions of mobility from immobility. In this particular snapshot of a supercooled water, the order parameter is based on how far the oxygen atoms are at a time, t, from to their initial positions at time 0. In the snapshot in Fig. 5.1a, an 8000 particle system has been evolved for $t = 0.2\ \tau_{\rm liq}$, where $\tau_{\rm liq}$ is the average time for a molecule to displace a full molecular diameter. Rather than the full system homogeneously reorganizing, which would manifest a uniform change in color, localized domains of around 10 molecules reorganize, colored red, in a background of immobilty, colored blue. In between these regions, their are smaller domains of motion on shorter lengths, interpolated between blue and red. The structure of these emergent dynamical patterns reflect the transient dynamical correlations that precede mobility. The emergent features in this field have been analyzed by others for simpler liquids, such as binary mixtures of soft spheres[72, 112]. In the next section, we illustrate the implications of

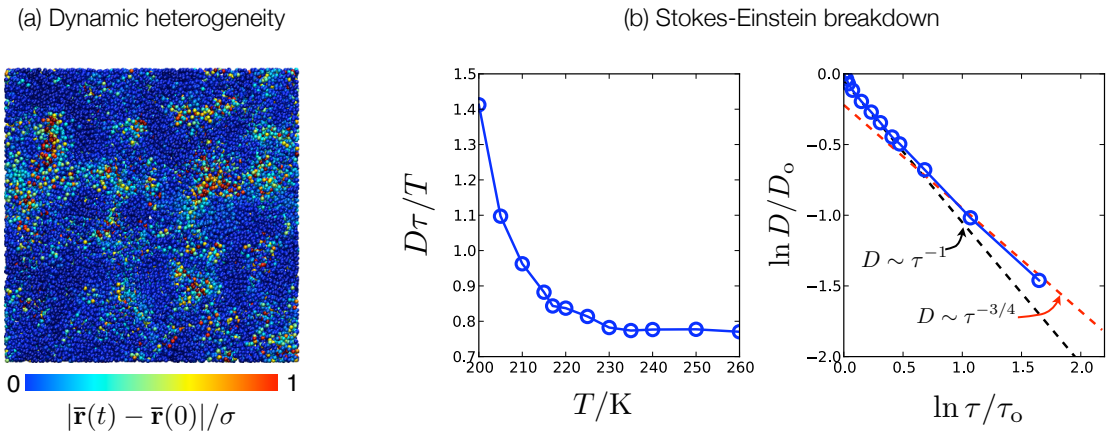

Figure 5.1: Dynamic heterogeneity and its implications on the dynamics of liquids. (a) A representative snapshot of the mobility field for the mW model at $T = 205$ K, $p = 1$ bar evolved for an observation time, $t = 0.2\ \tau_{\text{liq}}$. The code on the bottom colors particles based on the distance they have traveled in their coarse-grained coordinates over the observation time, in units of their molecular dimension. (b) Stokes-Enstein breakdown in supercooled mW model at ambient pressures. Middle panel plots the increasing deviation from the mean-field result, $D\tau_{\text{liq}}/T = \text{const.}$, upon decreasing temperature. Right panel plots the fractional relationship that the dynamics crosses over to below the onset temperature.

dynamic heterogeneity on the equilibrium relaxation properties, and define in a systematic way the relevant order parameter for supercooled dynamics.

5.2.1 Fluctuation dominated dynamics

At low temperatures where motion becomes sparse, supercooled liquid dynamics become dominated by rare fluctuations. As a consequence, mean field theories for liquid dynamics break down. For example, the over-damped Langevin equation, which successfully describes the motion of molecules at standard liquid conditions, predicts the temperature dependence of different timescales to be the same and nearly isothermal[28]. This is due to an assumption that a given tagged particle is surrounded by a linearly responding and adiabatically relaxing bath. At high temperatures these assumptions are valid and most dynamical properties are very nearly isothermal. At low temperatures, the bath no longer responds linearly or adiabatically, and different timescales can develop very different temperature dependencies[31, 83].

One experimental probable pair of timescales is the self-diffusion time and the structural relaxation time. At high temperatures, these two quantities are related by the Stokes-Einstein equation,

$$\frac{D}{T} \propto \tau_{\text{liq}}^{-1}\,, \tag{5.3}$$

where D is the self-diffusion constant, T is the temperature and $\tau_{\rm liq}$ is the structural relaxation time and proportional to the viscosity. The constant of proportionality, the shear modulus, is temperature independent. The diffusion constant is can be extracted from NMR experiments (See for example Ref. [31]). The structural relaxation time is typically calculated from the self-correlation function,

$$F_{\rm s}(k,t) = \left\langle e^{ik|\mathbf{r}_1(t)-\mathbf{r}_1(0)|} \right\rangle , \tag{5.4}$$

for a wave vector, $k = 2\pi/\sigma$, where $\sigma \approx 2.8$Åand can be extracted from neutron scattering[79]. The time at which, $F_{\rm s}(k,t)$, decays to $1/10$ of its initial value is defined as $\tau_{\rm liq}$. The relationship in Eq. 5.3 follows from linear response theory which equates the random forces of the bath to the viscous dissipation of Stokes' law[79]. Due to the heterogeneous dynamics of the supercooled liquid, however, at any given time the local environment of a particle can be different. As a result, there is a distribution of timescales for the response of the bath, and correlations between the structures that give rise to those timescales that persist over times, $t < \tau_{\rm liq}$.

Figure 5.1b shows the breakdown in the Stokes-Einstein relation for the mW model of water at ambient pressure. In the middle panel, the ratio $D\tau_{\rm liq}/T$ is plotted. At high temperatures this ratio is a constant, while at low temperatures it increases rapidly. This rise locates the onset temperature for dynamic heterogeneity, which for the mW model is close to the temperature of maximum density, $T_{\rm o}^* = T_{\rm o} = 250$ K. The separation of these timescales is reflective of different dynamical processes that occur in the supercooled liquid. In particular, the diffusion constant is a single particle property and therefore dominated by the most mobile particles at any given time. The structural relaxation time, on the other hand, is manifestly a function of the global density field and decays only when all particles have undergone reorganization. The right panel shows an apparent fractional Stokes-Einstein relationship that develops for the mW model $D \sim \tau_{\rm liq}^{-3/4}$. Such fractional relationships have been found previously in experiment[213, 224] and other simulations[236] and can be understood from KCMs[102]. Previous work has demonstrated a mapping between molecular configurations and a class of coarse-grained models. It this that mapping we turn to now.

5.2.2 Fundamental excitations

In order to understand this slowing down from a microscopic perspective, it is convenient to introduce an order parameter that measures instantaneous mobility. We follow the procedures of Keys et. al.[112] The procedures are based upon mapping the dynamics of atomic degrees of freedom to dynamics of a kinetically constrained East model.[94] The parabolic law, Eq. 5.1, is a consequence of that mapping.

To illustrate the procedure for water, we have carried out molecular dynamics simulations of equilibrated water models to determine the net number of enduring displacements of length a appearing in N-molecule trajectories that run for observation times $t_{\rm obs}$. This number of

displacements is

$$C_a = \sum_{i=1}^{N} \sum_{j=0}^{t_{obs}/\Delta t} \Theta\left(|\bar{\mathbf{r}}_i(j\Delta t + \Delta t) - \bar{\mathbf{r}}_i(j\Delta t)| - a\right) \tag{5.5}$$

where $\Theta(x)$ is 1 for $x > 0$ and zero otherwise, Δt is the mean instanton time for enduring displacements of length a, and $\bar{\mathbf{r}}_i(t)$ is the position of particle i averaged over the time interval $t - \delta t/2$ to $t + \delta t/2$. The averaging over δt coarse-grains out irrelevant vibrational motions. The instanton time, Δt, is taken to be large enough that non-enduring transitions are also removed from consideration. The two times, $\Delta t > \delta t$, are determined as prescribed by Keys et. al.[112]

The mean mobility (or excitation concentration) is the net number of enduring transitions per molecule per unit time, i.e.,

$$c_a = \langle C_a \rangle / (N t_{obs}/\Delta t). \tag{5.6}$$

Its dependence upon temperature and displacement length is illustrated in Fig. 5.2. According to facilitation theory, c_a should have a Boltzmann temperature dependence, with an energy scale that grows logarithmically with displacement length. That is,

$$c_a \propto \exp\left[-J_a\left(1/T - 1/T_o\right)\right] \quad \text{for} \quad T < T_o\,, \tag{5.7}$$

and

$$J_{a'} = J_a - g\, J_\sigma\, \ln\left(a'/a\right)\,, \tag{5.8}$$

where σ is a reference molecular length and g is a system-dependent constant.[2] The data graphed in Fig. 3 shows that for the model considered, the mW model of water, the theoretical expectations are obeyed. We have adopted the reference length $\sigma = 2.5$, which is close to the diameter of the molecule in the mW model, and find $g = 0.625$, $T_o = 244\,\mathrm{K} \approx T_o = 250\,\mathrm{K}$, and $J_\sigma/T_o = 23$.

According to facilitation theory[112], Eqs. 5.7 and 5.8 imply

$$\ln(\tau_{liq}/\tau_o) = \left(J_\sigma^2\, g/d_f\right)\left(1/T - 1/T_o\right)^2 \quad \text{for} \quad T < T_o\,, \tag{5.9}$$

where d_f is the fractal dimension of dynamic heterogeneity, which for $d = 3$ is about 2.6. Equation 5.9 therefore yields

$$J = J_\sigma \sqrt{g/2.3\, d_f} \tag{5.10}$$

where the factor of 2.3 in the square-root accounts for the conversion between base e and base 10 logarithms.[3] Applying Eq. 5.10 with the computed parameters yields $J/T_o = 7.4$, in good agreement with the universal empirical value reported in the previous section, that empirical value obtained from fitting data for various water models. Thus, we have succeeded

[2] Keys et. al[112] use the symbol γ for what we call g. We use γ to refer to the surface tension.

[3] Keys et. al[112] employ natural logarithms in their use of the parabolic law, and thus the factor of 2.3 does not appear in their equations.

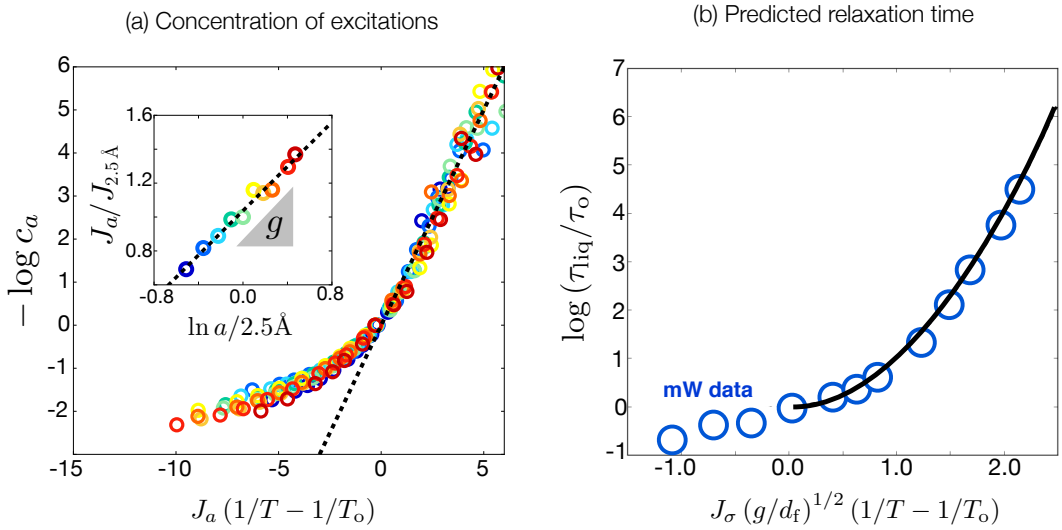

Figure 5.2: Concentration of excitations that led to reorganization for the mW model at ambient pressure. (a) The main panel plots the mean concentration of excitations, as defined in Eq. 5.5, for lengthscales, a, between 1.5 and 3.5 Å. The dashed line is has a unit slope illustrating the Boltzmann scaling in Eq. 5.7. The inset plots the free energy determined by fitting c_a as a function of a. The dashed line is a fit to the data for Eq. 5.8 with $\eta = 0.65$. (b) The structural relation time for the liquid versus the parameters extracted from the data in panel (a). Data generated for the mW model is plotted with blue circles and a parabola is plotted with the solid black line. This figure has been adapted from Ref. [135].

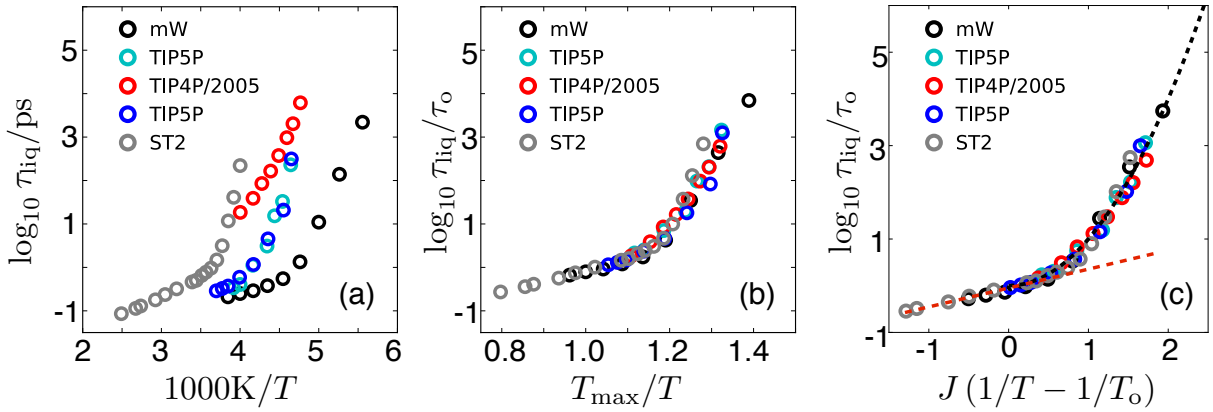

Figure 5.3: Structural relaxation for different models of water. (left) Structural relaxation as a function of absolute temperature and time. (middle) Structural relaxation as a function of temperature relative to the temperature of maximum density and reduce time. (right) Structural relaxation collapsed to the parabolic form, see Eq. 5.1. This figure has been adapted from Ref. [135].

at deriving this value from a molecular calculation. Figure 5.2b plots the relaxation time for the mW model at ambient pressures. The x-axis is in units of the prefactor to the temperature in Eq. 5.9 for convenience. The black line is the predicted parabola and the agreement with it and the data illustrates the success of the construction of the mobility field in terms of mobile excitations.

5.3 Determining T_g for water

Because liquid water easily crystallizes at moderately low temperatures, it is difficult to experimentally probe its dynamics deeply into the supercooled regime. Two different strategies are used to circumvent this problem, both relying on a solid theoretical understanding of the behavior of supercooled dynamics. First, molecular simulation of realistic models of water can be used together with proper means of excluding effects of crystallization. By studying different models, we can elucidate relevant energy and length scales that can be straightforwardly related to experiment. Second, by experimentally constraining water to nanoporous materials the melting temperature of water can be lowered (see. Chap. 4). Provided the confinement acts as a perturbation to the water inside these pores, we can relate transport data recorded experimentally under such conditions to the bulk with scaling arguments. We find below that this approach is successful down to pore sizes of $R \approx 1$ nm, beyond which fluctuation effects dominate and the confinement is no longer perturbative. This is similar to the conclusion we found in the previous chapter in which the melting temperature for water in such confinement disappears at this same lengthscale.

5.3.1 Relaxation in models of water

Figure 5.3 reports the structural relaxation time for several models of water taken from Refs. [180, 229, 238]. In all cases, the time is calculated by averaging the self-correlation function as in Eq. 5.4. In all of the models studied, the temperature dependence crosses over form almost athermal to super-Arrhenius. The location where this occurs varies from model to model as does the timescale in the high temperature limit. This is not surprising because even though all of this data is taken for models of water, the phase diagrams for each model are different. Previous chapters suggested that the temperature of maximum density, T_o, is related to the pertinent energy scale for the structure and thermodynamics of supercooled water. Physically, T_o reports on the temperature where the entropy of packing are balanced by the orientational forces of hydrogen bonding. The use of point charges[180, 229, 238] or three bodied interactions[161] may change the magnitude of the hydrogen bonding energy, but these results suggest that the change is proportional to T_o.

As shown in the middle panel of Fig. 5.3, by referencing the data to the temperature of maximum density for the different models, the relaxation behavior can be collapsed. While T_o varies widely for the different models 250 K to 320 K,[223] the collapse shows the the energy scale for relaxation in units of that temperature is universal for the different models. Accompanying the reference energy scales are different reference timescales, τ_o, for the different models. For the range of models considered here, τ_o varies between 0.3ps and 6.0ps.

We can quantify precisely the parameters that best represent the data by fitting each model data set to Eq. 5.1. Panel c in Fig. 5.3 shows the results of that fit. Within the error of the three parameter fit, τ_o, J, and T_o^*, an unbiased estimate of the onset temperature agrees with our previous assertion that it corresponds to the temperature of maximum density, i.e. $T_o^* \approx T_o$. The reduced energy scale, J/T_o^*, determined from the fit varies from model to model by no more that 5% and on average by only 1%. While there is not sufficient experimental data to determine whether this relationship holds for real bulk water, due to crystallization, in the next section we will show how we can estimate J and T_o from experiments of confined water.

5.3.2 Relaxation in confined water

Our strategy for examining relaxation in confined water is to use the same scaling principles used above, to bootstrap to the glass transition from knowledge of structural relaxation times at moderately supercooled conditions, and to use molecular simulation to test assumptions underlying that approach.

One experimentally measurable property of the dynamics of water in confinement is the location of the glass transition temperature, T_g. The blue surface shown in Fig. 4.8, $T_g(p, R)$, is defined to be the temperature below which the structural relaxation time, τ_{liq}, of supercooled liquid water would be larger than 100 s. Nonequilibrium perturbations taking place on shorter time scales, such as cooling rates in the range of 0.1 K/min to 1 K/min or

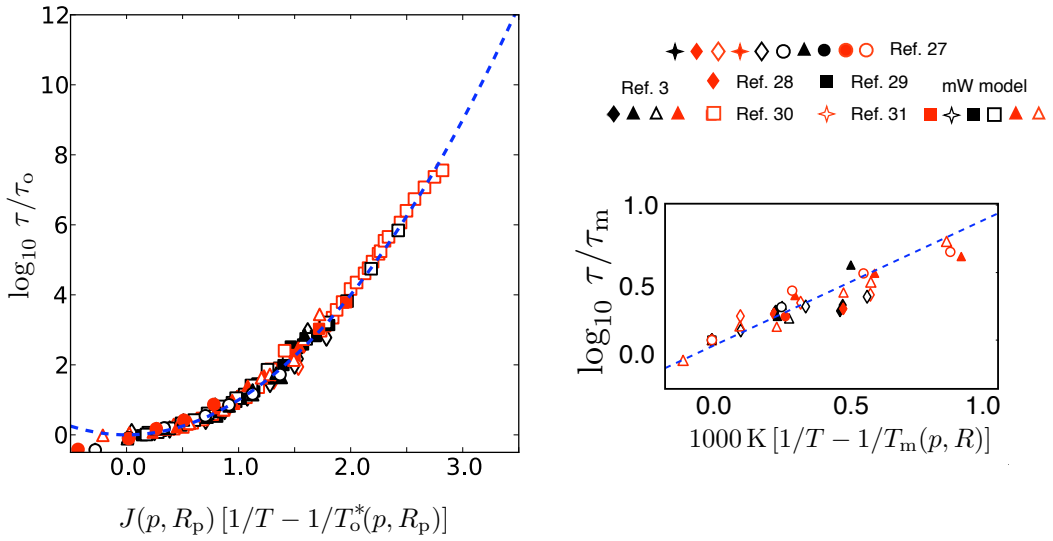

Figure 5.4: Collapse of confined liquid water relaxation times for different pore sizes and at different external pressures. Primary graph is for $T > T_m(p, R)$. The data is from our simulation results and experimental results[78, 84, 91, 142, 143, 149]. Inset graph is for relaxation times of crystal-like state, i.e., $T < T_m(p, R)$. It includes our simulation results and remaining data taken from Refs [84, 91, 142, 143, 149]. This figure has been adapted from Ref. [134].

faster, would take the liquid out of equilibrium. It is in that sense that $T_g(p, R)$ is the glass transition temperature. To estimate its behavior, we note that $\tau(T)$ generally follows the parabolic form below an onset temperature,[50, 51] i.e., Eq. 5.1. This plot was also referred to in the previous chapter in the context of freezing in confinement. We adopt this expression together with $100\,\mathrm{s} = \tau(T_g, p, R)$. The reference time, τ_o, the fitted onset temperature, T_o^f, and the energy scale, J, are generally functions of p and R. These functions can be determined from simulation and experiment. As shown in the previous section in bulk water, the fitted onset temperature is $T_o^* = T_o$ the temperature of maximum density, however at elevated pressures and in confinement this is no longer a straightforward correspondence.

One such determination is that τ_o for water is close to 1 ps throughout the range of p and R we find relevant. Accordingly, Fig. 4.8 graphs

$$T_g(p, R) \approx T_o^*(p, R) \Big/ \left[1 + \sqrt{14}\, T_o^*(p, R)/J(p, R)\right] . \tag{5.11}$$

From experiment and simulation of water, we can determine functional forms for $J(p, R)$ and $T_o^*(p, R)$. See below. While each depends monotonically on p and R, their systematic trends lead to the non-monotonic behavior $T_g(p, R)$ illustrated in Fig. 4.8. Most notable is how the slope of $T_g(p, R)$ with respect to p changes from small and negative when R is large to relatively large and positive when R is small.

A different variation is associated with the temperature of a liquid-to-crystal-like transition that occurs for R > 1 nm, a variation that is detected in a change in transport from super-Arrhenius in the liquid to Arrhenius in the crystal. This change in temperature variation of transport (a so-called fragile-to-strong transition) is discussed later. It should not be confused with a glass transition.

The pressure variation of $T_g(p, R)$ explains a few critical observations. In particular, recent calorimetry experiments probing glassy relaxation in confined systems have estimated $T_g(p, R)$ for several pore sizes [173] at low pressures. The results of those observations (the squares in Fig. 4.8) coincide closely with our predictions for this glass transition temperature. Furthermore, Zhang et al. [240] have, in effect, located the glass transition temperature at higher pressures through their observation of hysteretic behavior for density in nano-pores upon cooling at a rate of 0.2 K/min. Hysteresis occurs only because the system falls out of equilibrium. Data points from Ref. [240] (the circles in Fig. 4.8) fall close to our predicted glass transition temperature line. That reference attributes the hysteresis to something other than a glass transition, namely a hypothesized liquid-liquid transition[185]. Previous work by us casts doubt on that possibility,[133] leaving the glass transition as a plausible explanation for pore sizes as small as those reported in Refs. [202, 239, 240]. If the pore sizes were a factor of 2 larger than estimated by those authors, our phase diagram indicates that hysteresis could also reflect time scales for nucleating an ordered crystal-like material.

To evaluate the glass transition temperature from Eq. 5.1, we must determine τ_o, $T_o^*(p, R_p)$, and $J(p, R_p)$. These parameters control very long-time relaxation, but they can be accessed through computation and experiment that measure relatively short time behavior[112]. For bulk water, measured relaxation times yield $T_o(1\,\text{atm}) \equiv T_o \approx 271\,\text{K}$, while the mW model used in our simulation yields $T_o \approx 250\,\text{K}$; similarly, for bulk water $J(1\,\text{atm}) \equiv J \approx 7.5\,T_o$, while the mW model used in our simulation yields $J \approx 6.8\,T_o$. This number for the mW model agrees excellently with the one derived from the picture of fundamental excitations, $J/T_o = J_\sigma\sqrt{\gamma/d_f} = 6.7$.

In creating our phase diagram, we use the real-water values for these quantities. Nevertheless, the comparison between these quantities for real water and for the mW model give us confidence in using simulation to estimate quantities not available from experiment. In particular, because liquid structure of mW water is virtually identical to that of real water,[161] we expect that relative dependence upon R_p can be accurately estimated with the simulation. The dependence we find in that way for $R_p \gtrsim 5$ Åis $T_o^*(R_p) \approx T_o[1 + (6.0\,\text{Å}/R_p)^2]$, and $J(R_p) \approx J(1 - 4.4\,\text{Å}/R_p)$, where $T_o(R_p)$ and $J(R_p)$ stand for the low pressure values for $T_o^*(p, R_p)$ and $J(p, R_p)$, respectively.

For the pressure dependence of these quantities, we rely on experimental measurements of relaxation times at $R_p \approx 7.5$Å[142]. That data allows us to estimate first and second derivatives with respect to pressure, leading us to write

$$J(p, R_p) \approx J(R_p) + 490\,(\text{K/kbar}^2)p^2 \tag{5.12}$$

and

$$T_o^*(p, R_p) \approx T_o^*(R_p) - 26\,(\text{K/kbar})\,p\,, \tag{5.13}$$

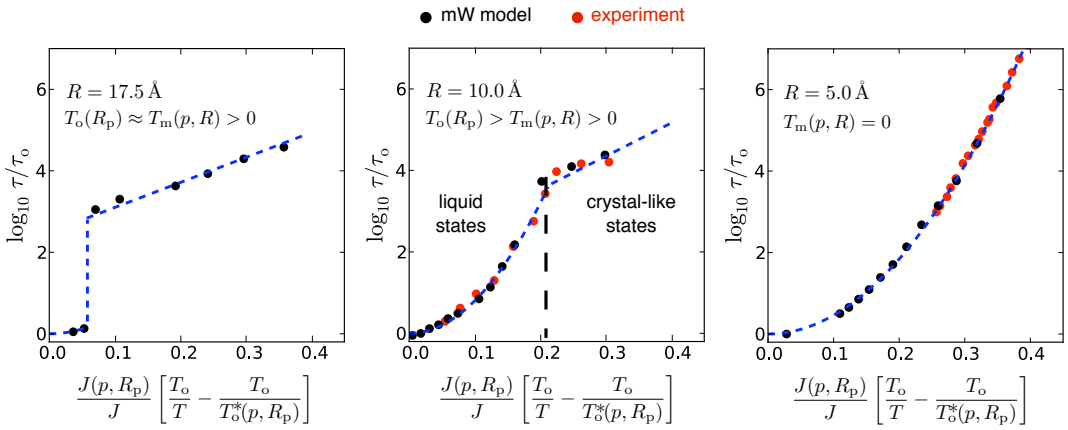

Figure 5.5: Transport behavior for different pore sizes as indicated. Data are from simulation results (black points) and experimental results (red points). Lines are predictions based on our phase diagram and scaling relations. Vertical dashed line in the middle panel locates the boundary between liquid and crystal-like states, i.e., where $T = T_m(p, R)$. This figure has been adapted from Ref. [134].

where $J(R_p)$ and $T_o^*(R_p)$ are given in the paragraph above. We have checked that these algebraic forms accurately extrapolate from the low-pressure values of the mW model at finite R_p to the high-pressure values for the mW model at $1/R_p \to 0$.

Using these forms for the transport parameters, and a value of $\tau_o = 1$ ps, we can collapse experimental data and our simulation results across pressures and pore sizes. Figure 5.4 shows this collapse where we have restricted the data to include only equilibrium liquid relaxation, i.e., $T > T_m(p, R)$. Figure. 5.4 includes data from both experiment [78, 84, 91, 142, 143, 149] and from our simulation study. While external pressures can be accurately controlled and reported, errors in pore sizes are large[150].

Previous simulation[67] and experiment [91, 142, 143, 149] studies have indicated that confined liquid water undergoes an abrupt crossover in the temperature scaling of its relaxation time. This crossover is a manifestation of a transition between the liquid and crystal-like regimes, which we turn to now.

5.3.3 Explanation of the fragile-to-strong crossover in confinement

Molecular motion of crystal-like states in confinement takes place preferentially near the water pore interface, where the molecules are locally disordered. Like defect motion in a bulk crystal, though with a smaller barrier due to the presence of the interface, the temperature dependence of such motion is expected to be Arrhenius. The inset of Fig. 5.4 shows experimental and simulation data for the average time for a particle to displace one molecular diameter as a function of temperature at conditions where water in the core is

ordered. Plotted is experimental data for $T < T_m(R)$ and simulation results for $R = 17.5$ Å. We find that this motion is activated with a barrier of approximately 20 kJ/mol, and an attempt frequency $1/\tau_m \approx 2$ ps^{-1}. There is negligible dependence on radius of confinement within the range considered.

By combining the information of the phase diagram with our understanding of the mobility in each state we can predict the observed equilibrium behavior of the relaxation time. We find that there are three different pore size regimes, each with a distinct temperature dependence of τ. These regimes are highlighted in Fig. 5.5. First, for larger pores, $R > 2$nm, the onset to glassy dynamics is close to $T_m(p, R)$, therefore an equilibrium measurement should show little temperature dependence for $T > T_m(p, R)$ and an Arrhenius temperature dependence for $T < T_m(p, R)$ reflecting the relaxation behavior of the crystal-like states. For smaller pores close to but larger than 1nm, the onset temperature is greater than $T_m(p, R)$, therefore an equilibrium measurement should show parabolic temperature dependence for $T > T_m(p, R)$, and a crossover to Arrhenius behavior for $T < T_m(p, R)$. For very small pores, $R < 1$nm (but still larger than a molecular diameter), $T_m(p, R) = 0$ therefore an equilibrium measurement should show parabolic temperature dependence for $T < T_o^*$. Figure 5.5 shows that each of these regimes are observed both in simulation and in experiment.

We are not the first to suggest that the abrupt crossover in relaxation might be linked to crystallization[203]. Some may have disregarded this possibility due to the absence of a freezing peak in the heat capacity, measured by differential scanning calorimetry. Our analysis shows that the absence of this peak is due to the pore size being close to 1nm. When $R \approx 1$nm, the ordering transition is smeared due to large structural fluctuations. As a consequence, there will be no sudden heat release. This explanation is consistent with a recent differential scanning calorimetry study that observed only partial crystallization for a pore size $R_p = 10.5$, with the accompanying heat capacity peak being of the order of the magnitude of the maximum liquid state heat capacity[173].

Experimentally determined vibrational density of states for confined supercooled water differs significantly from that of bulk ice, even at points in the phase diagram where we predict the presence of crystal-like behavior. This difference in density of states is expected because the domain of crystal-like behavior in the confined system is surrounded by a premelting layer, which in turn is surrounded by a layer of complete disorder. These layers, discussed previously, encompass a significant fraction of the total system, a fraction that grows with decreasing pore size. Further, even away from the disordered pore wall, crystal-like behavior in confinement exhibits a high concentration of stacking faults,[162] which will further modify the density of states.

A recent neutron scattering study [54] is in line with our analysis. It reports a monotonic pore size dependence of the temperature of the density minimum first reported in Ref. 5. But unlike Ref. 5, this new work considers both small and large R regimes. At large pores ($R > 1.7$ nm), the new work finds clear signatures of crystallization at the density minimum [54], i.e., this temperature of minimum density is a direct manifestation of freezing. Other signatures of freezing disappear for $R < 1.7$ nm, in accord with Ref. 5, but the variation of the temperature of minimum density continues smoothly from the larger R regime.

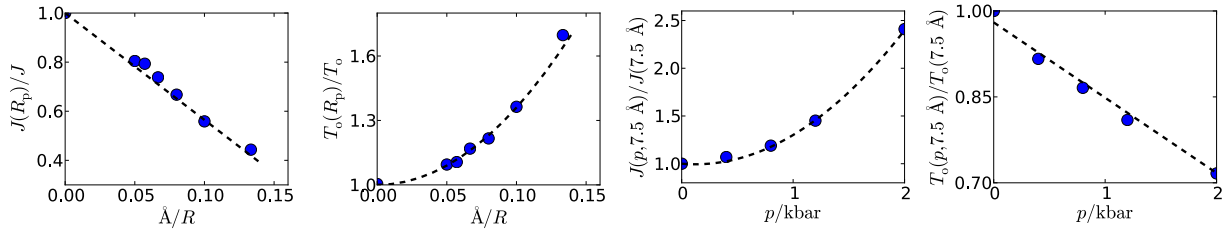

Figure 5.6: Onset temperature, $T_o^f(p,R)$ and energy scale, $J(p,R)$. The top two graphs are low pressure data found from simulations of the mW model. The bottom two graphs are high pressure data found from fitting experimental results of Ref. [142]. In that case, the experiments report $R_p = 7.5$Å.The dashed lines are the curves obtained with Eqs. 5.12 and 5.13. This figure has been adapted from Ref. [134].

We preformed a regression analysis on the algebraic forms used for $J(p,R_p)$ and $T_o^*(p,R_p)$, Eqs. 5.12 and 5.13. See Fig. 5.6. The top two panels concern the dependence upon R_p, and the data for relaxation times is obtained from our molecular dynamics simulations of the confined mW model. The bottom two panels concern the pressure dependence, and the data for relaxation times is taken from experiments on confined water with $R_p = 7.5$ Å[142]. The dashed lines are our algebraic fits, where the correlation coefficients indicate a certainty of 1% or better. Relaxation times for the molecular dynamics simulations were determined by calculating the mean time for a particle to displace one diameter,

While nominal nanopore radii are routinely reported in the literature, it is difficult to obtain a reliable estimate of R_p for $R_p < 1$ nm. Different techniques yield a range of different sizes.[150] Most commonly, pore sizes are inferred from a Barrett-Joyner-Halenda (BJH) analysis[11]. This method amounts to measuring a nitrogen absorption isotherm, and is thus an indirect measure of size. Mancinelli et al have demonstrated that this method can yield significant errors, up to 200 %. For example, using refined neutron scattering data and mass balance calculations, Mancinelli et al. have estimated a likely range of pore sizes for the system studied by Ref. [142] to be between 7.5Å– 12.6Å,[150] while the BJH method yields 7.5Å± 2Å.

Using the bounds provided by Ref. [150] as reliable estimates of possible errors, we find that we can collapse the experimental transport data, but such a collapse cannot be obtained within the errors reported from the BJH method. The pore sizes inferred from this collapse indicates that the BJH method systematically underestimates pore sizes[239]. Previous studies claiming to study the same pore sizes have observed widely different behavior. For instance, Ref. [142] report a pore radii $R_p = 7.5$Å, and measure a relaxation time that is never larger than 10's of nanoseconds. Reference [173] in one experiment also report using a pore of radii $R_p = 7.5$Åand measure thermal signatures indicative of a glass transition implying relaxation time on the order of seconds. In light of our results detailing the different transport regimes that can occur for slightly different pore sizes, the implications of the errors

associated with the reported values of the pore size become significant.

5.4 Timescales for metastability

Supercooled liquids exist in a metastable equilibrium that manifests a separation of timescales between local liquid equilibration and global crystallization[42]. The former, $\tau_{\rm liq}$, we have discussed in detail in this chapter. The later, which we denote $\tau_{\rm xtl}$, is a function of both local liquid reorganization and the rare fluctuations that led to interface formation. Below, we work we work out a simple scaling theory for $\tau_{\rm xtl}$, which is capable of collapsing previously published data for crystallization times. Further, the scaling arguments allow us to rationalize and compute the behavior of the separation of timescales, and importantly when such separation ceases.

5.4.1 Scaling theory for crystallization time

To estimate the timescale of crystallization, $\tau_{\rm xtl}$, we start with the usual form,

$$\tau_{\rm xtl} = \nu^{-1}(T) e^{\Delta F(T)/k_{\rm B}T} \tag{5.14}$$

where $\Delta F(T)$ reflects the free energetic penalty for growing a nascent crystal and $\nu^{-1}(T)$ is the timescale for adding material to the burgeoning phase. Typical forms for $\Delta F(T)$ can be motivated by classical nucleation theory, which has been shown previously to yield accurate results for nucleation rate of models of water at moderate supercooling. In general, this free energy can be written as,

$$\Delta F(T) = \Phi(\gamma/\Delta h)(T - T_{\rm m})^{-2} \tag{5.15}$$

where $\Phi(\gamma/\Delta h)$ is function of the ratio of surface to bulk energies and to lowest order, is temperature independent[42]. The temperature dependence $(T - T_{\rm m})^{-2}$ comes from expanding the chemical potential difference to lowest order in T. This form for the free energy has the right asymptotic behavior in that is monotonically increasing function for $T < T_{\rm m}$ and is infinite exactly at $T = T_{\rm m}$.

The timescale for adding material to a growing cluster, ν^{-1}, is expected to be relatively athermal at high temperatures, but increase with supercooling. A reasonable choice for the form of ν would relate it to the diffusion constant. As discussed, the diffusion constant and the structural relaxation time obey a fractional Stokes-Einstein relationship, which with Eq. 5.1 implies a super-Arrhenius form for ν,

$$\nu^{-1}(T) \propto \exp\left[\lambda \left(1/T - 1/T_{\rm o}\right)^2\right] , \tag{5.16}$$

where λ is related to J, the energy scale for structural relaxation, and $T_{\rm o}$ is the onset temperature, which for water is approximately the temperature of maximum density. In Section 3.3, we showed that to a good approximation the energy scale associated with transport is governed by $T_{\rm o}$ (see. Fig. 5.3), and universal for different models of water.

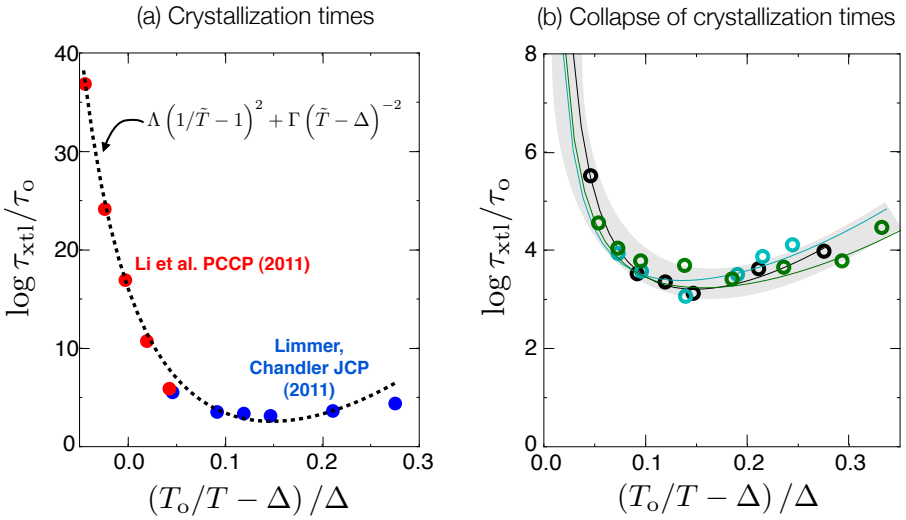

Figure 5.7: Collapse of the crystallization times for models of supercooled water. (a) Crystallization times calculated for the mW model spanning the nucleation and growth regimes. Red markers are taken from Ref. [130]. Blue markers are calculated in this work, see text. The dashed black line is given by Eq. 5.17. (b) Crystallization times for different models collapse. Cyan markers are our data for the mW model. Black and green markers are for TIP5P, taken from Ref. [238]. Lines individual fits to Eq. 5.17 for the different data sets. This figure has been adapted from Ref. [135]

Using Eqs. 5.14–5.16, we can write an expression for the crystallization time in terms of a reduced temperature, $\tilde{T} = T/T_o$. The resultant expression is,

$$\log(\tau_{xtl}/\tau_o) = \Lambda\left(1/\tilde{T}-1\right)^2 + \Gamma\left(\tilde{T}-\Delta\right)^{-2}, \tag{5.17}$$

where Λ is a coefficient for mass transport, Γ is a dimensionless ratio of surface to bulk free energies, $\Delta = T_m/T_o$ is the ratio of the melting temperature to the temperature of maximum density. While we have shown that the temperature dependence of the growth times, given by the energy scale Λ, is universal for models of water, Δ and Γ are not. We will show in the next section that typical sizes of Λ are $\mathcal{O}(10^2)$ and Γ are $\mathcal{O}(1)$. Before we can test how well this scaling form works, we need to calculate crystallization times.

5.4.2 Time-temperature diagrams

At conditions of liquid metastability, where a free energy barrier separates liquid and crystal basins, nucleation is the rate-determining step to form the equilibrium phase. For those conditions, we have computed this rate constant following a standard Bennett-Chandler procedure for rare-event sampling[65]. Specifically, we take Q_6 as the reaction coordinate, so that the rate constant for nucleation is $k_{nuc} = \nu \exp[-F(Q_6^*)/k_B T]$, where Q_6^* is the point

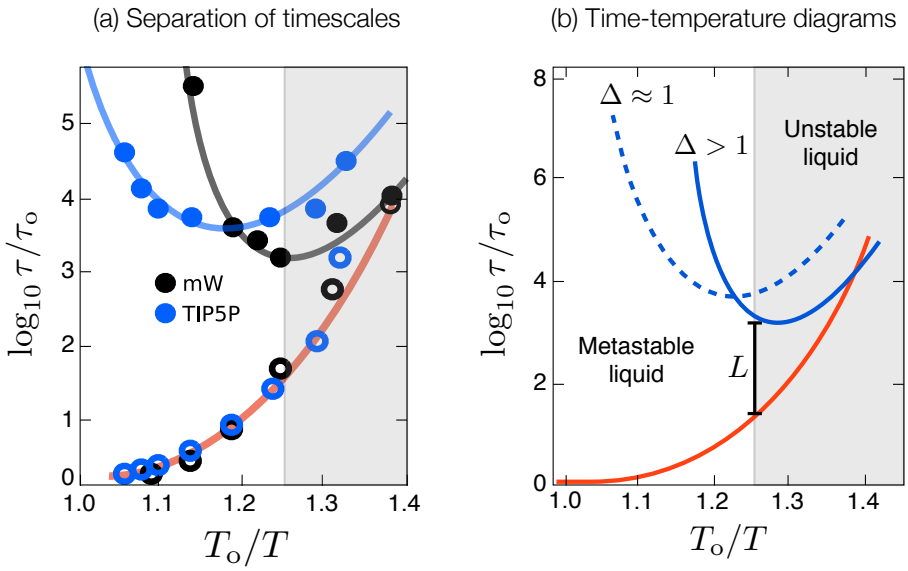

Figure 5.8: Time scales of the supercooled liquid mW and TIP5P water at 1 bar. (a)Computed structural relaxation times, $\tau_{\rm liq}$, are shown with open points. Computed crystallization times, $\tau_{\rm xtl}$, are shown with filled points. Statistical uncertainties are smaller than the symbols. Lines are the predicted fits to Eq. 5.1 and 5.17. The grey region is where the liquid is unstable. (b) Schematic dependence on $\Delta = T_{\rm m}/T_{\rm o}$ for the separation of timescales, L. This figure has been adapted from Ref. [135].

of maximum $F(Q_6)$ between liquid and crystal basins, and the prefactor, ν, includes the transmission coefficient. This prefactor is determined by sampling trajectories initialized at the top of the free energy barrier, i.e., initialized at configurations with $Q_6 = Q_6^*$[215]. Other choices of transition state are possible, but the net result is invariant to that choice[27]. Results obtained in that way with $N = 216$ mW particles are shown in Fig. 5.7. Similar rare-event methods have been used previously to calculate the the nucleation times for the mW model at even higher temperature. Specifically, Li et al have calculated the nucleation rate using forward-flux sampling with an order parameter based on a crystalline cluster sizes[130]. Results obtained in this way with are shown in Fig. 5.7a.

For conditions of liquid instability, (i.e. the no-man's land where there is no barrier between liquid and crystal), the method of rare-event sampling is no longer appropriate. For those conditions, we compute first-passage times[220]. The results obtained depend upon the initial preparation of the system because the unstable system is far from equilibrium. In the particular preparation we employ, we equilibrate the system in the liquid region at $T/T_o = 0.84$ where the liquid is metastable. Then at time $t = 0$, the system is quenched to the target temperature and allowed to evolve towards the crystal state. The first-passage time is taken as the first time a trajectory with initial conditions prepared in that way reaches

a configuration with $Q_6 = 0.2$. We find an exponential distribution of first-passage times. Mean values from that distribution are the values of $\tau_{\rm xtl}$ shown in Fig. 5.8 for no-man's land state points. Similar calculations based on first passage times have been calculated for the TIP5P model. In these calculations Yamada et al used as the potential energy as an order parameter for distinguishing crystallization[238]. These calculations are shown in Fig. 5.8b. Here $\tau_{\rm o}$ for the TIP5P model is 8 ps.

The crystallization time, $\tau_{\rm xtl}$, in Fig. 5.7 shows a non-monotonic temperature dependence expected from Eq. 5.17. At higher temperatures, nucleation rates increase because the barrier to nucleation decreases in size. In contrast, at lower temperatures, the process of crystallization is slowed by the onset of glassy dynamics. At conditions where the amorphous phase is unstable, $\tau_{\rm xtl}$ becomes limited by mass diffusion, which is proportional to $\tau_{\rm liq}$. In this region of the phase diagram the liquid state is no longer physically realizable. The boundary to unstable amorphous behavior is often referred to experimentally as the "homogeneous nucleation line," This terminology is possibly confusing because no significant barrier to nucleation exists in no-man's land. We identify it with the liquid instability line, $T_{\rm s}$. Indeed, studying the same model with straightforward molecular dynamics in the region of no-man's land, at $T/T_{\rm o} = 0.72 < T_{\rm s}/T_{\rm o}$, Moore and Molinero conclude that the critical nucleus is less than 10 molecules[165]. Coarsening times for relaxing defects in the crystal are necessarily longer than $\tau_{\rm xtl}$; and for mW water these times seem to be at least two orders of magnitude larger[165].

In the case of the mW model, we can determine the two constants in Eq. 5.17, Γ and Λ from specific material properties. In particular, we can combine the parabolic law and the fractional Stokes-Enstein relation, with the material properties measured with the fundamental excitations to determine,

$$\Lambda = \frac{3\eta}{4d_{\rm f}} \left(\frac{J_\sigma}{T_{\rm o}} \right)^2 . \tag{5.18}$$

For the mW model these parameters have been measured yielding, $\Lambda = 42$. If we make the assumption that classical nucleation theory is valid at high temperatures, then we can work out a form for Γ. In particular for spherical critical nuclei,

$$\Gamma = \frac{4\pi}{3} \left(\frac{2\gamma}{\Delta h} \right)^2 \frac{\gamma}{k_{\rm B} T_{\rm m}} \Delta^2 , \tag{5.19}$$

where γ is the liquid-crystal surface tension and Δh is the heat of fusion. All of these properties have been measured previously and yield, $\Gamma = 1.05$. Equation 5.17 with this parameterization is plotted along side the numerical data in Fig. 5.7. The agreement is good over some 10 orders of magnitudes, spanning ns to ms. The worst agreement is at the lowest temperature, where the rate is the most sensitive to the protocol by which it is calculated as the liquid is no long metastable at this condition.

In plotting $\tau_{\rm xtl}$ in Fig. 5.7, we use a different reduced temperature scale than previous plots of $\tau_{\rm liq}$. This scale is chosen to emphasis the crossover region, where nucleation and

growth compete. This particular scale also allows for crystallization times to be collapsed for different models. This is because to first order in $1-\Delta$ this scale locates the minima in $\tau_{\rm xtl}$. The precise minima is the solution to a quadratic polynomial[4]. This scaling only for holds $T \ll T_{\rm m}$. Away from the singular response at $T = T_{\rm m}$, this form is conserved from model to model as it reflects the universal structural relaxation times away from the nucleation dominated regime.

Figure 5.8 plots both $\tau_{\rm liq}$ and $\tau_{\rm xtl}$ to illustrate how the separation of timescales evolves as a function of temperature for different models of water. By considering two cases, where $T_{\rm o}$ is equal to $T_{\rm m}$ and where is it less than $T_{\rm m}$, the gap in timescales near the instability line, $T_{\rm s}$, changes. Specifically, $T_{\rm s}/T_{\rm o}$ is a constant for most models of water, $T_{\rm s}/T_{\rm o} \approx 0.8$ at ambient conditions. We can define a gap, $\Omega(T_{\rm s}) = \log \tau_{\rm xtl}/\tau_{\rm liq}$ in timescales evaluated the instability line, and ask how this changes with Δ. As shown in Fig. 5.8 for only two different models, this timescale can change by more than an order of magnitude. A specific functional dependence can be derived from Eq. 5.1 and 5.17, which yields,

$$\Omega(T_{\rm s}) = \Gamma\Delta^2/(T_{\rm s}/T_{\rm o} - \Delta)^{-2} - \Lambda(T_{\rm s}/T_{\rm o} - 1)^2/4 \ , \tag{5.20}$$

which for the mW model is nearly 2.5 in base 10. For experiment, in which $\Delta = 1.01$ and Γ can be computed using Eq. 5.19 which yields $\Gamma = 1.57$. From these parameters we would predict $\Omega(T_{\rm s}) = 4.0$. These is in indirect agreement with recent simulation work on the TIP4P/2005 model which has concluded that crystallization times are too long to be probable with straightforward simulation[189].

5.5 Amorphous ices

Polyamorphism is the ability of a single component material to form distinct amorphous states under different experimental protocols [153]. Polyamorphism in water has been achieved through various experimental protocols resulting in a multitude of disordered structures which have become known collectively as amorphous ices [6, 146]. These materials are thermodynamically unstable in that they easily crystallize when heated to temperatures where molecular reorganization can occur[52, 157]; however at the temperatures where they are produced these materials display a wide variety of reproducible structural, thermal, and dynamical behavior. Using rigorous statistical mechanical calculations for a minimal atomistic model of water we demonstrate that the transitions between liquid water and amorphous ice and between different amorphous ices are examples of first-order dynamical phase transitions. The singularity underlying the dynamical phase transition is distinct from one within a traditional equilibrium partition function of configuration space, but rather exists in an irreversible space of trajectories.

[4]The solution for the minima is $\tilde{T} = 1/2(((\Delta-1)^2+((\Gamma/\Lambda)^{1/2}-1)^2-1-2\Delta(\Gamma/\Lambda)^{1/2})^{1/2}+\Delta-(\Gamma/\Lambda)^{1/2}+1)$

5.5.1 Nonequiliubrium phase diagram

At equilibrium, the Boltzmann distribution provides a unique definition for the probability of configurations. Out-of-equilibrium, no similar distribution of states generically exists. In order to consider phase transitions out-of-equilibrium, we therefore start by identifying the ensemble that defines the phase space in which the singularity will exist. Do to this we follow Refs.[69, 93] by defining an ensemble of trajectories with well defined measure. Specifically, we consider an ensemble defined by, $\mathbf{X}(t_{\rm obs}) = (\mathbf{r}^{3N}(t_0), \mathbf{r}^{3N}(t_1), ..., \mathbf{r}^{3N}(t_{\rm obs}))$, which is a vector that contains the positions of all of the particles at all times up to an observation time, $t_{\rm obs}$. A particular member of the ensemble has a probability weight, $P[\mathbf{X}(t_{\rm obs})]$. Our starting point for this probability is one representative of an equilibrium distribution, i.e its initial conditions are Boltzmann distributed and its transition probabilities maintain detailed balance.

Generically, we can project this infinite dimensional probability function onto a finite number of degrees of freedom. Two degrees of freedom that will be particularly useful are $c, \tilde{\rho}$, which are intensive space-time quantities we will define in the next section. For any pair of observables however, this can be written as,

$$P(c, \tilde{\rho}) = \int \mathcal{D}\mathbf{X}\ \delta\left[c - c(\mathbf{X})\right] \delta[\tilde{\rho} - \tilde{\rho}(\mathbf{X}) P[\mathbf{X}(t_{\rm obs})]\,, \tag{5.21}$$

where $\mathcal{D}\mathbf{X}$ is the path element whose integration domain spans the space of all trajectories parameterized by their initial distributions and $t_{\rm obs}$, $c(\mathbf{X})$ and $\tilde{\rho}(\mathbf{X})$ are path observables. In order to move away from the equilibrium manifold of trajectories in a direction parallel to a given path observable, we can generically introduce the Legrendre transforms,

$$P_{s,\lambda}(c, \tilde{\rho}) \propto P(c, \tilde{\rho}) e^{-sc(\mathbf{X})Nt_{\rm obs}/\Delta t - \lambda\tilde{\rho}(\mathbf{X})t_{\rm obs}} \tag{5.22}$$

where, s and λ are fields conjugate to the order parameters $c, \tilde{\rho}$ and in effect define a new ensemble of trajectories. This is a straightforward generalization of previous work which constructed an analogous s-ensemble[82, 205]. In this new ensemble, trajectories need not obey equilibrium statistics, and in fact only do for $s = \lambda = 0$. Studying the stationary distribution of $P_{s,\lambda}(c, \tilde{\rho})$ under different values of s and λ allows us to probe the nonequilibrium phase diagram for supercooled water. While the results we present are compute with one specific model, the mW model of water, due to the correspondence we find with these results and experiment we expect these results to be generic or other models of water and to other similarly tetrahedral molecules.

The stationary states of this trajectory ensemble that we find are summarized in the phase diagram in Fig. 5.9. For positive s and $\lambda = 0$, the temperature, pressure plane divides into three regions: where the trajectories exhibit an extensive amount of mobility, where trajectories have vanishing mobility and low mean density, and where trajectories have vanishing mobility and high mean density. The configurations along those trajectories lack long range order by construction, therefore materials undergoing the dynamics in each ensemble of trajectories are amorphous. When the material is ergodic and continues to

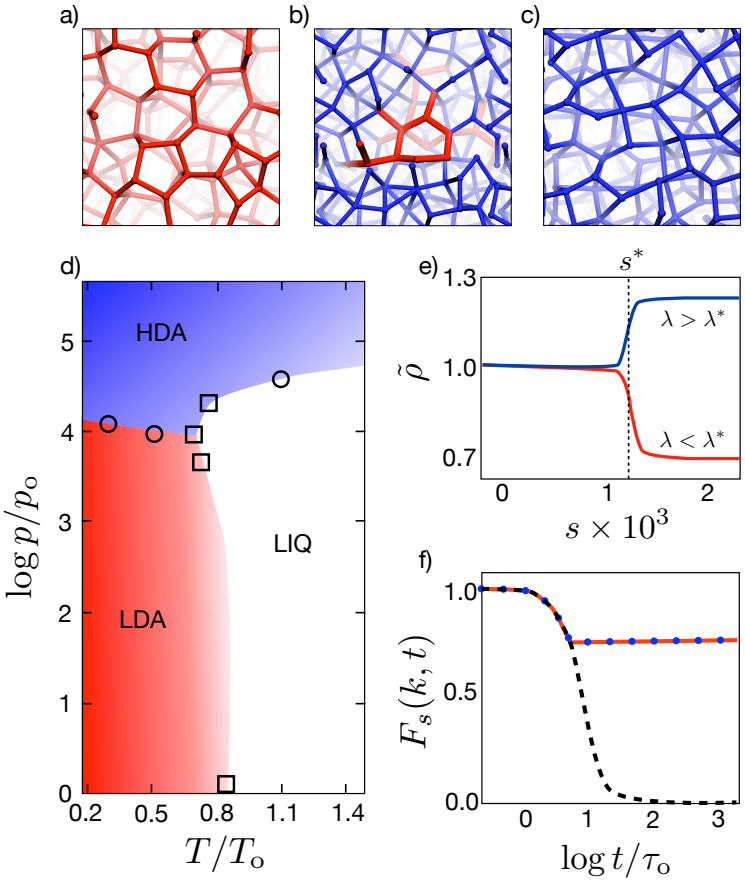

Figure 5.9: Nonequilbrium phases of supercooled water. (a-c) Typical configurations of amorphous ices and their coexistence computed with the mW model of water. The vertices indicate the position of the oxygen atoms and lines are drawn between nearest neighbors. (d) Phase diagram for the amorphous phases of water divides up intro three regions: where the material reorganizes and is ergodic (LIQ), where the material is glassy with lower density than the equilibrium liquid (LDA) and where the material is glassy with higher density than the equilibrium liquid (HDA). Circles locate experimentally observed transitions and squares locate simulated transitions[32, 157]. (e) Behavior of the density near the non-equiliubrium triple point. (f) Behavior of time correlation functions for the liquid, dashed line, and amorphous ices, solid and dotted lines.

sustain mobility, it is a liquid. When the material is kinetically arrested it is a glass. When the glass has low density we identify it with the low density amorphous ice of water and similarly when it glass has higher density we identify it with the high density amorphous ice.

The boundaries between liquid and glass and between glasses are located by markers, with shading interpolating between these points as a guide to the eye. The temperature and pressure units have been scaled by the temperature of maximum density at ambient pressures, T_o, and the inverse of the slope of the melting line evaluated at low pressures, $p_o = \Delta h/\Delta v$ where Δh and Δv is the heat and volume change on freezing. The square markers designate where explicit coexistence has been found within the s-ensemble. Circular markers designate the locations of experimental observations of transitions between HDA and LDA[157] and between HDA and the liquid[32]. The shape of the boundary between the liquid and glass follows the melting line to a good approximation[49]. For reduced pressures lower than $p/p_o < 10^4$, the boundary is relatively constant, though trends towards lower temperature. For higher pressures, the boundary moves to higher temperatures. The change in slope reflects the changing equilibrium state, which shifts from ordinary ice Ih at low pressures to higher density lattices at high pressures. For the mW model, the high pressure ice that is stable at these conditions is a BCC, ice VII-like, lattice. The approximate point at which this change in equilibrium stability occurs locates the triple point for HDA-LDA-liquid coexistence, $T/T_o \approx 0.75$, $p/p_o \approx 10^4$. The boundary moving away from the triple point, between LDA and HDA is roughly horizontal with a slight increase to higher pressures upon decreasing temperature. This boundary, which for experimental is $p/p_o = 3$ kbar, agrees with previous observations of transitions between HDA and LDA initially made in Ref. [157] and subsequent observations reviewed in Ref. [146].

Representative configurations taken from the different regions are shown in the top panels of Fig. 5.9. Panel a shows a typical configuration of LDA, where oxygen atoms are represented as nodes and vertices are drawn between nearest neighbors. The structure of this glass is locally tetrahedral, with the majority of molecules have four nearest neighbors. This can be quantified by measuring the mean-squared deviation from a tetrahedral angle, $\langle(\cos\Theta_{123} - \cos\Theta_T)^2\rangle$, where Θ_{123} is the angle made between neighboring triplets of molecules and $\Theta_T = 109.4^o$. For the mW model at ambient temperatures this is 0.3, but in the LDA prepared at $T = 205$ K and $p = 1$ bar, this is 0.05. Panel c shows a typical configuration of HDA, drawn in the same way as panel a. The high density amorphous ice is generally more compact and less locally tetrahedral, with an average structure very similar to high pressure liquid water[204]. Panel b shows a snapshot from a trajectory at the triple point with low average activity. The color code, delineates between molecules that have high local order (red), defined as an average mean-squared deviation of all the molecule's angels being less than 0.1, from those that have low local order (blue). The compactness of clustered LDA-like molecules is the type of structure anticipated between distinct phases where a surface tension makes it energetically favorable to decrease the area of the cluster.

Shown in Fig. 5.9e, are examples of how the average reduced density changes with applied s near triple point. For different values of the symmetry breaking field, λ, there is an abrupt change in the density from its liquid value to a higher, for $\lambda > \lambda^*$, or lower, for $\lambda < \lambda^*$

value. The location of the maximal change in $\tilde{\rho}$ locates s^* the value of the field that brings the two phases into coexistence. Shown in Fig. 5.9f, are examples of how time correlation functions, such as the self-intermediate scattering function, change within the liquid (dashed black line) or amorphous glass (blue dotted and red solid lines). In the liquid, the decay occurs at a mean value, τ_o. The decay of this function on timescales, $t \gg 1$s is what defines the laboratory glass transition[7].

5.5.2 Large deviation functions

To determine the phase boundaries in Fig. 5.9d, we compute large deviation functions for the trajectory ensemble given in Eq. 5.22. The large deviation function for the space of trajectories is the analogue to the free energy in typical equliubrium statisitical mechanics. These functions are projected onto order parameters that are expected to distinguish different stationary states, just as in the study of equilibrium phase transitions. Two types of transitions are found in Fig. 5.9, therefore we need at least two order parameters. To distinguish between liquids and glasses, we use the concentration of excitations as defined in Eq. 5.5, for $a = 1.75$Å. As we have shown above, these fundamental excitations are intimately related to the structural reorganization of the liquid. When they exist in sufficient concentration, the liquid is ergodic. When they are dilute and spaced far apart, the liquid is frozen, i.e. a glass[111].

The second order parameter must distinguish between multiple glasses and be similarly space-time extensive. For this we use the time-integrated reduced density,

$$\tilde{\rho} = \frac{1}{t_{\rm obs}} \sum_{j=0}^{t_{\rm obs}/\Delta t} \left[\rho\left(j\Delta t + \Delta t\right) - \rho_{\rm liq}\right] / \left[\rho_{\rm liq} - \rho_{\rm xtl}\right] \tag{5.23}$$

where $\rho_{\rm liq}$ and $\rho_{\rm xtl}$ are the average liquid and crystal densities, respectively. This order parameter reflects the expected difference between the two glasses, i.e. that one is a higher density than the other. Other measures of local density could be similarly used, however these would required an anticipation of the specific structures that exist in each glass. We use a scale relative to the crystal density in order to make contact with experiment, as the mW model underestimates the density difference in going from liquid to solid.

The large deviation function for rare fluctuations in these two, or more, order parameters is defined in analogy to a free energy,

$$G(\rho, c, ...) = -\log P_{s,\lambda}(\rho, c, ...) + \text{const.}\,, \tag{5.24}$$

where the constant reflects normalization or standard state convention. If the trajectory space over which $P_{s,\lambda}$ contains sufficiently many uncorrelated members, than from the principles of large deviations[217], G will be extensive in $t_{\rm obs}$ and N. We estimate this function using the same methods of umbrella sampling used to compute free energy functions in Chap 3. The only notable difference between those calculations and the ones used in this context are that the order parameters are trajectory observables. As such, rather than using hybrid

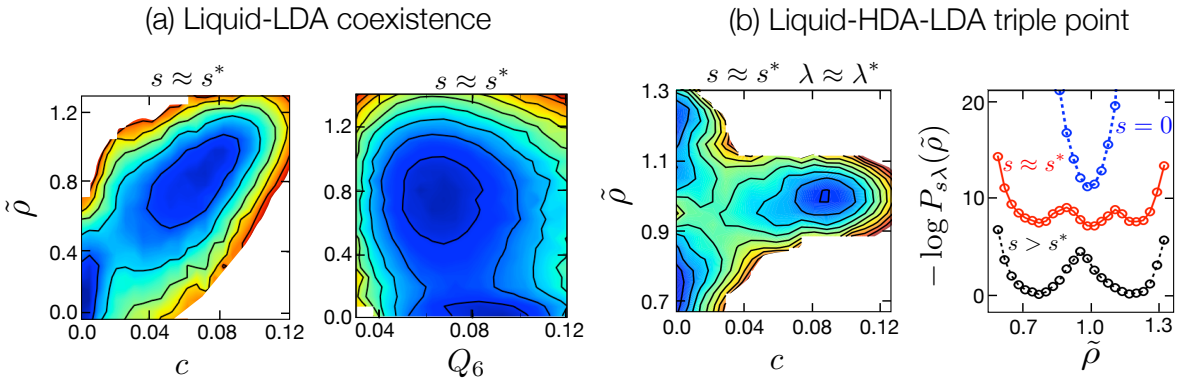

Figure 5.10: Large deviation functions for liquid, HDA and LDA non-equilibrium phases of water. (a) Coexistence between liquid and LDA phases of water. This surface was calculated with the mW model at $T/T_o = 0.8$, $p/p_o = 0$ and $t_{obs} = 300\Delta t$.(a) Coexistence between liquid, LDA and HDA phases of water. This surface was calculated with the mW model at $T/T_o = 0.75$, $p/p_o = 4$ and $t_{obs} = 200\Delta t$.

Monte Carlo moves in configuration space, we used Transition Path Sampling to sample trajectory space[22]. Specifically, we consider an ensemble with with constant N, p and T, and a dynamics that is evolved with a Nose-Hoover deterministic integrator[151]. The stepsize for the integrator is 3fs and the time constants its coupling to the temperature and pressure bath are both 1ps. The trajectory of length, t_{obs} is discretized into segments 3ps long, which locate the potential positions of shooting and shifting moves. Both types of moves are used, with a ratio of 3 shifting moves to 1 shooting move. Shooting moves follow the massive stochastic collision algorithm, used in previous s-ensemble work. Finally, the umbrella potentials are harmonic functions of $\tilde{\rho}$ and c, with spring constants of order 10^4 in both variables. This procedure is analogous to previous work for binary mixtures of Lennard-Jones spheres[205]. Finally, to ensure that artifact form crystallization do not effect our results we restrict out calculations to regions in the equilibrium phase diagram where there exists a separation of times between liquid reorganization and crystallization, and further we check that for the $N = 216$ particle system there is still a liquid basin in the reversible free energy surface. Even then, rare fluctuations can cause crystallization to occur. In order to account for this possibility, we reject any trajectory that fluctuates beyond cut-offs in long range order parameters $Q_6 = 0.14$ and $\psi_6 = 0.35$,[207] which in previous calculations encompass the liquid basin[133].

Figure 5.10 shows the large deviation surfaces for two of the state points considered on the phase diagram. In Fig. 5.10a, the state point is $T/T_o = 0.8$, and p/p_o=0. When the surface is reweighted to positive s, a change in convexity at equilibrium, $s = 0$, manifests itself as a bistable probability distribution. The left panel, shows a projection onto the $\tilde{\rho}$ and c plane. Basins are evident at high and low values of the mobility, indicating the existence of

liquid-glass coexistence, and also at high and low values of the density, indicating the glass is low density amorphous ice. We can confirm that both states are amorphous and metastable by similarly projecting the large deviation function onto the space of $\tilde{\rho}$ and Q_6, as shown in the right panel of part a. Both basins occur at low Q_6 values, though the LDA basin has a mean value slightly larger than the liquid that reflects the large structural correlations and local order.

The positive correlation between density and mobility fluctuations evident in Fig. 5.10a the nonequilibrium manifestations of the equilibrium order fluctuations that become prominent in water at low temperatures. The reduced density scale makes it clear that the LDA basin has the same density as the crystalline phase, ordinary ice Ih, at these conditions. This is consistent with a variety of experimentally prepared LDA ices[43]. While our pervious work has shown that thermal fluctuations make these locally order configurations thermodynamically unstable,[133, 136] when they are driven by the non-conserved s-field out-of-equiliubrium, the slow dynamics of these states make them long-lived.

Figure 5.10b illustrates how we have determined the existence and location of the triple point in the phase diagram. Specifically it plots $G(\tilde{\rho}, c)$ computed for $T/T_o = 0.7$ and $p/p_o = 10^4$. At this condition, for positive s, three basins exist. Low basins are found at low values of c and one at $c = 0.1$. The two glass basins, LDA and HDA, are separated along the density direction by a reduced density of 0.6. This relative density difference is also consistent with experimentally observed transitions between LDA and HDA[43]. At the specific state condition we consider, the two glass basins are not exactly equally probable. By increasing λ, the field conjugate to $\tilde{\rho}$, to a small positive value we can bring them into coexistence. The value of λ that provides equal weight to both basins we define as, λ^* in analogy to other coexistence fieldss^*.

The rightmost panel of Fig. 5.10 plots $-\log P_{s,\lambda}(\tilde{\rho})$ calculated from,

$$P_{s,\lambda}(\tilde{\rho}) = \int \mathrm{d}c\, P_{s,\lambda}(\rho, c)\,. \tag{5.25}$$

This plot illustrates how these basins grow in with increasing s at λ^*. Specifically, at $s = 0$, the liquid phase is the most likely state. At $s = s^*$, the three phase are in coexistence. For $s > s^*$, the two glasses are equally probably and the liquid basin disappears.

For the mW model, the location of the triple point coincides with a number of thermodynamic and dynamic observations. Thermodynamically, at pressures close to $p/p_o = 10^4$ the ground state for the mode changes from being like ordinary ice Ih, to being a bodied-centered cubic structure, such as the positions of the oxygens in ice VII[49]. Similarly, at these pressures the thermodynamic anomalies such as the density maximum have subsided to more normal liquid behavior, (see Chapter 3). Dynamically, correlations between local ordering and mobility no longer exists at equilibrium, nor does the diffusion change non-monotonically occur at these densities[161]. By these, and other measures, this pressure marks a smooth crossover to typical liquid behavior from the strongly associated behavior water normally adopts. While the average properties are smooth, these calculations show that temporal correlations between mobility and locally order regions and mobility and higher density regions

are strong. When acted on by the s-field, these correlations result in a collective transition into kinetically arrested states.

5.5.3 Relaxation in arrested states

Using the glassy configurations prepared within the s-ensemble, we can interrogate the microscopic details of how these states relax. Moreover, we can connect these details to previously made experimental observations that have until now not been possible. Two observations in particular deal with how a glass relaxes, either to the crystalline ground state or to another glass.

One observation made by Elsaesser et al. is that when LDA is heated up from a state prepared by hyperquenching liquid water, the thermal response in a nonmonotonic function of temperature[52]. Specifically, the material takes in heat, before it precipitously releases heat and crystallizes. This two-step relaxation of the crystal has been interpreted at accessing a so-called "ultra-viscous" liquid[146] at temperatures far below the predicted T_g of water. By taking configurations from the immobile basin, prepared with $s > s^*$, $t_{obs} = 500\Delta t$, $T/T_o = 0.8$ and ambient pressure, and quenching them instantaneously to $s = 0$ we can monitor the evolution of the thermal properties of the mW model and connect them with the observations of Elsaesser.

Figure 5.11a shows the results of such calculations averaged over 1000 realizations of this process, 100 distinct initial configurations and 10 realizations of randomly drawn momentum. The plot shows the average potential energy as a function of time away from the initial condition, $\overline{E(t)}$. Initially, the glass is in a low potential energy state relative to the supercooled liquid. Upon instantaneously turning off the s-field, the system remains immobile over an average waiting time of $t = 200\Delta t$ for mobility nucleates and the system begins to reorganize. Once this reorganization begins, the system immediately begins to crystallize, and by $t = 1000\Delta t$ on average the system has begun releasing energy as long ranged order builds up.

This ordering can be seen in the right panels of Fig. 5.11a which show the average radial distribution function for times $0 < t/\Delta t < 10$ and $1000 < t/\Delta t < 2000$. At the beginning of the trajectory, the radial distribution function shows the local order characteristic of LDA, indicated by the separation between the first and second solvation shell. At the end of the trajectory, this local ordering has developed into a long ranged order crystal, as indicated by the peak splitting part the first solvation shell and persistent correlations at large separations. This crystal can be identified as cubic ice using orientational order parameters. The ordering that evolves from LDA to the crystal, is not monotonic.

As evidenced by the initial increase in average energy in Fig. 5.11a, before the crystal can be accessed LDA must first "melt" and become sufficiently mobile to attempt to crystallize. A more direct measure of the mobility is to monitor the concentration of excitations as a function of time. This measure agrees with our interpretation of the behavior of the energy. Initially, there are zero excitations in the glass. After a rare fluctuations in which an excitation is produced, the system rapidly evolves to its equilibrium value at these conditions,

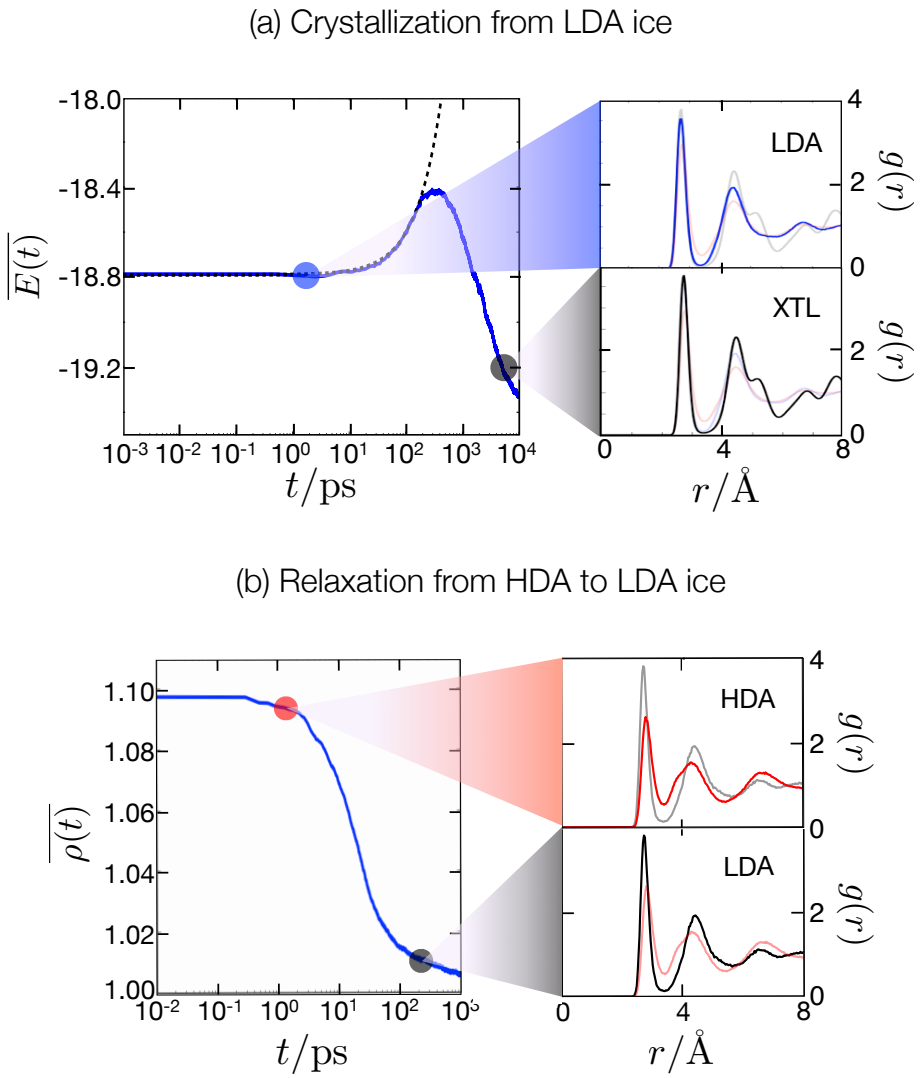

Figure 5.11: Relaxation behavior of amorphous ices produced with the s-ensemble. (a) Average energy as a function of time for the mW model prepared in an ensemble at $s > s^*$, $T/T_\mathrm{o} = 0.8$, $p/p_\mathrm{o} = 0$ and $t_\mathrm{obs} = 200\Delta t$ and evolved with $s = 0$, $T/T_\mathrm{o} = 0.76$, $p/p_\mathrm{o} = 0$. The dashed black line is an exponential function with characteristic time, $200\Delta t$. Right panels shown the average pair distribution functions along this average trajectory. (b) Average density as a function of time for the mW model prepared in an ensemble at $s > s^*$, $T/T_\mathrm{o} = 0.76$, $p/p_\mathrm{o} = 2 \times 10^4$ and $t_\mathrm{obs} = 200\Delta t$ and evolved with $s = 0$, $T/T_\mathrm{o} = 0.6$, $p/p_\mathrm{o} = 5 \times 10^3$. Right panels shown the average pair distribution functions along this average trajectory.

$c \approx 0.1$, after which mobility is eliminated through crystallization.

Another observation, originally made by Mishima is an abrupt transition between an initially prepared HDA, when it is quenched to lower pressure and kept at low temperature, to LDA. The signature this relaxation phenomena is the share change in density that occurs while the sample is held at $T \ll T_g$. By taking configurations from an immobile HDA basin, prepared with $s > s^*$, $t_{obs} = 200\Delta t$, $T/T_o = 0.6$ and ambient pressure, and quenching them instantaneously to $s = 0$ and a lower pressure we can monitor the evolution of the density and structural properties of the mW model and connect them with the observations of Mishima.

Figure 5.11b shows the results of such calculations averaged over 1000 realizations of this process, 100 distinct initial configurations and 10 realizations of randomly drawn momentum. The plot shows the average density energy as a function of time away from the initial condition, $\overline{\rho(t)}$. Initially, the glass is prepared in a high density amorphous basin. Upon instantaneously turning off the s-field, and lowering the pressure below the phase boundary between HDA and LDA, the system evolves to the lower density basin. The average waiting time for this transition to occur is on the order of the timescales for basic particle displacement in the high temperature liquid, i.e. $10\Delta t$. This short time is a reflection of the highly local reorganization that system undergoes in transitioning between two amorphous phases. The decrease in pressure creates a driving force for lowering the density, which activates local particle rearrangements. On average this excess free energy due to the change in pressure is dissipated through a concentration of mobility, $c = 0.02$ on average. After the initial burst of excitation, the system monotonically relaxes into the low density amorphous state. This behavior is in stark contrast to the high temperature behavior in shown in Fig. 5.11(a) where significant mobility is required to reorganize the glass into a crystal. In the right panels in Fig. 5.11(b) the average radial distribution functions are plotted along the trajectory. For times in the range $0 < t/\Delta t < 10$ the structure reflects the HDA configurations where the dynamics were initialized. For times in the range $10^2 < t/\Delta t < 10^3$ the structure adopts the open local order of LDA.

Chapter 6

Frustrating water at ordered surfaces

The life and soul of science is its practical application
- Sir William Kelvin [107]

In this chapter, we present our results for the behavior of water at ordered interfaces that are more or less commensurate with typical hydrogen bonding patterns. The techniques employed are molecular dynamics simulations of detailed models of water and metal surfaces. This chapter borrows largely from two previously published works, *Proc. Natl. Acad. Sci.* 110, 4200-4205 (2013) and *J. Chem. Phys.* 138, 184702 (2013). The principle phenomena presented is the emergence of dynamic heterogeneity and hydrophobicity at the liquid-solid interface. These results illustrate practical implications for the local order fluctuations that have been presented throughout the dissertation. In particular, by exposing water to an extended, ordered surface fluctuations that lead to long ranged ordering are enhanced. When the surface is incommensurate with local hydrogen bonding patterns, this local order is frustrated and the dynamics that result are heterogeneous. The surfaces we study in this chapter are particularly relevant to renewable energy sources and catalysis.

6.1 Preliminaries

We have applied molecular dynamics and methods of importance sampling to study structure and dynamics of liquid water in contact with metal surfaces. The specific surfaces considered resemble the 100 and 111 faces of platinum. Several results emerge that should apply generally, not just to platinum. These results are generic consequences of water molecules binding strongly to surfaces that are incommensurate with favorable hydrogen bonding patterns. We show that adlayers of water under these conditions have frustrated structures that interact unfavorably with adjacent liquid water. We elucidate dynamical processes of water in these cases that extend over a broad range of time scales, from less than picoseconds to more than nanoseconds. Associated spatial correlations extend over nanometers. We show that adlayer reorganization occurs intermittently, and each reorganization event correlates

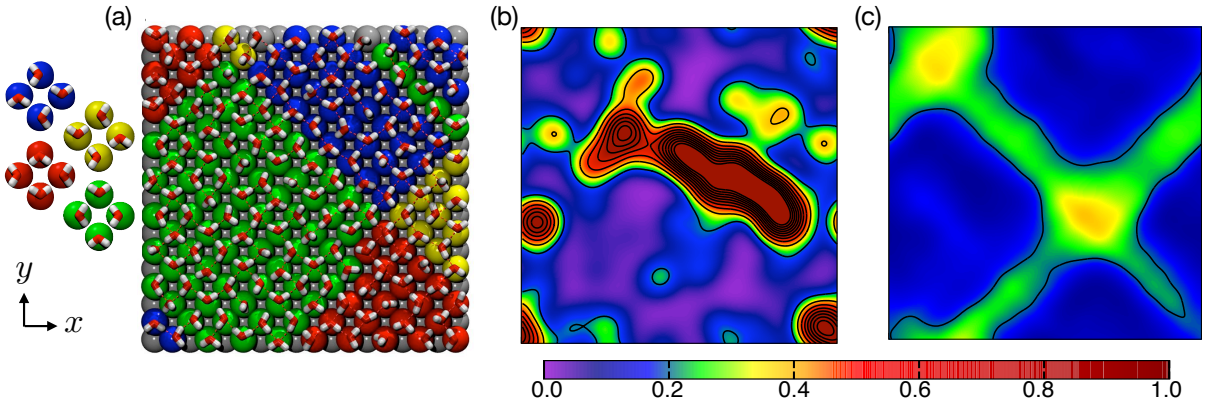

Figure 6.1: An instantaneous configuration and dynamic heterogeneity of the water ad-layer on the Pt 100 surface. The ad-layer is in equilibrium with adjacent bulk water (not shown). Panel (a) shows hydrogen bonding patterns with typical heterogeneous distribution of line defects. The four unit cells have been assigned a different color code (see left-hand side of panel). These colors are projected onto the underlying electrode atoms to highlight distinct domains of ad-layer waters with specific hydrogen bond arrangements. Panels (b) and (c) are instantaneous and time averaged mobility fields, $q(\mathbf{a};t)$ and $\bar{q}(\mathbf{a};t_{\rm obs})$, respectively, with $t_{\rm obs} = \tau_{\rm p}/3$. Horizontal and vertical axes represent position in the plane parallel to the electrode surface. The snap shots in (a) and (b) are taken at the midpoint of the trajectory that is averaged to produce (c). Color code for the mobility field is given by $q(\mathbf{a},t)\Delta x^3$ where $\Delta x = 0.1$Å. Figure adapted from Ref. [233].

motions of several molecules. We show that soft liquid interfaces form adjacent to the ad-layer, as is generally characteristic of liquid water adjacent to a hydrophobic surfaces. The infrequent ad-layer reorganization produces a hydrophobic heterogeneity that we detail by studying the degrees by which different regions of the adlayers attract small hydrophobic particles. Consequences for electrochemistry are discussed in the context of hydronium ions being attracted from the liquid to the metal-adlayer surface.

6.2 Dynamic heterogeneity at ordered interfaces

Strong metal-water bonding forces ad-layer waters into structures that are antithetical to favorable hydrogen bonding. Accordingly, the ad-layers contain defects. Motions are one- to two-orders of magnitude faster in the proximity of these defects than elsewhere on the surface. Further, rearrangements of these defects require coordinated motions of several water molecules. This type of heterogeneous dynamics is common in glass-forming materials[30, 48]. Some of the quantitative methods used to successfully interpret such behavior in molecular dynamics models of glass formers[30, 112] are used here to elucidate the nature of water dynamics at metal surfaces.

Depending on the surface geometry, adsorbed water molecules form qualitatively different

hydrogen bonding patterns. For the 100 surface, the four-fold coordination and lattice spacing are commensurate with a variety of two-dimensional hydrogen bonding patterns. Surface water molecules adsorb to nearly every available surface site and vacant surface atoms are rare. The surface patterns that emerge are domains distinguished by relative orientations of the adsorbed water molecules. Different colors in Fig. 6.1a help identify different domains. Transient disorder in the form of line defects between domains of dipole aligned molecules relax slowly, as we shall see.

For the 111 surface, the six-fold lattice coordination is incommensurate with planar arrangements that would allow all molecules to form four hydrogen bonds. In this case, the particularly stable configurations of water molecules involve the formation of three hydrogen bonds where a given water molecule donates two and accepts a single hydrogen bond in a triangular manner with molecules residing on alternating coordination sites. Blue coloring in Fig. 6.2a helps identify these patterns. These particular arrangements are facilitated by the presence of nearby surface vacancies that help eliminate hydrogen bond frustration and account for 15% of all surface sites on average. Since vacancy diffusion is slow, the spatial distribution of vacancies is heterogeneous over relatively long times, as shown below.

6.2.1 Orientational mobility and fields

The chemisorption energy (i.e., the metal-water bonding energy) is sufficiently strong that lateral diffusion of water is rare on picosecond timescales. As such, the dynamics of an adsorbed water molecule are dominated by rotations. To characterize changes in molecular orientations, we focus on the variables $\mathbf{u}_i(t)$, which denote the unit vector parallel to the dipole of the ith water molecule at time t.

There are different contributions to the time dependence of $\mathbf{u}_i(t)$ that act on different time scales. In typical trajectories, $\mathbf{u}_i(t)$ oscillates rapidly about a reference direction before jumping to new reference direction. The oscillations reflect small-amplitude vibrations and librations of the water molecule, and the jumps (or instantonic events) reflect changes in long lived arrangements of several molecules. The former generally have periods of 1 ps or less, while distinct molecular arrangements generally persist for more than 5 ps, and usually much longer. Indeed, as we detail later, the mean persistence time is 20 ns and 1 ns for the water ad-layers on the Pt 100 and Pt 111 surfaces, respectively.

As a result of this separation of time scales, it is useful to consider

$$\bar{\mathbf{u}}_i(t) = \frac{1}{\delta t} \int_t^{t+\delta t} dt' \mathbf{u}_i(t'). \tag{6.1}$$

The value of the coarse-graining time, δt, should be large enough to remove most vibrational and librational contributions to $\bar{\mathbf{u}}_i(t)$, and thereby highlight contributions from structural reorganization. For this purpose, we use $\delta t = 2$ ps. Distribution functions graphed later in this paper show that this value is indeed suitable.

In terms of these coarse-grained coordinates, an instantaneous measure of mobility is

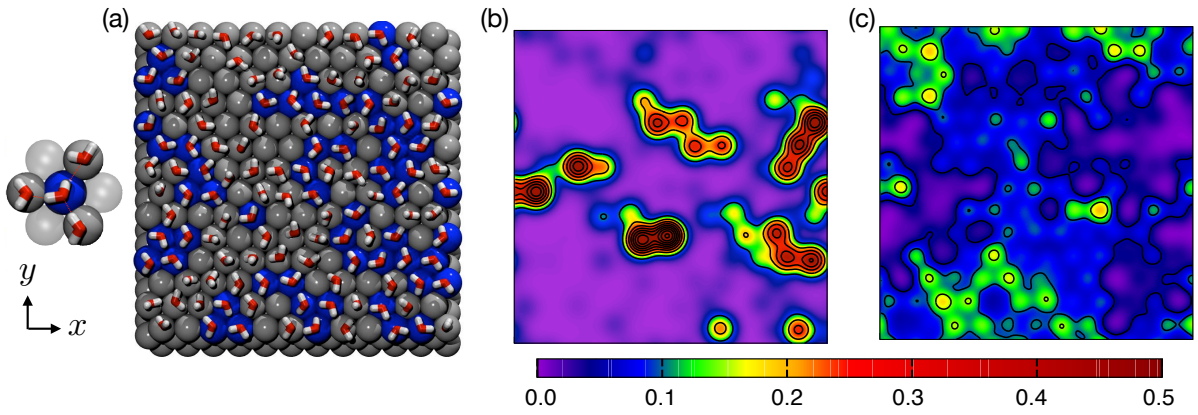

Figure 6.2: An instantaneous configuration and dynamic heterogeneity of the water ad-layer on the Pt 111 surface. The ad-layer is in equilibrium with adjacent bulk water (not shown). (a) Hydrogen bonding patterns: water molecules engaging in the preferred hydrogen bond pattern (see left-hand side of panel) have their underlying electrode atom colored blue. (b) and (c) Instantaneous and time averaged mobility fields, $q(\mathbf{a};t)$ and $\bar{q}(\mathbf{a};t_{\rm obs})$, respectively, with $t_{\rm obs} = \tau_{\rm p}/3$. Horizontal and vertical axes represent position in the plane parallel to the electrode surface. The snap shots in (a) and (b) are taken at the midpoint of the trajectory that is averaged to produce (c). Color code for the mobility field is given by $q(\mathbf{a},t)\Delta x^3$ where $\Delta x = 0.1$Å. Figure adapted from Ref. [233].

given by

$$q_i(t) = 1 - \bar{\mathbf{u}}_i(t) \cdot \bar{\mathbf{u}}_i(t + \Delta t). \tag{6.2}$$

To the extent that it is non-zero, the configuration at time $t + \Delta t$ differs from that at time t. To use this quantity to count relevant reorganization events, Δt must be both greater than the coarse-graining time, δt, and much less than the time to de-correlate enduring orientations. For this purpose, we use $\Delta t = 10\,$ps. This choice is suitable for describing ad-layer mobility because 10 ps is one- to two-orders of magnitude shorter than the relevant mean persistence times. Spatial resolution of mobility can be resolved with reference to a mobility field. Our specific choice mobility field focuses on ad-layer molecules and is coarse grained over a length ξ. In particular, we define

$$q(\mathbf{a},t) = \sum_i q_i(t)\phi(\mathbf{a} - \mathbf{a}_i(t);\xi)\Theta(2\xi - |z_i(t) - z^*|). \tag{6.3}$$

Here, $\mathbf{a}_i(t)$ is the two-dimensional projection of the ith water-oxygen position onto the plane of the electrode, and $z_i(t)$ is the projection perpendicular to the plane; z^* is the mean of $z_i(t)$ for water molecules in the ad-layer; $\Theta(x) = 1$ or 0 for $x \geqslant 0$ or $x < 0$, respectively; $\phi(\mathbf{a};\xi)$ is a delta-like function broadened over length scale ξ; we use a normalized Gaussian, $\phi(\mathbf{a};\xi) \propto \exp(-a^2/2\xi^2)$), and set $\xi = 1.5$ Å.

Snapshots of $q(\mathbf{a},t)$ for the 111 and 100 surfaces are shown in Figs. 6.2b and 6.1b, respectively. Both surfaces display significant heterogeneous dynamics, manifested as regions

of high mobility within a background of low mobility. For the 100 surface, the high mobility regions have a definite directionality in that they are aligned with the underlying lattice, and they are diffuse in that they encompass several neighboring molecules. Reorganization is therefore collective, occurring along existing hydrogen bond chains. Further, by transiently disrupting the local hydrogen bond network, reorganization of one molecule facilitates reorganization of neighboring molecules. Such behavior is characteristic of glassy systems in general[30].

For the 111 surface, the high-mobility patches also have a directionality, though the underlying lattice dictates that motion does not propagate in a straight line but rather jigsaws back and forth along the lattice. Mobile regions are more localized on the 111 surface compared to the 100 surface, but motion is similarly facilitated as evidenced by the connectivity of the mobile regions. Movies illustrating the time-evolution of dynamic heterogeneity for the water monolayers on the 100 and 111 surfaces can be viewed at http://youtu.be/cCYLPtckDWk and http://youtu.be/d0DDWuP-qTg, respectively.

The time scales over which immobile and mobile regions interconvert are the time scales of persistence. The mean persistence time, $\tau_{\rm p}$, is the structural relaxation time[30]. Over times smaller than $\tau_{\rm p}$, patches of high mobility occur with higher frequency at particular regions of space. The persistent structural degrees of freedom contributing to these motions can be highlighted by time-averaging the spatial mobility field,

$$\bar{q}(\mathbf{a}; t_{\rm obs}) = \frac{1}{t_{\rm obs}} \int_0^{t_{\rm obs}} dt\, q(\mathbf{a}, t). \tag{6.4}$$

where $t_{\rm obs}$ is an observation time. The time averaging causes mobile domains to become diffuse, as the higher frequency features disappear. Heterogeneity disappears completely as $t_{\rm obs}/\tau_{\rm p}$ becomes large.

For the 100 surface, this time averaging elucidates the role of line defects on the surface as promoters of reorganization. Shown in Fig. 6.1c for $t_{\rm obs} = \tau_{\rm p}/3$, integrated motion is primarily along lines that are fully connected and span the entire system. The linear structures run parallel to the surface close packing, and orthogonal to each other. The features can be readily identified with persisting line defects on the surface by analyzing the hydrogen bonding patterns. Figure 6.1a shows the molecular configuration at the midpoint of the trajectory used to calculate Fig. 6.1c, where the underlying metal lattice has been colored for one of four hydrogen bonding patterns (also shown).[1] The location of line defects formed at the boundaries between these different domains coincides with the regions high mobility.

For the 111 surface, time averaging the mobility field yields similar results. As shown in Fig. 6.2c for $t_{\rm obs} = \tau_{\rm p}/3$, integrated motion exhibits domains of high mobility. These domains, like the ones on the 100 surface, become more connected although their structure

[1]Stable hydrogen bond configurations can be generated by tiling the surface with a four-membered unit cell with no net dipole. By lattice symmetry four such tilings exist as shown on the left-hand side of Fig. 6.2a. If tiling begins from the bottom left-hand side of the electrode and works up and to the right-hand side each water molecule can be uniquely unique assigned to one of the four patterns based on the relative orientation of the molecular dipole projected onto the plane parallel to the electrode.

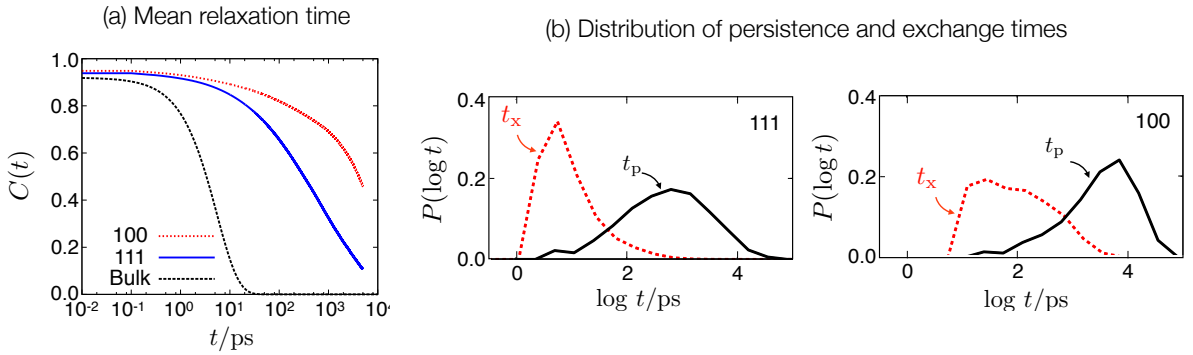

Figure 6.3: (a) The dipole autocorrelation function for water molecules adsorbed to the 100 (dotted red line) and 111 (solid blue line) electrode. The corresponding quantity for molecules in the bulk liquid is plotted as a dashed black line. (b) The probability distributions for the persistence, $t_{\rm p}$, and exchange times, $t_{\rm x}$, for the 111 surface, shown on a log scale where $P(\log\, t) = tP(t)$. (c) The probability distributions for the persistence and exchange times for the 100 surface. Figure adapted from Ref. [233].

is not as simple. The locations of the domains are not directly related to the location of surface vacancies but rather are spatially anti-correlated to the presence of stable hydrogen bond configurations in which an adsorbed molecule donates two and accepts one hydrogen bond with molecules adsorbed to alternating neighboring surface atoms as illustrated in Fig.6.2a.[2] Molecules with this preferred hydrogen bonding pattern typically reside within inactive patches. Figure 6.2a is taken from the midpoint of the trajectory used for Fig. 6.2c and designates these particularly stable hydrogen bond configurations as blue lattice sites.

6.2.2 Correlation and distribution functions

These heterogeneous, facilitated dynamics described above dictate that the timescales associated with relaxing a given tagged molecule will be large relative to the bulk liquid, and strongly dependent on its environment. The average timescale governing orientational reorganization can be extracted from the dipole autocorrelation function,

$$C(t) = \langle \mathbf{u}(0) \cdot \mathbf{u}(t) \rangle - |\langle \mathbf{u} \rangle|^2, \tag{6.5}$$

where the angle brackets represent an average over all electrode-adsorbed water molecules. Note that while $\langle \mathbf{u} \rangle$ vanishes in the bulk liquid, it does not necessarily at the surface. As shown in Fig. 6.3a, water on both surfaces undergo orientational relaxation over timescales that are of 2 to 20 ns. The more ordered 100 surface yields significantly slower relaxation

[2]Here we use a geometric criteria where two molecules are considered hydrogen bonded if the O-O distance is less than 3.5AA and the O-H...O angle is less than 35 degrees.

than for that of the locally over-coordinated 111 surface. These times are 3-4 orders of magnitude larger than the characteristic relaxation time for bulk water, $\tau_{\rm bulk} = 5$ ps. (For the computation of $C(t)$ for bulk water, the averaging implied by the angle brackets is carried out over all non-ad-layer waters.)

The functional form of the decay of $C(t)$ for bulk water is an expected exponential decay, indicative of an uncorrelated Poisson process characterized by a single timescale, $\tau_{\rm bulk}$. The functional form for the decay of $C(t)$ for the adsorbed water, however, is more complicated and resembles the stretched exponential decay associated with correlation functions of glass-forming liquid systems[48]. Such deviations from Poisson statistics highlight the important temporal correlations within the orientational dynamics.

These temporal correlations are manifested explicitly in the distributions of persistence and exchange times[30]. Persistence times, $t_{\rm p}$, are the waiting times for reorientations, and exchange times, $t_{\rm x}$, are the times between such motions. In cases of uncorrelated dynamics, persistence and exchange times are drawn from the same distribution, fully characterized by the decay time of $C(t)$. However, if the dynamics are temporally correlated then the probability for undergoing motion is conditionally dependent on what has already occurred, and these distributions will be therefore different[76]. In glassy dynamics, where motion in a region of space facilitates further motion in neighboring regions of space and time, the most probable $t_{\rm x}$ is much smaller than the most probable $t_{\rm p}$.

This decoupling of exchange and persistence is clearly evident in Figures 6.3(b) and (c), which depict distributions of persistence and exchange times for both the 111 (b) and 100 (c) surfaces. The times are calculated by recording the time for a dipole to change its orientation by 50$^{\rm o}$ either from an arbitrary time origin, for the persistence time, or given a reorientation just occurred, for the exchange time. This angular displacement is chosen to be much greater than the librational motion of water on the surface and commensurate with reorientations between stable hydrogen bonding patters on the surface, as dictated by the lattice geometry. In order to avoid counting reorganizations that only occur transiently, we also stipulate that the rotation persists for an additional Δt. (For reference to similar calculations of exchange and persistence distribution, but for a model of a structural glass-forming liquid, see Ref. [83, 104].)

For ad-layers to both metal surfaces, the mean exchange time, $\tau_{\rm x}$, is shorter by over an order of magnitude from the mean persistence time. The mean persistence time, $\tau_{\rm p}$, agrees with the $1/e$ time from the decay of $C(t)$. This separation of timescales, reflecting a dynamic facilitation mechanism, occurs in here because transient disorder within the adsorbed monolayer gives rise to spatial variations in the relative hydrogen bond stability, which in turn facilitates heterogeneous dynamics.

The total orientational mobility within the adsorbed monolayer is given by

$$Q(t) = \frac{1}{N} \sum_{i=1}^{N} q_i(t) \,, \tag{6.6}$$

where the sum is carried out over all N electrode-adsorbed molecules. (N can fluctuate due to exchange between the bulk and ad-layer, but the resulting time dependence of N

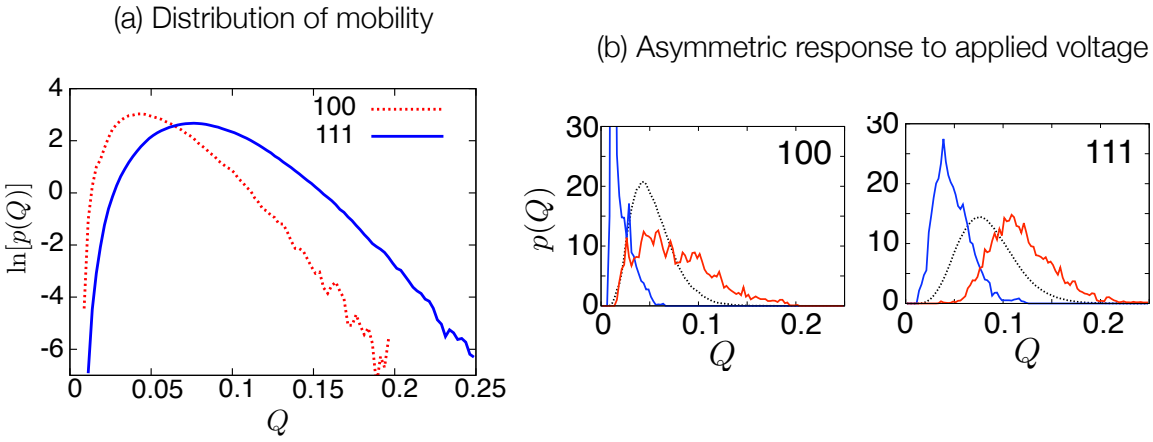

Figure 6.4: (a) The probability distribution for the total orientational mobility, Q, plotted for the 100 electrode surface (dashed red line) and the 111 electrode surface (solid blue line). (b) The probability distribution $p(Q)$ at different values of the applied electrode potential. Dotted black line correspond to the results at zero applied potential. Red and blue lines correspond to the results at the negative electrode ($V_0 = -1.36$V) and positive electrode ($V_0 = 1.36$V) respectively. Figure adapted from Ref. [233].

has a negligible effect on $Q(t)$ for the conditions we have studied.) This total orientational mobility variable serves as an order parameter distinguishing ad-layers of different mobility. Figure 6.4 shows the distribution functions of of this order parameter, $p(Q)$ for the 100 and 111 electrode surfaces. Both distributions are Gaussian around the mean, but both also possess fat tails at larger values of Q. The non-Gaussian tails indicate that highly active configurations are much more probable than one would expect given Gaussian statistics. The tails arise through the correlated nature of the surface dynamics. Their presence indicates, in principal, that it is possible to drive the ad-layers out of equilibrium into distinct phases, one of high mobility and one of low mobility[82].

This behavior does not change qualitativey under applied voltage. Interestingly, the distributions of total mobility respond asymmetrically at the positive and negative electrode. Figure 6.4 shows $p(Q)$ for both electrode geometries and for the positive ($V_0 = 1.36$V) and negative ($V_0 = -1.36$V) constant potential electrode. For both surfaces, the positive values of the applied potential have the effect of shifting the distribution of mobility to lower values of Q. This shift to lower Q manifests as a slowing in the timescales for relaxation dynamics. At the negative potential electrode we observe the opposite effect, a shift in $p(Q)$ to larger values of Q, indicating an increase in the surface relaxation times.

The asymmetric behavior can be understood in light of our previously published work in which we demonstrated that for moderate values of an applied electrode potential the orientations of adsorbed water molecules respond asymmetrically with respect to applied electrode potential[234]. The asymmetry arises because at the negative electrode adsorbed

water molecules can adopt an alternative orientation in which one oxygen-hydrogen bond is pointed straight towards the electrode thereby gaining a favorable image charge interaction between the partial positive charge on the hydrogen and the electrode. There is no corresponding orientation at the positive electrode and so at the negative electrode one relaxation pathway (rotation of an oxygen-hydrogen into the electrode) is enhanced while at the positive electrode the same pathway is inhibited. This asymmetry was found to be more prominent for 111 versus 100 due to the relative instability of the hydrogen bond network over the 111.

Consistent with the asymmetric behavior predicted from our model, others have noted that the electronic structures of metal interfaces respond sensitively to the electrostatic fields of the surrounding solvent[58, 98]. In particular, electronic structure theory[98] indicates that dipole reorientations of adsorbed water molecules on a Pt 111 surface can result in shifts in the potential of zero charge of up to 3 eV. The heterogeneous relaxation elucidated herein are therefore expected to modulate catalytic activities of metal surfaces. For a platinum-like surface, we expect modulating domains that extend over nanometers and that reorganize tens of nanoseconds. It remains to be seen whether asymmetric response can be tapped as a means to drive electrodes out of equilibrium in a fashion that will produce a non-equilibrium transition between phases of high and low orientational mobility, and whether such a transition can be of practical use.

6.3 Solvation at incommenserate ordered interfaces

To study the aqueous metal interface we use a molecular model [14, 199] that neglects explicit electronic degrees of freedom beyond accounting for electronic polarization of the metal. Despite its relative simplicity, the model is in reasonably good agreement with experimental values for the potential of zero charge and capacitance values of the aqueous platinum interface [234]. (This particular property – the potential of zero charge – is discussed later.) The model is not designed to reproduce many intricate details manifested at low temperature and near vacuum conditions[60]. Rather, it is designed to capture generic behavior of liquid water at standard conditions in contact with a metal surface. The behaviors we find in this way are expected to be general, and as we illustrate below, our principal results are qualitatively insensitive to many details of the underlying surfaces.

Accurate knowledge of the single molecule binding energy of water to a platinum surface is currently unknown, however quantum chemical calculations[155] and experimental thermal desorption measurements[216] yield a range spanning 0.3-0.6 eV. These energies are larger than typical hydrogen bond energies, which are $\lesssim$ 0.25 eV[216]. The model used here [199] has been parameterized to recover this relatively strong attraction with binding energies of 0.46 eV and 0.37 eV for the 100 and 111 surfaces respectively. The single molecule geometries predicted by the model are in reasonable agreement with quantum chemical calculations[155], including predicting the relative stability of top site binding over bridge site binding by 0.2 eV[86].

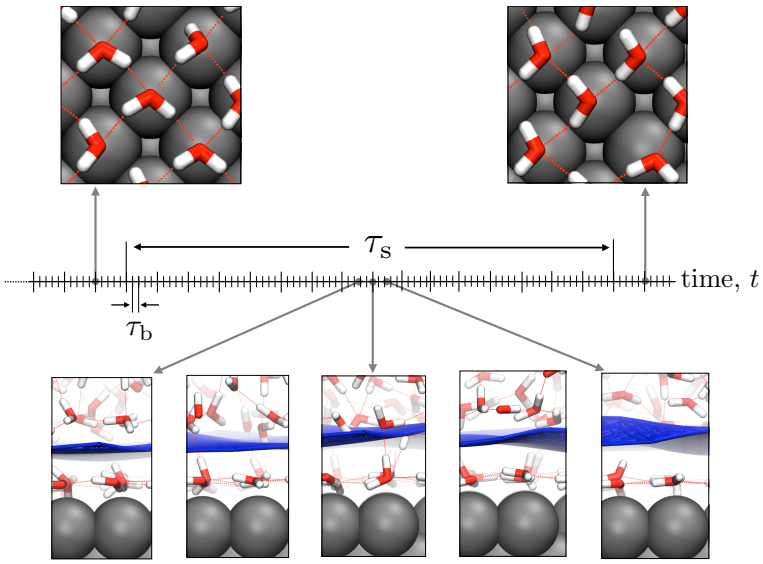

Figure 6.5: Illustration of the separation of timescales between reorganizing surface configurations, which occur on average every τ_s, and reorganizing the bulk density, which occur on average every τ_b. Small tic marks are separated by 20 ps, which is on the order of though larger than timescales for typical density fluctuations. Large tick marks are separated by 100 ps, which is of the order of the typical relaxation times for relevant interfacial fluctuations. Figure adapted from Ref. [137].

These features of single molecule geometries and binding energies depend weakly on the structure of the exposed metal. In contrast, the behavior of a full monolayer of water is sensitive to the underlying metal surface structure. This sensitivity at high coverage is the result of competition between water-metal and water-water interactions, is mediated by geometry, and for the platinum 111 surface, it results in the $\sqrt{39}$ ground state[60]. The model we employ reproduces crucial features of the $\sqrt{39}$ structure: the preference for water to bond predominately in the plane of the monolayer and the preference of non-bonded hydrogens to point towards the metal rather than away. These features, we shall see, are responsible for the hydrophobicity and heterogeneity of the hydrated metal surface. The model also reproduces the preference in the $\sqrt{39}$ structure for local hexagonal rings of waters on atop sites of the metal. On the other hand, the model is not sufficiently comprehensive to capture the formation of five and seven membered rings that also appear in the $\sqrt{39}$ structure. Those details are interesting and possibly important in other contexts, but they are specific to Pt, and they do not change the generic features relevant to this work that the metal surface dictates a structure of the water monolayer that is both frustrated and incapable of favorable bonding to the adjacent liquid.

Using this model we can access length and time scales far beyond those currently available to *ab inito* calculations. We find that water adlayers on metal surfaces are hydrophobic, and the degree of hydrophobicity depends on the amount of passivation of the hydrogen bond network within the adsorbed water layer. Strong, favorable interactions pin the oxygens of water to the top sites of the crystal lattice creating a spatially ordered arrangement of molecules. This paper considers two surfaces of a planar metal surface, whose geometry and lattice spacing most closely corresponds to the 100 and 111 platinum surfaces. In both cases, the imposed water structures allow for facile hydrogen bonding within the adlayer and subsequently only a few, fleeting, hydrogen bonds are donated from the adlayer to the surrounding bulk. While the adsorbed oxygens at both surfaces still afford hydrogen bond acceptor sites, the asymmetry associated with lacking donor sites results in an interface that is liquid-vapor-like in the sense that large density fluctuations occur though the collective formation and deformation of an interface[29].

Even though the underlying metal lattices we study are ordered, over large length scales the planar geometry of the surface is incommensurate with water's preferred tetrahedral structure. A consequence of this frustration is the presence of an equilibrium number of defects in the hydrogen bond network within the adlayer. These defects facilitate reorganization within the surface and the resulting dynamics are heterogeneous and relax on timescales larger than nanoseconds. The characteristic time for this surface relaxation, $\tau_s \gtrsim 1\,\text{ns}$, is much larger then that for typical equilibrium density fluctuations in the bulk liquid, $\tau_b \approx 5\,\text{ps}$. Therefore, while the presence of the surface introduces a static inhomogeneity, the water bound to this surface introduces a dynamic inhomogeneity. The resultant separation of timescales between bulk and surface reorganization is illustrated in Fig. 6.5. The top panels of Fig. 6.5 show snapshots during slow reorganization of the surface water dipoles, while the bottom panels of Fig. 6.5 illustrate faster interfacial fluctuations.

These two features of the metal interface, the static heterogeneity of the extended in-

terface and the slow dynamics of water at its surface, cause a decoupling of ensemble and dynamic averaging on timescales $t < \tau_s$. The decoupling implies that for a given configuration of the adlayer, liquid water swiftly equilibrates, and for $t \gg \tau_b$ the properties of the subsequent hydration layers are in dynamic equilibrium. Over intermediate timescales, however, temporal heterogeneity of the hydrogen bond network couples to the dynamically heterogeneous properties of the interface.

The next section illustrates the dependence of the adlayer structure with the exposed metal surface geometry and shows how the passivation of the hydrogen bond network on the surface creates a liquid-vapor-like interface that attracts hydrophobic particles. The subsequent section shows how frustration of water structure on the surface, coupled with a separation of relaxation times between the surface and bulk, creates temporal regions of spatially heterogeneous hydrophobicity that decays over nanoseconds. We then discuss how the effects we have detailed can influence electrochemical properties. The techniques we apply to simulate this system are outlined later and in previous work [234].

6.3.1 Static heterogeneity of the extended metal interface

Equilibrium adlayer structures can exhibit incomplete surface coverage, the extent of which depends on surface geometry and reflects a competition between adsorption and hydrogen bonding energetics[86]. The interplay between water-metal and water-water interaction energetics is reflected in the structural motifs present on the different crystal faces. Figures 6.6a and c shows characteristic snapshots of the adlayer of water for both surfaces obtained from our simulations, as well as their subsequent effect on wetting b and d. (A liquid phase lies above the pictured metal surfaces and adlayers in a and c, but the liquid molecules are not rendered.) For the 100 surface, metal atoms are locally four fold coordinated and are commensurate with a two-dimensional projection of local hydrogen bonding patterns. As a result, the structure of water on the surface is highly ordered with water dipoles oriented parallel to the surface and approximately all top sites are occupied. At any particular instant, however, line defects exist on the surface separating planes of dipole aligned molecules by 90° turns in their orientations. For the 111 surface, metal atoms are locally six fold coordinated and though they also have lattice spacings that are commensurate with a hydrogen bond, the six-fold coordination frustrates preferred bonding patterns. As a result this surface has regions of local hexagonal order, rings of waters surrounding a vacancy, that are seen in the monolayer structures of water absorbed on the 111 surface of many FCC metals [214]. Since such a hexagonal arrangement cannot tile space, this surface also has a fluctuating concentration of interstitials that occupy the empty top sites with water dipoles that point away from the surface on average. This disorder results in an average coverage of about 85% of all top sites. For both surfaces the lattices are entirely regular, and therefore the heterogeneity in the hydrogen bonding network is dynamic. However, the imposed order within the adlayer dictates that relaxation occurs over long timescales. Similar hydrogen bonding defects have been observed experimentally under ultrahigh vacuum conditions at low temperatures on Pd(111)[25] and in water-hydroxyl films on Cu(110)[64].

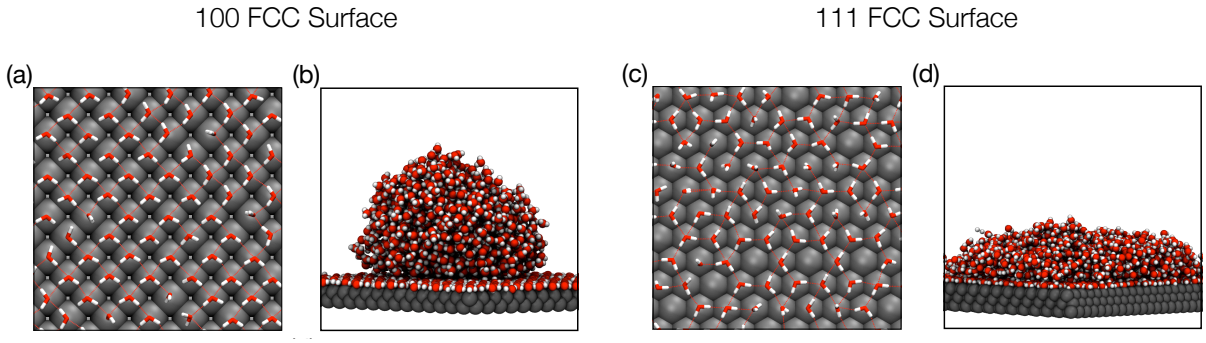

Figure 6.6: Sections of the 100 and 111 adlayers each measuring 3 nm^2 and and their effect on macroscopic solvation. (a) The 100 surface is locally four coordinated and commensurate with favorable hydrogen bonding patterns. Large ordered domains are separated by line defects. (b) The highly ordered domains donate few hydrogen bonds to the subsequent water layers discouraging those layers to wet the composite metal-water surface. (c) The 111 surface is locally six coordinated and frustrates hydrogen bonding. Though water is still ordered, vacancies and interstitial defects are common. (d) Hydrogen bond donor sites are more common than on the 100 surface, and subsequently the contact angle is smaller. Figure adapted from Ref. [137].

The presence of extended interfaces in solution, such as the solvated metal surface, are expected to influence the properties of subsequent solvent layers over distances corresponding to the bulk correlation length. For a liquid near coexistence with its vapor, such as water at ambient conditions, extended inhomogeneities can give rise to a de-wetting transition [29], whose interfaces subsequently have larger correlation lengths. Figure 6.7a graphs the mean density of water molecules as a functions of the distance away from the metal surface. Although the structure on the adlayer depends intimately on the metal geometry, the surrounding water is fairly insensitive to the exposed crystal face. We find for both surface geometries that the density profile for water away from the interface exhibits a sharp peak at the metal surface, indicative of the adlayer, followed by a region of a density depletion approximately 3 Å thick. Density oscillations decay over 1 nm away from the surface. The asymmetry between hydrogen bond donors and acceptors at the interface results in an unbalanced attraction, however the effective interaction with the surface is not so weak so as to allow the formation of capillary waves that would destroy the density oscillations seen away from the metal.

The water-metal interface is hydrophobic The unbalanced attraction immediately adjacent to the adlayer is enough to make solvation of ideal hydrophobes (hard-spheres) favorable at the interface. Figure 6.7c illustrates a representative configuration of water near the interface. In this snapshot, the instantaneous liquid interface constructed using the procedure in Ref. [232], shows the characteristic large fluctuations expected for a hydrophobic interface that easily accommodates the solvation of small solutes. Figure 6.7b, plots the

excess chemical potential for a hard sphere with a radius of 3 Å. We calculate this quantity by monitoring the number fluctuations within a probe volume. Specifically, we calculate the probability of observing N molecules in the probe volume, v,

$$\begin{aligned} P_v(N) &= \langle \delta(N_v - N) \rangle \\ &= \lim_{t\to\infty} \frac{1}{t} \int_0^t dt' \, \delta(N_v(t') - N) \,, \end{aligned} \tag{6.7}$$

where $\delta(N_v - N)$ is a Kronecker delta function and $\langle \dots \rangle$ denotes equilibrium average. This distribution is related to the excess solvation free energy for an ideal hydrophobe through the relation[90]

$$P_v(0) = e^{-\beta \Delta\mu_v} \tag{6.8}$$

where $\Delta\mu_v$ is the reversible work to create a cavity of size and shape v and β is one over temperature times Boltzmann's constant.

For the systems we consider here, the existence of the planar surface breaks translational invariance. In order to accommodate this aspect we denote, $P_{v(\mathbf{r})}(N)$, where $\mathbf{r}$ is the position of the center of the probe volume. This distribution reduces to $P_{v(\mathbf{r})}(N) \to P_v(N)$ when $\mathbf{r}$ is far away from the surface. Correspondingly, we also define $P_{v(\mathbf{r})}(0) = \exp\left[-\beta \Delta\mu_{v(\mathbf{r})}\right]$. In other words, solvation free energy in an inhomogeneous system is generally spatially dependent.

Due to the separation of timescales between surface and bulk relaxation, our system is also dynamically heterogeneous. Therefore, on intermediate timescales, $\tau_{\rm b} \ll t < \tau_{\rm s}$, the solvation free energy carries a time-dependence. This time dependence is denoted as,

$$P_{v(\mathbf{r})}(N, t; \mathbf{x}_0) = \frac{1}{t} \int_0^t dt' \, \delta\left[N_{v(\mathbf{r})}(t'; \mathbf{x}_0) - N\right] \tag{6.9}$$

where $\mathbf{x}_0$ denotes the initial surface configuration and t is the timescale over which the distribution is averaged. For $t \gg \tau_{\rm s}$, Eq. 6.9 simplifies to, $P_{v(\mathbf{r})}(N, t;\, \mathbf{x}_0) \to P_{v(\mathbf{r})}(N)$. For the case of $N = 0$, Eq. 3 yields a time dependent generalization of the solvation free energy,

$$P_{v(\mathbf{r})}(0, t; \mathbf{x}_0) = e^{-\beta \Delta\mu_{v(\mathbf{r})}(t;\, \mathbf{x}_0)} \tag{6.10}$$

Finally, the difference between the value of the solvation free energy located at $\mathbf{r}$, averaged over a time t, and its equilibrium bulk value is defined as

$$\delta\mu_v(\mathbf{r}, t;\, \mathbf{x}_0) = \Delta\mu_{v(\mathbf{r})}(t;\, \mathbf{x}_0) - \Delta\mu_v \,. \tag{6.11}$$

For $t \to \infty, \delta\mu_v(\mathbf{r}, t;\, \mathbf{x}_0) \to \delta\mu_v(\mathbf{r})$ and for $\mathbf{r}$ far away from the surface $\delta\mu_v(\mathbf{r}) \to 0$. At long times, and averaged over the plane of the surface, the solvation free energy has a minimum at the distance of closest approach to the composite water-metal surface, z^*, indicated by a dashed line in Fig. 6.7(a,b). The negative solvation free energy implies that while the bare metal surface attracts water, the composite water-metal surface is hydrophobic and as

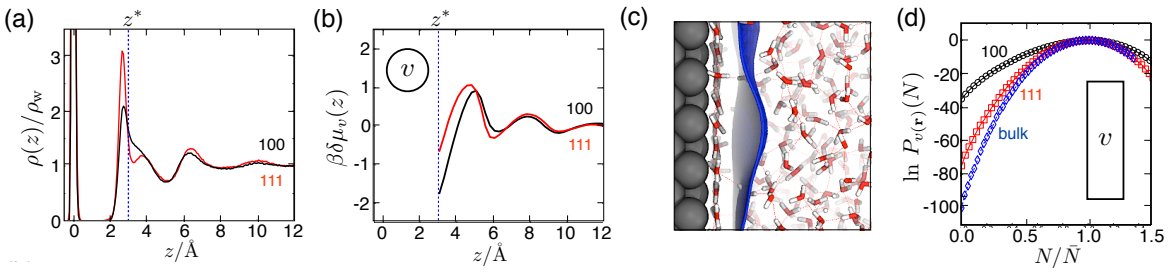

Figure 6.7: Structure and solvation of the composite water-metal interface. (a) The density profile of water molecules away from both surfaces, divided by the bulk water density, $\rho_w = 0.033$ Å^{-3}. The density is characterized by a strongly bound adsorbed layer and solvent layering that extends roughly 10 Å into the bulk. Immediately adjacent to the adsorbed layer is a region of density depletion. (b) The excess solvation free energy for a 3 Å in radius ideal hydrophobe as a function of distance away from the 111 and 100 surfaces. The dashed lines in (a) and (b) define z^* as the distance of closest approach of the 3 Åsphere to the adlayer. (c) For the 100 surface, shown, or a 111 surface, a typical configuration of water molecules and its instantaneous liquid interface (blue). (d) Probability distribution for finding N particles in a cuboid probe volume, $v = 20 \times 20 \times 3$Å^3, whose outer edge is located at z^*, with a mean occupancy $\bar{N}$. $\bar{N}$ = 31,34 and 40 for the 100 surface, 111 surface and bulk, respectively. Figure adapted from Ref. [137].

such preferentially attracts oil. While both metal geometries exhibit enhanced hydrophobic solubility, the 100 surface is more hydrophobic as measured by its excess solvation free energy at z^*, $\beta\delta\mu_v(z^*) \approx -2.0$, compared to the 111 surface, $\beta\delta\mu_v(z^*) \approx -0.7$ for the 3 Å sphere. Modulating the strength of the water-metal binding energy up to 30% through changes in the model parameters effect changes in these mean chemical potential values by less then 10%.

Hydrophobicity is a manifestation of a liquid-vapor-like interface Using the method of indirect umbrella sampling (INDUS) [174] we are able to compute stationary distribution functions, $P_{v(\mathbf{r})}(N)$, for extremely rare fluctuations involved in solvating large probe volumes. By studying the tails of these distributions we can determine to what extent interface formation, as opposed to Gaussian density fluctuations, are important in solvation at the interface.

The specific dimensions of the probe volume we use are chosen to focus on the role of interfacial fluctuations. In particular, the probe volume is thin enough, 3 Å, to include molecules that can be part of a liquid interface while not also containing molecules that are part of the bulk; and it is wide enough, 20×20 Å^2, to capture nano-scale fluctuations intrinsic to the soft liquid interface. Figure 6.7c shows a configuration of water and the instantaneous liquid interface[232] highlighting how solvation at the surface occurs by deforming a soft interface. The signature of this behavior is demonstrated in Fig. 6.7d where highly correlated behavior, interface formation in this case, is apparent by the appearance of an exponential

tail in the probability distribution, $P_{v(\mathbf{r})}(N)$, for small N for both surfaces relative to the bulk.

The pictured distributions along with Eqs. 6.10 and 6.11 allow us to calculate the excess solvation free energy for this large probe volume. We find that this is negative at both surfaces, however solvation for this large probe volume at the 100 surface is more favorable by $40\,k_{\mathrm{B}}T$ compared to the 111 surface. While both surfaces afford hydrogen bond acceptor sites, only the 111 surface has a nonzero number of hydrogen bond donors. Using a standard criteria for defining a hydrogen bond [148], we calculate an average hydrogen bond donor density on the surface to be approximately $1.0/\mathrm{nm}^2$ for the 111 surface and $0.0/\mathrm{nm}^2$ for the 100 surface. This means that in the large probe volume on the 111 surface, there is on average 4 hydrogen bonds donated to the bulk. These few hydrogen bonds, produce the $40\,k_{\mathrm{B}}T$ change in solvation and it is expected that the addition of further hydrogen bond defects would make the surface hydrophilic.

This microscopic measure of solvation can be related to traditional macroscopic measures probed experimentally. As described above large length scale solvation at hydrophobic surfaces is dominated by deforming existing interfaces, so the excess chemical potential is expected to be well approximated by $\beta\delta\mu(z^*) = -A\gamma_{\mathrm{LV}}(1-\cos\theta)$ where A is the cross-sectional area of a large probe volume, γ_{LV} is the liquid-vapor surface tension, and θ is the water droplet contact angle on the surface. The more favorable solvation at the surface of the 100 surface is expected to result in a contact angle $\theta \approx 90^{\mathrm{o}}$, whereas the subtly favorable solvation at the 111 surface is expected to result in a contact angle of $\theta \approx 40^{\mathrm{o}}$. These are in qualitative agreement with the configurations shown in Fig. 6.6.

These results are in agreement with previous experiments on the platinum 111 surface that inferred hydrophobicity under low temperature ultrahigh vacuum conditions [113] and in mixed water-hydroxyl overlayers [241]. As discussed, the model we use does not account for water dissociation at the surface or produce the correct ground state structure for platinum at low temperatures. However it simply patterns fully hydrogen bonded contact layers. For this reason these results are not expected to be unique to water on metals but rather a general result of surfaces that similarly constrain the number of donated hydrogen bonds. Instances of this behavior have already been observed in clays [88] and could potentially be observed in other oxides and even in biological settings[170].

6.3.2 Dynamic heterogeneity of slowly relaxing surface water

The data presented in Fig. 6.7 graphs equilibrium values of the excess solvation free energy averaged over the plane parallel to the surface, computed by averaging over long molecular dynamics trajectories, of roughly 10 ns. The presence of a region of strong water density depletion induced by the local structure of the water adlayer implies that only on timescales much longer than the correlation time for typical bulk density fluctuations, $\tau_{\mathrm{b}} \approx$ 5ps [53], will solvation within this plane be homogeneous, i.e. $\beta\delta\mu(x,y) \approx$ const. However, the ordering within this surface adlayer makes reorganization difficult, and as a result the timescale associated with de-correlating surface configurations, $\tau_{\mathrm{s}} \approx 1-10$ns, is long. For

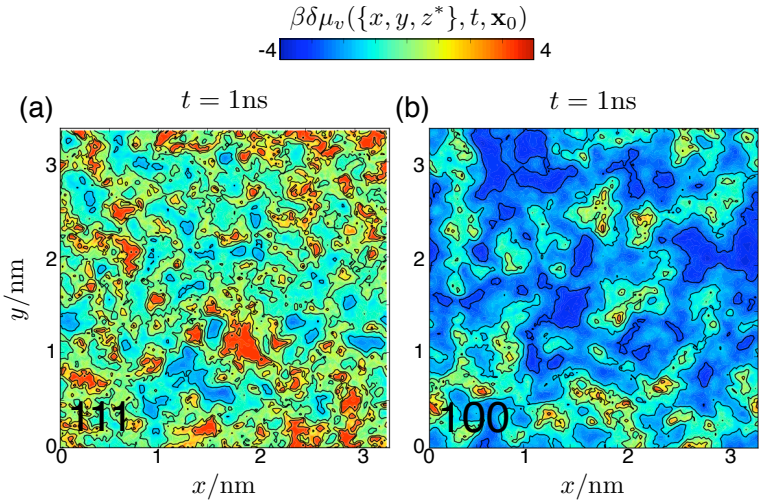

Figure 6.8: Heterogeneous solvation at the metal surface. (a,b) The excess free energy for a 3 Å ideal hydrophobe is heterogeneous at both 111 and 100 surfaces. Regions of favorable and unfavorable solvation have been determined by averaging over 1 ns from an initial surface configuration, $\mathbf{x}_0$. Figure adapted from Ref. [137].

intermediate times, $\tau_b \ll t < \tau_s$, this long time surface relaxation couples to the solvation in interesting ways. In particular, we find that for averages computed over this time, $1\,\text{ns} < t < 10\,\text{ns}$, the solvation calculated within the surface is heterogeneous. Figure 6.8 depicts the spatially resolved solvation free energy, $\beta\delta\mu(\{x,y,z^*\},t;\mathbf{x}_0)$ at both surface geometries for a 3 Å sphere, as a function of position in the x,y plane and observation time, for a given surface configuration. This method of spatially resolving the local hydrophobicity is a time dependent extension of previous work by others on protein surfaces, which have static heterogeneity[3]. As shown in Fig. 6.8 the structure of the solvation on this surface reflects neither the underlying lattice symmetry nor the homogeneous symmetry of the above liquid, but rather the coupling between hydrogen bonding defect structures of the bound water adlayer and the above solvent layers. We can quantify the surface heterogeneity by calculating a time-dependent variance $C(t) = \langle[\,\delta\mu(\{x,y,z^*\},t;\mathbf{x}_0) - \delta\mu(z^*)]^2\rangle$, where $\delta\mu(z^*)$ is an average excess solvation free energy at z^* and as before $\langle\ldots\rangle$ denote averages over realizations of initial surface conditions. We find for times satisfying $t \gg \tau_b$, the spatial average over the surface is equal to the long time average. Using this measure we find that for all times the solvation on the 111 is more heterogeneous than on the 100 surface, owing to the larger domain sizes seen on the ordered bound layer in the 100 surface. These domains sizes are on average approximately 1Å^2 for the 111 surface and 3 Å^2 for the 100 surface, as obtained by coarse-graining Figs. 6.8a and b over 1 k_BT. Figures 6.9a-c show $\beta\delta\mu(\{x,y,z^*\},t;\mathbf{x}_0)$ as t is increased for the 111 surface. Generically, reorganization on the surface occurs as t is increased, and the amount of heterogeneity is reduced. Similar behavior is found for the 100 surface. In order to quantify the timescales for relaxing this

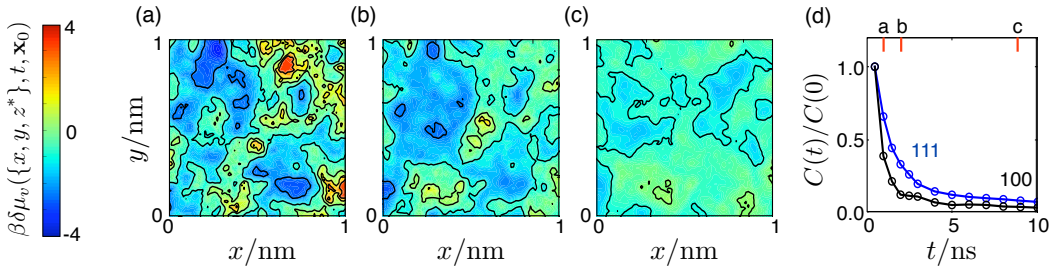

Figure 6.9: Evolution of the solvation free energy as the surface reorganizes from an initial configuration, $\mathbf{x}_0$. (a-c) Maps of the excess free energy averaged over different observation times for a 1nm^2 section of the 111 surface. Contour plots are reported using the same scale shown in the colorbar on the left. (d) The time correlation function for solvation heterogeneities for each surface. Points a, b and c coincides with times for panels (a), (b) and (c). Figure adapted from Ref. [137].

heterogeneity we measure the decay of $C(t)/C(0)$, where the argument of the denominator is taken at the smallest t where $\tau_b \ll t \approx 0.5$ns. Figure 6.9d plots $C(t)/C(0)$ for both surfaces and illustrates that the time to reach a uniform solvation potential at the surface is on the order of 10 ns. This time is on the order of many of the slow processes the occur on the metal surface such as the mean dipole correlation time 1-10 ns.

6.3.3 Implications for electrochemistry

In this paper, we have shown that a hydrophobic surface formed from a passivated adlayer of water is accompanied by the existence of a liquid-vapor-like interface separating the adlayer from the bulk liquid. Previous work has discussed how such a soft liquid interface can itself act catalytically, offering dangling OH bond that can stabilize transition states or donate protons[103]. Others have demonstrated that excess protons [24, 176], as well as some anions[105], preferentially adsorb to a liquid-vapor interface.

As one means of testing the assertion of a proton enhancement at the water-metal interface, we have calculated the density profile for a fixed point charge model of a hydronium[219] cation using umbrella sampling. We choose this model as it has been shown previously that excess protons at the liquid vapor interface preferentially adopt a hydronium geometry over other forms, such as the Zundel cation[24, 176]. The local solvation structure of a hydronium in bulk is characterized by donation of a hydrogen bond by each of its three hydrogens, but its inability to accept any hydrogen bonds at the oxygen position due to the localized positive charge on the molecule. It has been demonstrated previously that this structure is conserved at the liquid vapor interface [176].

At the water-metal interface the adlayer is composed almost entirely of hydrogen bond acceptor sites and thus it is expected that density of hydronium ions will be even further enhanced by their ability to donate hydrogen bonds into the adlayer. A characteristic snap

shot of this type of configuration at the 111 surface is shown in the inset of Fig. 6.10. The main panel of Fig. 6.10 confirms a large density enhancement of hydronium ions at the interface relative to the bulk. This density distribution is calculated from, $\rho_{H_3O^+}(z) = \rho_{\text{ref}} \exp[-\beta F(z)]$, where ρ_{ref} is the density of the hydronium in the bulk and $F(z)$ is the potential of mean force for moving the center of mass of the hydronium along the z direction. The enhancement found from this simplistic calculation is $\rho(z^*) \approx 10\rho_{\text{bulk}}$, much larger than the enhancement found at the liquid vapor interface, which for this model we calculate to be $1.5\rho_{\text{bulk}}$. We note that while important aspects of proton delocalization and polarizability are neglected in this calculation, each affect is expected to further enhance interfacial adsorption. Thus while this calculation is overly simplistic, we nevertheless suspect this behavior to be conserved in more detailed models.

In the specific case of hydrogen evolution at a platinum electrode, it is generally assumed that the reaction proceeds through two steps: the Volmer step, where a proton is transferred form the bulk and discharged at the metal surface, followed by the Tafel step where two adsorbed protons combine to form hydrogen and desorb from the surface[39]. The latter is considered to be the rate determining step. The enhancement of the hydronium concentration at the interface is consistent with platinum's ability to easily transfer and accumulate protons on and near the surface, while the long time relaxation on the surface detailed here undoubtably makes diffusion of adsorbents slow. While these results are consistent with mechanistic assertions for hydrogen evolution, further work must be done to explore the full implications of the effects illustrated here on catalysis.

6.3.4 Molecular model

The system simulated consists of a slab of water in contact with a metal on one side and with a free interface on the other side with a vacuum layer of 40 Å. The metal surface consists of three layers of atoms, totaling nearly 500 particles, held fixed in an FCC lattice with spacing of 3.92 Å and with either the 100 or 111 facet exposed to the solution. A slab of water nearly 40 Å thick was placed in contact with the metal, and the dynamics of the nearly 1800 molecules are propagated using a Nose Hover integrator [151], with SHAKE imposing bond and angle constraints for the water as implemented in LAMMPS [177]. All simulations were run at 298 K. Interactions between the water molecules are computed from the SPC/E potential [14]. The water-metal potential is modeled following Siepmann and Sprik [199] where the platinum water interaction is a sum of two and three body terms, parameterized to get the correct value of the adsorption energy and ground state geometry as determined by quantum chemical calculations. Additionally, to model the polarizable metal surface each atom carries a Gaussian charge of fixed width but variable amplitude, which is updated at each timestep by minimizing the energy of the slab subject to a constraint of equal potential across the conductor. Periodic boundary conditions are employed in the plane parallel to the surface. Ewald summations appropriate for mixed point and Gaussian charge densities were employed[70]. A more thorough description of the model can be found elsewhere [199, 234]. The calculations of the excess hydronium ion were accomplish using umbrella sampling along

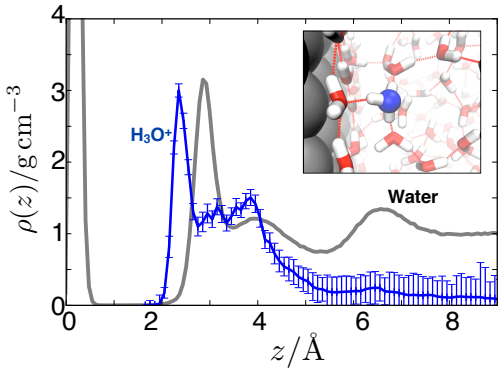

Figure 6.10: Structure and density enhancement of hydronium ions at the liquid-vapor and water-metal interface. (main) Density distributions for the water (grey) and hydronium (blue), with a reference bulk density of the hydronium, $\rho_{\text{ref}} = 0.1\text{g/cm}^3$ chosen for scale. (inset) A characteristic snapshot of a H_3O^+ at the 111 interface. Figure adapted from Ref. [137].

the z coordinate. For charge neutrality a small anion was placed in the water slab but kept at distances greater than 15 Å from the hydronium.

As discussed, relaxation of the water on the metal surface is slow . In order to quantify the timescales associated with surface reorganization we calculate a water's dipole time correlation function given it starts and ends adsorbed to the surface, $C_{\mu\mu}(t) = \langle \delta\vec{\mu}_i(t) \cdot \delta\vec{\mu}_i(0) h[i(t)] h[i(0)] \rangle$, where $\vec{\mu}_i$ is the dipole vector for the i water molecule and h_i is an indicator function which is equal to 1 if the center of mass of water molecule i is within 3 Å of a metal atom and is 0 otherwise. Correlation functions for both surfaces have stretched exponential forms and decay over timescales greater than 1 ns.

The long relaxation times in the system relative to the timescales accessible by our simulations make ensuring equilibration on the surface difficult. In order to check the sensitivity of our results to their initial conditions we have prepared an ensemble of 40 independent surfaces, for both the 100 and 111 crystal faces. Twenty surfaces were produced through quenching the system at a rate of 10 K/ns from a system equilibrated at T=400 K, and 20 from a process of vapor deposition where water molecules are exposed to the surface at a rate of 2 molecules/ 1 ns nm^2. We have redone all of the calculations presented in the main text over this extended surface ensemble and found results that were indistinguishable from those presented above.

Using our atomistic model for the water-metal interface, we compute potential of zero charge, U_{pzc}, relative to the hydrogen electrode compare it to the known experimental value[33]. Previous work has shown that the surface dipole induced by the adsorption of water on a platinum surface can be decomposed into two components: an indirect polarization of the metal surface and a direct contribution from the dipoles of the water. While the latter effect is strongly dependent on surface coverage and instantaneous configuration of the adsorbed water, the former is relatively constant. Thus, while the classical model we employ

here is expected to underestimate the polarization contribution, we would expect a reasonable estimate for the direct water contribution. For the 111 surface, the contact potential across the water bilayer we measure is, $\psi_{\mathrm{D}} = -0.7V$. Using the polarization contribution found from quantum chemical calculations, $\psi_{\mathrm{P}} = 1.2V$[98] we calculate the potential of zero charge to be $U_{\mathrm{pzc}} = 0.9V$ compared to the experimental value of $U_{\mathrm{pzc}} = 0.4V$[98].

Bibliography

[1] J. L. Abascal and C. Vega. A general purpose model for the condensed phases of water: Tip4p/2005. *Journal of Chemical Physics*, 123:234505, 2005.

[2] J. L. Abascal and C. Vega. Widom line and the liquid-liquid critical point for the tip4p/2005 water model. *Journal of Chemical Physics*, 133(23):234502, 2010.

[3] H. Acharya, S. Vembanur, S. N. Jamadagni, and S. Garde. Mapping hydrophobicity at the nanoscale: Applications to heterogeneous surfaces and proteins. *Faraday discussions*, 146:353–365, 2010.

[4] P. Agre. The aquaporin water channels. *Proceedings of the American Thoraic Society*, 3(1):5–13, Jan 2006.

[5] C. Alba-Simionesco, B. Coasne, G. Dosseh, G. Dudziak, K. Gubbins, R. Radhakrishnan, and M. Sliwinska-Bartkowiak. Effects of confinement on freezing and melting. *Journal of Physics: Condensed Matter*, 18(6):R15, 2006.

[6] C. Angell. Supercooled water. *Annual Review of Physical Chemistry*, 34(1):593–630, 1983.

[7] C. A. Angell. Formation of glasses from liquids and biopolymers. *Science*, 267(5206):1924–1935, 1995.

[8] S. Augustine and J. H. Taylor. *The literal meaning of Genesis*, volume 1. Paulist Press, 1982.

[9] R. Bader and G. Jones. The electron density distributions in hydride molecules: I. the water molecule. *Canadian Journal of Chemistry*, 41(3):586–606, 1963.

[10] P. Ball. *Life's matrix: a biography of water*. Univ of California Press, 2001.

[11] E. P. Barrett, L. G. Joyner, and P. P. Halenda. The determination of pore volume and area distributions in porous substances. i. computations from nitrogen isotherms. *Journal of the American Chemical Society*, 73(1):373–380, Jan 1951.

[12] D. Beaglehole and D. Nason. Transition layer on the surface on ice. *Surface Science*, 96(1):357–363, 1980.

[13] P. Beaucage and N. Mousseau. Liquid–liquid phase transition in stillinger–weber silicon. *Journal of Physics: Condensed Matter*, 17(15):2269, 2005.

[14] H. Berendsen, J. Grigera, and T. Straatsma. The missing term in effective pair potentials. *Journal of Physical Chemistry*, 91(24):6269–6271, 1987.

[15] H. J. C. Berendsen, J. R. Grigera, and T. P. Straatsma. *Journal of Chemical Physics*, 91(24):6269–6271, 1987.

[16] C. E. Bertrand, Y. Zhang, and S.-H. Chen. Deeply-cooled water under strong confinement: neutron scattering investigations and the liquid–liquid critical point hypothesis. *Physical Chemistry Chemical Physics*, 15(3):721–745, 2013.

[17] K. Binder. Monte-carlo calculation of the surface-tension for two-dimensional and three-dimensional lattice-gas models. *Physical Review A*, 25(3):1699–1709, Jan 1982.

[18] K. Binder. *Monte Carlo and Molecular Dynamics Simulations Polymer*. Oxford University Press, Inc., 1995.

[19] C. L. Bishop, D. Pan, L. M. Liu, G. A. Tribello, A. Michaelides, E. G. Wang, and B. Slater. On thin ice: Surface order and disorder during pre-melting. *Faraday discussions*, 141:277–292, 2009.

[20] H. Bluhm, T. Inoue, and M. Salmeron. Friction of ice measured using lateral force microscopy. *Physical Review B*, 61(11):7760, 2000.

[21] H. Bluhm, D. F. Ogletree, C. S. Fadley, Z. Hussain, and M. Salmeron. The premelting of ice studied with photoelectron spectroscopy. *Journal of Physics: Condensed Matter*, 14(8):L227, 2002.

[22] P. G. Bolhuis, D. Chandler, C. Dellago, and P. L. Geissler. Transition path sampling: Throwing ropes over rough mountain passes, in the dark. *Annual Review of Physical Chemistry*, 53(1):291–318, 2002.

[23] I. Brovchenko, A. Geiger, and A. Oleinikova. Liquid-liquid phase transitions in supercooled water studied by computer simulations of various water models. *Journal of Chemical Physics*, 123:044515, 2005.

[24] V. Buch, A. Milet, R. Vácha, P. Jungwirth, and J. P. Devlin. Water surface is acidic. *Proceedings of the National Academy of Sciences*, 104(18):7342–7347, 2007.

[25] J. Cerda, A. Michaelides, M.-L. Bocquet, P. J. Feibelman, T. Mitsui, M. Rose, E. Fomin, and M. Salmeron. Novel water overlayer growth on pd (111) characterized with scanning tunneling microscopy and density functional theory. *Physical Review Letters*, 93(11):116101, 2004.

[26] P. M. Chaikin and T. C. Lubensky. *Principles of condensed matter physics*, volume 1. Cambridge Univ Press, 2000.

[27] D. Chandler. Statistical mechanics of isomerization dynamics in liquids and the transition state approximation. *Journal of Chemical Physics*, 68:2959, 1978.

[28] D. Chandler. *Introduction to Modern Statistical Mechanics*. Oxford University Press, USA, 1987.

[29] D. Chandler. Interfaces and the driving force of hydrophobic assembly. *Nature*, 437(7059):640–647, 2005.

[30] D. Chandler, J. P. Garrahan, et al. Dynamics on the way to forming glass: bubbles in space-time. *Annual review of physical chemistry*, 61:191, 2010.

[31] I. Chang and H. Sillescu. Heterogeneity at the glass transition: Translational and rotational self-diffusion. *The Journal of Physical Chemistry B*, 101(43):8794–8801, 1997.

[32] J.-Y. Chen and C.-S. Yoo. High density amorphous ice at room temperature. *Proceedings of the National Academy of Sciences*, 108(19):7685–7688, 2011.

[33] J. Cheng and M. Sprik. Alignment of electronic energy levels at electrochemical interfaces. *Physical Chemistry Chemical Physics*, 14(32):11245–11267, 2012.

[34] M. T. Cicerone and M. Ediger. Relaxation of spatially heterogeneous dynamic domains in supercooled ortho-terphenyl. *Journal of Chemical Physics*, 103(13):5684–5692, 1995.

[35] G. N. Clark, G. L. Hura, J. Teixeira, A. K. Soper, and T. Head-Gordon. Small-angle scattering and the structure of ambient liquid water. *Proceedings of the National Academy of Sciences*, 107(32):14003–14007, 2010.

[36] M. Conde, C. Vega, and A. Patrykiejew. The thickness of a liquid layer on the free surface of ice as obtained from computer simulation. *Journal of Chemical Physics*, 129:014702, 2008.

[37] M. J. Cuthbertson and P. H. Poole. Mixturelike behavior near a liquid-liquid phase transition in simulations of supercooled water. *Physical Review Letters*, 106(11):115706, 2011.

[38] J. Dash, A. Rempel, and J. Wettlaufer. The physics of premelted ice and its geophysical consequences. *Reviews of modern physics*, 78(3):695, 2006.

[39] H. Dau, C. Limberg, T. Reier, M. Risch, S. Roggan, and P. Strasser. The mechanism of water oxidation: from electrolysis via homogeneous to biological catalysis. *ChemCatChem*, 2(7):724–761, 2010.

[40] P. L. Davies and B. D. Sykes. Antifreeze proteins. *Current opinion in structural biology*, 7(6):828–834, 1997.

[41] E. de La Llave, V. Molinero, and D. A. Scherlis. Water filling of hydrophilic nanopores. *Journal of Chemical Physics*, 133:034513, Jan 2010.

[42] P. G. Debenedetti. *Metastable liquids: concepts and principles*. Princeton University Press, 1996.

[43] P. G. Debenedetti. Supercooled and glassy water. *Journal of Physics: Condensed Matter*, 15(45):R1669, 2003.

[44] C. Despretz. I. researches on the maximum density of liquids. *The London and Edinburgh Philosophical Magazine and Journal of Science*, 12(71-72):1–10, 1838.

[45] S. Duane, A. Kennedy, B. Pendleton, and D. Roweth. Hybrid monte carlo. *Physics Letters B*, 195(2):216–222, 1987.

[46] A. Duncan and J. Pople. The structure of some simple molecules with lone pair electrons. *Transactions of the Faraday Society*, 49:217–224, 1953.

[47] M. Ediger. Spatially heterogeneous dynamics in supercooled liquids. *Annual review of physical chemistry*, 51(1):99–128, 2000.

[48] M. D. Ediger, C. A. Angell, and S. R. Nagel. *Journal of Chemical Physics*, 100(31):13200–13212, 1996.

[49] D. S. Eisenberg and W. Kauzmann. *The structure and properties of water*. Clarendon Press London, 2005.

[50] Y. S. Elmatad, D. Chandler, and J. P. Garrahan. Corresponding states of structural glass formers. *Journal of Physical Chemistry B*, 113(16):5563–5567, Jan 2009.

[51] Y. S. Elmatad, D. Chandler, and J. P. Garrahan. Corresponding states of structural glass formers. ii. *The Journal of Physical Chemistry B*, 114(51):17113–17119, 2010.

[52] M. Elsaesser, K. Winkel, E. Mayer, and T. Loerting. Reversibility and isotope effect of the calorimetric glass liquid transition of low-density amorphous ice. *Physical Chemistry Chemical Physics*, 12(3):708–712, 2010.

[53] N. J. English and J. S. Tse. Density fluctuations in liquid water. *Physical Review Letters*, 106(3):037801, 2011.

[54] M. Erko, D. Wallacher, A. Hoell, T. Hauß, I. Zizak, and O. Paris. Density minimum of confined water at low temperatures: a combined study by small-angle scattering of x-rays and neutrons. *Physical Chemistry Chemical Physics*, 14(11):3852–3858, 2012.

[55] R. Evans. Fluids adsorbed in narrow pores: phase equilibria and structure. *Journal of Physics: Condensed Matter*, 2:8989, Nov 1990.

[56] M. Faraday. Athenaeum 1181, 640 (1850). *Philos. Mag*, 17:162, 1859.

[57] A. Faraone, L. Liu, C.-Y. Mou, C.-W. Yen, and S.-H. Chen. Fragile-to-strong liquid transition in deeply supercooled confined water. *Journal of Chemical Physics*, 121:10843, 2004.

[58] V. Fatemi, M. Kamenetska, J. B. Neaton, and L. Venkataraman. *Nano Letters*, 11(5):1988, 2011.

[59] C. Fecko, J. Eaves, J. Loparo, A. Tokmakoff, and P. Geissler. Ultrafast hydrogen-bond dynamics in the infrared spectroscopy of water. *Science*, 301(5640):1698–1702, 2003.

[60] P. J. Feibelman, G. A. Kimmel, R. S. Smith, N. G. Petrik, T. Zubkov, and B. D. Kay. A unique vibrational signature of rotated water monolayers on pt (111): Predicted and observed. *Journal of Chemical Physics*, 134:204702, 2011.

[61] B. Feuston and S. H. Garofalini. Water-induced relaxation of the vitreous silica surface. *Journal of applied physics*, 68(9):4830–4836, 1990.

[62] R. P. Feynman. *The Meaning of It All: Thoughts of a Citizen Scientis*. Da Capo Press, 1998.

[63] G. Findenegg, S. Jähnert, D. Akcakayiran, and A. Schreiber. Freezing and melting of water confined in silica nanopores. *European Journal of Chemical Physics and Physical Chemistry*, 9(18):2651–2659, Jan 2008.

[64] M. Forster, R. Raval, A. Hodgson, J. Carrasco, and A. Michaelides. c (2× 2) water-hydroxyl layer on cu (110): A wetting layer stabilized by bjerrum defects. *Physical Review Letters*, 106(4):046103, 2011.

[65] D. Frenkel and B. Smit. *Understanding molecular simulation: from algorithms to applications*. Academic press, 2001.

[66] D. Fuentevilla and M. Anisimov. Scaled equation of state for supercooled water near the liquid-liquid critical point. *Physical Review Letters*, 97(19):195702, 2006.

[67] P. Gallo, M. Rovere, and S.-H. Chen. Dynamic crossover in supercooled confined water: Understanding bulk properties through confinement. *The Journal of Physical Chemistry Letters*, 1:729–733, Jan 2010.

[68] P. Ganesh and M. Widom. Liquid-liquid transition in supercooled silicon determined by first-principles simulation. *Physical Review Letters*, 102(7):075701, 2009.

[69] J. P. Garrahan, R. L. Jack, V. Lecomte, E. Pitard, K. van Duijvendijk, and F. van Wijland. Dynamical first-order phase transition in kinetically constrained models of

glasses. *Physical Review Letters*, 98(19):195702, 2007.

[70] T. Gingrich. *Simulating surface charge effects in carbon nanotube templated ionic crystal growth*. PhD thesis, Masters thesis (Oxford University, Oxford), 2010.

[71] N. Giovambattista, T. Loerting, B. R. Lukanov, and F. W. Starr. Interplay of the glass transition and the liquid-liquid phase transition in water. *Scientific Reports*, 2, 2012.

[72] S. C. Glotzer. Spatially heterogeneous dynamics in liquids: insights from simulation. *Journal of Non-Crystalline Solids*, 274(1):342–355, 2000.

[73] N. Goldenfeld. *Lectures on phase transitions and the renormalization group*. Addison-Wesley, Advanced Book Program, Reading, 1992.

[74] W. Gotze and L. Sjogren. Relaxation processes in supercooled liquids. *Reports on Progress in Physics*, 55(3):241, 1992.

[75] L. Gránásy, T. Pusztai, and P. F. James. Interfacial properties deduced from nucleation experiments: A cahn–hilliard analysis. *Journal of Chemical Physics*, 117:6157, 2002.

[76] G. Grimmett and D. Stirzaker. *Probability and random processes*, volume 2. Clarendon press Oxford, 1992.

[77] A. Hallbrucker, E. Mayer, and G. P. Johari. Glass-liquid transition and the enthalpy of devitrification of annealed vapor-deposited amorphous solid water: a comparison with hyperquenched glassy water. *The Journal of Physical Chemistry*, 93(12):4986–4990, 1989.

[78] J. Hallett. The temperature dependence of the viscosity of supercooled water. *Proceedings of the Physical Society*, 82(6):1046, 1963.

[79] J.-P. Hansen and I. R. McDonald. *Theory of simple liquids*. Academic press, 2006.

[80] S. Harrington, R. Zhang, P. H. Poole, F. Sciortino, and H. E. Stanley. Liquid-liquid phase transition: Evidence from simulations. *Physical Review Letters*, 78(12):2409–2412, 1997.

[81] D. M. Hassett, C. J. Marsden, and B. J. Smith. The ammonia dimer potential energy surface: resolution of the apparent discrepancy between theory and experiment? *Chemical physics letters*, 183(5):449–456, 1991.

[82] L. O. Hedges, R. L. Jack, J. P. Garrahan, and D. Chandler. Dynamic order-disorder in atomistic models of structural glass formers. *Science*, 323(5919):1309–1313, 2009.

[83] L. O. Hedges, L. Maibaum, D. Chandler, and J. P. Garrahan. Decoupling of exchange and persistence times in atomistic models of glass formers. *Journal of Chemical Physics*, 127:211101, 2007.

[84] J. Hedstrom, J. Swenson, R. Bergman, H. Jansson, and S. Kittaka. Does confined water exhibit a fragile-to-strong transition? *The European Physical Journal Special Topics*, 141:53–56, Jan 2007.

[85] H. Herce, A. Garcia, and T. Darden. The electrostatic surface term:(i) periodic systems. *Journal of Chemical Physics*, 126(12):124106–124106, 2007.

[86] A. Hodgson and S. Haq. Water adsorption and the wetting of metal surfaces. *Surface Science Reports*, 64(9):381–451, 2009.

[87] V. Holten and M. Anisimov. Entropy-driven liquid-liquid separation in supercooled water. *Scientific reports*, 2, 2012.

[88] X. L. Hu and A. Michaelides. Water on the hydroxylated (001) surface of kaolinite: From monomer adsorption to a flat 2d wetting layer. *Surface Science*, 602(4):960–974, 2008.

[89] C. Huang, C. Li, P. Y. Choi, K. Nandakumar, and L. W. Kostiuk. A novel method for molecular dynamics simulation in the isothermal–isobaric ensemble. *Molecular Physics*, 109(2):191–202, 2011.

[90] G. Hummer, S. Garde, A. E. García, A. Pohorille, and L. R. Pratt. An information theory model of hydrophobic interactions. *Proceedings of the National Academy of Sciences*, 93(17):8951–8955, 1996.

[91] D. W. Hwang, C.-C. Chu, A. K. Sinha, and L.-P. Hwang. Dynamics of supercooled water in various mesopore sizes. *Journal of Chemical Physics*, 126:044702, 2007.

[92] E. Isaacson and H. Keller. *Analysis of numerical methods*. Dover Publications, 1994.

[93] R. Jack and P. Sollich. Large deviations and ensembles of trajectories in stochastic models. *Progress of Theoretical Physics*, 184:304–317, 2010.

[94] J. Jäckle and S. Eisinger. A hierarchically constrained kinetic ising model. *Zeitschrift für Physik B Condensed Matter*, 84(1):115–124, 1991.

[95] L. C. Jacobson, W. Hujo, and V. Molinero. Thermodynamic stability and growth of guest-free clathrate hydrates: a low-density crystal phase of water. *The Journal of Physical Chemistry B*, 113(30):10298–10307, 2009.

[96] E. Jagla. Liquid-liquid equilibrium for monodisperse spherical particles. *Physical Review E*, 63(6):061501, 2001.

[97] F. Jiao and H. Frei. Nanostructured cobalt oxide clusters in mesoporous silica as efficient oxygenâĂŘevolving catalysts. *Angewandte Chemie International Edition*, 48(10):1841–1844, 2009.

[98] R. Jinnouchi and A. B. Anderson. Electronic structure calculations of liquid-solid interfaces: Combination of density functional theory and modified poisson-boltzmann theory. *Physical Review B*, 77(24):245417, 2008.

[99] G. P. Johari, A. Hallbrucker, and E. Mayer. The glass–liquid transition of hyperquenched water. *Nature*, 330(6148):552–553, 1987.

[100] E. R. Johnson and A. D. Becke. A post-hartree–fock model of intermolecular interactions. *Journal of Chemical Physics*, 123:024101, 2005.

[101] J. Johnston and V. Molinero. Crystallization, melting, and structure of water nanoparticles at atmospherically relevant temperatures. *Journal of the American Chemical Society*, 134(15):650–6659, Jan 2012.

[102] Y. Jung, J. P. Garrahan, and D. Chandler. Excitation lines and the breakdown of stokes-einstein relations in supercooled liquids. *Physical Review E*, 69(6):061205, 2004.

[103] Y. Jung and R. Marcus. On the theory of organic catalysis Òon waterÓ. *Journal of the American Chemical Society*, 129(17):5492–5502, 2007.

[104] Y. J. Jung, J. P. Garrahan, and D. Chandler. *Journal of Chemical Physics*, 123:084509, 2005.

[105] P. Jungwirth and D. J. Tobias. Ions at the air/water interface. *The Journal of Physical Chemistry B*, 106(25):6361–6373, 2002.

[106] N. Kastelowitz, J. C. Johnston, and V. Molinero. The anomalously high melting temperature of bilayer ice. *Journal of Chemical Physics*, 132:124511, Jan 2010.

[107] W. T. B. Kelvin. *Electrical units of measurement*. Institution, 1883.

[108] T. Kesselring. *Liquid-liquid critical point in ST2 water*. PhD thesis, Diss., Eidgenössische Technische Hochschule ETH Zürich, Nr. 20138, 2012, 2012.

[109] T. Kesselring, G. Franzese, S. Buldyrev, H. Herrmann, and H. Stanley. Nanoscale dynamics of phase flipping in water near its hypothesized liquid-liquid critical point. *Scientific Reports*, 2, 2012.

[110] T. A. Kesselring, E. Lascaris, G. Franzese, S. V. Buldyrev, H. J. Herrmann, and H. E. Stanley. Finite-size scaling investigation of the liquid-liquid critical point in st2 water and its stability with respect to crystallization. *arXiv preprint arXiv:1302.1894*, 2013.

[111] A. S. Keys, J. P. Garrahan, and D. Chandler. Calorimetric glass transition explained by hierarchical dynamic facilitation. *Proceedings of the National Academy of Sciences*, 2013.

[112] A. S. Keys, L. O. Hedges, J. P. Garrahan, S. C. Glotzer, and D. Chandler. Excitations are localized and relaxation is hierarchical in glass-forming liquids. *Physical Review X*, 1(2):021013, 2011.

[113] G. A. Kimmel, N. G. Petrik, Z. Dohnálek, and B. D. Kay. Crystalline ice growth on pt (111): Observation of a hydrophobic water monolayer. *Physical Review Letters*, 95(16):166102, 2005.

[114] T. Kirkpatrick, D. Thirumalai, and P. G. Wolynes. Scaling concepts for the dynamics of viscous liquids near an ideal glassy state. *Physical Review A*, 40(2):1045, 1989.

[115] W. Kob, C. Donati, S. J. Plimpton, P. H. Poole, and S. C. Glotzer. Dynamical heterogeneities in a supercooled lennard-jones liquid. *Physical Review Letters*, 79(15):2827–2830, 1997.

[116] K. Koga, G. Gao, H. Tanaka, and X. C. Zeng. Formation of ordered ice nanotubes inside carbon nanotubes. *Nature*, 412(6849):802–805, 2001.

[117] K. Koga, H. Tanaka, and X. Zeng. First-order transition in confined water between high-density liquid and low-density amorphous phases. *Nature*, 408(6812):564–567, 2000.

[118] I. Kohl, L. Bachmann, A. Hallbrucker, E. Mayer, and T. Loerting. Liquid-like relaxation in hyperquenched water atš 140 k. *Physical Chemistry Chemical Physics*, 7(17):3210–3220, 2005.

[119] J. Kolafa and J. W. Perram. Cutoff errors in the ewald summation formulae for point charge systems. *Molecular Simulation*, 9(5):351–368, 1992.

[120] C. E. Kolb, R. A. Cox, J. P. D. Abbatt, M. Ammann, E. J. Davis, D. J. Donaldson, B. C. Garrett, C. George, P. T. Griffiths, D. R. Hanson, M. Kulmala, G. McFiggans, U. P. oschl, I. Riipinen, M. J. Rossi, Y. Rudich, P. E. Wagner, P. M. Winkler, D. R. Worsnop, and C. D. O. Dowd. An overview of current issues in the uptake of atmospheric trace gases by aerosols and clouds. *Atmos. Chem. Phys.,*, 10:10561–10605, Jan 2010.

[121] T. Koop, B. Luo, A. Tsias, and T. Peter. Water activity as the determinant for

homogeneous ice nucleation in aqueous solutions. *Nature*, 406(6796):611–614, 2000.

[122] A. Kouchi, Y. Furukawa, and T. Kuroda. X-ray diffraction pattern of quasi-liquid layer on ice crystal surface. *Le Journal de Physique Colloques*, 48(C1):C1–675, 1987.

[123] C. Kresge, M. Leonowicz, W. Roth, J. Vartuli, and J. Beck. Ordered mesoporous molecular sieves synthesized by a liquid-crystal template mechanism. *Nature*, 359(6397):710–712, 1992.

[124] P. Kumar, S. Buldyrev, S. Chen, P. H. Poole, F. Sciortino, and H. E. Stanley. Relation between the widom line and the dynamic crossover in systems with a liquid–liquid phase transition. *Proceedings of the National Academy of Science*, 102(46):16558–16562, Jan 2005.

[125] A. Laio and F. L. Gervasio. Metadynamics: a method to simulate rare events and reconstruct the free energy in biophysics, chemistry and material science. *Reports on Progress in Physics*, 71(12):126601, 2008.

[126] D. Landau, S.-H. Tsai, and M. Exler. A new approach to monte carlo simulations in statistical physics: Wang-landau sampling. *American Journal of Physics*, 72:1294, 2004.

[127] D. P. Landau and K. Binder. *A guide to Monte Carlo simulations in statistical physics*. Cambridge university press, 2005.

[128] L. D. Landau and D. Ter Haar. *Collected papers of LD Landau*. Pergamon Press Oxford, 1965.

[129] A. L. Lavoisier. *Mémoire dans lequel on a pour objet de prouver que l'eau n'est point une substance simple, un élément proprement dit, mais qu'elle est susceptible de décomposition & de recomposition*. Académie des sciences, 1781.

[130] T. Li, D. Donadio, G. Russo, and G. Galli. Homogeneous ice nucleation from supercooled water. *Physical Chemistry Chemical Physics*, 13(44):19807–19813, 2011.

[131] Y. Li and G. A. Somorjai. Surface premelting of ice. *The Journal of Physical Chemistry C*, 111(27):9631–9637, 2007.

[132] D. R. Lide and T. J. Bruno. *CRC handbook of chemistry and physics*. CRC PressI Llc, 2012.

[133] D. T. Limmer and D. Chandler. The putative liquid-liquid transition is a liquid-solid transition in atomistic models of water. *Journal of Chemical Physics*, 135:134503, 2011.

[134] D. T. Limmer and D. Chandler. Phase diagram of supercooled water confined to hydrophilic nanopores. *Journal of Chemical Physics*, 137(4):044509, 2012.

[135] D. T. Limmer and D. Chandler. Corresponding states for mesostructure and dynamics of supercooled water. *Faraday Discussions, submitted*, 2013.

[136] D. T. Limmer and D. Chandler. The putative liquid-liquid transition is a liquid-solid transition in atomistic models of water, part ii. *Journal of Chemical Physics, in press*, 2013.

[137] D. T. Limmer, A. P. Willard, P. Madden, and D. Chandler. Hydration of metal surfaces can be dynamically heterogeneous and hydrophobic. *Proceedings of the National Academy of Sciences*, 110(11):4200–4205, 2013.

[138] R. Lipowsky. Critical surface phenomena at first-order bulk transitions. *Physical Review Letters*, 49(21):1575–1578, 1982.

[139] R. Lipowsky. Surface-induced order and disorder: Critical phenomena at first-order phase transitions. *Journal of Applied Physics*, 55:2485, 1984.

[140] R. Lipowsky and G. Gompper. Interface delocalization transitions in finite systems. *Physical Review B*, 29(9):5213, 1984.

[141] D. Liu, Y. Zhang, C.-C. Chen, C.-Y. Mou, P. H. Poole, and S.-H. Chen. Observation of the density minimum in deeply supercooled confined water. *Proceedings of the National Academy of Sciences*, 104(23):9570–9574, 2007.

[142] L. Liu, S.-H. Chen, A. Faraone, C.-W. Yen, and C.-Y. Mou. Pressure dependence of fragile-to-strong transition and a possible second critical point in supercooled confined water. *Physical Review Letters*, 95(11):117802, 2005.

[143] L. Liu, S.-H. Chen, A. Faraone, C.-W. Yen, C.-Y. Mou, A. I. Kolesnikov, E. Mamontov, and J. Leao. Quasielastic and inelastic neutron scattering investigation of fragile-to-strong crossover in deeply supercooled water confined in nanoporous silica matrices. *Journal of Physics: Condensed Matter*, 18:S2261–S2284, Jan 2006.

[144] Y. Liu, J. C. Palmer, A. Z. Panagiotopoulos, and P. G. Debenedetti. Liquid-liquid transition in st2 water. *Journal of Chemical Physics*, 137(21):214505–214505, 2012.

[145] Y. Liu, A. Z. Panagiotopoulos, and P. G. Debenedetti. Low-temperature fluid-phase behavior of st2 water. *Journal of Chemical Physics*, 131:104508, 2009.

[146] T. Loerting and N. Giovambattista. Amorphous ices: experiments and numerical simulations. *Journal of Physics: Condensed Matter*, 18(50):R919, 2006.

[147] T. Loerting, C. Salzmann, I. Kohl, E. Mayer, and A. Hallbrucker. A second distinct structural ÒstateÓ of high-density amorphous ice at 77 k and 1 bar. *Physical Chemistry Chemical Physics*, 3(24):5355–5357, 2001.

[148] A. Luzar and D. Chandler. Effect of environment on hydrogen bond dynamics in liquid water. *Physical Review Letters*, 76(6):928–931, 1996.

[149] F. Mallamace, M. Broccio, C. Corsaro, A. Faraone, U. Wanderlingh, L. Liu, C.-Y. Mou, and S. H. Chen. The fragile-to-strong dynamic crossover transition in confined water: nuclear magnetic resonance results. *Journal of Chemical Physics*, 124:161102, Jan 2006.

[150] R. Mancinelli, S. Imberti, A. K. Soper, K. H. Liu, C. Y. Mou, F. Bruni, and M. A. Ricci. Multiscale approach to the structural study of water confined in mcm41. *Journal of Chemical Physics B*, 113:16169–16177, Jan 2009.

[151] G. J. Martyna, D. J. Tobias, and M. L. Klein. Constant pressure molecular dynamics algorithms. *Journal of Chemical Physics*, 101:4177, 1994.

[152] O. Matsuoka, E. Clementi, and M. Yoshimine. Ci study of the water dimer potential surface. *Journal of Chemical Physics*, 64:1351, 1976.

[153] P. F. McMillan. Polyamorphic transformations in liquids and glasses. *J. Mater. Chem.*, 14(10):1506–1512, 2004.

[154] N. Metropolis, A. W. Rosenbluth, M. N. Rosenbluth, A. H. Teller, and E. Teller. Equation of state calculations by fast computing machines. *Journal of Chemical Physics*,

21:1087, 1953.

[155] A. Michaelides, V. Ranea, P. De Andres, and D. King. General model for water monomer adsorption on close-packed transition and noble metal surfaces. *Physical Review Letters*, 90(21):216102, 2003.

[156] B. Militzer and H. F. Wilson. New phases of water ice predicted at megabar pressures. *Physical Review Letters*, 105(19):195701, 2010.

[157] O. Mishima, L. D. Calvert, and E. Whalley. An apparently first-order transition between two amorphous phases of ice induced by pressure. *Nature*, 314(6006):76–78, 1985.

[158] O. Mishima and H. E. Stanley. The relationship between liquid, supercooled and glassy water. *Nature*, 396(6709):329–335, 1998.

[159] H. Miyagawa, Y. Hiwatari, B. Bernu, and J. Hansen. Molecular dynamics study of binary soft-sphere mixtures: Jump motions of atoms in the glassy state. *Journal of Chemical Physics*, 88:3879, 1988.

[160] S. Miyamoto and P. Kollman. Settle: an analytical version of the shake and rattle algorithm for rigid water models. *Journal of Computational Chemistry*, 13(8):952–962, 1992.

[161] V. Molinero and E. B. Moore. Water modeled as an intermediate element between carbon and silicon. *Journal of Physical Chemistry B*, 113(13):4008, 2009.

[162] E. B. Moore, J. Allen, and V. Molinero. Liquid-ice coexistence below the melting temperature for water confined in hydrophilic and hydrophobic nanopores. *Journal of Chemical Physics C.*, 116:7507–7514, Jan 2012.

[163] E. B. Moore, E. de La Llave, K. Welke, D. A. Scherlis, and V. Molinero. Freezing, melting and structure of ice in a hydrophilic nanopore. *Physical Chemistry Chemical Physics*, 12(16):4124–4134, 2010.

[164] E. B. Moore and V. Molinero. Growing correlation length in supercooled water. *Journal of Chemical Physics*, 130:244505, 2009.

[165] E. B. Moore and V. Molinero. Ice crystallization in waterÕs Òno-manÕs landÓ. *Journal of Chemical Physics*, 132:244504, 2010.

[166] E. B. Moore and V. Molinero. Structural transformation in supercooled water controls the crystallization rate of ice. *Nature*, 479(7374):506–508, 2011.

[167] K. Murata and H. Tanaka. Liquid–liquid transition without macroscopic phase separation in a water–glycerol mixture. *Nature Materials*, 11:436–443, 2012.

[168] A. Narten and H. Levy. Liquid water: Molecular correlation functions from x-ray diffraction. *Journal of Chemical Physics*, 55:2263, 1971.

[169] D. Nelson, T. Piran, and S. Weinberg. Statistical mechanics of membranes and surfaces, volume 5 of jerusalem winter school for theoretical physics, 1989.

[170] R. Nelson, M. R. Sawaya, M. Balbirnie, A. Ø. Madsen, C. Riekel, R. Grothe, and D. Eisenberg. Structure of the cross-β spine of amyloid-like fibrils. *Nature*, 435(7043):773–778, 2005.

[171] S. Neshyba, E. Nugent, M. Roeselová, and P. Jungwirth. Molecular dynamics study of ice- vapor interactions via the quasi-liquid layer. *The Journal of Physical Chemistry*

C, 113(11):4597–4604, 2009.

[172] A. Nilsson. private communication, 2011.

[173] M. Oguni, Y. Kanke, A. Nagoe, and S. Namba. Calorimetric study of water's glass transition in nanoscale confinement, suggesting a value of 210 k for bulk water. *Journal of Physical Chemistry B*, 115(48):14023–14029, Aug 2011.

[174] A. J. Patel, P. Varilly, D. Chandler, and S. Garde. Quantifying density fluctuations in volumes of all shapes and sizes using indirect umbrella sampling. *Journal of statistical physics*, 145(2):265–275, 2011.

[175] L. Pauling. The structure and entropy of ice and of other crystals with some randomness of atomic arrangement. *Journal of the American Chemical Society*, 57(12):2680–2684, 1935.

[176] M. K. Petersen, S. S. Iyengar, T. J. Day, and G. A. Voth. The hydrated proton at the water liquid/vapor interface. *The Journal of Physical Chemistry B*, 108(39):14804–14806, 2004.

[177] S. Plimpton. Fast parallel algorithms for short-range molecular dynamics. *Journal of Computational Physics*, 117(1):1–19, 1995.

[178] A. Pohorille, C. Jarzynski, and C. Chipot. Good practices in free-energy calculations. *Journal of Physical Chemistry B*, 114(32):10235–10253, 2010.

[179] A. Polian and M. Grimsditch. New high-pressure phase of h_ {2} o: Ice x. *Physical review letters*, 52(15):1312–1314, 1984.

[180] P. H. Poole, S. R. Becker, F. Sciortino, and F. W. Starr. Dynamical behavior near a liquid–liquid phase transition in simulations of supercooled water. *The Journal of Physical Chemistry B*, 115(48):14176–14183, 2011.

[181] P. H. Poole, R. K. Bowles, I. Saika-Voivod, and F. Sciortino. Free energy surface of st2 water near the liquid-liquid phase transition. *Journal of Chemical Physics*, 138:034505, 2013.

[182] P. H. Poole, U. Essmann, F. Sciortino, and H. E. Stanley. Phase diagram for amorphous solid water. *Physical Review E*, 48(6):4605, 1993.

[183] P. H. Poole, T. Grande, C. A. Angell, and P. F. McMillan. Polymorphic phase transitions in liquids and glasses. *Science*, 275(5298):322–323, 1997.

[184] P. H. Poole, I. Saika-Voivod, and F. Sciortino. Density minimum and liquid–liquid phase transition. *Journal of Physics: Condensed Matter*, 17(43):L431, 2005.

[185] P. H. Poole, F. Sciortino, U. Essmann, and H. E. Stanley. Phase behaviour of metastable water. *Nature*, 360(6402):324–328, 1992.

[186] P. H. Poole, F. Sciortino, T. Grande, H. E. Stanley, and C. A. Angell. Effect of hydrogen bonds on the thermodynamic behavior of liquid water. *Physical Review Letters*, 73(12):1632–1635, 1994.

[187] K. R. Popper. Objective knowledge: an evolutionary approach. clarendon, 1972.

[188] D. Rasmussen, A. MacKenzie, C. Angell, and J. Tucker. Anomalous heat capacities of supercooled water and heavy water. *Science*, 181:342–344, 1973.

[189] A. Reinhardt, J. P. Doye, E. G. Noya, and C. Vega. Local order parameters for use in driving homogeneous ice nucleation with all-atom models of water. *Journal of Chemical*

Physics, 137(19):194504–194504, 2012.

[190] F. Ritort and P. Sollich. Glassy dynamics of kinetically constrained models. *Advances in Physics*, 52(4):219–342, 2003.

[191] R. Rosenberg. Why is ice slippery? *Physics Today*, 58:50, 2005.

[192] J. S. Rowlinson and B. Widom. *Molecular theory of capillarity*, volume 8. Courier Dover Publications, 2002.

[193] V. Sadtchenko, M. Brindza, M. Chonde, B. Palmore, and R. Eom. The vaporization rate of ice at temperatures near its melting point. *Journal of Chemical Physics*, 121:11980, 2004.

[194] S. Sastry and C. Angell. Liquid–liquid phase transition in supercooled silicon. *Nature Materials*, 2(11):739–743, 2003.

[195] K. Schmidt-Rohr and H. Spiess. Nature of nonexponential loss of correlation above the glass transition investigated by multidimensional nmr. *Physical Review Letters*, 66(23):3020–3023, 1991.

[196] F. Sciortino, I. Saika-Voivod, and P. H. Poole. Study of the st2 model of water close to the liquid–liquid critical point. *Physical Chemistry Chemical Physics*, 13(44):19759–19764, 2011.

[197] J. V. Sengers and J. M. H. L. Sengers. Thermodynamic behavior of fluids near the critical point. *Annual Review of Physical Chemistry*, 37:189–222, Jan 1986.

[198] M. Shirts and J. Chodera. Statistically optimal analysis of samples from multiple equilibrium states. *Journal of Chemical Physics*, 129(12), 2008.

[199] J. I. Siepmann and M. Sprik. Influence of surface topology and electrostatic potential on water/electrode systems. *Journal of Chemical Physics*, 102:511, 1995.

[200] B. Smit and D. Frenkel. Vapor–liquid equilibria of the two-dimensional lennard-jones fluid (s). *Journal of Chemical Physics*, 94(8):5663–5668, 1991.

[201] E. Smith. Calculating the pressure in simulations using periodic boundary conditions. *Journal of Statistical Physics*, 77(1):449–472, 1994.

[202] A. K. Soper. Density minimum in supercooled confined water. *Proceedings of the National Academy of Science*, 108(47):E1192, 2011.

[203] A. K. Soper. Density profile of water confined in cylindrical pores in mcm-41 silica. *Journal of Physics: Condensed Matter*, 24:064107, Jan 2012.

[204] A. K. Soper and M. A. Ricci. Structures of high-density and low-density water. *Physical Review Letters*, 84(13):2881–2884, 2000.

[205] T. Speck and D. Chandler. Constrained dynamics of localized excitations causes a non-equilibrium phase transition in an atomistic model of glass formers. *Journal of Chemical Physics*, 136:184509, 2012.

[206] R. Speedy and C. Angell. Isothermal compressibility of supercooled water and evidence for a thermodynamic singularity at- 45 c. *Journal of Chemical Physics*, 65(3):851, 1976.

[207] P. J. Steinhardt, D. R. Nelson, and M. Ronchetti. Bond-orientational order in liquids and glasses. *Physical Review B*, 28(2):784, 1983.

[208] O. Steinhauser. Reaction field simulation of water. *Molecular Physics*, 45(2):335–348, 1982.

[209] F. H. Stillinger. Theory and molecular models for water. *Advances in Chemical Physics*, 31:1–101, 1975.

[210] F. H. Stillinger and A. Rahman. Improved simulation of liquid water by molecular dynamics. *Journal of Chemical Physics*, 60:1545, 1974.

[211] F. H. Stillinger and T. Weber. Computer simulation of local order in condensed phases of silicon. *Physical Review B*, 31(8):5262, 1985.

[212] K. Stokely, M. Mazza, H. Stanley, and G. Franzese. Effect of hydrogen bond cooperativity on the behavior of water. *Proceedings of the National Academy of Sciences*, 107(4):1301, 2010.

[213] S. F. Swallen, P. A. Bonvallet, R. J. McMahon, and M. Ediger. Self-diffusion of tris-naphthylbenzene near the glass transition temperature. *Physical Review Letters*, 90(1):015901, 2003.

[214] M. Tatarkhanov, D. F. Ogletree, F. Rose, T. Mitsui, E. Fomin, S. Maier, M. Rose, J. I. CerdĞ, and M. Salmeron. Metal-and hydrogen-bonding competition during water adsorption on pd (111) and ru (0001). *Journal of the American Chemical Society*, 131(51):18425–18434, 2009.

[215] P. R. Ten Wolde, M. J. Ruiz-Montero, and D. Frenkel. Numerical evidence for bcc ordering at the surface of a critical fcc nucleus. *Physical Review Letters*, 75(14):2714–2717, 1995.

[216] P. A. Thiel and T. E. Madey. The interaction of water with solid surfaces: fundamental aspects. *Surface Science Reports*, 7(6):211–385, 1987.

[217] H. Touchette. The large deviation approach to statistical mechanics. *Physics Reports*, 478(1):1–69, 2009.

[218] D. Turnbull. Formation of crystal nuclei in liquid metals. *Journal of Applied Physics*, 21(10):1022–1028, Jan 1950.

[219] R. Vácha, D. Horinek, M. L. Berkowitz, and P. Jungwirth. Hydronium and hydroxide at the interface between water and hydrophobic media. *Physical Chemistry Chemical Physics*, 10(32):4975–4980, 2008.

[220] N. G. Van Kampen. *Stochastic processes in physics and chemistry*, volume 1. North holland, 1992.

[221] P. Varilly and D. Chandler. Water evaporation: A transition path sampling study. *The Journal of Physical Chemistry B*, 2012.

[222] V. Vasisht, S. Saw, and S. Sastry. Liquid-liquid critical point in supercooled silicon. *Nature Physics*, 7(7):549–553, 2011.

[223] C. Vega and J. L. Abascal. Relation between the melting temperature and the temperature of maximum density for the most common models of water. *Journal of Chemical Physics*, 123:144504, 2005.

[224] A. Voronel, E. Veliyulin, V. S. Machavariani, A. Kisliuk, and D. Quitmann. Fractional stokes-einstein law for ionic transport in liquids. *Physical Review Letters*, 80(12):2630–2633, 1998.

[225] W. Wagner, T. Riethmann, R. Feistel, and A. H. Harvey. New equations for the sublimation pressure and melting pressure of h2o ice ih. *Journal of Physical and*

Chemical Reference Data, 40(4):043103–043103, 2011.

[226] M. Watkins, D. Pan, E. Wang, A. Michaelides, J. VandeVondele, and B. Slater. Large variation of vacancy formation energies in the surface of crystalline ice. *Nature materials*, 10(10):794–798, 2011.

[227] J. D. Weeks, D. Chandler, and H. C. Andersen. Role of repulsive forces in determining the equilibrium structure of simple liquids. *Journal of Chemical Physics*, 54:5237, 1971.

[228] X. Wei, P. B. Miranda, and Y. Shen. Surface vibrational spectroscopic study of surface melting of ice. *Physical Review Letters*, 86(8):1554–1557, 2001.

[229] K. T. Wikfeldt, C. Huang, A. Nilsson, and L. G. Pettersson. Enhanced small-angle scattering connected to the widom line in simulations of supercooled water. *Journal of Chemical Physics*, 134:214506, 2011.

[230] K. T. Wikfeldt, A. Nilsson, and L. G. M. Pettersson. Spatially inhomogeneous bimodal inherent structure of simulated liquid water. *Physical Chemistry Chemical Physics*, 13(44):19918–19924, 2011.

[231] N. Wilding and J. Magee. Phase behavior and thermodynamic anomalies of core-softened fluids. *Physical Review E*, 66(3):031509, 2002.

[232] A. P. Willard and D. Chandler. Instantaneous liquid interfaces. *The Journal of Physical Chemistry B*, 114(5):1954–1958, 2010.

[233] A. P. Willard, D. T. Limmer, P. A. Madden, and D. Chandler. Characterizing heterogeneous dynamics at hydrated electrode surfaces. *Journal of Chemical Physics, in press*, 2013.

[234] A. P. Willard, S. K. Reed, P. A. Madden, and D. Chandler. Water at an electrochemical interfaceÑa simulation study. *Faraday discussions*, 141:423–441, 2009.

[235] L. Xu, P. Kumar, S. V. Buldyrev, S.-H. Chen, P. H. Poole, F. Sciortino, and H. E. Stanley. Relation between the widom line and the dynamic crossover in systems with a liquid–liquid phase transition. *Proceedings of the National Academy of Sciences of the United States of America*, 102(46):16558–16562, 2005.

[236] L. Xu, F. Mallamace, Z. Yan, F. W. Starr, S. V. Buldyrev, and H. E. Stanley. Appearance of a fractional stokes–einstein relation in water and a structural interpretation of its onset. *Nature Physics*, 5(8):565–569, 2009.

[237] L. Xu and V. Molinero. Liquid-vapor oscillations of water nanoconfined between hydrophobic disks: Thermodynamics and kinetics. *Journal of Physical Chemistry B*, 114(21):7320–7328, Jan 2010.

[238] M. Yamada, S. Mossa, H. E. Stanley, and F. Sciortino. Interplay between time-temperature transformation and the liquid-liquid phase transition in water. *Physical Review Letters*, 88(19):195701, 2002.

[239] Y. Zhang, A. Faraone, W. Kamitakahara, C.-Y. Mou, J. Leao, S. Chang, and S. Chen. Reply to soper: Density measurement of confined water with neutron scattering. *Proceedings of the National Academy of Science*, 108(47):E1193–E1194, 2011.

[240] Y. Zhang, A. Faraone, W. A. Kamitakahara, K.-H. Liu, C.-Y. Mou, J. B. Leão, S. Chang, and S.-H. Chen. Density hysteresis of heavy water confined in a nanoporous silica matrix. *Proceedings of the National Academy of Sciences*, 108(30):12206–12211,

2011.

[241] G. Zimbitas, M. E. Gallagher, G. R. Darling, and A. Hodgson. Wetting of mixed oh/ho layers on pt (111). *Journal of Chemical Physics*, 128:074701, 2008.

[242] R. Zwanzig. *Nonequilibrium statistical mechanics*. Oxford University Press, USA, 2001.